

Monolithic Q-switched and mode-locked lasers using liquid crystal modulators

Author:

Lei, Xinyue

Publication Date:

2021

DOI:

<https://doi.org/10.26190/unsworks/1615>

License:

<https://creativecommons.org/licenses/by/4.0/>

Link to license to see what you are allowed to do with this resource.

Downloaded from <http://hdl.handle.net/1959.4/100015> in <https://unsworks.unsw.edu.au> on 2024-05-02

Monolithic Q-switched and mode-locked lasers using liquid crystal modulators



Xinyue LEI

Supervisor: Prof F. Ladouceur

Dr L. Silvestri

Prof A. Fuerbach

Department of Engineering
University of New South Wales

This dissertation is submitted for the degree of

Doctor of Philosophy

1. THESIS TITLE & ABSTRACT

Thesis Title

Monolithic Q-switched and mode-locked lasers using liquid crystal modulators

Thesis Abstract

Recent innovations in the area of liquid crystals have led to the development of passive electro-optic liquid crystal transducers that enables a new approach to compact, monolithic, and even portable Q-switched and mode-locked lasers. My Ph.D. study concentrates on the liquid crystal cells with a thin gap filled with nano-scale pitch ferroelectric smectic-C* liquid crystals, of which the molecular arrangement can be continuously deformed by the electric fields, giving rise to the "deformed helix" mode of operation. The deformation of molecular helical structure gives rise to the electric field controlled birefringence and orientation of the optical axis, which illustrates the possibility of using the liquid crystal modulator as an active intracavity loss modulator in laser applications.

This thesis presents the basic liquid crystal physics, design, modeling approaches, and characterisation of liquid crystal modulator in great detail for readers to understand its basic principles. To theoretically study its performance when applied to the 1 μm Q-switched lasers, the numerical model was developed. The numerical model predicted that the pulse width can be reduced to 17 ns and the peak power can be enhanced to 1.15 kW, when the absorbed pump power, the external optical loss, and the temperature are optimised. To utilise this novel technique in the industry, the University of New South Wales, Macquarie University, and Lastek started the collaboration for the development of a commercial prototype of compact actively Q-switched lasers in 2017. Later, the operation wavelength range was extended further to 1.88 μm in Tm³⁺-doped ZBLAN waveguide chip lasers. The experimental results demonstrated that the shortest pulse duration was around 31 ns, which provided the peak power of 1.3 kW at the repetition rate of 200 Hz. Additionally, all-in-one fibre lasers operating at 1.55 μm were designed and experimentally developed in an all-fibre setup. The proposed all-in-one fibre lasers support CW, Q-switched, AM, and FM mode-locked operation modes, and the mode can be easily switched by applying different electrical signals.

The simulation and experimental results illustrate the feasibility of utilising liquid crystal modulators in lasers, nonlinear applications. Additionally, utilising this novel optical technology for the development of the new generation of neural interfaces, that can record activation potentials at different positions, is another ambitious goal to achieve in the future.

2. ORIGINALITY, COPYRIGHT & AUTHENTICITY STATEMENTS

ORIGINALITY STATEMENT

I hereby declare that this submission is my own work and to the best of my knowledge it contains no materials previously published or written by another person, or substantial proportions of material which have been accepted for the award of any other degree or diploma at UNSW or any other educational institution, except where due acknowledgement is made in the thesis. Any contribution made to the research by others, with whom I have worked at UNSW or elsewhere, is explicitly acknowledged in the thesis. I also declare that the intellectual content of this thesis is the product of my own work, except to the extent that assistance from others in the project's design and conception or in style, presentation and linguistic expression is acknowledged.

COPYRIGHT STATEMENT

I hereby grant the University of New South Wales or its agents a non-exclusive licence to archive and to make available (including to members of the public) my thesis or dissertation in whole or part in the University libraries in all forms of media, now or here after known. I acknowledge that I retain all intellectual property rights which subsist in my thesis or dissertation, such as copyright and patent rights, subject to applicable law. I also retain the right to use all or part of my thesis or dissertation in future works (such as articles or books).

For any substantial portions of copyright material used in this thesis, written permission for use has been obtained, or the copyright material is removed from the final public version of the thesis.

AUTHENTICITY STATEMENT

I certify that the Library deposit digital copy is a direct equivalent of the final officially approved version of my thesis.

3. INCLUSION OF PUBLICATIONS STATEMENT

UNSW is supportive of candidates publishing their research results during their candidature as detailed in the UNSW Thesis Examination Procedure.

Publications can be used in the candidate's thesis in lieu of a Chapter provided:

- The candidate contributed **greater than 50%** of the content in the publication and are the "primary author", i.e. they were responsible primarily for the planning, execution and preparation of the work for publication.
- The candidate has obtained approval to include the publication in their thesis in lieu of a Chapter from their Supervisor and Postgraduate Coordinator.
- The publication is not subject to any obligations or contractual agreements with a third party that would constrain its inclusion in the thesis.

The candidate has declared that **some of the work described in their thesis has been published and has been documented in the relevant Chapters with acknowledgement.**

A short statement on where this work appears in the thesis and how this work is acknowledged within chapter/s:

Chapter 4 - Modelling of actively Q-switched waveguide lasers is partially comprised of a journal article entitled "Numerical modelling and optimization of actively Q-switched waveguide lasers based on liquid crystal transducers" that I contribute to as the first author and published in the journal of OSA Optics Express in 2019.

Chapter 5 - Compact actively Q-switched waveguide lasers operating at 1 μm is partially comprised of one journal article entitled "Compact actively Q-switched laser for sensing applications" that I contribute to as the first author and published in the journal of Elsevier Measurement in 2021. This chapter also contains results from two conference papers that I contribute to as the first author and published in SPIE and IEEE Proceedings. One conference paper entitled "Compact design of Q-switched laser systems based on liquid crystal transducers" was presented on the Australian and New Zealand Conferences on Optics and Photonics (ANZCOP) in 2019 and the other one entitled "High Efficiency and Low Voltage Actively Q-Switched Yb-doped Waveguide Lasers Using a Liquid Crystal Modulator" was presented on the Asia Communications and Photonics Conference (ACP) in 2020.

Chapter 6 - All-in-one fiber lasers operating at 1.55 μm is partially comprised of one journal article entitled "All-in-one fiber laser based on a liquid crystal transducer" that I contribute to as the first author and published in the journal of IEEE Photonics Technology letter in 2019. This chapter also contains results from one conference paper entitled "All-in-one fiber laser based on liquid crystal transducer" that I contribute to as the first author and published in OSA Proceeding on the Advanced Photonics in 2018.

Appendix A - Other Liquid Crystal Related Research is partially comprised of three conference papers that I contribute to as a co-author and published in the SPIE Proceeding on the Australian and New Zealand Conferences on Optics and Photonics (ANZCOP) in 2019.

Acknowledge of the work of the other authors of this paper has been made at the beginning of the chapter as well as in my acknowledgements section.

Candidate's Declaration



I declare that I have complied with the Thesis Examination Procedure.

Declaration

I hereby declare that except where specific reference is made to the work of others, the contents of this dissertation are original and have not been submitted in whole or in part for consideration for any other degree or qualification in this, or any other university. This dissertation is my own work and contains nothing which is the outcome of work done in collaboration with others, except as specified in the text and Acknowledgements. This dissertation contains fewer than 65,000 words including appendices, bibliography, footnotes, tables and equations and has fewer than 150 figures.

Xinyue LEI

December 2021

Acknowledgements

From 2015 to 2021, I have been living and studying in Australia for six years. I still remember, when I first arrived in Australia, I didn't have any friends, and facing the unknown made me feel scared of the future in a new country. Looking back now, I think that moving to Australia for my Master's and Ph.D. studies is one of the best decisions I have ever made in my life. With mental and financial supports from my parents and friends and professional guidance and suggestions from my supervisors, collaborators, and colleagues, my Ph.D. study turns out to be an enjoyable and unforgettable experience.

First, I would like to acknowledge Professor François Ladouceur who supervised my Ph.D. study and provided financial supports for my research and living allowance through his grants. Working with Prof. François Ladouceur is a pleasant experience, because he always provided sufficient and helpful guidance for my research, encouraged me to face exciting challenges, and helped me solve practical problems. His attitude to research makes me understand how to be a respectable physicist and scientist. With his guidance and encouragement, I am no longer that young, shy woman and now become a mature Ph.D. student on my way towards a future research career. Meanwhile, I count myself very lucky to be selected in Prof. François Ladouceur's class in 2016, which opened the door for me in the research field of photonics particularly.

I would like to express my sincere gratitude to Dr. Leonardo Silvestri, who co-supervised my Ph.D. study and provided me with numerous suggestions and generous help for my research. I will remember the time we spent together exchanging new ideas, designing experiments, discussing experimental results, and writing papers. I am much obliged to you for your patience in the past four years.

Meanwhile, my heartfelt thanks go to my secondary supervisor Prof. Alex Fuerbach, who gave me a precious opportunity to be a visiting scholar at Macquarie University, allowing me to have access to their experimental facilities and conduct experiments in his labs. Working with Professor Alex Fuerbach makes me feel warm because no matter how stupid my questions are, he is always patient to answer them. His guidance and suggestions helped me obtain solid background knowledge of photonics and built my confidence in research. What I learned from Prof. Alex Fuerbach makes me become a confident and optimistic research student now.

In the past four years, I have received invaluable technical and spiritual supports from my current and previous colleagues in the University of New South Wales and Macquarie University: Professor Nigel Lovell, Professor Torsten Lehmann, Dr. Josiah Firth, Ms. Yingge Chen, Dr. Zourab Brodzeli, Mr. Frederik Crous, Dr. Amr Al Abed, Mr. Han Wang, Professor Michael Withford, Professor David Spence, Dr. Christoph Wieschendorf, Dr. Gayathri Bharathan, Dr. Simon Gross, Dr. Toney Teddy Fernandez, Dr. Benjamin Johnston, Dr. Alex Stokes, Ms. Nathalie Gouailhardou. Additionally, I would like to extend my gratitude to collaborators from our industrial partner Lastek Pty Ltd in Adelaide, Dr. Alex Stanco, and Dr. Victor Karaganov.

I would like to acknowledge the financial support provided by the Macquarie University from the Australian Research Council's Discovery Projects funding scheme (DP160104625), the Australian Research Council Centre of Excellence for Ultrahigh Bandwidth Devices for Optical Systems (CE110001018), Australian Cooperative Research Centres Projects Program (CRC-P-49) and the Office of Naval Research Global (N62909-18-1-2147). This work was performed in part at the Australian National Fabrication Facility (ANFF) (OptoFab Node and UNSW Node, NCRIS), utilizing NCRIS and NSW state government funding.

Last but not least, I would like to express my heartfelt thanks to my dear friends: Dr. Zhan Shi, Ms. Miao Li, Ms. Jian Zhang, Mr. Zongye(Jason) Wu, Mr. Hua Chai, Dr. Shibo Lu and Ms. Zhi Chen. They give me a lot of accompaniment and encouragement to help me overcome difficulties and get me through the hard times.

I would like to give my special thanks to Ms. Lu Hao, who brought me courage, confidence, and belief over three years of Ph.D. study. I believe she will have more opportunities to show her talents in research as a Ph.D. student and have a successful research career in the future.

List of publications

Journal papers

1. **Xinyue Lei**, Christoph Wieschendorf, Josiah Firth, Francois Ladouceur, Alex Fuerbach, and Leonardo Silvestri, "Numerical modelling and optimization of actively Q-switched waveguide lasers based on liquid crystal transducers," *Opt. Express*, vol. 27, pp. 8777–8791, 2019.
2. **Xinyue Lei**, Christoph Wieschendorf, Josiah Firth and Francois Ladouceur and Leonardo Silvestri and Alex Fuerbach, "All-in-one fiber laser based on a liquid crystal transducer," *IEEE Photonics Technology Letters*, vol. 31, no. 17, pp. 1409-1412, 2019.
3. **Xinyue Lei**, Christoph Wieschendorf, Lu Hao, Josiah Firth, Leonardo Silvestri, Simon Gross, Francois Ladouceur, Michael Withford, David Spence, and Alex Fuerbach, "Compact actively Q-switched laser for sensing applications," *Measurement*, 173:108631, 2021.
4. **Xinyue Lei**, Leonardo Silvestri and Francois Ladouceur, "Liquid Crystal Cell with Parallel Configuration Based Dynamic Birefringence Measurement," to be submitted.
5. Amr Al Abed, Yuan Wei, Reem M. Almasri, Han Wang, Josiah Firth, Yingge Chen, **Xinyue Lei**, Natalie Gouailhardou, Leonardo Silvestri, Torsten Lehmann, Francois Ladouceur, Nigel H. Lovell, "Passive sensing optrodes for electrophysiology," to be submitted.

Conference papers

1. **Xinyue Lei**, Christoph Wieschendorf, Alex Fuerbach, François Ladouceur, and Leonardo Silvestri, "All-in-one fiber laser based on liquid crystal transducer," in Advanced Photonics 2018 (BGPP, IPR, NP, NOMA, Sensors, Networks, SPPCom, SOF), OSA Technical Digest (online) (Optical Society of America, 2018), paper ITh4H.3.
2. **Xinyue Lei**, Victor Karaganov, Francois Ladouceur, Leonardo Silvestri, Alex Fuerbach, "Compact design of Q-switched laser systems based on liquid crystal transducers," Proc. SPIE 11200, AOS Australian Conference on Optical Fibre Technology (ACOFT) and Australian Conference on Optics, Lasers, and Spectroscopy (ACOLS), 2019.
3. François Ladouceur, **Xinyue Lei**, Yuan Wei, Josiah Firth, Alexander Fuerbach, Nigel Lovell, Leonardo Silvestri, "Towards the next generation of brain/machine interface," Proc. SPIE 11200, AOS Australian Conference on Optical Fibre Technology (ACOFT) and Australian Conference on Optics, Lasers, and Spectroscopy (ACOLS), 2019.
4. Han Wang, Udo Römer, **Xinyue Lei**, Yuan Wei, Amr Al Abed, Francois Ladouceur, Leonardo Silvestri, Nigel Lovell, "Towards bi-directional electro-optic neuronal interfaces," Proc. SPIE 11202, Biophotonics Australasia, 2019.
5. Yuan Wei, Amr Al Abed, Nathalie Gouailhardou, Han Wang, **Xinyue Lei**, François Ladouceur, Torsten Lehmann, Nigel H. Lovell, Leonardo Silvestri, "Optically measuring nerve activity based on an electro-optical detection system," Proc. SPIE 11202, Biophotonics Australasia, 2019.
6. **Xinyue Lei**, Lu Hao, Josiah Firth, Francois Ladouceur, Leonardo Silvestri, and Alex Fuerbach, "High Efficiency and Low Voltage Actively Q-Switched Yb-doped Waveguide Lasers Using a Liquid Crystal Modulator," In Asia Communications and Photonics Conference/International Conference on Information Photonics and Optical Communications 2020 (ACP/IPOC), page M4D.8. Optical Society of America, Post-deadline, 2020.

Abstract

Recent innovations in the area of liquid crystals have led to the development of passive electro-optic liquid crystal transducers that enables a new approach to compact, monolithic, and even portable Q-switched and mode-locked lasers. My Ph.D. study concentrates on the liquid crystal cells with a thin gap filled with nano-scale pitch ferroelectric smectic-C* liquid crystals, of which the molecular arrangement can be continuously deformed by the electric fields, giving rise to the "deformed helix" mode of operation. The deformation of molecular helical structure gives rise to the electric field controlled birefringence and orientation of the optical axis, which illustrates the possibility of using the liquid crystal modulator as an active intracavity loss modulator in laser applications.

This thesis presents the basic liquid crystal physics, design, modelling approaches, and characterisation of liquid crystal modulator in great detail for readers to understand its basic principles. To theoretically study its performance when applied to the 1 μm Q-switched lasers, a numerical model was developed. The numerical model predicted that the pulse width can be reduced to 17 ns and the peak power can be enhanced to 1.15 kW, when the absorbed pump power, the external optical loss, and the temperature are optimised. To utilise this novel technique in the industry, the University of New South Wales, Macquarie University, and Lastek started the collaboration for the development of a commercial prototype of compact actively Q-switched lasers in 2017. Later, the operation wavelength range was extended further to 1.88 μm in Tm^{3+} -doped ZBLAN waveguide chip lasers. The experimental results demonstrated that the shortest pulse duration was around 31 ns, which provided the peak power of 1.3 kW at the repetition rate of 200 Hz. Additionally, all-in-one fibre lasers operating at 1.55 μm were designed and experimentally developed in an all-fibre setup. The proposed

all-in-one fibre lasers support CW, Q-switched, AM, and FM mode-locked operation modes, and the mode can be easily switched by applying different electrical signals.

The simulation and experimental results illustrate the feasibility of utilising liquid crystal modulators in lasers, nonlinear applications. Additionally, utilising this novel optical technology for the development of the new generation of neural interfaces, that can record activation potentials at different positions, is another ambitious goal to achieve in the future.

Table of contents

List of publications	vi
List of figures	xiv
List of tables	xix
Nomenclature	xx
1 Research Motivation	1
1.1 Pulsed laser and applications	1
1.1.1 Laser radars or LIDARs	1
1.1.2 Continuum Generation	3
1.1.3 Pulsed laser ablation	6
1.2 Current actively Q-switched laser sources	9
1.3 Current actively mode-locked laser sources	15
1.4 Liquid crystal modulator and lasers	19
1.5 Research Objective	21
1.6 Outline of Thesis	22
2 Background Theory	25
2.1 History of liquid crystals	25
2.2 Basic Liquid Crystal Physics	26
2.2.1 Physical model and phase	27
2.2.2 Orientation of liquid crystals	30

2.2.3	Spontaneous polarization and structure of chiral smectic-C liquid crystals	31
2.3	Design of the liquid crystal device	34
2.4	Modelling approach	38
2.4.1	Jones matrix method	38
2.4.2	Mueller matrix method	41
2.4.3	Transfer matrix method	44
2.5	Femtosecond direct-written waveguide	48
2.5.1	Glass Material	48
2.5.2	Waveguide fabrication process	50
2.5.3	Waveguide geometry	51
3	Characterisation of liquid crystal devices	55
3.1	Deformed helix structure by electric fields	55
3.2	Birefringence, rotation of optical axes and tilt angle	58
3.3	Modulation depth	65
3.4	Optical transmission	70
4	Modelling of actively Q-switched waveguide lasers	72
4.1	Relevant publications	72
4.2	Liquid crystal cell design and characterisation	72
4.3	Numerical modelling for Q-switched waveguide lasers	77
4.4	Model Validation	80
4.5	Optimisation of Q-switched waveguide lasers	86
4.6	Summary	89
5	Compact actively Q-switched waveguide lasers operating at 1 μm	91
5.1	Relevant publications	91
5.2	Compact actively Q-switched laser for sensing applications	92
5.2.1	Theory and simulation	92

5.2.2	Material and methods	96
5.2.3	Results and discussion	99
5.2.4	Conclusion	103
5.3	Compact design of actively Q-switched waveguide lasers	103
5.3.1	Experimental setup	104
5.3.2	Experimental results	105
5.4	Summary	107
6	Q-switched Tm³⁺:ZBLAN waveguide lasers operating at 1.86 μm	108
6.1	Introduction	108
6.2	Femtosecond direct-written Tm ³⁺ :ZBLAN waveguide	109
6.3	Experimental setup	111
6.4	Laser Performance	114
6.5	Four wave mixing phenomenon	125
6.6	Summary	128
7	All-in-one fibre lasers operating at 1.55 μm	130
7.1	Relevant publications	130
7.2	Introduction	131
7.3	Experimental setup	131
7.4	Continuous-wave mode	134
7.5	Q-switching mode	135
7.5.1	Q-switched Laser Performance v.s. Cavity Length	135
7.5.2	Q-switched Laser Performance v.s. Duty Cycle	137
7.5.3	Optimised Configuration of Q-Switch Mode	139
7.6	Amplitude Modulation Mode-Locking Mode	141
7.6.1	Fundamentals of Amplitude Modulation Mode-Locking	141
7.6.2	Indication of AM Mode-Locking	143
7.6.3	AM Mode-Locking Performance v.s. Modulation Signal	146
7.6.4	AM Mode-Locking Performance v.s. Pump Power	148

7.6.5	AM Mode-Locking Output	149
7.7	Frequency Modulation Mode-Locking Mode	151
7.7.1	Fundamentals of Frequency Modulation Mode-Locking	152
7.7.2	Modified Liquid Crystal Modulator for Phase Modulation	153
7.7.3	FM Mode-Lock Output	155
7.7.4	FM Mode-Locking Performance v.s. Cavity Length	156
7.8	Summary	159
8	Conclusion and future work	160
8.1	Conclusion	160
8.2	Future work: fully monolithic actively Q-switched waveguide lasers	165
	References	168
	Appendix A Other Liquid Crystal Related Research	200
A.1	Liquid crystal optrode for electro-physiology recording	200
A.1.1	Improvement of the sensitivity of optrode	205
A.1.2	Fabrication of the multi-optrode device	208

List of figures

1.1	TOF Laser Range Finder	2
1.2	Supercontinuum Generation	5
1.3	Glass Material Ablation	7
1.4	Laser Ablation Inductively Coupled Plasma Mass Spectrometry (LA-ICP-MS)	8
1.5	Active Q-Switch	12
1.6	Mode-Lock Laser System	16
1.7	Liquid Crystal Display and Liquid Crystal based SLM	20
1.8	First Q-Switched Lasers Based on Liquid Crystals	21
1.9	Design of monolithic actively Q-switched waveguide lasers	22
2.1	Typical Shapes of Liquid Crystal Molecules	27
2.2	2D Representation of Liquid Crystal Phases	28
2.3	Orientation of a Rod-shaped Liquid Crystal Molecule	30
2.4	Schematic Diagram of the Structure of Chiral Smectic-C	33
2.5	Spontaneous Polarization of Chiral Smectic-C* Liquid Crystals	34
2.6	Design of Liquid Crystal Cells	35
2.7	Layered Structure of Liquid Crystal Cells	37
2.8	Typical Configuration of Liquid Crystal Modulators	39
2.9	Schematic of Forward and Backward Traveling Waves on LC Interfaces . .	45
2.10	Energy Level Diagrams of Er ³⁺ , Tm ³⁺ and Ho ³⁺ Ions in the ZBLAN Host .	49
2.11	Schematic of Femtosecond Direct Writing Method for Waveguide Fabrication Process	51

2.12	Refractive Index Profile of Femtosecond Direct Written Waveguides	52
2.13	Confinement Losses of Inscribed Waveguides as a Function of the Depressed Cladding Diameter From 10 μm To 24 μm	53
3.1	Deformation of Helix Structure Under Electric Fields	56
3.2	Microscopy Views of Liquid Crystal Cell under the Polarizer at Different Voltage Levels	57
3.3	Liquid Crystal Birefringence Measurement by Shin-Tson Wu	59
3.4	Experimental Setup for Liquid Crystal Birefringence Measurements	60
3.5	Normalized Reflection Intensities for Birefringence Measurements	62
3.6	Electric Field controlled Birefringence $\Delta n(E)$ v.s. Electric Field	63
3.7	Electric Field controlled Optical Axes Rotation $\Omega(E)$ v.s. Electric Field	64
3.8	Optical Responses of Liquid Crystal Modulators Under Sine Waves	65
3.9	Modulation Depth and Phase Shift v.s. Electric Field	66
3.10	Normalized Modulation Depth v.s. Signal Frequency	67
3.11	Bipolar and Uni-polar Waveforms	68
3.12	Optical Responses Under Bipolar and Uni-polar Waveforms	69
3.13	Optical Responses from Bipolar and Uni-polar Waveforms with Varying Frequencies	70
3.14	Modulation Depth Driven by Bipolar and Uni-polar Waveforms with Varying Frequencies	71
3.15	Optical Transmissions of Different Liquid Crystal Cells	71
4.1	Crossed Reflectance as a Function of Half-wave and Quarter-wave Plate Angles	75
4.2	Modulation Depth Measurement	76
4.3	100 % Modulation Depth of Liquid Crystal Modulator	76
4.4	Schematic of Yb-doped Waveguide Laser Setup for Modelling	80
4.5	Optical Responses of LC Modulator under Driving Signals	84
4.6	Simulation Results of Pulse Width and Peak Power from Numerical Model	85
4.7	Simulation Results of Output Power from Numerical Model	86

4.8	Optimisation of Q-switched Laser Pulses by Numerical Model	88
5.1	Two Types of Liquid Crystal Modulators	92
5.2	Schematic of Cross-Polarized Setup	93
5.3	Schematic of Optimised Cross-Polarized Setup	94
5.4	Laser Dynamics of a Slow Q-switch	97
5.5	Q-switched Laser Setup for Sensing Applications	97
5.6	Dynamics of Cavity Losses	99
5.7	Modulation Depth of Various LC Modulators	100
5.8	Effects of Duty Cycle on Laser Performance	101
5.9	Average Output Power and Pulse Width of Q-Switched Laser Pulses	102
5.10	Oscilloscope Trace and Emission Spectrum of Laser Output	103
5.11	Schematic of Optimised Yb-doped Waveguide Lasers	104
5.12	Slope Efficiency of Optimised Yb-doped Waveguide Lasers	105
5.13	Performance Parameters of Optimised Yb-doped Waveguide Laser Pulses	106
5.14	Shortest Pulse of Optimised Yb-doped Waveguide Lasers	106
6.1	Tm ³⁺ -doped ZBLAN Waveguide Chip	110
6.2	Experimental Setup of Tm ³⁺ -doped ZBLAN Waveguide Lasers	112
6.3	Laser cavity of Tm ³⁺ -doped ZBLAN Waveguide Lasers	114
6.4	Average Output Power v.s. Pump Power for Three Output Coupling Mirrors in the CW Mode without LC Cell	115
6.5	Average Output Power v.s. Pump Power in the CW Mode with/without LC Cell and Polarizer	116
6.6	Laser Performance v.s. Peak-to-peak Voltage of Applied Signal in the Q- Switch Mode	118
6.7	Laser Performance v.s. Repetition Rate of Applied Signals in the Q-Switch Mode	120
6.8	Laser Performance v.s. Pump Power in the Q-Switch Mode	122
6.9	Q-Switched Laser Pulse with the Shortest Pulse Width	123

6.10	Measured Optical Spectrum of Q-Switched Laser Pulses	124
6.11	Schematic of As ₂ Se ₃ Fibre Taper and Experimental Setup for Nonlinearity Study	127
6.12	Output Optical Spectrum of Q-switched Lasers from a As ₂ Se ₃ chalcogenide fibre taper	129
7.1	Schematic of All-in-one fibre Laser	131
7.2	Measured reflection of laser-inscribed FBG	133
7.3	Measured Optical Loss of 5 µm Thick Liquid Crystal Modulator	134
7.4	Average Output Power of CW Lasers in All-in-one fibre Laser System	135
7.5	Q-switched Laser Performance v.s. Cavity Length	136
7.6	Q-switched Laser Performance v.s. Duty Cycle	138
7.7	Q-switched laser pulses at 0.2 kHz	139
7.8	Q-switched Laser Performance v.s. Repetition Rate	140
7.9	Frequency and Time Domains of Active Mode-Locking	143
7.10	AM Mode Locking v.s. Modulation Frequency	144
7.11	RF Spectrum of AM Mode-Locking	145
7.12	AM Mode-Locking Performance v.s. Modulation Signal	147
7.13	AM Mode-Locking Performance v.s. Pump Power	149
7.14	AM Mode-Locked Pulses	150
7.15	Optical Spectra of AM Mode-Locking Pulses	151
7.16	Pulse Transmission Through a FM (Phase) Modulator	152
7.17	Configuration of Liquid Crystal Cell for FM Mode-Lock	155
7.18	FM Mode-Locked Pulses	156
7.19	FM Mode-Locked Pulses at Different Modulation Frequency	157
7.20	FM Mode-Locking Performance v.s. Cavity Length	158
8.1	Schematic of Fully Monolithic Q-switched Laser Setup	166
A.1	Experimental Setup of Two Channel Electro-physiology Recording System Using LC Transducer	202

A.2	Optical and Electrical Recordings from Rabbit Nerve Preparation in vitro at Two Positions in Parallel	203
A.3	Baseline Noise and Optical Recording Without Averaging from Rabbit Nerve Preparation in Vitro	204
A.4	Ex-vivo Cardiac Electro-physiology Recording Setup	205
A.5	One Cardiac Electro-physiology Recording Using LC Transducer	206
A.6	Experimental Setup for the Characterisation of LC Transducers	207
A.7	Sensitivity and Bandwidth Measurement Results of Existing LC Transducers with Different LC Mixtures or Alignment Materials	208
A.8	Prototype of Multiple Optrode Array Device	209
A.9	64-channel Multi-optrode Device with Inscribed Waveguides	210
A.10	Pre-assembled Two-dimensional Fibre Array	212

List of tables

1.1	List of Publications on Q-switched Waveguide Lasers	14
1.2	List of Publications on Mode-Locked fibre Lasers	18
2.1	Summary of Dimensional Parameters for Liquid Crystal Cells in This Work	36
2.2	Summary of Thickness Parameters in the Layered Structure of Liquid Crystal Cells	38
2.3	Geometric Parameters, Doping Ions and Emission Wavelengths of the Femtosecond Direct Written waveguides	53
4.1	Optical and Physical Parameters in Numerical Model	82
4.2	Prediction of Q-switched Lasers with Low Optical Losses and/or High Pump Power	87
4.3	Prediction of Q-switched Lasers at Temperature of 55 °C	89
5.1	Typical Values of Crucial Variables in Modelling	96
5.2	Cavity Losses of Q-switched Laser Setup for Sensing Applications	98
6.1	Slope Efficiencies for Three Output Coupling Mirrors in the CW Mode without LC Cell	115
6.2	Slope Efficiencies and Pump Thresholds With/Without LC Modulator	117
7.1	Modulation Frequency for AM Mode-Locking	146
7.2	Modulation Frequency for FM Mode-Locking	154

Nomenclature

Acronyms / Abbreviations

AM amplitude modulation

AOM acousto-optic modulator

CPO chirped pulse oscillator

CW continuous-wave

DAQ data acquisition

LA-ICP-MS laser ablation inductively coupled plasma mass spectrometry

DESI-MS desorption electrospray ionization mass spectrometry

DFH deformed helix ferroelectric

DHFLC deformed-helix ferroelectric liquid crystal

DWDM dense wavelength division multiplexing

EAM electro-anatomical mapping

EOM electro-optic modulator

FBG fibre Bragg grating

FLDW femtosecond laser direct-writing

FM	frequency modulation
FPD	flat panel display
FWHM	full width at half maximum
FWM	four-wave mixing
GRIN	gradient index
HMF	heavy metal fluoride
IMITO	index-matched indium tin oxide
ITO	indium tin oxide
LCD	liquid crystal display
LED	light-emitting diode
MALDI-MS	matrix-assisted laser desorption/ionization mass spectrometry
MEA	multi-electrode array
MIR	mid-infrared
MOA	multi-optrode array
NIR	near-infrared
OLED	organic light-emitting diode
OSA	Optical Spectrum Analyser
PBS	polarizing beamsplitter
PCF	photonic crystal fibre
PC	personal computer

PLA	pulsed laser ablation
PM	polarization-maintaining
ppb	parts per billion
RF	radio-frequency
RIP	refractive index profile
SA	saturable absorber
SBS	stimulated Brillouin scattering
SIMS	secondary ion mass spectrometry
SLM	spatial light modulator
SMF	single-mode fibre
SNR	signal-to-noise ratio
SPM	self-phase modulation
SRS	stimulated Raman scattering
SSF	surface-stabilized ferroelectric
TOF	time-of-flight
TPA	two-photon absorption
TSV	through silicon via
UAV	unmanned aerial vehicle
UV	ultraviolet
VOA	variable optical attenuator

WDM wavelength division multiplexer

XPM cross-phase modulation

ZDW zero-dispersion wavelength

Chapter 1

Research Motivation

1.1 Pulsed laser and applications

There are two key methods of generating short pulses of laser light, mode-locking and Q-switching. Mode-locking generates ultra-short laser pulses between femto-second and pico-second duration with a pulse energy of tens of nanojoules, while Q-switched laser sources generate longer pulses in the hundreds of pico-seconds to micro-second regime with a larger pulse energy of several micro-joules and even milli-joules. In terms of the repetition rate, mode-locked laser pulses are typically generated at repetition rates range from MHz to GHz, while Q-switched laser pulses normally occur at repetition rates of tens of kHz. With a very short , intense burst of laser output, there are many practical applications, including LIDAR, continuum generation and pulsed laser ablation (PLA).

1.1.1 Laser radars or LIDARs

Laser radar or LIDAR as an optical detection system for determining the range, angle, or velocity of objects, started to be studied and widely developed in the early 1960s, motivated by the invention of lasers in 1960 by Theodore H. Maiman [1–3]. Unlike the alternative detection methods, such as microwave radar [4, 5] or passive electro-optic sensors [6], LIDARs are relatively inexpensive and reliable, which makes it much more competitive compared to its

counterparts. The simplest kind of LIDARs can be designed based on a laser pulse and one single photo-detector, by which the distance between the light source and a target can be calculated from the measured time delay between the incident pulse and reflected pulse, if the speed of light is known. Considering the resolution of measurements, the short laser pulses are desired, because the reflected pulse can be more easily distinguished from the incident pulse. With the rapid development and significant progress of laser technologies, short laser pulses with higher energy and efficiency generated from Q-switched lasers facilitated the revolution of the LIDAR technique [7, 8]. The example of time-of-flight (TOF) laser range finder using a short laser pulse has been introduced in [7] with full width at half maximum (FWHM) ≈ 35 ps. By using this device, the time delay between the transmitted pulse and the received pulse can be precisely measured to evaluate the distance between the light source and target with a high resolution. The precision of this measurement was mainly determined by the total noise level and the signal-to-noise ratio (SNR) in the receiver channel. The example of basic blocks of the TOF laser range finder and laser pulses measured at transmitter and receiver are shown in Fig. 1.1.

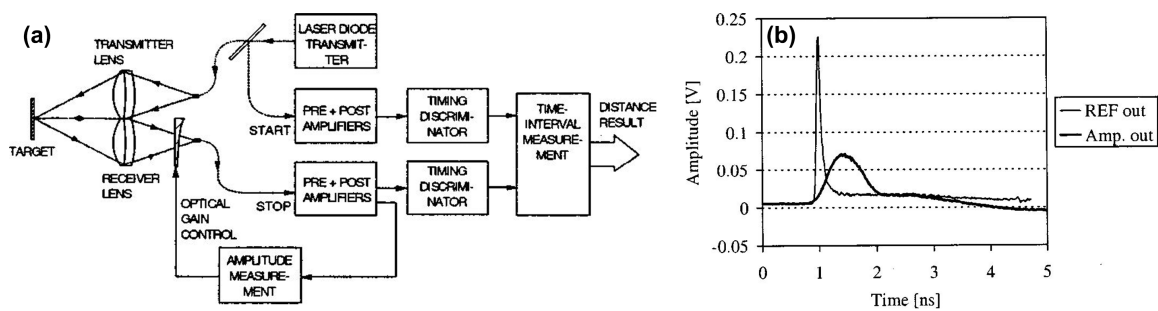


Fig. 1.1 (a) Block diagram of the TOF laser range finder and (b) Measured laser pulses at both transmitter and receiver in the system. Images are from [7].

The basic structure is composed of a transmitter, two receivers. At the transmitter, the Q-switched laser source generates high-power pulses. For example, a commercially available single heterostructure (SH) laser was used in some previous work to provide laser pulses with pulse duration of 30–65 ps and power of 200 W. At the receiver, the photo-detector needs to have some specific properties, including small noise, large enough bandwidth, and linearity

over a wide dynamic range. The precision of this method is affected by both amplifier (e.g. noise levels and bandwidth) and input pulse (e.g. amplitude and rise/fall times). To improve the final precision, averaging several pulses is usually used in the TOF distance measurement. The transmitted laser pulse from the transmitter and the response from the receiver are presented in Fig. 1.1 (b). With the compactness and portability of Q-switched laser sources, laser radars have been used in some military applications, such as range finding and weapon guidance. In addition to the military applications, pulsed laser sources also facilitate the development of 2-D and 3-D laser imaging systems [9], remote sensing for the atmosphere and the ocean, self-driving cars, and unmanned aerial vehicles (UAVs), commonly known as drones for multiple commercial and military applications [10–12].

1.1.2 Continuum Generation

Since nonlinear optical effects were observed for the first time, nonlinear effects have been widely discussed and deeply studied in recent years. In general, nonlinear optical effects include self-phase modulation (SPM) [13–16], cross-phase modulation (XPM) [17–19], stimulated Raman scattering (SRS) [20–24], and four-wave mixing (FWM) [25–29]. The study on the nonlinear optical effects has attracted numerous attention because of its great potential to be utilised for a wide variety of applications, including spectroscopy, medical imaging, remote sensing, breath analysis, and optical coherence tomography. Spectral broadening and the generation of new frequency components are inherent features of nonlinear optics and have been studied intensively since the early 1960s. In principle, when a highly nonlinear fibre is utilised to propagate short and intense laser pulses, the nonlinear effects and dispersive properties of the highly nonlinear fibre affect both temporal and spectral properties of the laser pulses. In the optical spectrum, new frequencies are generated by the nonlinear effects and dispersive properties and the presence of highly intense laser pulses. According to the physical mechanisms of continuum generation, if the pulse width of the laser pulses is several femtoseconds or picoseconds, a high-order soliton can be excited by the intense laser pulses in the anomalous dispersion regime. As a result, the spectral broadening occurs and extreme spectral broadening (e.g. over 100 THz) is regarded as

supercontinuum generation. For broadband emission, the SPM through the nonlinear refractive index n_2 is an important mechanism. This effect is often combined with drastic changes in the beam geometry, i.e., optical self-focusing via n_2 . However, the spectral broadening introduced by the sole effect of SPM is typically limited to tens of nanometers by two-photon absorption (TPA) [13, 14, 18, 30], because TPA enables the simultaneous absorption of two photons for energy transition from the ground state to a higher energy state, which introduces an additional propagation loss over the nonlinear fibre or material. To overcome the limitation caused by TPA and broaden the optical spectrum by a larger factor, a lot of efforts were made on numerical and experimental studies of the spectral and temporal characteristics of the supercontinuum generation in photonic crystal fibre (PCF) from the femtosecond to the CW regime, including SRS, the processes of soliton fission and dispersive wave generation [31].

When narrow-band incident ultrashort optical pulses propagate through a strongly nonlinear component, they will undergo extreme nonlinear spectral broadening to generate broadband or spectrally continuous output (e.g. white light), which is called supercontinuum generation. The earliest supercontinuum generation was observed and reported by Alfano and Shapiro in bulk glass [32, 33]. After that, the process of supercontinuum generation has been studied in different nonlinear media, including solids [34], gases [35], various types of waveguide [36], and PCFs [37–39].

Since supercontinuum generation can generate a broadband optical output, it has a wide variety of applications, e.g. spectroscopy [42], pulse compression [43, 44], broadband or tunable laser sources [45, 46]. In optical communication systems, the broadband supercontinuum generation spectra have shown the possibility to create multiwavelength optical sources for dense wavelength division multiplexing (DWDM) via spectral slicing [47, 48]. The example of mid-infrared (MIR) supercontinuum generation spanning from 2 to 6 μm [41] and from 1.8 to 9.5 μm [40] are shown in Fig. 1.2. Most supercontinuum generation experiments are demonstrated with ultra-short pulses with a pulse duration of tens of femtoseconds from mode-locked fibre lasers [49, 50]. In that case, the SPM, soliton effects, and pulse walk-off are more dominant, and the generalized nonlinear Schrödinger

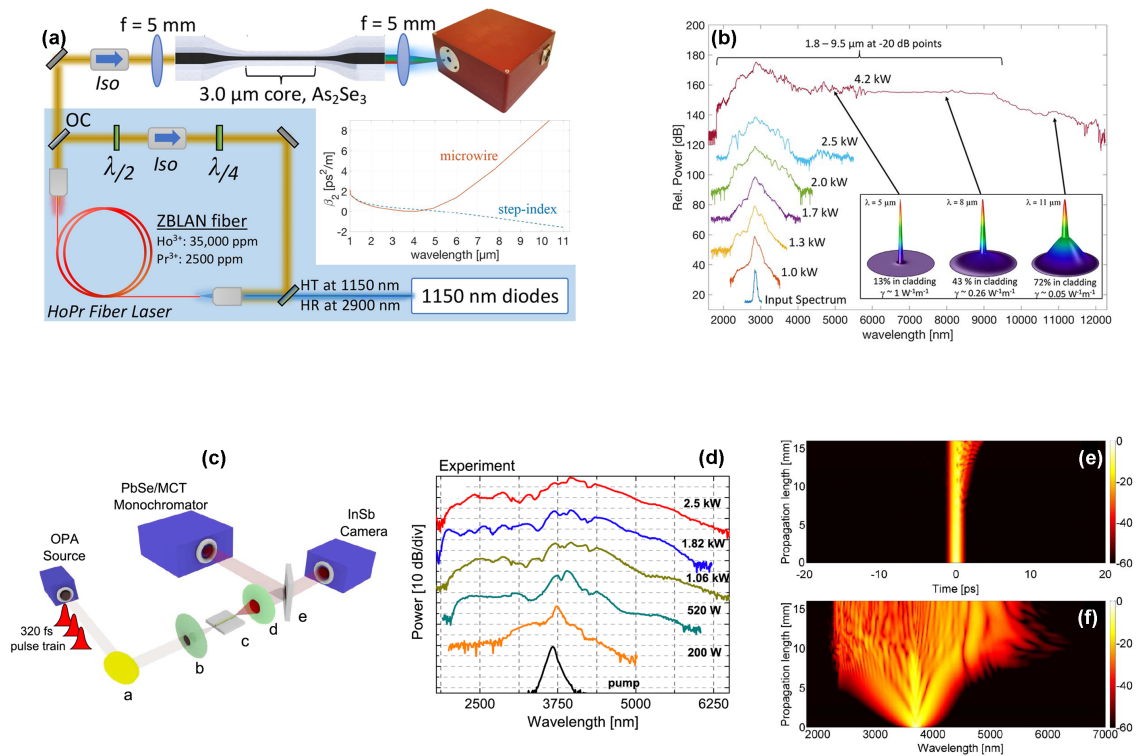


Fig. 1.2 (a) Schematic of the laser cavity for supercontinuum generation and (b) spectral expansion at the increasing peak power. The inset shows the simulated mode profile within the microwire at different wavelengths. Images are from [40]. (c) Experimental setup for midinfrared supercontinuum generation in a silicon nanowire, (d) experimental measurement results with the increasing peak power from 200 W to 2.5 kW, (e) simulated temporal evolution and (f) spectral evolution of supercontinuum generation at a peak power of 2.5 kW. Images are from [41]

equation [51, 52] can be used to describe the light propagation. In addition to femtosecond laser pulses, W. J. Wadsworth and N. Joly successfully observed nonlinear optical effects of Q-switched laser pulses with pulse width of sub-nanosecond. Their work demonstrates a compact source of continuum radiation with a broad and flat optical spectrum, and it also illustrates the feasibility of producing pulses at a selected wavelength in the near-infrared (NIR) via compact efficient wavelength conversion [53].

1.1.3 Pulsed laser ablation

Soon after the invention of the pulsed ruby laser by Maiman in 1960 [1, 2], researchers were eager to investigate the potential of pulsed laser radiation in a wide variety of materials, including liquids [54], solids [55] and biological tissue [56], for sensing, optoelectronics, and biomedical applications, etc. In the recent decades, the significant progress made in PLA applications was driven by the rapid technological developments of high efficiency, high-intensity pulsed laser radiation from reliable Q-switching methods to new, pulsed laser sources (e.g. nanosecond pulsed Nd-YAG lasers) and, more recently, the intense pico- and femtosecond pulses. Theoretically, laser ablation induced by pulsed lasers with high power density ($> 10^6$ W/cm²) due to its small spot size and high peak power can be applied to nearly all classes of materials. By definition, laser ablation is usually resulted from the interaction of intense ($\approx 10^6$ to 10^{14} W/cm²) and short ($\approx 10^{-13}$ to 10^{-8} s) laser pulses, because the removal of material by laser ablation is determined by the amount of energy absorbed by material and the pulse width of laser pulses [54]. For the laser ablation produced by long pulses i.e., pulse width of a few nanoseconds, the heat generated diffuses within the material because the laser pulse duration is longer than the heat diffusion time. This kind of material interaction affects adjacent structures and typically results in micro-cracks. In comparison, the laser ablation caused by ultrashort laser pulses i.e., shorter than 10 picoseconds exhibits a different mechanism and changes the material removal process. Because the pulse width of ultrashort laser pulses is shorter than the heat diffusion time, a plasma is created on the material surface due to the exposure to the intense and ultrashort laser pulses. Therefore, no damage to the adjacent structure occurs and no micro-cracks in the material are produced in this process.

One major application of laser ablation is focused on the material processing of metals [57–59] and glasses [60, 61] in two or three-dimensional machining [62]. For the laser processing of opaque material like metals, the ablative processing is mainly caused by two mechanisms, heat accumulation, and pulse-particle interactions. When the ultrashort laser pulses are focused on the metal surface, the energy of laser pulses will be deposited on the surface within a short period, which is generally less than 1 ns. The deposited energy

will transfer to the thermal load and the heat will be accumulated if the next laser pulse occurs before the heat is diffused within the metal piece. The pulse-particle interaction is the interaction between the laser pulse and the particles, vapor, or plasma from the ablated material by the previous laser pulse. For the transparent material like glasses, when ultrashort laser pulses with high peak power and pulse energy are focused on or in a transparent substrate, the induced large photo fluxes will initiate a multiphoton absorption process, which allows a single electron in the valence band to absorb multiple photons and jump up into the conduction band as a free carrier. When the deposited optical power density is large enough, a large number of free carriers from the multiphoton absorption process give rise to avalanche ionization. Therefore, material ablation will take place, when the peak intensity of ultrashort laser pulses is greater than the ablation threshold, and the density of free electrons in the conduction band reaches the critical density. For different glass materials ablated by a single laser pulse with different pulse durations, the images of material damages are shown in Fig. 1.3.

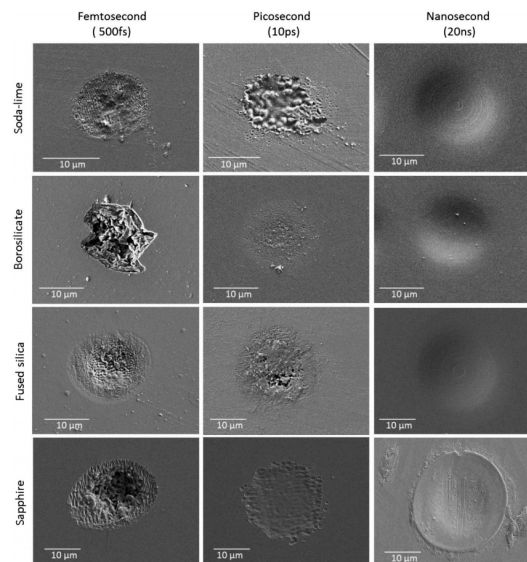


Fig. 1.3 The images of the ablated soda-lime, borosilicate, fused silica, and sapphire glass substrate by a single laser pulse with a pulse duration of 500 fs or 10 ps or 20 ns. Image is from Daniel Nieto [61]

In addition to laser ablation of solid material like metals or glasses, the pulsed lasers could also be used to manipulate and destruct biological tissues with unprecedented precision and selectivity, since 1961, when Milton M. Zaret observed instantaneous thermal injury caused by a single 0.5 ms laser pulse to the pigmented retina and iris of the brown rabbit for the first time [63]. In the last decade, the point of interest in life sciences has shifted to qualitative and quantitative maps of elemental distribution (metals, semimetals, and non-metals) in biological tissues [64, 65]. As a result, laser ablation inductively coupled plasma mass spectrometry (LA-ICP-MS) as one of the major applications of PLA has attracted a lot of attention and has become a widespread technique to analyse the elemental distribution in thin tissue from various biological samples, e.g. brain [66], liver [67], cartilage. In this process, the short laser pulses are focused on the sample surface for laser ablation, the ablated particles are then transported with the carrier gas, Ar or mixtures of Ar and He, to the secondary excitation source of the ICP-MS instrument for ionization of the sampled mass. The ions within a mass range of interest are separated by their mass-to-charge ratio and detected by the detection system of the mass spectrometer. The simplified scheme of an LA-ICP-MS instrument is shown in Fig. 1.4.

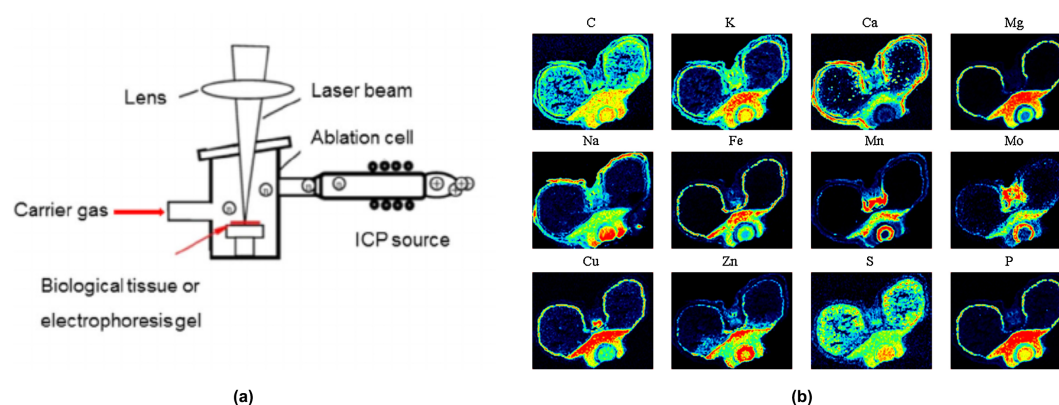


Fig. 1.4 (a) The simplified scheme of a LA-ICP-MS instrument. From [65] (b) Optical image of a wheat grain cross section and corresponding multielement LA-ICP-MS images, separate for each element. From [64]

Compared to other mass spectrometry imaging techniques, e.g. matrix-assisted laser desorption/ionization mass spectrometry (MALDI-MS), desorption electrospray ionization

mass spectrometry (DESI-MS), secondary ion mass spectrometry (SIMS), LA-ICP-MS offers several benefits. The analysis can be performed in the air without the need for a complex vacuum system. Additionally, results can be available within seconds. Therefore, LA-ICP-MS delivers the fastest analysis speed among all analytical techniques with limit of detection approaching parts per billion (ppb) level.

1.2 Current actively Q-switched laser sources

For the generation of laser light in general, i.e., for continuous-wave lasers, Q-switched lasers and mode-locked lasers, three fundamental components are required within the system, including (i) laser gain medium, (ii) optical resonator and (iii) pumping system [68]. The presence of the laser gain medium allows the interaction between matter and light, because the molecules within this gain medium can be characterised by discrete energy levels which enables the absorption process through electronic transitions in molecules. In the absorption process, the atoms absorb the photons produced by the optical pumping system which must have the same energy as the energy difference between involved energy levels ($E_2 - E_1$) and thus transition from the lower energy level (E_1) to the upper energy level (E_2). After that, the atoms either drop to the ground state spontaneously, or to metastable energy levels while emitting photons (radiative) or phonons (non-radiative). In the spontaneous emission process, the phase of electromagnetic waves emitted by atoms are incoherent, so the emitted electromagnetic waves from spontaneous emission process have no definite emission direction. Therefore, amplified spontaneous emission (ASE) is typically considered as an undesirable effects occurring in optical amplifiers. In the other case, if an electromagnetic wave with the same energy as the energy difference between energy levels ($E_2 - E_1$) is incident on the laser gain medium, stimulated emission occurs, whereby the atoms in the upper energy level undergo a transition to the lower energy level. Because the emission process is stimulated by the incident electromagnetic wave, the generated electromagnetic waves that are emitted exhibit the same phase and emission direction. Under thermal equilibrium condition, the atoms in the system are distributed at different energy levels

obeying Boltzmann statistics, where the population of the higher energy level is smaller than that of the lower energy level. However, if through the absorption process enough atoms can be brought to the upper energy level in a 3- or 4-level system, population inversion is produced, and a non-equilibrium condition is achieved. As a result, when the population inversion is greater than the threshold population, the gain is larger than the losses within the cavity and laser behaviour is initiated.

In addition to the laser gain medium, the optical resonator is another critical component required for the generation of laser light. In general, the laser resonator is composed of two mirrors separated by the specific cavity length L , namely highly reflective input-coupling mirror and partially reflective output-coupling mirror. To describe the quality of the laser resonator, the cavity quality factor, or simply Q factor is commonly used in the field of laser study. By definition, the Q factor can be calculated using the ratio of the stored energy within the laser gain medium and the lost energy caused by partial reflectivity of mirrors, diffraction and scattering losses, after a round trip of oscillation within the laser resonator. As a result, the cavity photon lifetime depends on the Q factor, since it is also equal to the transit time of the beam in the laser cavity divided by the cavity loss.

To allow Q-switched laser behaviour, a so-called Q-switch is required in the laser resonator to control the population inversion of the gain medium resulting in the release of short and intense laser pulses. If the Q-switch is off, the cavity Q factor is reduced by the high cavity losses. Therefore, no laser behaviour is observed, despite the population inversion being greater than the threshold population. Once the Q-switch is turned on, the cavity Q factor is increased by the low cavity losses, so the gain seen by the population inversion is now far greater than the cavity losses. As a result, the stored energy within the atoms in the high energy level is released as an intense laser pulse. Thus, Q-switching can be considered as a technique which utilises changes in the cavity Q factor to the generation of laser pulses.

After the principle of Q-switching was first introduced by R. W. Hellwarth and F. J. McClung in 1962 [69], classical solid-state bulk lasers became the dominant type of Q-Switched lasers, owing to their energy storage capacity. A few decades later, classical bulk

lasers were gradually replaced by guided-wave lasers [70]. In 1998, H. Suche reported the first efficient Q-switched Ti:Er:LiNbO₃ waveguide laser [71], in which a compact and rugged laser design was introduced with a monolithically integrated folded Mach-Zehnder type modulator of high extinction ratio to generate Q-Switched laser pulses with a duration of 4.3 ns and a peak power of up to 1.44 kW at a repetition frequency of 1 kHz. Since then, femtosecond laser direct-writing (FLDW) has evolved into a major technology for the fabrication of optical waveguides within bulk glasses [72]. Integrated CW waveguide lasers with and without incorporating Bragg gratings have been demonstrated using this technique [73, 74].

Q-switching is a technique commonly applied with solid-state bulk lasers for the generation of laser pulses with a short pulse duration of a few nanoseconds and high peak power. Q-switched lasers have a wide range of applications, including trace gas sensing [75], LIDAR (e.g. for range finding and autonomous driving) [76] and nonlinear optics [77, 78]. They are also used in industry for cutting or drilling, in hospitals for clinical applications, such as tattoo or nevi removal. For many of the above applications, it is desirable to have a device that is both small and actively Q-switched, meaning that the repetition rate can be controlled externally. Waveguide lasers are a promising option, as they typically feature a monolithic laser resonator and thus offer a more stable and compact setup compared to a bulk laser. Over the past decades, a variety of techniques for the fabrication of optical waveguides in active media have been reported, including FLDW [79, 80]. The main advantage of this technique is that the waveguides can be inscribed in almost any host material independent of its doping ions. The FLDW technique provides a flexible 3-dimensional fabrication method that allows, for example, the creation of both, a waveguide and Bragg grating in a single processing step, enabling a truly monolithic laser design [74].

To date, pulsed operation of waveguide lasers has been demonstrated in both actively and passively modulated setups. Due to their inherently small size, the use of passive saturable absorbers is appealing for monolithic pulsed waveguides lasers. However, in passively Q-switched lasers, the repetition rate is determined by the properties of the gain medium, e.g. saturable absorber (SA) [86–88], which means the repetition rate of passive Q-switching

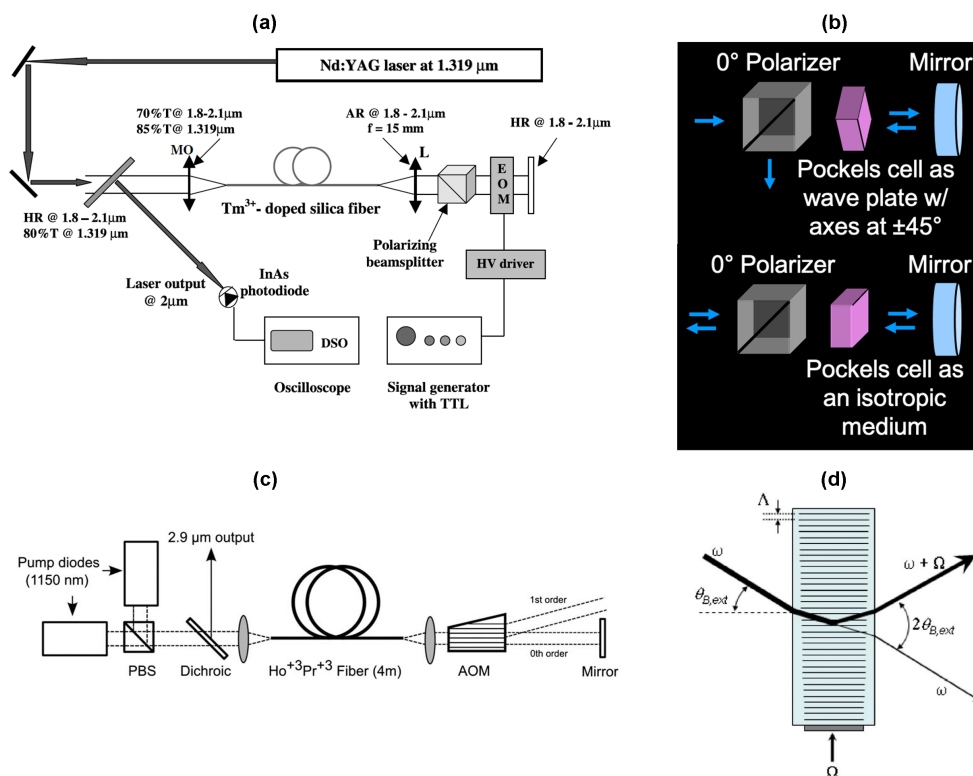


Fig. 1.5 (a) Schematic of actively Q-switched Tm^{3+} -doped silica fibre laser from [81], (b) electro-optic intensity modulator (Pockels cell Q-switch) from [82, 83], (c) schematic of Q-switched $\text{Ho}^{3+}\text{Pr}^{3+}$ fibre laser [84] and (d) basic operation principles of an AOM. Within the Bragg diffraction regime of the AOM, the part of the incident light is diffracted into the first order and the laser frequency becomes $\omega + \Omega$, which indicates an up-shift of the frequency by the RF modulation frequency Ω [85].

cannot be controlled externally. To actively control the repetition rate, commercially available acousto-optic modulators (AOMs) [89, 90] and electro-optic modulators (EOMs) [91–93] are typically used for the active Q-switching. With these two kinds of active optical modulators, the repetition rate of the laser can be controlled based on requirements. Take the Pockels cell as an example of EOMs shown in Fig. 1.5(b), when a voltage is applied to a crystal, its refractive indices changes and then results in a voltage-controlled birefringence. The driving voltage of a few kV can turn a crystal into a half- or quarter-wave plate [94]. Similarly, applying a sinusoidal voltage yields sinusoidal phase modulation to the light beam, which can be converted into an intensity modulation by adding an optical polarizer or a polarizing beamsplitter (PBS). Without a polarizer, an EOM can produce a phase modulation via

externally applied electrical signals. The phase modulation can be regarded as a sinusoidal shift of the modes into and out of the actual cavity modes. Apart from the EOMs, AOMs are another kind of active optical modulator, in which an acoustic wave is required to induce a sinusoidal refractive index variation within the crystal medium due to the photo-elastic effect. With the refractive index modulation or refractive index grating within the crystal medium, the acousto-optic interactions can give rise to the partial diffraction of the light beam by a small diffraction angle which is generally a few degrees. For the AOMs widely used in the laser applications, their Bragg diffraction can result in a single diffraction order, namely first order, by which the intensity of transmitted light, i.e., the zeroth diffraction order, can be actively controlled by the acoustic power of the sound waves generated by a piezoelectric transducer attached to the crystal. Therefore, it is clear that the diffraction in the Bragg regime caused by acousto-optic interactions can enable the conversion of the acoustic wave amplitude modulation to an intensity modulation of the transmitted light beam. To modulate light by acousto-optic interactions, the radio-frequency (RF) signals required to drive AOMs usually have the center frequency around 40 MHz, the frequency shift around 20 MHz, and RF power around 10 W [85]. Example schematics of EOM and AOM based laser systems are shown in Fig. 1.5. Previous publications on Q-switched waveguide lasers operating at different wavelengths are listed from high peak power to lower peak power in Table 1.1. In the table, "P" represents the passive Q-switching, while "A" represents the active Q-switching.

Table 1.1 List of Publications on Q-switched Waveguide Lasers

Peak Power(W)	Pulse Width(ns)	Average Power(mW)	Repetition Rate(kHz)	λ (nm)	Type(A/P)	Ref
0.14	50	10.4	1480	1912	P	[95]
0.39	83	45.6	1390	1835	P	[96]
0.44	203	85.2	1100	1064	P	[97]
0.50	78	60.0	1590	1029	P	[98]
0.52	67	275	7900	1064	P	[99]
0.53	1100	14.0	24	1064	P	[100]
0.78	46	169	4700	1064	P	[101]
1.00	24	126	6100	1064	P	[102]
4.40	1780	151	19.25	1988	P	[103]
90.9	11	5600	5400	1030	P	[104]
414	14.5	72.0	0.012	1470	A	[105]
1000	1.3	38.8	28	1054	P	[106]
1850	21.0	94.3	2.054	1890	A	[79]
6000	25	390	2.7	1920	P	[107]
6500	14	34.0	607	1027	P	[108]
8000	50	2000	5	1123	A	[109]
24300	6.5	2640	10	1340	A	[110]
38500	6.5	2500	10	1064	A	[111]
51700	35.8	1660	0.481	1935	P	[112]
138000	10	10000	7.2	1890	P	[113]
166000	7.6	203	0.161	1027	P	[114]
175000	9.9	17500	10	1030	A	[115]

1.3 Current actively mode-locked laser sources

With the extreme intensities and short timescale, ultrashort pulsed lasers have been widely used in a variety of scientific and industrial applications, including material processing [116], laser ablation [117] and remote sensing [118]. Mode-locking as an important form of mode coupling in lasers provide a novel approach to generating ultrashort light pulses with femtosecond or picosecond pulse width and other periodical laser signals.

In the case of a laser resonator with two mirrors, e.g. highly refractive input-coupling mirror and partially refractive output-coupling mirror, the axial modes in the frequency domain are separated by the specific distance $\Delta\Omega$ which is determined by the effective refractive index and the cavity length. To enable the mode-locking operation, a passive or an active modulator is added into the laser cavity. If the modulator is operated with the frequency equal to the axial-mode spacing, the modulation sidebands overlap with the axial modes, and the mode-locking action occurs. Practically, mode-locking for generating ultrashort laser pulses can be achieved when modulation of the resonator losses at a frequency that is exactly the inverse of the cavity's fundamental round trip time establishes a phase-coherence between the longitudinal resonator modes (also called axial modes), resulting in a well-defined train of optical pulses [119]. In other words, the generation of mode-locking can be understood as the locking of multiple axial modes in a laser cavity. Therefore, once the phases of different modes become coherent, pulsed radiation can be observed. Practically, when the amplitude or phase modulation with a modulation depth greater than 5 % is synchronous with the round-trip time of radiation circulating in the laser cavity, a short laser pulse is initiated and can be shortened after every round-trip within the cavity. The laser pulse keeps becoming shorter, until the short laser pulse and its wide spectral bandwidth make pulse lengthening mechanisms or spectrum narrowing processes spring into action, such as the finite bandwidth of the gain. The invention of laser mode-locking provides people with a new and better way to generate ultrashort laser pulses, and paves the way for the deeper understanding of the mode-locking and nonlinear optics [120].

The first theoretical analysis of mode-locking was presented by Didomenico at Bell Telephone Laboratories in 1964 [121]. In the same year, the first experimental mode-locking

was demonstrated by L. E. Hargrove [122]. The analytic theory of active mode-locking was firmly established in a classic paper by Siegman and Kuizenga [119] in 1970. In terms of the cavity structure, ring cavity and Fabry-Perot cavity are two major types of optical cavities widely used for mode-locked fibre lasers. While a Fabry-Perot cavity has two end mirrors with the perpendicular incidence of light, a ring cavity does not have any end mirrors and commonly needs to incorporate an optical isolator to ensure unidirectional lasing.

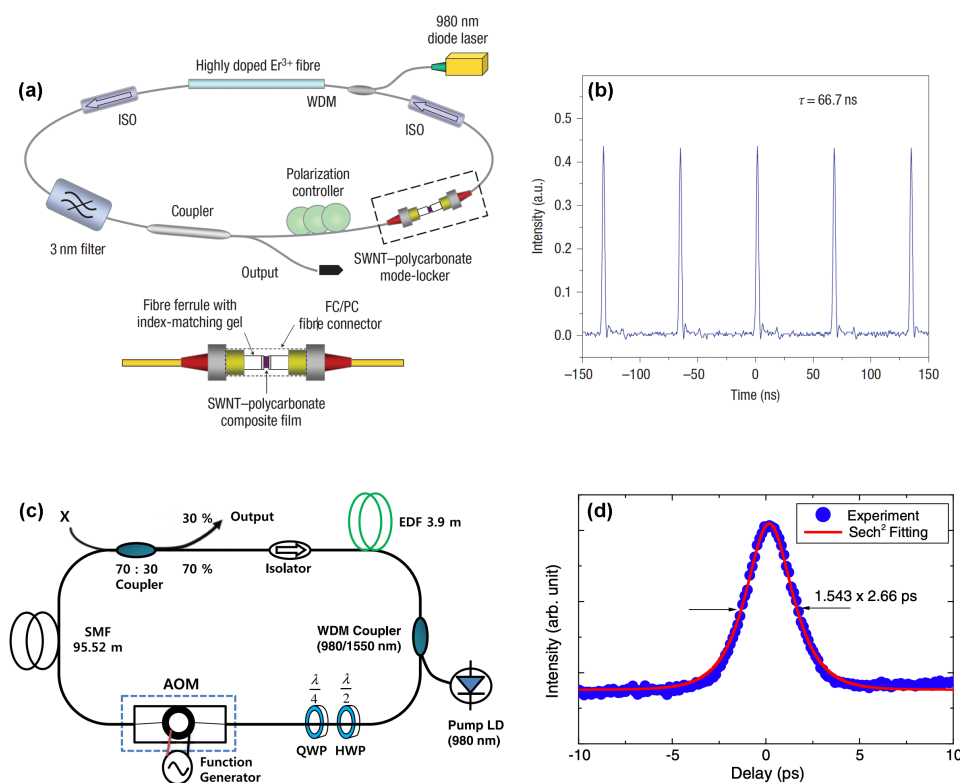


Fig. 1.6 (a) Laser setup of Er-doped mode-locked fibre laser using ring cavity configuration, which consists of a wavelength division multiplexer (WDM), an optical isolator, a polarization controller and an optical splitter and (b) example of oscilloscope trace of output laser pulses from [123]. (c) Experimental schematic of the mode-locked fibre laser incorporating an AOM in fibre and (d) measured autocorrelation trace of output mode-locked laser pulses from [124].

Based on the properties of the intracavity modulator used, mode-locking techniques can generally be categorized into passive and active methods. Passive mode-locking can be obtained by using suitable nonlinear optical materials such as fast saturable absorbers

[125] like carbon nanotubes [126]. The classic schematic of Er-doped mode-locked fibre laser with ring cavity configuration is shown in Fig. 1.6 (a). For active mode-locking, the loss modulation is implemented via an externally controlled modulator, such as a variable optical attenuator (VOA) [127], an EOM or an AOM [128] as shown in Fig. 1.6 (c). In principle, any amplitude modulator based on either electro-optic or acousto-optic interactions can actively control the intensity of transmitted light, thus it can be used to initiate a laser mode-locking. Also modulating the gain within the laser cavity, known as gain switching, is essentially the same as active mode-locking [82]. Gain-switching is commonly used for mode-locking in semiconductor lasers [129]. Previous publications on mode-locked fibre lasers operating at different wavelengths are listed from high peak power to lower peak power in Table 1.2. In this table, "P" represents the passive mode-locking, while "A" represents the active mode-locking.

Table 1.2 List of Publications on Mode-Locked fibre Lasers

Peak Power(W)	Pulse Width(ps)	Average Power(mW)	Repetition Rate(MHz)	λ (nm)	Type(A/P)	Ref
0.004	24	1	10000	1569	A	[130]
0.006	440.4	2.82	994.4	1555	A	[131]
0.017	1000	0.2	12	1550	A	[132]
0.065	2.8	7.2	39630	1531	A	[133]
0.105	169	0.25	14.11	1567	A	[134]
0.115	4850	4.3	7.68	1561	P	[135]
0.511	155400	22.16	0.279	1563	P	[136]
0.988	2.49	5.02	2040	1558	P	[137]
2.062	97	20	100	2066	A	[138]
2.650	446	14.3	12.10	1950	A	[139]
3.165	740	26	11.1	1091	A	[140]
21.03	0.61	5.9	463	1556	P	[141]
45.62	1.6	0.4	5.48	1559	P	[142]
105.3	0.19	1.0	50	1900	P	[143]
218.2	0.66	1.8	12.5	1557	P	[144]
220.0	2.66	1.1	1.84	1560	A	[124]
252.0	0.17	1.2	27.4	1558	P	[145]
270.9	1.57	3.7	8.7	1560	A	[146]
352.4	4.4	20	12.9	1934	A	[147]
491.4	0.074	1.2	33	1550	P	[148]
1300	3000	300	0.077	1078	P	[149]
3278	0.19	5.6	8.85	1561	P	[150]
4912	1.5	700	95	1026	P	[151]
16873	0.04	18	25.4	2784	P	[152]

1.4 Liquid crystal modulator and lasers

Nowadays, liquid crystal devices can be seen anywhere in people's daily lives, such as smart TVs, smartphones, tablets, laptops, smart wearable devices, kindles, and vehicle displays. In the last three decades, the liquid crystal has been one of the biggest commercial successes, as they have been widely used in commercial applications, e.g. electro-optic flat panel display (FPD) for entertainment devices and even flexible panel and transparent panel display recently. The display includes screens that project information such as images, videos, and texts. There are also a series of promising technologies in the market for display screen manufacturing, including light-emitting diode (LED), liquid crystal display (LCD), organic light-emitting diode (OLED), and others [153]. In addition to the display applications, there are some attractive applications of liquid crystal in the optics and photonics field, such as spatial light modulators (SLMs) [154–157] and liquid crystal based VOAs [158, 159]. The example of a liquid crystal-based SLM is shown in Fig. 1.7 (a-d).

Liquid crystals exhibit mesophases, which are different from crystalline solid and isotropic liquid [160]. Take the rod-like (calamitic) liquid crystal molecule as an example, the typical size of liquid crystals is around a few nanometers and the molecule has a rigid core and a flexible tail. At different temperatures, liquid crystal molecules are arranged in different forms, so they exhibit different liquid crystal phases, including crystal solid, Smectic-C, Smectic-A, Nematic, and isotropic liquid [161]. The most simple liquid crystal phase is the nematic phase, in which the molecules possess orientational ordering like a crystal but no positional ordering like a liquid. When the liquid crystal is transformed into the Smectic-C phase, the liquid crystal director is no longer perpendicular to the layer but tilted, and both position and orientation of molecules are in the same order [162].

In terms of the electro-optic applications of liquid crystal, its response to applied electric fields is one of the major interests related to the electro-optic properties of the material. In the smectic-C* phase, the director rotates around the smectic cone by the azimuthal angle φ via the 'Goldstone' mode, so that the polarization aligns with the applied field. The surface-stabilized ferroelectric (SSF) LCD was invented by Clark and Lagerwall in 1980 [164]. In their paper, they presented a new geometry of ferroelectric smectic-C liquid crystals,

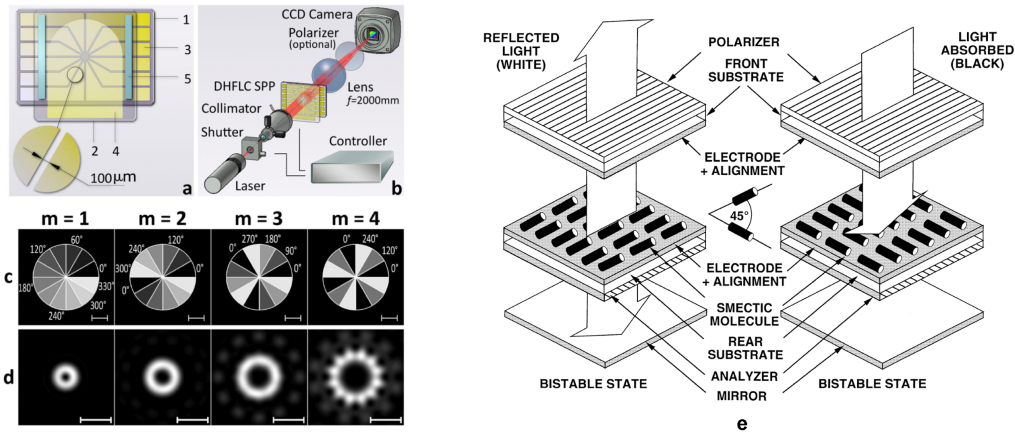


Fig. 1.7 (a-d) Design and experimental setup for deformed-helix ferroelectric liquid crystal (DHFLC) based SLM using a 50 μm thick liquid crystal layer from [163]. (e) Schematic representation of a surface-stabilized ferroelectric LCD (SSF-LCD) from [153]

surface-stabilized, in which the liquid crystal layer is so thin that the helical structure is suppressed. Therefore, the optical axis of liquid crystals is along with one of two degenerate directions which are separated by 45° in the plane of the surface of liquid crystal cells. When no electric field is applied, the incident polarized light travels through the smectic- C^* liquid crystal and is absorbed by the analyser. Therefore, it is called "Dark Mode". With an external DC electric field, the director rotates around the smectic cone to its second bistable state, which is so-called "Bright Mode" [153]. In their work, the molecular orientation of liquid crystals was successfully controlled by an applied electric field and thus the birefringence changed as well. To conclude, the controllable molecular orientation and birefringence are the essence of the operation of a LCD.

The first combination of liquid crystal and pulsed lasers was demonstrated by D. Grebe and R. Macdonald at the Technical University of Berlin in 1996 [166]. In their paper, cholesteric liquid crystals have been used as mirrors in an optical resonator for pulsed solid-state lasers. They successfully obtained laser pulses of 10 ns duration with peak intensities up to $1 \text{ GW}/\text{cm}^2$. Later, in 1998, the same group utilised nematic liquid crystal as an active Q-switch in Nd:YAG solid-state lasers. In their works, laser pulses of 35-70 ns duration (FWHM) with energies between 10-25 mJ were presented [165]. However, the

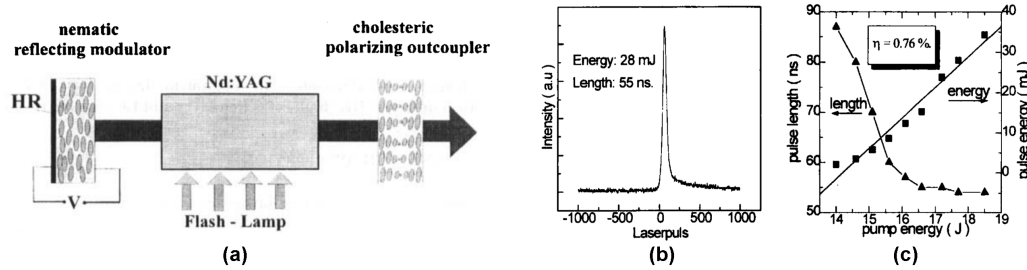


Fig. 1.8 (a) Schematic set-up of liquid crystals Q-switch solid state laser resonator. (b) Measurements of Q-switch laser pulses. From [165]

slope efficiency was limited to only 0.33 % - 0.76 %, because of the slow switching speed of their liquid crystal devices.

1.5 Research Objective

For conventional AOMs and EOMs, high driving voltage, high power consumption, bad integration ability, and the requirement of additional facilities for cooling represent major obstacles to developing monolithic and portable laser sources, which are highly desired for some applications, including remote sensing, breath analysis, and material processing. One of the major objectives of my research is to demonstrate a novel approach to active Q-switching of an integrated waveguide chip laser and active mode-locking of an all-fibre laser system, which makes use of a compact liquid crystal (LC) cell to modulate the cavity losses with a high speed and large efficiency. In my research, a particular class of liquid crystals in the deformed helix ferroelectric (DHF) mode of operation was selected and characterised, which enables the generation of very short laser pulses with an FWHM pulse width (\approx ns) much shorter than the typical response time (\approx μ s) of liquid crystals. Unlike previously demonstrated methods [166, 165], the high-speed liquid crystal modulator can be directly integrated onto the waveguide chip and can be controlled by low power, low voltage drivers ($<$ 100 V). The technique investigated in my research thus enables the fabrication of a fully monolithic and compact laser source that can emit short laser pulses with high peak power

levels and variable repetition rates. The idea of developing a monolithic actively Q-switched waveguide lasers utilising liquid crystal modulators is shown in Fig. 1.9.



Fig. 1.9 Schematic of monolithic actively Q-switched waveguide lasers designed by the collaborators Zedelef Pty Ltd and Macquarie University.

1.6 Outline of Thesis

With regard to the structure of this work, it is composed of eight chapters and one appendix. In Chapter 1, a wide variety of applications for Q-switched and mode-locked lasers are introduced, showing the high demand for ultrashort and short laser pulses in different applications, including sensing, material processing, and nonlinear optics. Moreover, the limitations of existing Q-switched and mode-locked laser sources are discussed. Compared to conventional AOMs and EOMs, the low driving voltage, low power consumption, good integration ability, and no requirement of additional facilities for cooling make liquid crystal modulators become an appealing alternative approach to a miniaturized and robust pulsed laser source. In Chapter 2, the basic liquid crystal physics and design of liquid crystal cells are presented in detail. Three modeling methods are introduced to theoretically study the

effects of externally applied electric fields on the light propagation in the liquid crystal cell. This chapter also provides a brief introduction to the basic principles and process of the femtosecond direct-written technique as the fabrication method for waveguides. In Chapter 3, liquid crystal modulators are characterised as intracavity optical loss modulators by electrical signals of different waveforms. This chapter provides readers with important modulation quality parameters of liquid crystal modulators, including modulation depth, modulation speed, bandwidth, and optical transmission. In Chapter 4, the numerical modeling for actively Q-switched waveguide lasers using liquid crystal modulators is proposed and discussed, showing an excellent agreement with experimental results. The proposed numerical model illustrates the possibility to optimise laser performances by adjusting specific parameters, including pump power, internal optical loss, and operating temperature. Chapter 5 demonstrates the practical utilisation of liquid crystal modulators in actively Q-switched Yb-doped waveguide lasers operating at 1 μm . The surprise experimental results facilitate the development of a commercial prototype of compact and portable actively Q-switched lasers supported by a collaboration with an industrial partner, Lastek Pty. Ltd. Chapter 6 explores the possibility of extending the operation wavelength of active Q-switching to 1.86 μm utilising a Tm^{3+} -doped ZBLAN waveguide. The achieved Q-switched lasers with high peak power and short pulse duration give rise to the FWM phenomenon in a tapered chalcogenide fibre. In Chapter 7, all-in-one fibre lasers operating at 1.55 μm are demonstrated. The proposed all-fibre setup supports the simple switch among operation modes, e.g. continuous wave (CW), Q-switched, amplitude modulation (AM), and frequency modulation (FM) mode-locked. In Chapter 8, this work is concluded with the feasibility of utilising liquid crystal modulators as optical intensity or loss modulators for the generation of both Q-switched and mode-locked lasers in fibre or waveguide platforms. Additionally, the design of fully monolithic actively Q-switched waveguide lasers is presented as the future work in Chapter 8. Liquid crystal optrode for electrophysiology recording is introduced and experimentally demonstrated in Appendix A as a liquid crystal-related research out of scope for laser applications. It is a collaborative project with

the UNSW Graduate School of Biomedical Engineering, aiming to develop a new generation of neural interfaces that can record activation potentials from multiple positions in parallel.

Chapter 2

Background Theory

Over the past decades, the rapid advance of liquid crystal material and relevant technologies have been playing an essential role in the development of modern electronic instruments and smart devices, such as flat-screen TVs, PCs, laptops, and smartphones. LCDs can be found everywhere in our life. There is no doubt that the LCD provides an interface for people to communicate with others all over the world via the internet and it has become an indispensable component of real-time and fast information interaction. Due to the great ability to provide rich-colored and clear images on the screen, liquid crystals have been widely used for display technologies. Apart from the display applications, they have demonstrated their applicability to a wide variety of applications, such as electro-optical devices [167, 168], telemetry system [169], light beam steering and shaping [156, 170] and optical communication systems [171, 172] in the recent decades. The feasibility of liquid crystals in laser applications has been explored and studied in the past three years of my Ph.D. study.

2.1 History of liquid crystals

Liquid crystals were first observed by physicist Otto Lehmann from Germany and chemist Friedrich Reinitzer from Austria in 1888, and they found that liquid crystals were an intermediate phase of matter which had properties of both crystal and liquid [173, 174]. In 1927, the phase transitions of liquid crystals were produced for the first time by applying

electric or magnetic fields. The observed phase transitions were named by physicist Vsevolod Fréedericksz from Russia as Fréedericksz transitions. In the 1960s, liquid crystals started to be used for display applications, as the synthesized liquid crystal samples by mixing various chemical compounds were able to produce phase transitions at room temperatures. In 1991, physicist Pierre-Gilles de Gennes from France was awarded the Nobel Prize in Physics because of his outstanding achievement in the research field of liquid crystals and the epoch-making significance of liquid crystal technologies to contemporary human life [175]. With the rapid development of LCDs since the 1990s, the display screen of contemporary entertainment devices has become bright, clear, light-weight, energy-efficient, and even flexible.

2.2 Liquid crystal material physics

To determine the phase of a given material, the degree of both positional and orientational orders need to be considered. The positional order is a parameter depicting how orderly the molecules are aligned in the system with a consistent distance and no movement. The orientational order describes whether the long or short molecule axis of all molecules in the system is pointed in one direction. For material with the solid phase, the molecules in the material are arranged with a high degree of positional order and orientational order. However, when the material with the solid phase is placed into a high-temperature environment, the degree of order within the material decreases. As a result, the material transforms from solid to liquid due to the high temperature, and the molecules in the liquid phase are arranged randomly or irregularly in both position and orientation. At room temperature, the liquid crystals in this work are arranged in a layered structure with partial positional and orientational orders. Therefore, liquid crystal materials in this work have properties of both solid and liquid materials simultaneously, and their phases can be considered as intermediate phases or mesomorphic phases [175–177].

2.2.1 Physical model and phase

The physical models of liquid crystal molecules can be typically categorized into three types by their shapes, including rod-like calamitic liquid crystal [178, 179], disk-shaped discotic liquid crystal [180] and banana-shaped bent-core liquid crystal [181, 182]. The physical models of typical liquid crystal molecules with three different shapes are shown in Fig. 2.1.

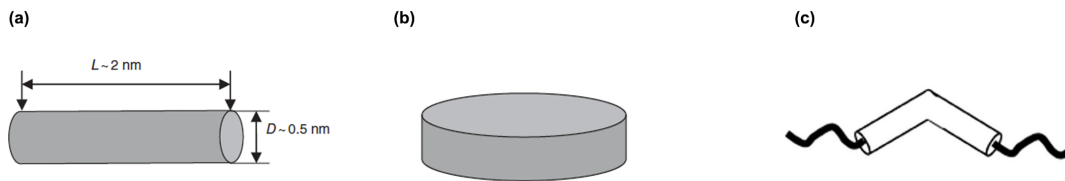


Fig. 2.1 The physical model of (a) rod-like calamitic, (b) disk-shaped discotic and (c) banana-shaped bent core liquid crystal molecules [182, 183].

The typical rod-like calamitic liquid crystal molecules consist of a rigid core and a flexible tail, while the disk-shaped discotic liquid crystal molecules have multiple flexible tails connected to one rigid core. Unlike both rod-like calamitic and disk-shaped discotic molecules, the rigid core of banana-shaped bent-core liquid crystal molecules is bent-shape rather than linear, which results in the polar order and chiral superstructures of liquid crystal molecules.

In my Ph.D. study, the particular class of liquid crystals used in the liquid crystal cell is rod-like calamitic liquid crystal molecules. In the following sections, the focus of the discussion is on rod-like liquid crystals only. The phase of a liquid crystal material can be changed by some external conditional parameters, such as temperature and concentration. If the phase transitions of the liquid crystal material are induced by the temperature change, this kind of material is called thermotropic liquid crystal material with particular transition temperatures. Unlike the thermotropic material, the phase transitions of the lyotropic liquid crystal material are controlled by varying the solvent concentration. Because the rod-like liquid crystal material used in this work is thermotropic, its phase is controlled by the environment temperature. By varying the temperature, the phase of liquid crystals can change between crystal solid, smectic-C, smectic-A, nematic and isotropic liquid phases.

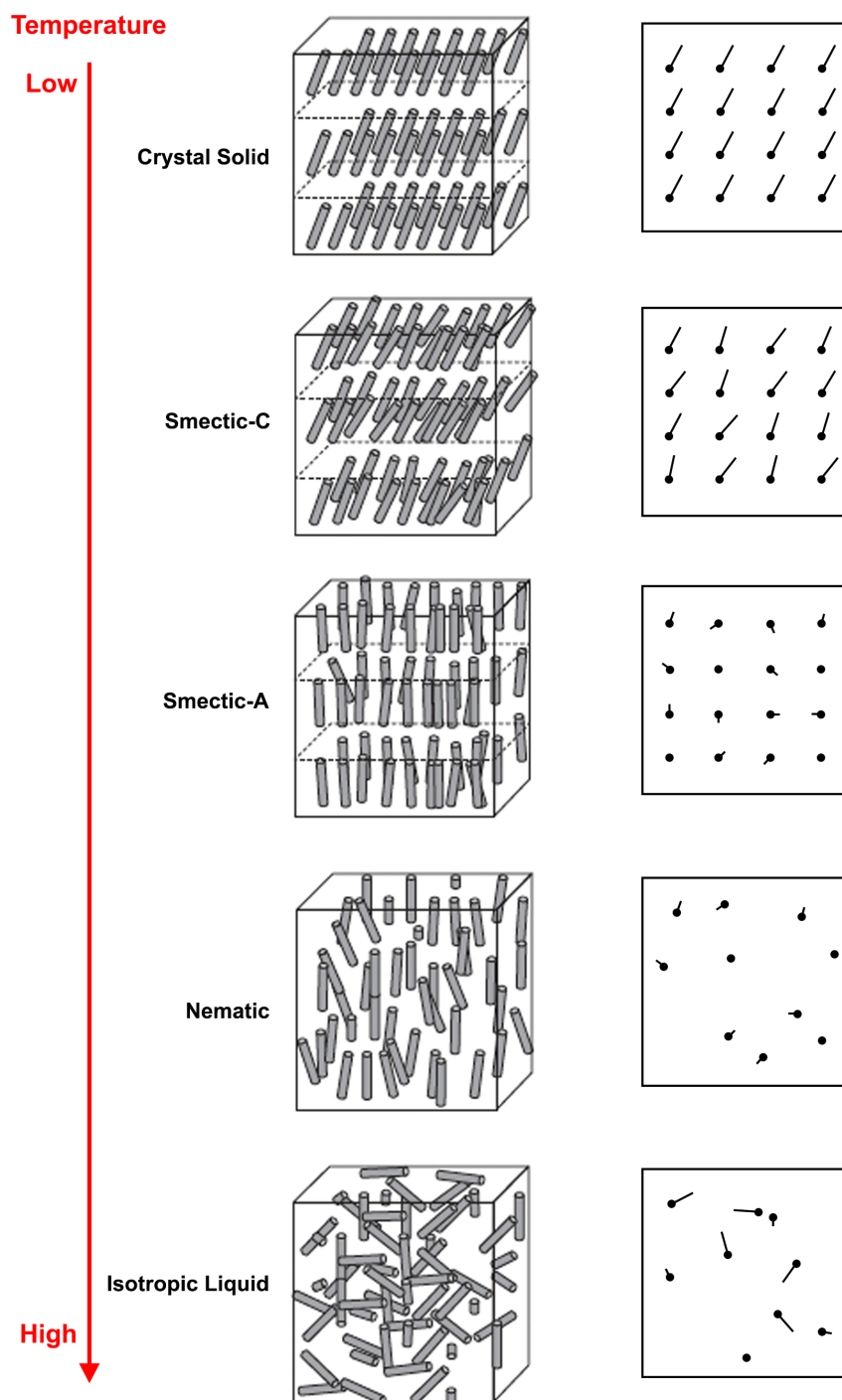


Fig. 2.2 The two-dimensional schematic of five typical phases of rod-like liquid crystal material, including crystal solid, smectic-C, smectic-A, nematic and isotropic liquid phases from top to bottom. Image reproduced from Deng-Ke Yang [183].

When the rod-like liquid crystal material is at low temperature, it exhibits the crystal solid phase, in which all molecules in the system are orderly arranged in a grid pattern and they all are pointed in the same direction with a tilt angle to the layer. The high degree of both positional order and orientational order illustrates the stability of the material structure, high translational viscosity, and extremely low diffusion rate. When the environment temperature increases, the phase of liquid crystal material can be transformed from crystal solid phase to smectic-C phase. In the smectic-C phase, the degree of positional order is maintained, while the degree of orientational order is destroyed by heat to some extent. For the liquid crystal material in the smectic-C phase, the molecules in the system are still orderly arranged in a grid pattern, but the direction of long molecule axes is not consistent. Because of the thermal motion, all liquid crystal molecules in the system rotate along one direction, which is considered the preferred direction. Therefore, although the direction of the long molecule axes varies among the liquid crystal molecules in one layer, they all exhibit one preferred direction with a tilt angle to the layer. It is worth noting that the preferred direction of orientation can be defined as the liquid crystal director \vec{n} . When the environment temperature keeps increasing, the liquid crystal material transfers to the smectic-A phase, in which the liquid crystal molecules have partial positional order, and the layered structure is maintained. For the orientation of the long molecule axis in this phase, the long molecule axis still rotates along one direction, but the preferred direction is perpendicular to the smectic layers without a tilt angle. If the environment temperature is increased more, the liquid crystal material exhibits a phase transition from the smectic-A to the nematic phase. Compared with the smectic-A phase, the nematic phase still has an orientation order with a preferred orientation direction of long molecule axes, which is perpendicular to the layers, but the positional order is eliminated by heat and the liquid molecules can move across the boundary of layers. As a result, the liquid crystal material in the nematic phase no longer has the layered structure, which makes it more similar to liquid material. In a higher environment temperature, the phase transition occurs again from the nematic phase and isotropic liquid phase. In this phase, no positional order and orientational order can be observed in the system, where the molecules can diffuse anywhere and their long molecule axes are randomly orientated

without order. The two-dimensional representation of five typical phases of rod-like liquid crystal material is shown in Fig. 2.2.

2.2.2 Orientation of liquid crystals

To study the optical properties of liquid crystal material, it is critical to understand its orientation order parameter in the system. For the rod-like liquid crystal material discussed in the previous section, the rod-like molecules have one long molecule axis and one short molecule axis. Since the rod-shaped calamitic liquid crystals used in this work are uniaxial [184, 185], the orientation of molecules can be described as a unit vector \vec{d} , which is along the long molecular axis.

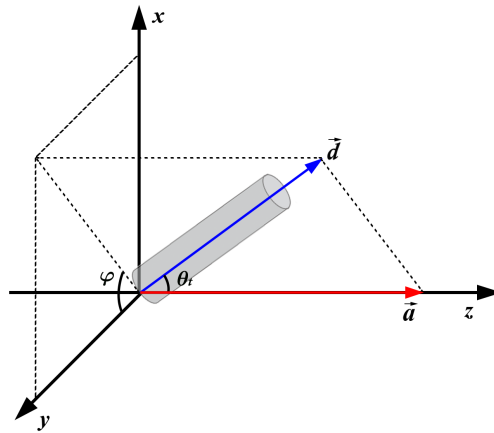


Fig. 2.3 The orientation of a rod-shaped liquid crystal molecule with a tilt angle θ_t and an azimuthal angle φ .

When liquid crystal molecules are in the smectic-A or smectic-C phase, the molecules twist along one axis (i.e., helical axis), which is parallel to the z-axis and represented by a unit vector \vec{a} . For the rod-shaped liquid crystal molecules, the liquid crystal director \vec{d} is defined as a unit vector along the long molecular axis of the liquid crystal molecule. For the orientational representation of the liquid crystal director \vec{d} , there are two typical angles required. One angle is the tilt angle θ_t and the other one is the azimuthal angle φ . The tilt angle θ_t represents the angle between the liquid crystal director \vec{d} and the helical axis \vec{a} , while the azimuthal angle φ represents the rotation angle of a molecule on the xy plane with

respect to the y -axis. The orientation of a rod-shaped liquid crystal molecule is shown in Fig. 2.3.

The degree of orientation order in a liquid crystal material is defined as a quantitative parameter S representing whether the long molecule axis of all molecules in the system is oriented in one direction. At low temperatures, rod-shaped liquid crystals exhibit the crystal solid phase, where all molecules in the system are oriented in one direction. Therefore, the orientation parameter of liquid crystals in the crystal solid phase is maximum, $S = 1$. With the increasing temperature, the orientation parameter S decreases until it reaches the minimum $S = 0$, when the long molecule axes of molecules are randomly orientated without order, which means the liquid crystals transform into the isotropic liquid phase.

2.2.3 Spontaneous polarization and structure of chiral smectic-C liquid crystals

Liquid crystal material has been widely used in display applications for several reasons. The major reason making the liquid crystal irreplaceable in display devices is its fast and S-shaped response to the electric fields. The ferroelectricity and flexoelectricity given by particular liquid crystals are two typical electric effects contributing to various electro-optic effects of liquid crystals [186, 187]. In theory, the external electric field can result in the deformation or reorientation of liquid crystals in the system. As a result, when the electric field is applied, the optical properties of liquid crystals change significantly due to the large anisotropy of their susceptibility tensors [188]. The liquid crystal materials can be classified into two categories, dielectric and ferroelectric materials. The ferroelectric liquid crystal material is a kind of liquid crystal in which a spontaneous polarization exists in the system and orients with the applied electric fields. Conversely, no spontaneous polarization can be found in the dielectric liquid crystal due to its reflection symmetry. In this section, the effects of electric fields on liquid crystals are studied to understand the interaction between them.

As discussed earlier, the typical rod-like calamitic liquid crystal molecules have a rigid core and a flexible tail. The calamitic liquid crystal molecule rotates along the long molecular

axis at high speed by the thermal motion, so a cylinder is formed by the fast rotation and its physical model can be represented by a rod or cylinder. The cylinder is a typical structure with reflection symmetry, so the rod-like molecules are also called achiral molecules. When the rod-like uniaxial nematic liquid crystal molecules are uniformly oriented, the reflection symmetry makes the liquid crystal director \vec{d} equivalent to the inverse director $-\vec{d}$, which means the spontaneous polarization can not be produced in this case [189, 190]. Even if the rod-like liquid crystals transform into other liquid crystal phases by heat, the liquid crystal director still satisfies $\vec{d} = -\vec{d}$ and no spontaneous polarization occurs.

The chiral liquid crystal molecule is always represented as a screw or helix as its physical model. Unlike the achiral molecule represented by a rod in Fig. 2.1, the chiral molecules have no reflection symmetry, which makes it possible to have spontaneous polarization. The existence of spontaneous polarization is determined not only by chiral molecules but also by what liquid crystal phase those chiral molecules exhibit. The chiral smectic-A liquid crystals have a preferred direction, which is perpendicular to the smectic layers. Although the chiral molecule itself has no reflection symmetry, it has a reflection plane perpendicular to the liquid crystal director \vec{d} . Therefore, the chiral smectic-A liquid crystals cannot produce spontaneous polarization, although they are composed of chiral molecules. The chiral smectic-C liquid crystals were demonstrated as a ferroelectric material for the first time by R. B. Meyer and L. Liebert in 1974 [186]. As shown in Fig. 2.2(c), the rod-like smectic-C liquid crystals have a layered structure. In each smectic layer, liquid crystal molecules are oriented in one direction. However, when the smectic-C liquid crystals are composed of chiral molecules, the molecules in one layer are still oriented along with one direction, but the liquid crystal director \vec{d} of these molecules twists between adjacent layers. In this smectic-C phase, the liquid crystal director \vec{d} twists and forms a helical structure, which negates the reflection symmetry and validates the existence of spontaneous polarization. After their work, chiral liquid crystals in the smectic-C phase have been noted as smectic-C* until now. The schematic of chiral smectic-C (smectic-C*) liquid crystals is shown in Fig. 2.4.

As shown in Fig. 2.4, the tilt angle θ_t is defined as the angle between the liquid crystal director \vec{d} and the unit vector (i.e., helical axis) \vec{a} , which is normal to the smectic layers.

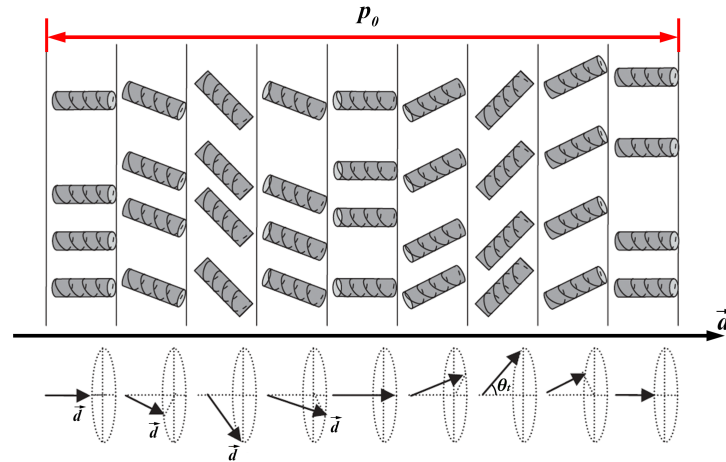


Fig. 2.4 The schematic of chiral smectic-C (smectic-C*) liquid crystals. The unit vector \vec{a} represents a direction perpendicular to the smectic-C layers. The liquid crystal director \vec{d} of all molecules is consistent in each layer, but it twists along the axis \vec{a} which enables the formation of the cone shape and helical structure. In this case, the unit vector \vec{a} can be used to represent the helix axis as well. The tilt angle θ_t is the angle between the liquid crystal director \vec{d} and the helical axis, which is perpendicular to smectic layers. p_0 is the period of the helical structure, by which the director \vec{d} changes back to the original state. Image reproduced from Deng-Ke Yang [183].

Although the chiral molecules of smectic-C* liquid crystals are oriented in the same direction \vec{d} within each layer, the liquid crystal director \vec{d} twists by a particular angle around the helical axis \vec{a} from layer to layer. The rotation of director \vec{d} within the cone shape gives rise to a helical structure, in which \vec{a} is the helical axis perpendicular to the smectic-C* layers and p_0 is the helical pitch. To find out the spontaneous polarization of chiral smectic-C* liquid crystals, the symmetry of molecules was studied. In the smectic-C*, because the smectic-C* liquid crystals are composed of chiral molecules and exhibit a helical structure, no reflection symmetry can be observed about the liquid crystal director \vec{d} or helical axis \vec{a} . As a result, the spontaneous polarization P_s is always perpendicular to the plane containing liquid crystal director \vec{d} and the helical axis \vec{a} . In other words, the spontaneous polarization P_s is normal to the helical axis \vec{a} and liquid crystal director \vec{d} and also twists from layer to layer due to the rotation of liquid crystal director \vec{d} between layers. The direction of spontaneous polarization for two chiral molecules in different layers is shown in Fig. 2.5.

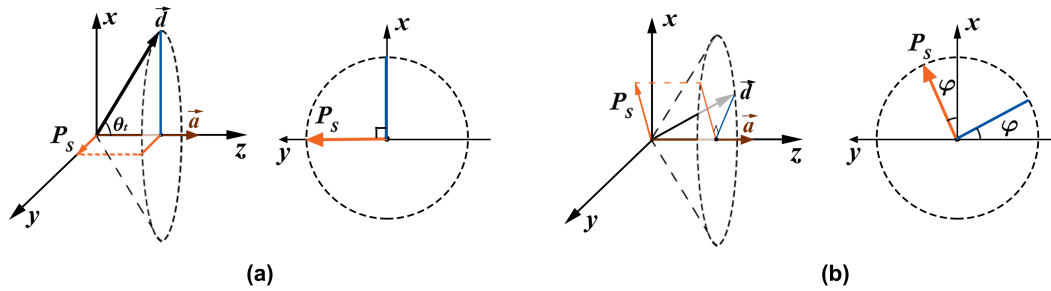


Fig. 2.5 Schematic of the spontaneous polarization in chiral smectic-C* liquid crystals, where \vec{a} represents the helical axis and θ_t represents the tilt angle. (a) When the liquid crystal director \vec{d} is on the xz plane, the direction of spontaneous polarization P_s is along the y-axis, which means the azimuthal angle φ is 0. (b) When the liquid crystal director \vec{d} is not on the xz plane, the direction of spontaneous polarization is tilted, which means the azimuthal angle φ is not 0. It is clear that the spontaneous polarization P_s is always on the xy plane and its direction changes by the rotation of director \vec{d} .

2.3 Design of the liquid crystal device

To enable the orientation deformation of liquid crystals by applying electric fields externally, the liquid crystal cell usually has a layered structure, in which the liquid crystal molecules are typically placed between two electrode layers with high optical transmission at the particular operation wavelength. Considering the three-dimensional structure of liquid crystal cells and the existence of an additional guarding electrode beside the top and bottom electrodes in its structure, the liquid crystal cells used in this work can be generally classified into two groups, namely S-type and SG-type. The schematic diagrams of S-type and SG-type liquid crystal cells are shown in Fig. 2.6 (a) and (b).

The S-type cells have only two electrode layers, in which one transparent electrically conductive layer is coated on the top substrate, while the other electrically conductive layer made of ITO is coated on the bottom substrate. It is worth noting that two electrically conductive layers on the top and bottom substrate have individual connections with two electrode areas (green and blue) on the bottom substrate. The SG-type liquid crystal cell has three electrodes, drive, return, and guarding electrodes respectively. The drive and return electrodes play the same role as top and bottom electrodes in the S-type liquid crystal cell, while an additional guarding electrode represented by a grey area is placed on the side of

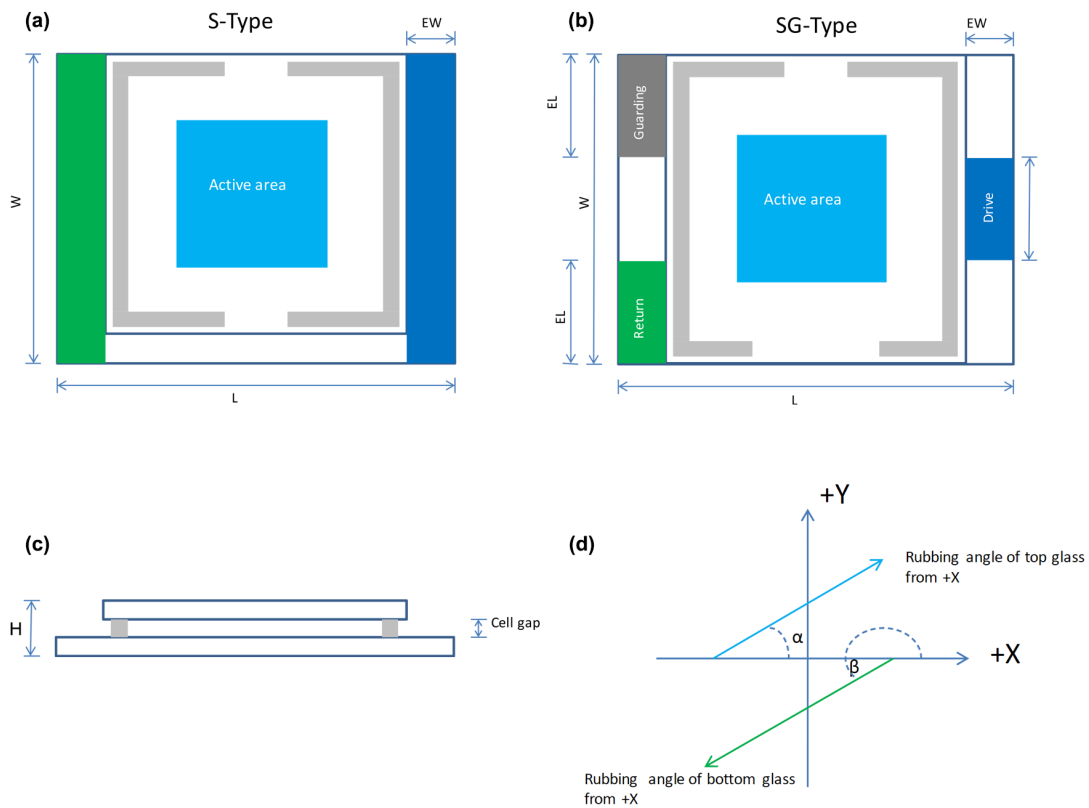


Fig. 2.6 Schematic diagram of (a) S-type and (b) SG-type liquid crystal cells. (c) A glass spacer is placed between the top and bottom glass substrates to create a small gap for liquid crystal. (d) The polyimide alignment layers of liquid crystal cell are mechanically rubbed with anti-parallel rubbing, where $\alpha = 0^\circ$ and $\beta = 180^\circ$. L , W , EW and H represent the length, width, electrode width and height of the liquid crystal cell. Images are from Instec Inc.

the bottom substrate. Because the top and bottom conductive layers are surrounded by an additional electrical conductive coating contacted with the guarding electrode, the guarding electrode can be considered as a grounding electrode, which can ensure the electric fields generated by the top (drive) and bottom (return) electrodes are perpendicular to the surface and well confined in the active area to minimize parasitic capacitance. To create a thin liquid crystal layer, the top and bottom substrates are separated by a glass spacer (light grey), which indicates a cell gap for the liquid crystal material ranging from $3.3 \mu\text{m}$ up to $22 \mu\text{m}$. To improve the ferroelectric effects of ferroelectric smectic- C^* liquid crystals under external electric fields, liquid crystals within the cell need to be homogeneously aligned along the

same direction. Therefore, homogeneous alignment layers are also included in the layered structure of the cell. The alignment layers in the liquid crystal cells used in my work were made by mechanically rubbing the surface of thin polyimide layers coated on both the top and bottom substrates. Along the rubbing direction, some microgrooves can be generated on the polyimide layers and the mechanical rubbing can also be observed clearly under the microscope. Compared with the direct rubbing on the glass substrates, the polymer chains caused by rubbing can give rise to a high anchoring strength around 10^{-3} J/m². Due to the effects of microgrooves and polymer chains on the homogeneous polyimide layers, the liquid crystal molecules in the cell are homogeneously aligned along the direction of mechanical rubbing [191, 192]. Apart from the rubbing technique, the photo-alignment technique is a new approach to the alignment of liquid crystals, which might be used in the future [193]. The small angle between the rubbing direction and the plane of the substrate is defined as the pretilt angle, which is between 1° and 3° in our liquid crystal cells. In this work, two thin polyimide layers exhibit the anti-parallel rubbing, where the rubbing angle α is 0° and the rubbing angle β is 180°. The dimensional parameters of liquid crystal cells used in this work are summarized in Table 2.1.

Table 2.1 Summary of Dimensional Parameters for Liquid Crystal Cells in This Work

Model	Cell gap(μ m)	L(mm)	W(mm)	EW(mm)	H(mm)	Active area(mm ²)
S025A033uG180	3.3	25	21	3	2.2	25
S100A050uG180	5.0	25	21	3	1.4	100
S100A077uG180	7.7	25	21	3	2.2	100
S100A090uG180	9.0	25	21	3	2.2	100
SG100A150uG180	14.6	25	21	3	2.2	25
S006A050uG180	5.0	7	7	1	1.4	9

As discussed earlier, the liquid crystal cells used in this work have a layered structure. The entire structure of the liquid crystal cell consists of two glass substrates, two indium tin oxide (ITO) layers for electrical conduction [194], two polyimide alignment layers, and a ferroelectric liquid crystal mixture filled in the cell gap generated by two glass spacers. For the liquid crystal cells used in this work, both the top and bottom substrates are made of soda-

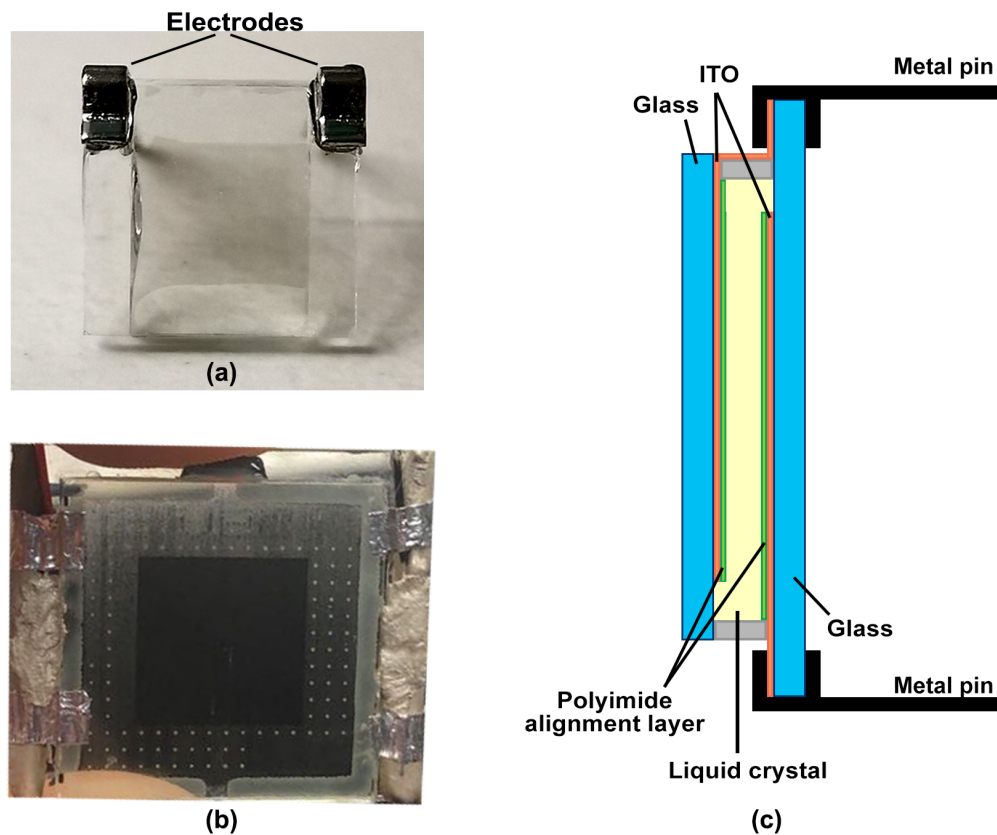


Fig. 2.7 The schematic diagrams of (a) $7\text{ mm} \times 7\text{ mm}$ and (b) $25\text{ mm} \times 21\text{ mm}$ liquid crystal cells and (c) their layered structure.

lime glass. To create the electric fields across the liquid crystals, two electrically conductive layers are required with a high optical transmission rate, so two transparent conducting oxide thin-films from ITO are coated on one side of both top and bottom substrates. The resistance of the ITO layer is $100\ \Omega$. To align the liquid crystal molecules homogeneously along the defined direction with high anchoring energy, two polyimide layers are mechanically rubbed with anti-parallel rubbing and coated next to the ITO layers. The ferroelectric liquid crystal mixtures developed by P. N. Lebedev Physical Institute of Russian Academy of Sciences are loaded into the thin gap between two substrates and sealed by UV-curing optical adhesives. The schematic diagrams of $7\text{ mm} \times 7\text{ mm}$ and $25\text{ mm} \times 21\text{ mm}$ liquid crystal cells and their layered structure are presented in Fig. 2.7. The thickness of each layer in the liquid crystal cell is summarized in Table 2.2.

Table 2.2 Summary of Thickness Parameters in the Layered Structure of Liquid Crystal Cells

Layer name	Material	Thickness
Glass layer	Soda lime glass	1 mm
ITO layer	Indium tin oxide	25 nm
Alignment layer	Polyimide	50 nm
Liquid crystal layer	Ferroelectric liquid crystal	3.3-15 μm

2.4 Modelling approach

To study how the liquid crystal cell interacts with the externally applied electric fields, an understanding of light propagation in the liquid crystal cell is required. The ferroelectric smectic-C* liquid crystals composed of chiral molecules is an anisotropic material, because of their orientation order and physical model. When a light beam propagates within an anisotropic film, the refractive indexes are different along the ordinary and extraordinary axes, which results in the birefringence $\Delta n = n_e - n_o$. Because of the different propagation velocities along the ordinary and extraordinary axes, two polarization components of light will experience a phase shift, and the polarization state will be changed. To transform the polarization state change into the change in the light intensity, and optical polarizer and analyser can be placed in front of and behind the liquid crystal cell respectively and the output light intensity can be measured behind the analyser. In this work, the PBS and gold mirror are placed in front of and behind the liquid crystal cell, so the PBS can act as an analyser when the light is reflected from the gold mirror. The schematic of a typical configuration of liquid crystal modulator is shown in Fig. 2.8.

2.4.1 Jones matrix method

The Jones matrix was demonstrated for the first time by R. Clark Jones in 1941 [195] as a new method representing optical components and analyse optical systems. By using this approach, all-optical components can be represented by a 2×2 Jones matrix and the state of light can be represented by 2×1 Jones vector. As discussed earlier, the liquid crystal cell

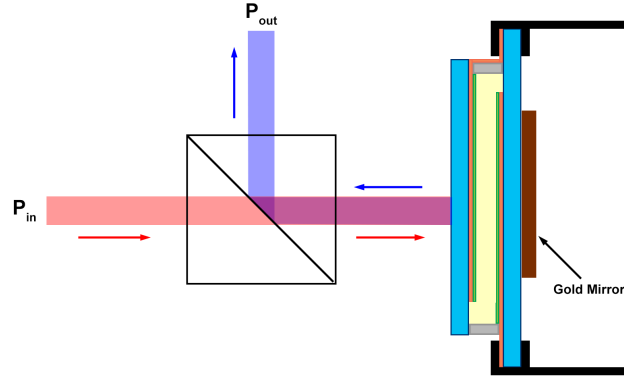


Fig. 2.8 Schematic of the typical configuration of liquid crystal modulator with a PBS and gold mirror.

is an anisotropic component in which the ordinary refractive index n_o is different from the extraordinary refractive index n_e , and their difference is defined as birefringence Δn . As a result, the liquid crystal cell can give rise to the phase retardation Γ , which can be expressed as

$$\Gamma = \frac{2\pi d(n_e - n_o)}{\lambda} = \frac{2\pi d\Delta n}{\lambda}. \quad (2.1)$$

where d refers to the thickness of the liquid crystal layer, λ is the wavelength of incident light and Δn represents the birefringence of liquid crystals. Therefore, the phase retardation can be represented in the Jones matrix like

$$L(\Gamma) = \begin{pmatrix} e^{-i\frac{\Gamma}{2}} & 0 \\ 0 & e^{i\frac{\Gamma}{2}} \end{pmatrix}. \quad (2.2)$$

In the numerical model, the gold mirror behind the liquid crystal cell can be assumed to be a mirror with 100 % reflectivity. Its Jones matrix can be expressed by

$$M = \begin{pmatrix} 1 & 0 \\ 0 & 1 \end{pmatrix}. \quad (2.3)$$

In practice, the liquid crystal cell can be rotated freely to control the output light intensity P_{out} . Therefore, β is defined as the angle between the direction of P-polarization after the PBS and the helix axis of the liquid crystal cell. In this case, we can assume the direction of P-polarization is the same as the x-axis of the lab frame, and the optical axis of the liquid crystal cell remains unchanged without the applied electric field. Therefore, the rotation matrix with the rotation angle β is added into the optical system as

$$R(\beta) = \begin{pmatrix} \cos \beta & -\sin \beta \\ \sin \beta & \cos \beta \end{pmatrix}. \quad (2.4)$$

As shown in Fig. 2.8, only the P-polarization component of incident light can pass through the PBS and enter the liquid crystal cell, so the Jones vector of the incident light to the cell can be expressed as

$$\vec{E}_{in} = \begin{pmatrix} E_{x,in} \\ E_{y,in} \end{pmatrix} = \begin{pmatrix} 1 \\ 0 \end{pmatrix}. \quad (2.5)$$

Therefore, the Jones vector of output light \vec{E}_{out} from the liquid crystal cell can be expressed by

$$\begin{aligned} \vec{E}_{out} &= R(\beta) \cdot L(\Gamma) \cdot M \cdot L(-\Gamma) \cdot R(-\beta) \cdot \vec{E}_{in} \\ &= \begin{pmatrix} \cos^2 \beta e^{-i\Gamma} - \sin^2 \beta e^{i\Gamma} \\ \sin \beta \cos \beta e^{-i\Gamma} + \sin \beta \cos \beta e^{i\Gamma} \end{pmatrix} = \begin{pmatrix} E_{x,out} \\ E_{y,out} \end{pmatrix}. \end{aligned} \quad (2.6)$$

Because the light beam reflected from the PBS is regarded as the output light in Fig. 2.8, the direction of S-polarization is the transmission axis of the analyser, which is perpendicular to the transmission axis of the polarizer (P-polarization). Thus, the intensity of the output light can be considered as the crossed reflectance R_{\perp} and calculated by

$$R_{\perp} = |E_{y,out}|^2 = |\sin \beta \cos \beta e^{-i\Gamma} + \sin \beta \cos \beta e^{i\Gamma}|^2 = \sin^2(\Gamma) \sin^2(2\beta) \quad (2.7)$$

$$R_{\perp} = \sin^2 \left(\frac{2\pi d \Delta n}{\lambda} \right) \sin^2(2\beta). \quad (2.8)$$

The above equation is achieved under the assumption that the optical axis of the liquid crystal cell remains unchanged without the applied electric field. When the external electric fields are applied to the liquid crystal cell, the birefringence will change and the optical axis of the liquid crystal cell will rotate. Thus, the birefringence $\Delta n(E)$ and the rotation angle $\Omega(E)$ are controlled by the direction and strength of applied electric fields. Therefore, the general expression of the crossed reflectance R_{\perp} is shown as

$$R_{\perp} = \sin^2 \left(\frac{2\pi d \Delta n(E)}{\lambda} \right) \sin^2(2\beta - 2\Omega(E)). \quad (2.9)$$

2.4.2 Mueller matrix method

The Mueller matrix is another approach that can be used to numerically model the light propagation behaviors after passing through the liquid crystal cells. In this approach, the 4×1 Stokes vector, $\vec{S} = [S_0, S_1, S_2, S_3]^T$ is used to represent the polarization state of light, where S_0 refers to the light intensity, S_1 refers to the intensity difference between x-axis and y-axis components, S_2 refers to the state along $\pm 45^\circ$ and S_3 refers to the circular polarization state. The 4×4 Mueller matrix, M , is used to describe the impacts of optical components on the polarization state of light. If \vec{S}_i represents the Stokes vector of the incident light, the Stokes vector of the outgoing light \vec{S}_o can be calculated by

$$\vec{S}_o = M \cdot \vec{S}_i. \quad (2.10)$$

If the liquid crystal cell is considered as a retarder with the phase retardation of Γ , in which β is the angle between its slow or optical axis and the x-axis of lab frame and the phase retardation, Γ , can be calculated by Eq. (2.1). Therefore, its Mueller matrix $M_{LC}(\Gamma, \beta)$ can be represented by

$$M_{LC}(\Gamma, \beta) = \begin{pmatrix} 1 & 0 & 0 & 0 \\ 0 & \cos^2(2\beta) + \sin^2(2\beta) \cos \Gamma & \sin(2\beta) \cos(2\beta)(1 - \cos \Gamma) & \sin(2\beta) \sin \Gamma \\ 0 & \sin(2\beta) \cos(2\beta)(1 - \cos \Gamma) & \sin^2(2\beta) + \cos^2(2\beta) \cos \Gamma & -\cos(2\beta) \sin \Gamma \\ 0 & -\sin(2\beta) \sin \Gamma & \cos(2\beta) \sin \Gamma & \cos \Gamma \end{pmatrix}. \quad (2.11)$$

Since the linear polarizer can be considered as an optical absorber along the defined direction, the linear polarizer along the y-axis can be regarded as a vertical polarizer represented by M_v , and the one along the x-axis can be regarded as a horizontal polarizer represented by M_h . The Mueller matrices of a vertical and horizontal polarizer can be expressed as

$$M_v = \frac{1}{2} \begin{pmatrix} 1 & -1 & 0 & 0 \\ -1 & 1 & 0 & 0 \\ 0 & 0 & 0 & 0 \\ 0 & 0 & 0 & 0 \end{pmatrix}, \quad (2.12)$$

$$M_h = \frac{1}{2} \begin{pmatrix} 1 & 1 & 0 & 0 \\ 1 & 1 & 0 & 0 \\ 0 & 0 & 0 & 0 \\ 0 & 0 & 0 & 0 \end{pmatrix}. \quad (2.13)$$

Because the gold mirror is integrated behind the liquid crystal cell, it also needs to be added into the system and its Mueller matrix M_m can be expressed as

$$M_m = \begin{pmatrix} 1 & 0 & 0 & 0 \\ 0 & 1 & 0 & 0 \\ 0 & 0 & -1 & 0 \\ 0 & 0 & 0 & -1 \end{pmatrix}. \quad (2.14)$$

According to the typical configuration of liquid crystal modulator shown in Fig. 2.8, the light beam passes through a horizontal linear polarizer (P-polarized component from PBS), which is followed by a liquid crystal cell, a gold mirror and a vertical linear polarizer (S-polarized component from PBS). Therefore, the Mueller matrix M of the entire system with all optical elements can be derived from the direct multiplication on the Mueller matrix of each element in reverse order along the light path. Therefore, the Mueller matrix M of the entire setup can be derived as

$$\begin{aligned}
 M &= M_v \cdot M_{LC}(\Gamma, -\beta) \cdot M_m \cdot M_{LC}(\Gamma, \beta) \cdot M_h \\
 &= \begin{pmatrix} \frac{1}{2} \sin^2 \Gamma \sin^2(2\beta) & \frac{1}{2} \sin^2 \Gamma \sin^2(2\beta) & 0 & 0 \\ -\frac{1}{2} \sin^2 \Gamma \sin^2(2\beta) & -\frac{1}{2} \sin^2 \Gamma \sin^2(2\beta) & 0 & 0 \\ 0 & 0 & 0 & 0 \\ 0 & 0 & 0 & 0 \end{pmatrix}. \quad (2.15)
 \end{aligned}$$

In this case, we can assume the incident light is P-polarized or horizontally polarized. As a result, the Stokes vector \vec{S}_i of the incident light can be represented by

$$\vec{S}_i = \begin{pmatrix} 1 \\ 1 \\ 0 \\ 0 \end{pmatrix}. \quad (2.16)$$

Therefore, the Stokes vector \vec{S}_o of outgoing light from the liquid crystal device can be expressed as

$$\vec{S}_o = M \cdot \vec{S}_i = \begin{pmatrix} \sin^2 \Gamma \sin^2(2\beta) \\ -\sin^2 \Gamma \sin^2(2\beta) \\ 0 \\ 0 \end{pmatrix}. \quad (2.17)$$

From the definition of Stokes vector as discussed at the beginning of this section, the first element in \vec{S}_o represents the light intensity of outgoing light. Therefore, the crossed reflectance R_{\perp} from the typical configuration of liquid crystal device can be calculated by

$$R_{\perp} = \sin^2 \left(\frac{2\pi d \Delta n(E)}{\lambda} \right) \sin^2 (2\beta - 2\Omega(E)), \quad (2.18)$$

where $\Delta n(E)$ represents the birefringence of liquid crystals and $\Omega(E)$ represents the rotation angle of optical axis of liquid crystal cell. Both of them are externally controlled by the direction and strength of applied electric fields.

2.4.3 Transfer matrix method

To figure out the transmission and reflection coefficients of the layered systems, such as a substrate or a slab, an analytical algorithm was reported by Mathias Schubert in 1995 based on Berreman 4×4 method [196, 197]. In this approach, the arbitrarily anisotropic homogeneous layered systems are represented by the partial transfer 4×4 matrices, T_p . For the liquid crystal cell introduced earlier, the anisotropic media, liquid crystals, is sandwiched between two glass substrates, so the transition matrices for the incidence and emergence need to be added into the optical system as the incident matrix L_a and exit matrix L_f respectively. In this approach, the reflection and transmission coefficients of the anisotropic layered system can be easily obtained from the product of the incident matrix L_a , partial transfer matrix T_p , and exit matrix L_f . The general schematic of electromagnetic plane waves traveled forward and backward in the liquid crystal cell is shown in Fig. 2.9.

Based on the direction of the electric field, each wave can be divided into two modes, s-mode and p-mode, where s-mode represents the component with the electric field perpendicular to the xz plane of the wave traveling and p-mode represents the component with the electric field parallel to the xz plane of the wave traveling. In the above figure, four electromagnetic plane wave components can be observed at the front and back interfaces of a liquid crystal cell, in which A_s and A_p represent the complex amplitudes of incident wave in s- and p-mode, B_s and B_p represent the complex amplitudes of the reflected wave in two

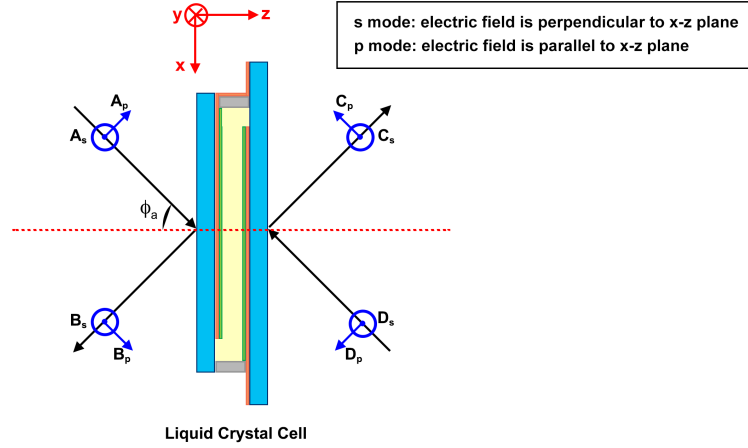


Fig. 2.9 Schematic of forward and backward traveling waves on the interfaces of liquid crystal cell. ϕ_a is the angle between the incident wave and surface normal. A , B , C and D represent the complex amplitude of forward traveling wave and backward traveling waves. These waves consist of two components, in which s-mode indicates the electric field perpendicular to the x-z plane of wave traveling and p-mode indicates the electric field parallel to the x-z plane of wave traveling.

modes, C_s and C_p represent the complex amplitudes of the transmitted wave in two modes and D_s and D_p represent the complex amplitudes of back-traveling wave in two modes. In this case, there is no back-traveling wave, so it can be ignored by assuming $D_s = D_p = 0$. Therefore, the transfer matrix T for liquid crystal cell can be expressed as a 4×4 matrix [196], like

$$\begin{pmatrix} A_s \\ B_s \\ A_p \\ B_p \end{pmatrix} = \begin{pmatrix} T_{11} & T_{12} & T_{13} & T_{14} \\ T_{21} & T_{22} & T_{23} & T_{24} \\ T_{31} & T_{32} & T_{33} & T_{34} \\ T_{41} & T_{42} & T_{43} & T_{44} \end{pmatrix} \cdot \begin{pmatrix} C_s \\ 0 \\ C_p \\ 0 \end{pmatrix} \quad (2.19)$$

Therefore, the transmission and reflection coefficients can be calculated by the elements of the transfer matrix T . For example, the reflection coefficient r_{ss} of the layered system considering the s-mode can be expressed as

$$r_{ss} = \left(\frac{B_s}{A_s} \right)_{A_p=0} = \frac{T_{21}T_{33} - T_{23}T_{31}}{T_{11}T_{33} - T_{13}T_{31}}. \quad (2.20)$$

To obtain the transmission and reflection coefficients of the anisotropic layered system as a liquid crystal cell, both the incident matrix L_a and the exit matrix L_f are required, and these transition matrices were derived and reported by Mathias Schubert in [196]. In this case, the incident light is perpendicular to the surface of the liquid crystal cell, so the incident angle ϕ_a is 0. The incident matrix L_a and the inverse of the incident matrix L_a^{-1} can be expressed by

$$L_a = \left(\begin{array}{cccc} 0 & 0 & \cos \phi_a & -\cos \phi_a \\ 1 & 1 & 0 & 0 \\ -n_a \cos \phi_a & n_a \cos \phi_a & 0 & 0 \\ 0 & 0 & n_a & n_a \end{array} \right)_{\phi_a=0} = \left(\begin{array}{cccc} 0 & 0 & 1 & -1 \\ 1 & 1 & 0 & 0 \\ -n_a & n_a & 0 & 0 \\ 0 & 0 & n_a & n_a \end{array} \right), \quad (2.21)$$

$$L_a^{-1} = \frac{1}{2} \left(\begin{array}{cccc} 0 & 1 & -\frac{1}{n_a} & 0 \\ 0 & 1 & \frac{1}{n_a} & 0 \\ 1 & 0 & 0 & \frac{1}{n_a} \\ -1 & 0 & 0 & \frac{1}{n_a} \end{array} \right). \quad (2.22)$$

In the incident matrix, n_a represents the refractive index of the material in front of the liquid crystal cell. Because the propagation direction of incident light is normal to the front surface of liquid crystal cell, the emergence angle ϕ_f is 0 as well. The exit matrix L_f can be written as

$$L_f = \left(\begin{array}{cccc} 0 & 0 & \cos \phi_f & 0 \\ 1 & 0 & 0 & 0 \\ -n_f \cos \phi_f & 0 & 0 & 0 \\ 0 & 0 & n_f & 0 \end{array} \right)_{\phi_f=0} = \left(\begin{array}{cccc} 0 & 0 & 1 & 0 \\ 1 & 0 & 0 & 0 \\ -n_f & 0 & 0 & 0 \\ 0 & 0 & n_f & 0 \end{array} \right). \quad (2.23)$$

In the exit matrix, n_f represents the refractive index of the material behind the liquid crystal cell. In M. Schubert's paper, the partial transfer matrices for the anisotropic layered system were derived as well. For the cell with the liquid crystal thickness represented by d , its partial transfer matrix T_p can be expressed as

$$T_p = \begin{pmatrix} \cos k_x & 0 & 0 & \frac{i}{n_x \sin k_x} \\ 0 & \cos k_y & -\frac{i}{n_y \sin k_y} & 0 \\ 0 & -\frac{i}{n_y \sin k_y} & \cos k_y & 0 \\ in_x \sin k_x & 0 & 0 & \cos k_x \end{pmatrix}. \quad (2.24)$$

In the partial transfer matrix of liquid crystal cell, k_x and k_y are the wave vectors along the x- and y-axis in the liquid crystal cell, which can be written by

$$k_x = \frac{2\pi d n_x}{\lambda}, \quad (2.25)$$

$$k_y = \frac{2\pi d n_y}{\lambda}. \quad (2.26)$$

In the above equations, d is the thickness of the liquid crystal layer, λ is the operating wavelength and n_x and n_y are the refractive indexes along x- and y-axis, which can also be represented as the ordinary n_o and extraordinary refractive index n_e respectively. In this approach, the transfer matrix T of the entire layered system can be expressed as

$$T = L_a^{-1} \cdot T_p \cdot L_f. \quad (2.27)$$

To calculate the crossed reflectance R_{\perp} shown in Fig. 2.8, three assumptions need to be made, including

- Assumption 1: $n_f \rightarrow +\infty$, because the light beam will be reflected by the gold mirror integrated to the liquid crystal cell.
- Assumption 2: $A_p = -\cos \beta$ and $A_s = -\sin \beta$, because the normalised incident linearly polarised light at an angle β to the x-axis.
- Assumption 3: $n_a = n_x = n_y = 1$, because the multiple reflections at interfaces can be neglected.

Considering the above assumptions made in our work, the s component B_s and p component B_p of the reflected electromagnetic plane wave can be solved by Eq. (2.19) and

Eq. (2.27). In the typical configuration of liquid crystal device, the transmission axis of the analyser has an angle of $\beta + \frac{\pi}{2}$ to the x-axis, so the complex expression of the reflected wave using the crossed analyser can be written as

$$r = B_s \cos \beta + B_p \sin \beta. \quad (2.28)$$

As the intensity of incident light is normalized, the crossed reflection coefficient of the liquid crystal device can be calculated as the intensity of reflected wave as

$$\begin{aligned} R_{\perp} &= \bar{r} \cdot r = \sin^2(k_x - k_y) \sin^2(2\beta) \\ &= \sin^2\left(\frac{2\pi d \Delta n}{\lambda}\right) \sin^2(2\beta). \end{aligned} \quad (2.29)$$

For the ferroelectric liquid crystal cell, both the birefringence $\Delta n(E)$ and the optical axis orientation $\Omega(E)$ change with the direction and strength of the applied electric field, thus the crossed reflection has the same expression as other methods,

$$R_{\perp} = \sin^2\left(\frac{2\pi d \Delta n(E)}{\lambda}\right) \sin^2(2\beta - 2\Omega(E)). \quad (2.30)$$

2.5 Femtosecond direct-written waveguide

2.5.1 Glass Material

Since the laser was demonstrated for the first time in 1960, the laser emissions at different wavelengths have been successfully developed utilising a variety of crystals and glasses doped with rare-earth ions, including Er^{3+} , Tm^{3+} , Ho^{3+} , Dy^{3+} , Pr^{3+} , Yb^{3+} , Nd^{3+} . Comparing to silicate and phosphate glasses, fluoride glasses have attracted much attention because people found these specific glasses have low phonon energy which results in high infrared transparency, and a high rare-earth solubility which makes them an excellent platform for MIR lasers. In addition to their excellent optical properties, fluoride glasses as host materials are of significant importance, because they have a high limit on doping levels (maximum 10 mol%), high stability, relatively high strength and low background loss smaller than 0.05

dB/m. As a result, fluoride glasses are considered to be excellent options for lasers in visible and MIR regimes [198]. The energy level diagrams of Er^{3+} , Tm^{3+} and Ho^{3+} ions doped in the ZBLAN host material are shown in Fig. 2.10.

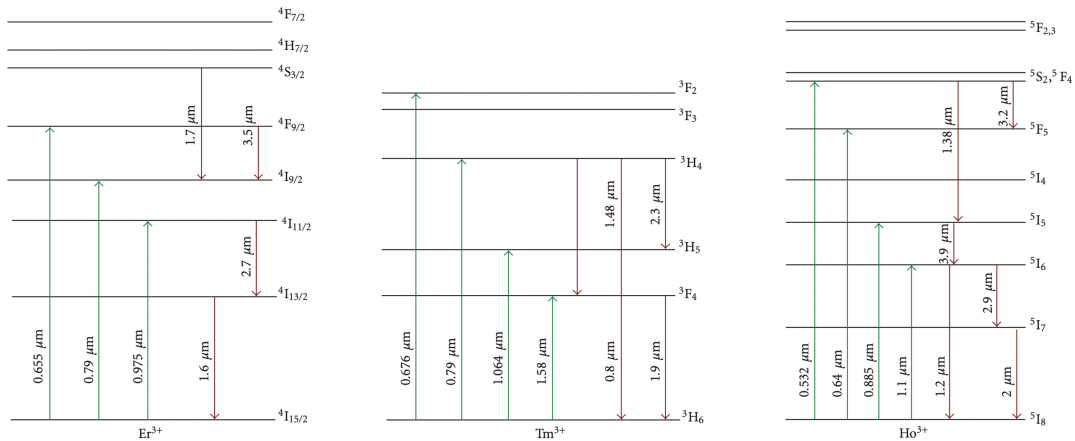


Fig. 2.10 Energy level diagrams of Er^{3+} , Tm^{3+} and Ho^{3+} ions in the ZBLAN host material. Image reproduced from X. Zhu [198].

The ZBLAN glass formation in the mixture of ZrF_4 - BaF_2 - LaF_3 - AlF_3 - NaF was reported for the first time by Ohsawa et al. in 1981 [199]. After the discovery of ZBLAN glass, its optical and mechanical properties were extensively investigated. Due to its broad transmission window, low refractive index, small thermal dependence of the optical properties, and ease of machining and polishing, ZBLAN glass was considered as the most stable heavy metal fluoride (HMF) glass and the best choice for optical fibre fabrication.

Because the fluoride ion is singly charged, ZBLAN glasses have a lower bond strength than silica glasses. The ZBLAN glass with a lower bonding strength give rise to higher chemical reactivity and greater infrared transparency. However, the ZBLAN glass has a higher transparency than of silica glass, but its stability and hardness are not as good as those of silica glass. Additional attention is required to avoid handling damage on the ZBLAN glass and ZBLAN fibres are always protected by a special coating, which can improve their stability and hardness for practical applications.

2.5.2 Waveguide fabrication process

To write multiple optical waveguides with the desired geometry into ZBLAN glass with composition $\text{ZrF}_4\text{-BaF}_2\text{-LaF}_3\text{-AlF}_3\text{-NaF}$, the femtosecond laser direct-write technique was selected and utilised in the fabrication process. To obtain the expected structural modification within the bulk transparent material, a pulsed laser source with an ultrashort pulse width (10s fs), large pulse energy (100s nJ), and high repetition rate (several MHz) is required for the femtosecond laser direct-write (FLDW) technique. In the fabrication process, an ultrafast compact Ti:Sapphire oscillator system (FEMTOSOURCE XL500 from Femtolasers GmbH) based on chirped pulse oscillator (CPO) technology was utilised [200, 201]. This oscillator system provided the ultrashort laser pulses at 800 nm wavelength (optical bandwidth > 30 nm) with a pulse width of less than 50 fs in combination with high pulse energy (> 500 nJ) and extremely high peak power (> 10 MW). Because of the high repetition rate around 5.1 MHz, the heat generated by a single laser pulse cannot be diffused out before the occurrence of the following laser pulses. Therefore, the heat accumulates within the host material and results in melting and structural modification of the glass. The laser pulses were focused by a high-NA objective to a spot which was 300 μm below the top surface of the ZBLAN glass sample. To inscribe a uniform waveguide within the ZBLAN glass and enable the rapid quenching in the inscription process, the glass sample was placed on Aerotech ABL-series linear stage and moved at a constant speed of around 1000 mm/min.

From the above figure, the ultrashort laser pulses less than 50 fs were focused by a focusing immersion oil objective with a magnification of 100 times. The heat was generated by the laser pulses and accumulated on a small spot, giving rise to the direct writing in the ZBLAN glass sample. To write continuous tubular waveguides, the glass sample was placed on a high precision automatic translation stage and moved horizontally, vertically, and along the writing direction. As a result, multiple waveguides can be written within a single ZBLAN glass substrate with the desired geometry and spacing.

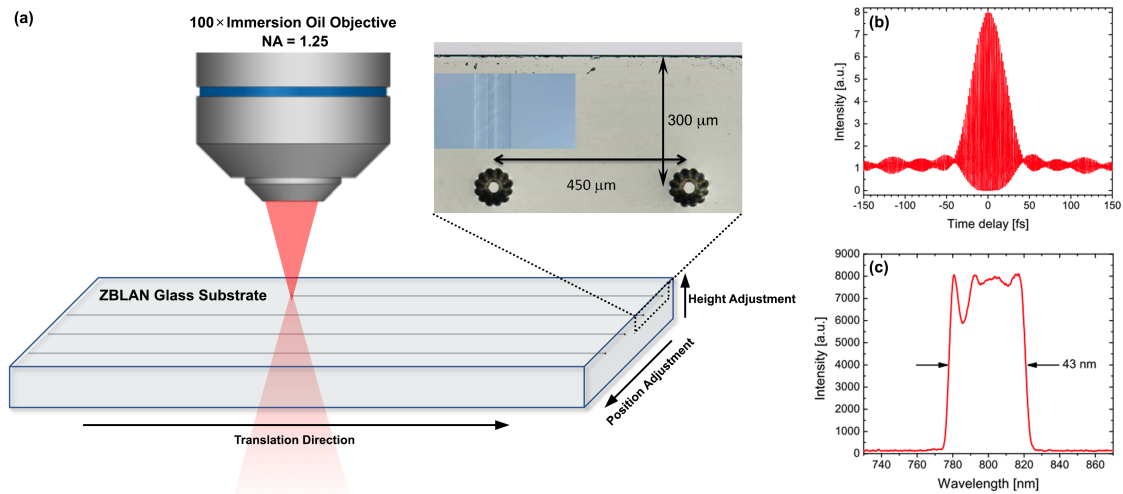


Fig. 2.11 (a) Schematic of ZBLAN waveguide fabrication by using femtosecond direct-writing method (FDWM). The femtosecond ultrashort laser pulses were focused by a 100× immersion oil objective with a NA of 1.25. The focusing spot was set to be 300 μm below the top surface of the ZBLAN glass substrate on the translation stage. The power density of the ultrashort laser pulses can be controlled by varying the magnification of the focusing objective and the beam spot size. The continuous tubular waveguide can be directly written by moving the ZBLAN glass substrate horizontally (position), vertically (height), and along the transition direction. (b) The measured autocorrelation trace and (c) optical spectrum of the ultrashort laser pulses with a pulse width of less than 50 fs in combination with high pulse energy (> 500 nJ) and extremely high peak power (> 10 MW). The emission wavelength of ultrashort laser pulses is at 800 nm wavelength with an optical bandwidth around 43 nm. (b) and (c) are from Femtolasers GmbH.

2.5.3 Waveguide geometry

To study the structural modification in the ZBLAN glass created by applying the femtosecond direct-writing technique, the absolute refractive index profile (RIP) of the single modification and the inscribed cylinder waveguide by multiple modifications were measured by a RINCK Elektronik refractive index profilometer with the incident wavelength of 635 nm by Dr. Simon Gross and Dr. D. G. Lancaster in 2011 and 2013 [80, 202]. As shown in Fig. 2.12, the femtosecond laser can lead to a change in the refractive index by a single inscribed modification, which is around -1.0×10^{-3} at the center. For the fabrication of a tubular waveguide with a depressed cladding structure, multiple cylinders were written by the ultrafast compact Ti:Sapphire oscillator system to form one or more than one overlapping

ring within the host glass. As a result, the depressed cladding in the ring structures can give rise to a refractive index change from -1.0×10^{-3} to -1.5×10^{-3} , which enables the guiding behavior of the inscribed waveguide.

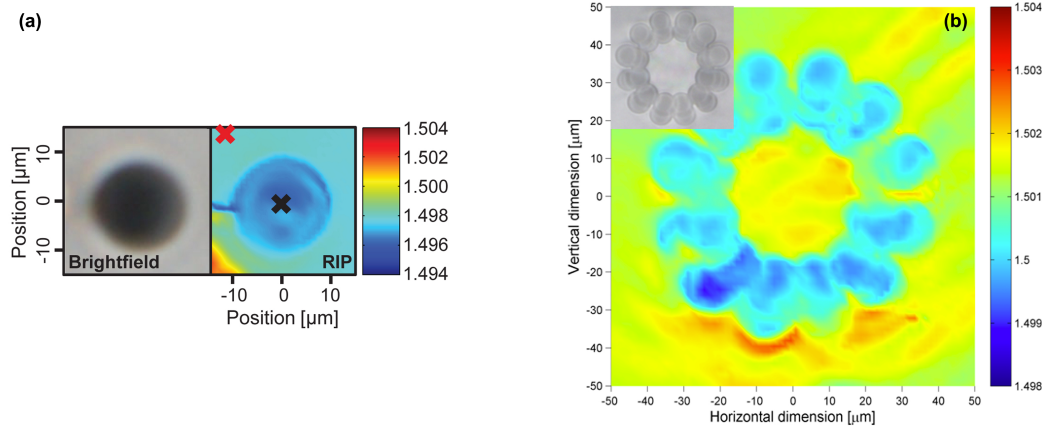


Fig. 2.12 (a) The microscopy images and the measured RIPs of one inscribed modification in a Yb-doped ZBLAN glass substrate [202] and (b) the tubular waveguide structure formed by two partial overlapping rings of the inscribed modifications in a Tm³⁺-doped ZBLAN glass substrate [80].

To minimize the confinement loss of the inscribed waveguide, the effects of the cladding diameter and index contrast on the confinement loss have been investigated and discussed by D. G. Lancaster et. al in 2011 [80]. In their work, the confinement losses of the fundamental mode and the first higher-order mode of the inscribed Tm³⁺-doped waveguide were analysed as a function of the depressed cladding diameter varying from 10 μm to 24 μm, when the core diameter was maintained at 30 μm for all waveguides as shown in Fig. 2.13. The simulation results showed that, when the inscribed waveguide within the ZBLAN glass was composed of 24 partially overlapping cylinders in the form of two rings, in which 12 partially overlapping cylinders form one ring, the depressed cladding width was around 23 μm, which can give rise to the lowest confinement loss down to only 0.018 dB/cm. Additionally, the effects of changing the refractive index contrast Δn on the confinement loss were also investigated. It is clear that both a wider cladding area and a larger refractive index contrast can lead to a smaller confinement loss for both fundamental mode and higher-order modes. It is also worth noting that the confinement loss of the first higher-order mode is 100 times larger than that

of the fundamental mode, which means the higher-order mode will not reach the threshold in a laser resonator and the laser is therefore quasi single mode.

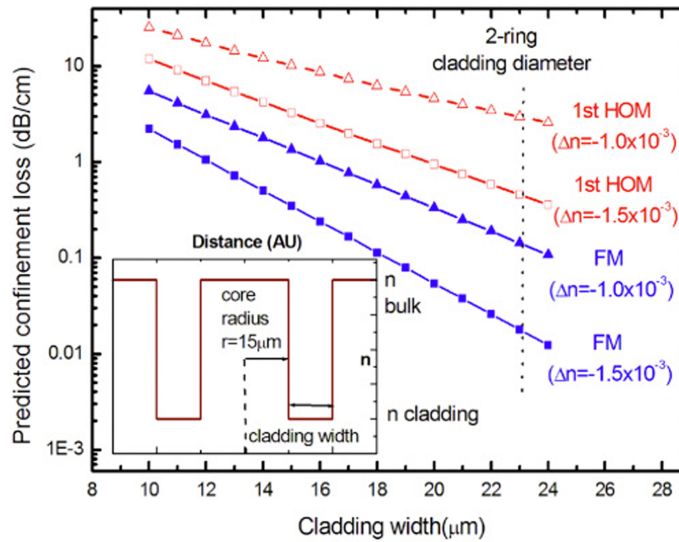


Fig. 2.13 The confinement losses for different modes of the inscribed Tm^{3+} -doped waveguide as a function of the depresses cladding width ranging from 10 μm to 24 μm , when the core diameter is 30 μm [80].

Table 2.3 Geometric Parameters, Doping Ions and Emission Wavelengths of the Femtosecond Direct Written waveguides

Host Material	Doping-ions	D_{core} (μm)	$D_{cladding}$ (μm)	Index Contrast	Wavelength(μm)	Ref
ZBLAN	Yb^{3+}	13	32	-1.2×10^{-3}	1.0	[203]
ZBLAN	$\text{Er}^{3+}, \text{Yb}^{3+}, \text{Ce}^{3+}$	34	32	-1.0×10^{-3}	1.5	[204]
ZBLAN	Tm^{3+}	30	23	-1.5×10^{-3}	1.9	[80]
ZBLAN	$\text{Ho}^{3+}, \text{Tm}^{3+}$	24	32	-1.6×10^{-3}	2.1	[79]
ZBLAN	Ho^{3+}	25	52	-1×10^{-3}	2.9	[205]
ZBLAN	Passive	50	60	-0.6×10^{-3}	3.0-4.0	[206]

The femtosecond direct writing method provides the great flexibility and feasibility of fabricating the waveguide chips with the desired geometry and RIP. So far, the inscribed waveguide chips by ultrashort laser pulses have been widely utilised in a variety of waveguide laser applications at different wavelengths. The geometric parameters, doping ions and

emission wavelengths of the inscribed waveguides in the previous publications are listed in Table 2.3.

Chapter 3

Characterisation of liquid crystal devices

In our work, the thin gap between two ITO layers of the liquid crystal cell is filled with nano-scale pitch ferroelectric chiral smectic-C* liquid crystals. Due to ferroelectric effects, its molecular arrangement can be continuously deformed by the presence of electric fields, giving rise to the "deformed helix" mode of operation. This deformation of the molecular helical structure of liquid crystals gives rise to electric field controlled changes in its optical properties, including birefringence and orientation of optical axes. The deformed helix structure, the controllable birefringence and optical axes by applying electric fields provide the possibility of using liquid crystal modulators as actively controlled intracavity loss modulators in Q-switched and mode-locked laser applications. In this chapter, the deformation of the helix structure in liquid crystals, the variance of the birefringence, the rotation of optical axes, the tilt angle and the optical transmission will be studied and discussed in great detail both theoretically and experimentally.

3.1 Deformed helix structure by electric fields

As discussed in Chapter 2, chiral smectic-C* liquid crystal molecules in successive layers exhibit a twist of the director around the mechanical rubbing direction on the alignment layer. As a result, the helix structure can be formed as shown in Fig. 2.4. Moreover, when the helix pitch p_o is much smaller than the liquid crystal thickness d and the applied electric

field E is smaller than the critical electric field E_{crit} for unwinding, ferroelectric smectic- C^* liquid crystal molecules can operate in the DHF mode. Therefore, these liquid crystals are also known as deformed helix ferroelectric liquid crystals (DHFLC). In this work, the helix pitch p_o of liquid crystals is only 200 nm and the critical electric field is around 1.3 V/ μm . When the liquid crystal thickness d is much larger than the helix pitch p_o and the applied electric field is no larger than 1.3 V/ μm , two requirements of deformed helix ferroelectric liquid crystals (DHFLC) are satisfied and DHF effects can be observed in experiments. The deformations of the helix structure of liquid crystals driven by different electric fields are shown in Fig. 3.1.

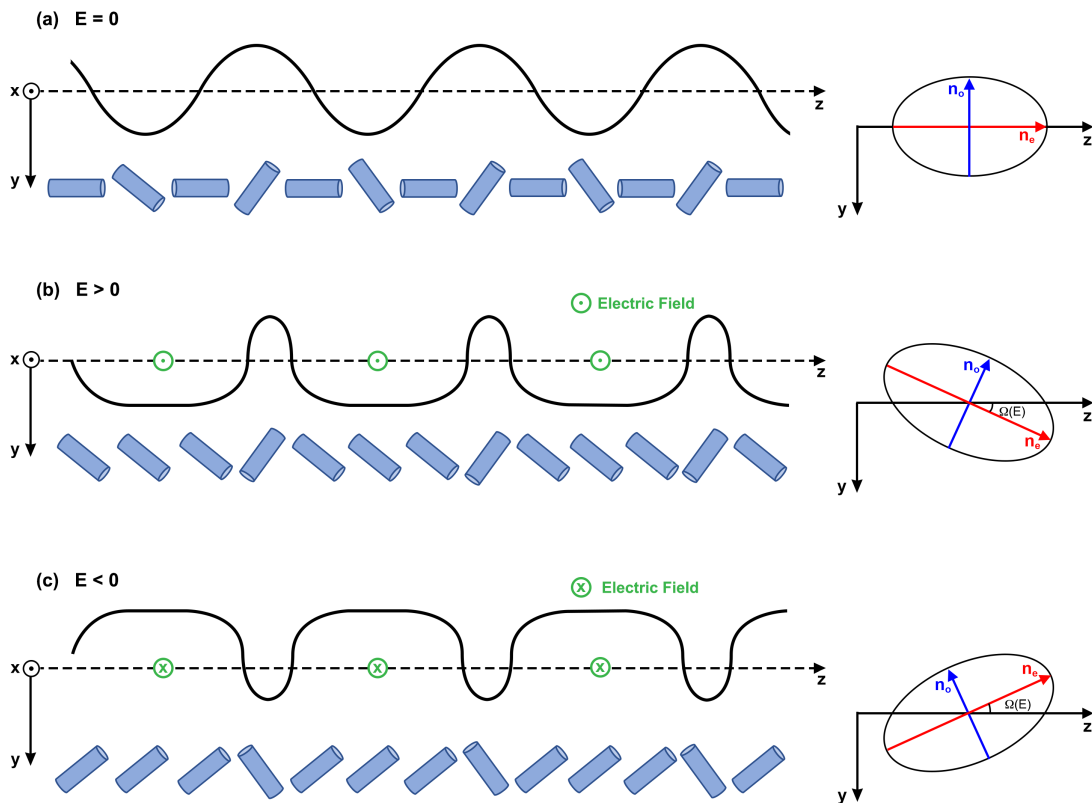


Fig. 3.1 Schematic of the deformed helix structures of liquid crystals in the presence of electric fields (a) $E = 0$, (b) $E > 0$ and (c) $E < 0$ and the averaged refractive index ellipsoids of smectic- C^* liquid crystals over the light aperture on the cell, where $\Omega(E)$ is the rotation of optical axes controlled by the direction and strength of applied electric field.

In Fig. 3.1, when no electric field is applied on the liquid crystal cell, the optical axis of liquid crystals is along the rubbing direction on the alignment layer (z-axis), and the refractive index ellipsoid shows the extraordinary refractive index n_e is larger than the ordinary refractive index n_o . When the electric field is applied with the direction from the bottom substrate to the top substrate ($E > 0$), the helix structure is deformed and the refractive index ellipsoid shows optical axes rotates clockwise by $\Omega(E)$. At the same time, the birefringence $\Delta n = n_e - n_o$ becomes larger. If the direction of the electric field is inverted ($E < 0$), the helix structure will be deformed as well, but optical axes will rotate counterclockwise by $\Omega(E)$. To conclude, the birefringence $\Delta n = n_e - n_o$ increases with the increasing strength of the applied electric field, while the orientation of optical axes $\Omega(E)$ relative to the rubbing direction on the alignment layer (z-axis) is controlled by both the direction and strength of the applied electric field. It is worth noting that, the long axes of molecules of liquid crystal directors twist from layer to layer and the molecular size is only 1 nm, so the refractive index ellipsoid is obtained by averaging the molecular arrangement of all molecules over the light aperture on the liquid crystal cell.

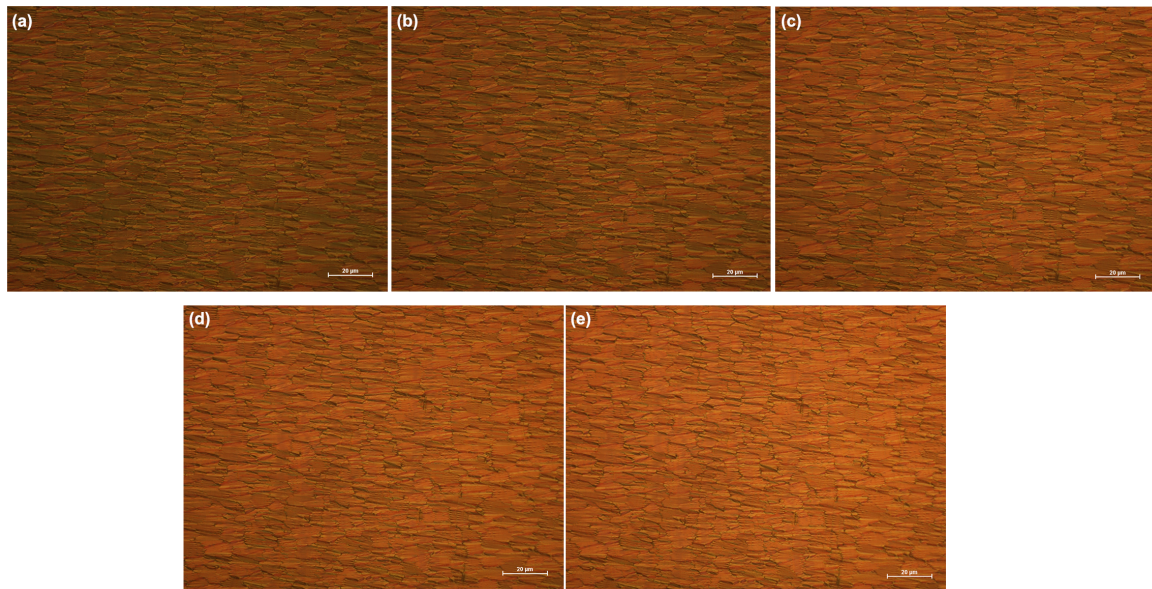


Fig. 3.2 Microscopy photos of the liquid crystal cell with a thickness of 5 μm under the polarizer when (a) -2 V, (b) -1 V, (c) 0 V, (d) +1 V and (e) +2 V were applied on the liquid crystal cell.

To characterise liquid crystal cells with a gold mirror, the optical microscope with a polarizer/analyser was used to observe their optical responses to applied electrical signals. As explained in the previous chapter, applied electric fields on a liquid crystal cell can give rise to changes in the polarization state of light due to birefringence and optical axes rotation, so these changes can be transformed to the intensity modulation via a polarizer and an analyser. In experiments, when the applied voltage level increased from -2 V to +2 V in a step of 1 V, the microscopy photos taken by the polarized optical microscope became brighter. When a square waveform signal with a frequency of 2 Hz was applied, the blinking light reflected from the liquid crystal cell can be observed clearly by a polarized optical microscope. The microscopy photos of a 5 μm thick liquid crystal cell taken at different DC voltage levels are shown in Fig. 3.2.

3.2 Birefringence, rotation of optical axes and tilt angle

The magnitude and wavelength dependence of the birefringence of liquid crystals (LCs) is of fundamental interest and is a crucial parameter which affects the operation of liquid crystal based electro-optic devices. A convenient and direct approach of birefringence measurement has been introduced for the first time by Shin-Tson Wu in 1984 [207]. They reported an improved technique which is useful for measuring the birefringence of liquid crystal materials at any wavelength in the UV, visible, or infrared spectral regions. In their work, the LC cell is placed between a polarizer and analyser as shown in Fig. 3.3, the transmitted intensities I_{\perp} and I_{\parallel} , corresponding to perpendicular and parallel orientations of the analyser, respectively.

$$I_{\perp} = I_0 \exp(-\alpha_0 d) \sin^2\left(\frac{\delta}{2}\right), \quad (3.1)$$

$$I_{\parallel} = I_0 \exp(-\alpha_0 d) \cos^2\left(\frac{\delta}{2}\right), \quad (3.2)$$

where I_0 refers to the intensity of incident light, α_o represents the absorption coefficient of the ordinary component of light, d is the thickness of the birefringent film and δ is the

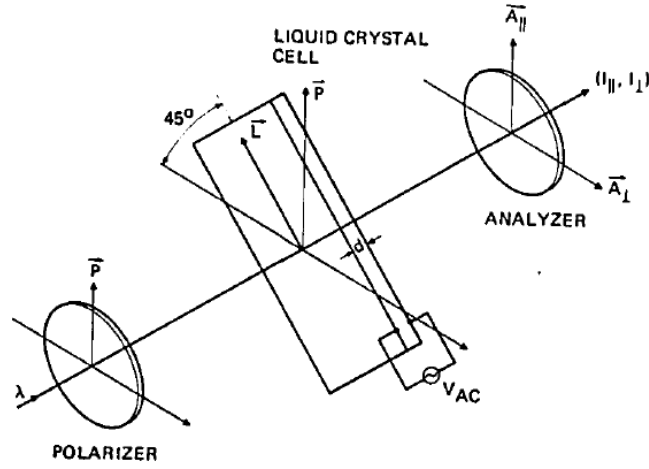


Fig. 3.3 Schematic of the optical configuration for birefringence measurements of liquid crystals reported by Shin-Tson Wu in 1984 [207].

phase difference between extraordinary and ordinary rays in the outgoing light, which can be expressed by

$$\delta = \frac{2\pi d \Delta n}{\lambda} \sin^2 \theta, \quad (3.3)$$

Δn is the birefringence of liquid crystals, λ is the wavelength, and θ is the angle between the optical axis of liquid crystals and the light propagation direction. In their experiments, the light propagation direction is perpendicular to the optical axis of liquid crystals, so θ is 90° and $\sin^2 \theta$ is 1. Therefore, the phase retardation δ can be simplified to be $\frac{2\pi d \Delta n}{\lambda}$. The birefringence can be solved by measuring the ratio $\frac{I_\perp}{I_\parallel}$.

$$|\delta| = N\pi + 2 \tan^{-1} \sqrt{\frac{I_\perp}{I_\parallel}}, \text{ for } N = 0, 2, 4, \dots \quad (3.4)$$

$$|\delta| = (N+1)\pi - 2 \tan^{-1} \sqrt{\frac{I_\perp}{I_\parallel}}, \text{ for } N = 1, 3, 5, \dots, \quad (3.5)$$

However, this approach is accurate for nematic liquid crystal cells because the angle θ between the optical axis of liquid crystals and the light propagation direction is independent on the applied electric field. In our case, the angle between the optical axis of liquid crystals

and the light propagation direction, θ , varies with the electric field caused by the applied signal, so the angle is expressed by $\theta(E)$. Additionally, it is convenient for us to only use R_{\parallel} , because no additional optical analyser or PBS is required for setup. As a result, this method is not convenient for measuring the birefringence of smectic-C* liquid crystal cells.

In addition to this, the spectrometer detection of electrically controlled birefringence of a polarized light beam transmitted by a DHF microlayer was reported by Alfredo Strigazzi in 2016 [208] as an alternative approach to birefringence measurement on the liquid crystal cell. In their method, if the angle between the optical axis of the polarizer and the optical axis of the cell is 45° , then the birefringence can be calculated from the normalized transmission. However, this approach requires the adjustment of the analyser for each square wave signal with a different peak voltage. It is clear that this method is more time-consuming and can not be used to study the effects of the sinusoidal wave on the birefringence and the rotation of optical axes in liquid crystals.

To overcome the limitations of existing approaches on the birefringence measurement of liquid crystal cells under varying electric fields, this section will introduce a new approach based on the half-wave plate rotation, instead of the optical analyser rotation. To maintain the position of light on the liquid crystal cell to improve the reliability of measurements, a half-wave plate is inserted between a linear polarizer and a liquid crystal cell. The experimental setup is shown in Fig. 3.4.

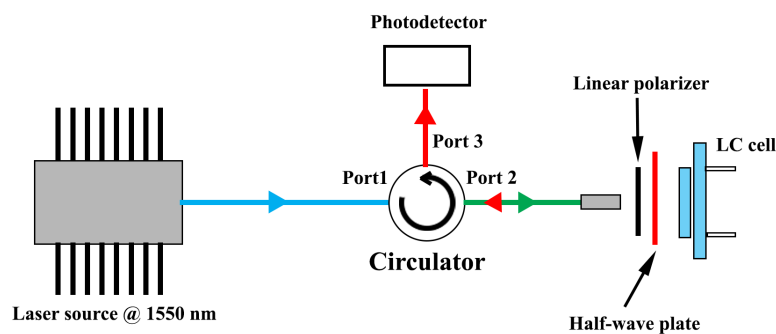


Fig. 3.4 Schematic diagram of experimental setup, in which a half-wave plate is placed behind the polarizer to change the polarization state.

Based on the experimental setup presented in Fig. 3.4, the light source at 1550 nm wavelength is connected to port 1 of an optical circulator, then the light is transmitted to port 2 and the collimated light is emitted from the GRIN lens. The aim of adding a half-wave plate is to change the polarization state of light after the linear polarizer. Due to the phase retardation caused by electric field-controlled birefringence and the optical axes rotation of LC, the polarization state of the reflected light is different from that of incident light. The reflected light is transmitted from port 2 to port 3 of the optical circulator, then the transmitted intensities are measured by the photodetector. Based on the assumptions that the incident light is normal to the liquid crystal surface and the multiple reflections can be neglected in experiments, the expression of the outgoing light intensity can be obtained by Jones matrix, Mueller matrix, or transfer matrix method as discussed in Chapter 2. Based on the setup shown in Fig. 3.4, the outgoing light intensity can be considered as the parallel reflectance with the presence of a half-wave plate, it can be expressed as

$$R_{\parallel} = 1 - R_{\perp} = 1 - \sin^2 \left(\frac{2\pi d \Delta n(E)}{\lambda} \right) \sin^2 \left[2\beta - 2 \left(\Omega(E) - 2\theta_{\text{wph}} \right) \right]. \quad (3.6)$$

Here, d is the cell gap (i.e., the thickness of the LC layer), λ is the incident light wavelength, Δn is the LC birefringence for normal incidence, β is the angle between the linear polarizer and the optical axis of liquid crystals without the external electric field, $\Omega(E)$ is the rotation of optical axes in the liquid crystal cell, which varies under applied electric fields, and θ is the angle between the optical axis of the liquid crystal cell and the fast axis of the half-wave plate. When the half-wave plate is inserted between the linear polarizer and the liquid crystal cell, the rotation of the half-wave plate is equivalent to the rotation of the liquid crystal cell. It is because the half-wave plate can change the polarization direction of the incident light, which means the angle between the incident polarization and the optical axis can be controlled by rotating either the liquid crystal cell or the half-wave plate.

To separate the birefringence $\Delta n(E)$ from $\Omega(E)$, the half-wave plate can be rotated by a specific angle. If $2\beta + 4\theta = N\pi$, the normalized reflection in this case can be simplified as

$$R_1 = 1 - \sin^2 \left[\frac{2\pi d \Delta n(E)}{\lambda} \right] \sin^2[2\Omega(E)], \quad (3.7)$$

If the half-wave plate is rotated by 22.5° , $2\beta + 4\theta = N\pi \pm \frac{\pi}{2}$. Then, the normalized reflection can be expressed as

$$R_2 = 1 - \sin^2 \left[\frac{2\pi d \Delta n(E)}{\lambda} \right] \cos^2[2\Omega(E)], \quad (3.8)$$

Therefore, the birefringence $\Delta n(E)$ can be obtained by the sum of R_1 and R_2 , while the rotation of optical axes can be obtained by the ratio of $\frac{1-R_1}{1-R_2}$ as

$$\Delta n(E) = \frac{\lambda \left(N\pi \pm \sin^{-1} \sqrt{\frac{2-(R_1+R_2)}{2}} \right)}{2\pi d}, \quad (3.9)$$

$$\Delta\Omega(E) = \frac{\tan^{-1} \sqrt{\frac{1-R_1}{1-R_2}}}{2}, \quad (3.10)$$

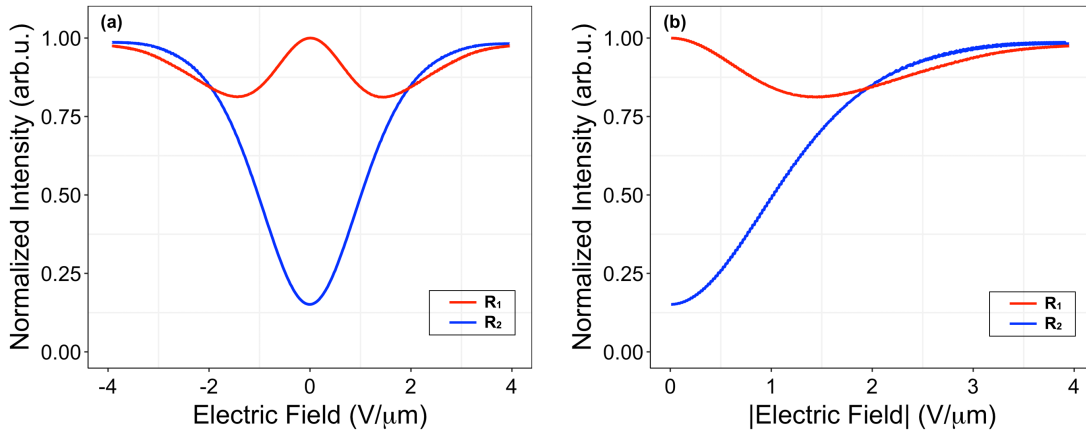


Fig. 3.5 The normalized intensities of outgoing light, R_1 and R_2 , which are measured when $2\beta + 4\theta = N\pi$ and $2\beta + 4\theta = N\pi \pm \frac{\pi}{2}$, as a function of the strength of electric fields.

In this work, the thickness of the liquid crystal cell used in this work is around $5 \mu\text{m}$. All-optical components are fixed on a fibre-to-fibre U-bench. In experiments, a sine-wave waveform signal with a peak-to-peak voltage of $\pm 19.8 \text{ V}$ and a frequency of 100 Hz is applied on the liquid crystal cell. The reflection intensities R_1 and R_2 are measured individually

by rotating the half-wave plate by $\pm 22.5^\circ$. The normalized intensities of outgoing light measured by the photodetector at two particular rotation angles of the half-wave plate, R_1 and R_2 , are presented in Fig. 3.5.

As shown in Fig. 3.5, it is clear that the intensity of reflected light R_1 decreases with the strength of applied electric field, while the intensity of reflected light R_2 increases with the strength of applied electric field. And R_1 and R_2 are completely out of phase. Based on the normalized intensities of outgoing light, R_1 and R_2 , measured when $2\beta + 4\theta = N\pi$ and $2\beta + 4\theta = N\pi \pm \frac{\pi}{2}$, the birefringence controlled by the applied electric field, $\Delta n(E)$, and the controllable rotation of optical axes, $\Delta\Omega(E)$, can be calculated by Eq. (3.9) and Eq. (3.10) individually. The calculated results of the electric field controlled birefringence $\Delta n(E)$ as a function of the strength of electric field and the square of electric field are presented in Fig. 3.6.

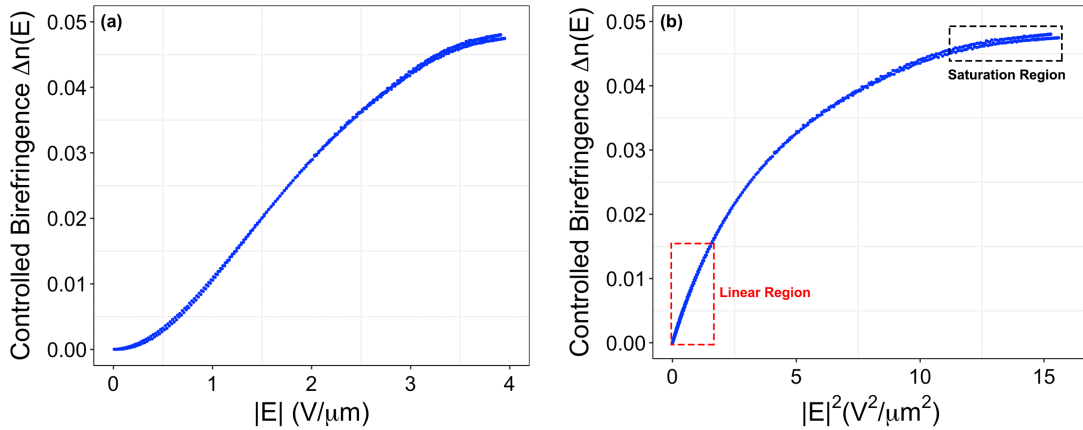


Fig. 3.6 The electric field controlled birefringence $\Delta n(E)$ as a function of (a) the strength of electric field $|E|$ and (b) the square of the strength of electric field $|E|^2$.

From Fig. 3.6, we can see that, for the applied electric field smaller than 1.3 V/ μm , the electric field controlled birefringence $\Delta n(E)$ is linearly proportional to the square of the applied electric field $|E|^2$, which indicates the quadratic behavior of birefringence to the electric field. However, when the strength of the applied electric field increases further, the electric field controlled birefringence $\Delta n(E)$ will not increase as fast as before and it reaches the saturation point around 0.048 when the applied electric field increases up to 3.8 V/ μm .

As shown in Eq. (3.10), the electric field-controlled orientation of optical axes in a liquid crystal cell can be calculated from two reflected light beams R_1 and R_2 as well. The results of optical axes orientation as a function of the applied electric field is shown in Fig. 3.7.

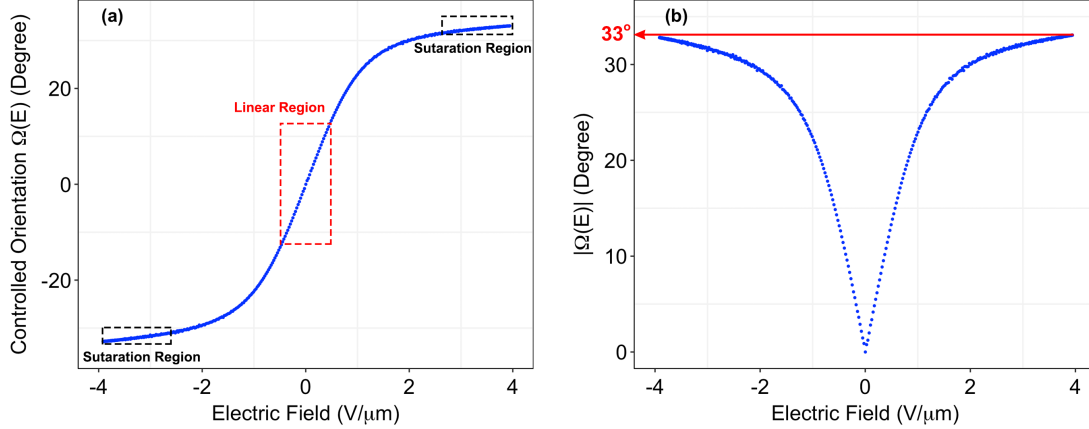


Fig. 3.7 The electric field controlled orientation $\Omega(E)$ of optical axes in liquid crystals as a function of electric field.

In this case, we can assume $\Omega(E) = 0$, when no electric field is applied on the liquid crystal cell, $E = 0$. It is clear that the direction of the applied electric field controls the sign of the optical axes' orientation. When the electric field is smaller than $1.3 \text{ V}/\mu\text{m}$, the orientation of optical axes has a good linear relationship with the electric field. However, when the strength of the electric field goes up, the orientation of optical axes increases slowly and eventually gets saturated at 33° for the positive electric field and -33° for the negative electric field. As discussed earlier, the orientation of optical axes in liquid crystals varies between $-\theta_t$ and $+\theta_t$, when the electric field is applied to the cell. Therefore, the measurement results illustrate that the tilt angle θ_t is around 33° for the liquid crystal cell used in this work. As shown in Fig. 3.6 and Fig. 3.7, both the birefringence $\Delta n(E)$ and the rotation of optical axes $\Omega(E)$ increase with the increasing electric field strength until the strength of electric field $|E|$ is greater than $1.3 \text{ V}/\mu\text{m}$. Therefore, the threshold value around $1.3 \text{ V}/\mu\text{m}$, at which the birefringence and the rotation of the optical axes start to be saturated, can be defined as the critical electric field E_{crit} unwinding the helical structure of a liquid crystal cell with the thickness of $5 \mu\text{m}$.

3.3 Modulation depth

The modulation depth is one of major performance parameters of optical modulators which illustrates their ability of responding to the applied electric field by changing optical properties of the incident light, such as phase and intensity of the outgoing light. In this work, the combination of a liquid crystal cell and a linear polarizer or a PBS can be regarded as an optical loss modulator which can actively control the intensity of the outgoing light. In this work, the modulation depth is represented by the difference between the maximal reflection and the minimal reflection of the liquid crystal cell under applied electrical signals as

$$\text{Modulation Depth} = R_{\max} - R_{\min}. \quad (3.11)$$

In this section, the modulation depths of liquid crystal modulators with different liquid crystal thicknesses are studied individually by applying a sine-waveform electrical signal with varying amplitudes and frequencies. To study the modulation depth as a function of the strength of applied electric fields, S-type liquid crystal cells with different thickness, namely 3.3 μm , 5.0 μm , 7.7 μm and 9.0 μm , were selected and their optical responses were measured individually. In experiments, the sine-waveform signals with different amplitudes were applied to generate varying electric field strength ranging from 0 to 1.45 V/ μm .

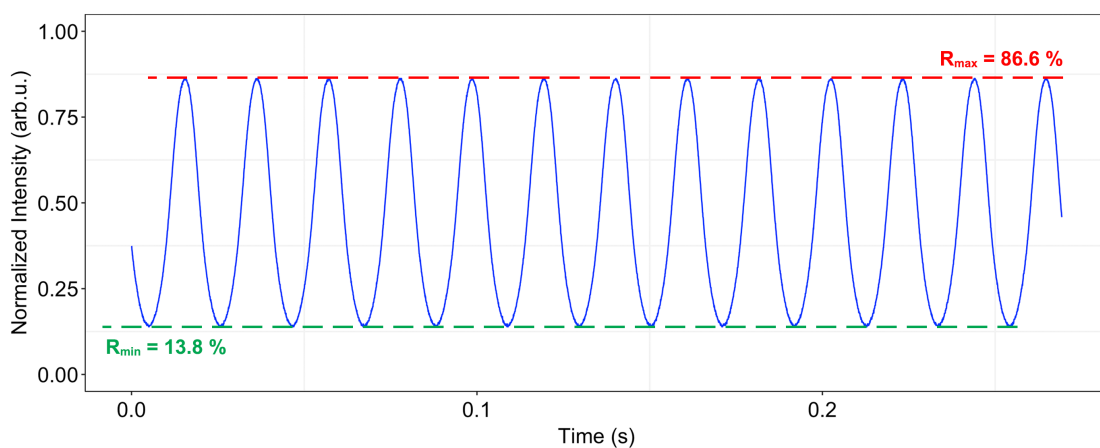


Fig. 3.8 The normalized intensity of optical responses from the S-type 9.0 μm liquid crystal cell under a 50 Hz sine wave electrical signal.

As shown in Fig. 3.8, when the sine waveform signal with an amplitude of ± 13 V was applied on the S-type 9.0 μm thick liquid crystal modulator, the maximal reflectance, and minimal reflectance were 86.6 % and 13.8 % respectively, which means the modulation depth is around 72.8 %. The measured modulation depths for different S-type liquid crystal cells are shown in Fig. 3.9 (a). The phase shifts between the applied signal and detected optical response was measured as well, which is shown in Fig. 3.9 (b).

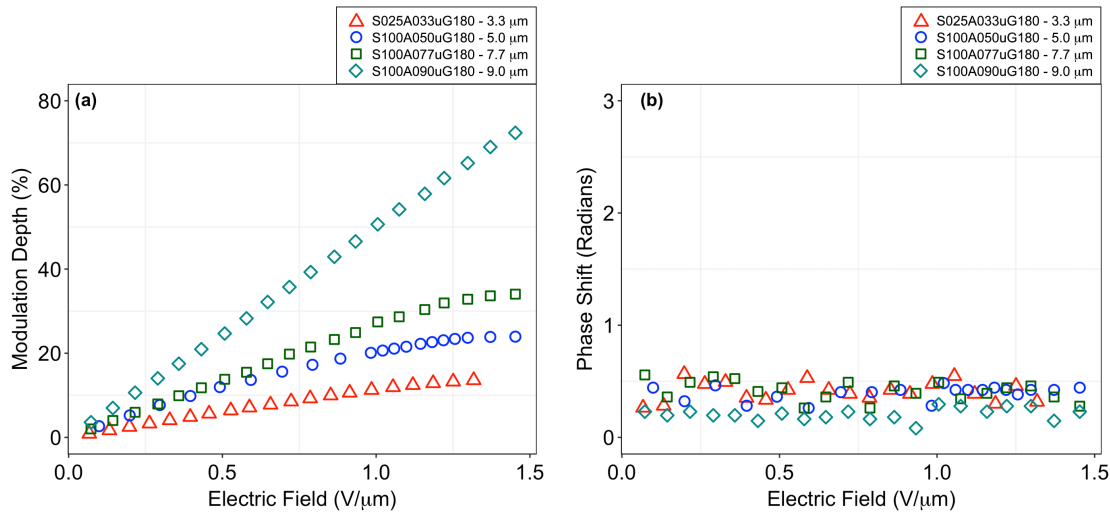


Fig. 3.9 The measured (a) modulation depths and (b) phase shifts as a function of the electric field applied on S-type liquid crystal cells with different thickness, 3.3 μm , 5.0 μm , 7.7 μm and 9.0 μm respectively.

It is clear that the modulation depth increases with the strength of applied electric fields for all liquid crystal cells. However, for the same electric field strength, the thicker liquid crystal cell has a larger modulation depth due to a significant reduction in the effects of boundary surfaces. It is worth noting that the modulation depth increases linearly with the strength of the applied electric field when the applied electric field is small, and then starts to saturate when the electric field is close to the critical electric field E_{crit} for unwinding. In general, because the effect of boundary surfaces becomes less significant when the liquid crystal layer becomes thicker. Thus, the critical electric field E_{crit} of liquid crystal cells increases with the increasing thickness of liquid crystal layers. Additionally, the measurements on the phase

shift illustrate that there is no obvious relation between the applied electric fields and the phase shifts caused by S-type liquid crystal cells.

Because the equivalent electronic circuit of a liquid crystal cell can be represented as a simple RC circuit with its impedance and capacitance, the bandwidth of a liquid crystal modulator is an important parameter affecting the modulation depth and switching speed. The normalized modulation depths as a function of the frequency of applied signals applied on four different liquid crystal cells are shown in Fig. 3.10.

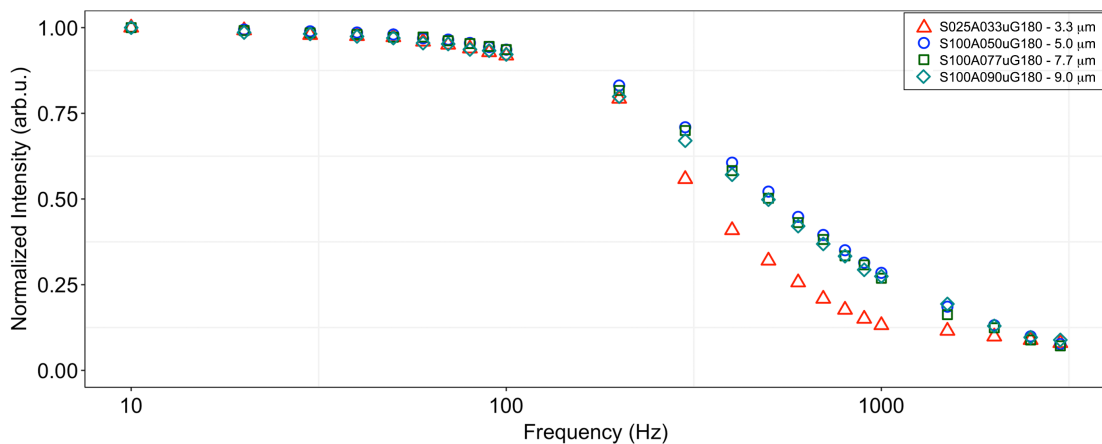


Fig. 3.10 The normalized modulation depths as a function of the frequency of signals applied on S-type liquid crystal cells with different thicknesses, including 3.3 μm , 5.0 μm , 7.7 μm and 9.0 μm .

Because the liquid crystal cell can be considered as an electronic component with limited bandwidth, the modulation depth decreases with the increasing signal frequency for all cells. Comparing with thicker liquid crystal cells, the cell with a thickness of 3.3 μm demonstrated the smallest bandwidth, because surface anchoring effects are more significant in thin liquid crystal cells.

For Q-switching, the cavity loss needs to be switched from the high level to the low level rapidly on a time scale shorter than 2 μs , a square waveform signals with a small duty cycle is always used to drive liquid crystal modulators in Q-switching experiments. More details will be discussed in the following sections. In experiments, when no electric field is applied or the signal is 0 V, the optical loss or the light intensity measured in Fig. 2.8 reaches the

maximum of around 100 %. When the electric field is applied or the signal is at a high voltage, the optical loss is minimized to obtain the largest modulation depth. For optimisation of the performance of our modulators, two different waveforms, bipolar and unipolar, were designed and tested on the S-type liquid crystal cell with a thickness of 7.7 μm . Both bipolar and unipolar square waveform signals have an amplitude of 29.7 V, pulse duration of 2 μs , and frequency of 1 kHz. These two waveforms (bipolar and unipolar) are presented in Fig. 3.11, and the normalized intensity of reflected light or optical loss are presented separately in Fig. 3.12.

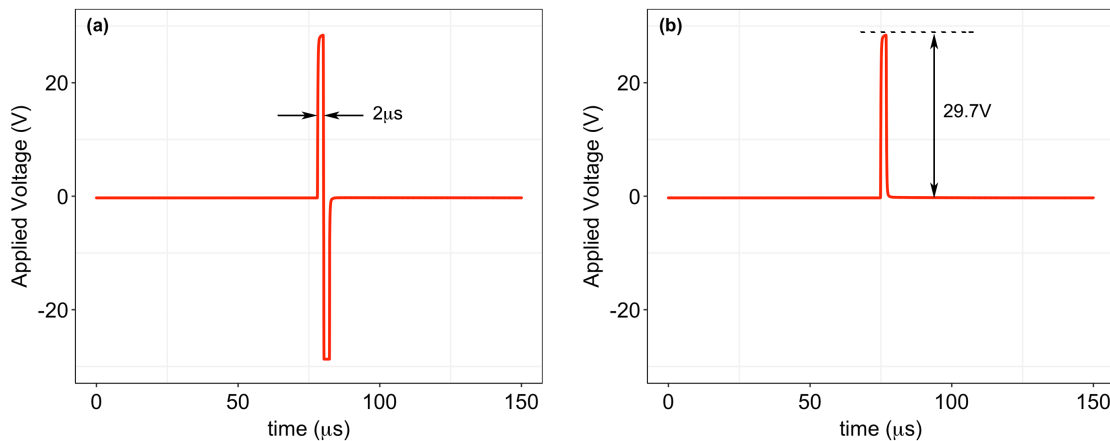


Fig. 3.11 (a) Bipolar and (b) unipolar waveforms with the amplitude of 29.7 V and pulse duration of 2 μs .

From the above figures, although the modulation depth is not impacted by the waveform of the applied signal at 1 kHz, the switch-off times are very different in these two cases. When the bipolar square waveform signals are applied, both the switch-on time and switch-off time are around 1.5 μs . However, if the applied signal is replaced with a unipolar square waveform signal, the switch-on time is maintained at 1.5 μs , but the switch-off time is increased to 8 μs due to the long relaxation time of liquid crystals. It is worth noting that the switch-off time can also be considered as the recovery time of optical response, during which the optical response increases from the minimum value to the initial stable value. Therefore, it is clear that applying a bipolar square waveform can significantly shorten the recovery time, which means the emission of the multiple Q-switched laser pulses can be avoided in the experiments

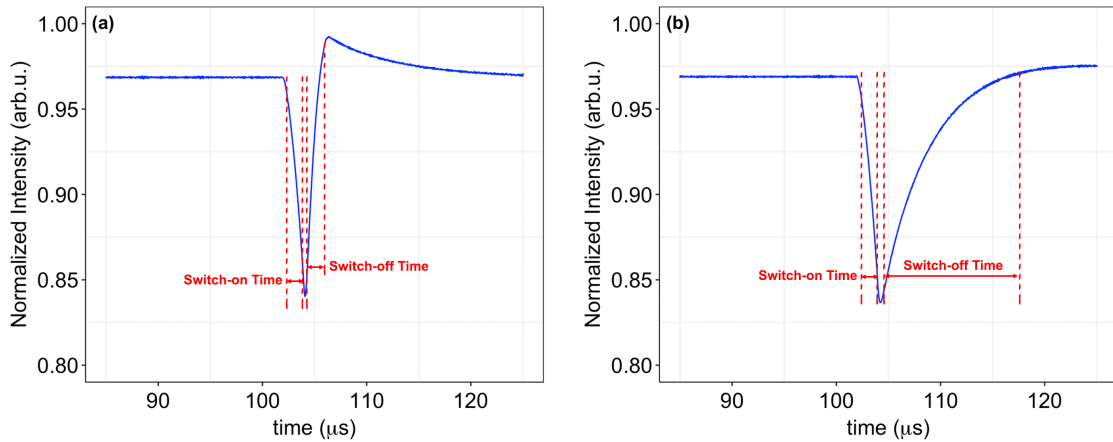


Fig. 3.12 The normalized intensities of reflected lights or optical losses under the applied (a) bipolar and (b) unipolar square-waveform signals with a amplitude of 29.7 V and a pulse duration of 2 μs .

later. Additionally, the shorter recovery time also reduces the negative impacts of the high repetition rate on the modulation depth. To demonstrate its effects, the normalized intensity or optical loss were recorded by applying bipolar and unipolar waveform signals with different frequencies varying from 0.2 kHz to 100 kHz. The measurement results are presented in Fig. 3.13. From the figure, we can see that two optical responses from bipolar and unipolar signals had the same modulation depth when the signal frequency was smaller than 5 kHz. When the signal frequency was increased to 30 kHz and 80 kHz, the modulation depth driven by unipolar signals decreased from 14 % to 5 % with the increasing frequency due to its long switch-off or recovery time. Conversely, the modulation depth driven by bipolar signals was not significantly affected by the increasing signal frequency even greater than 50 kHz, which is maintained around 14 %. The measured modulation depths as a function of the frequency of bipolar and unipolar square waveform signals are illustrated in Fig. 3.14.

From the figure, it is clear that the bipolar square waveform can result in a larger modulation depth and a better modulation performance from liquid crystal modulators, especially when the frequency is higher than 5 kHz.

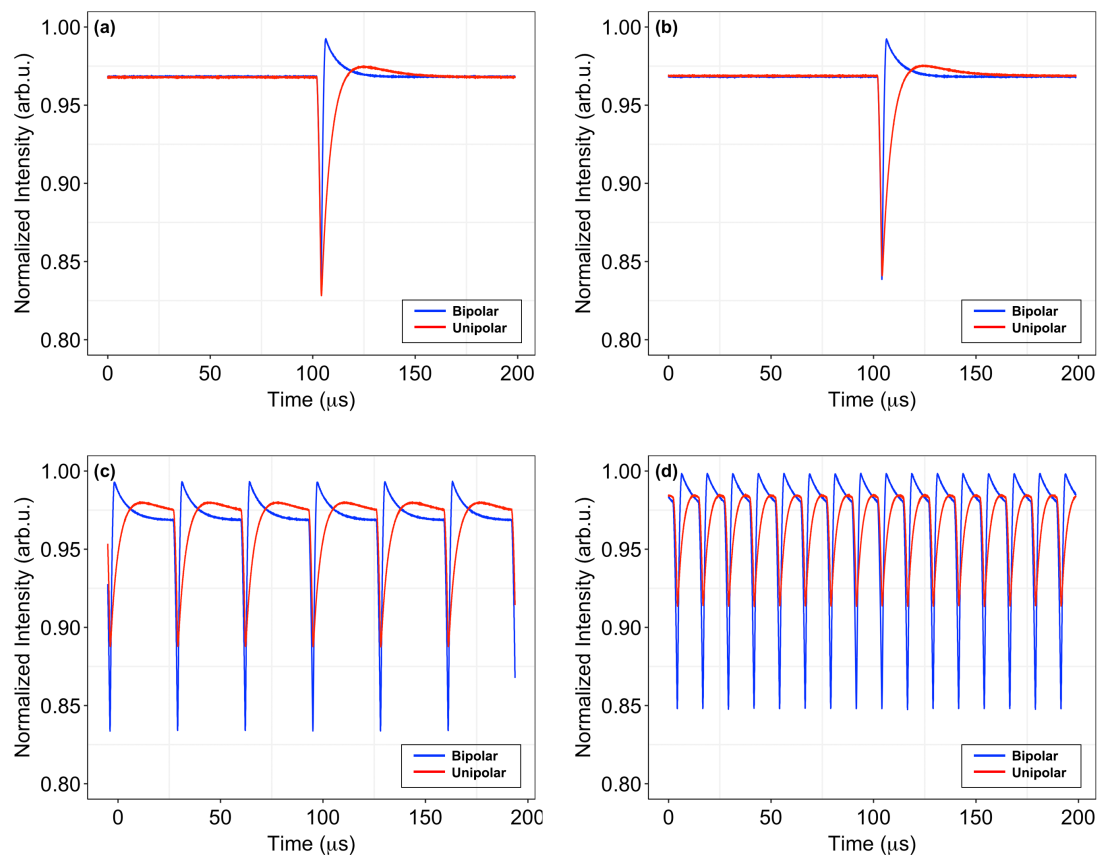


Fig. 3.13 The normalized intensity of reflected light or optical loss by applying bipolar (blue) and unipolar (red) square-waveform signals with different frequencies, including (a) 1 kHz, (b) 5 kHz, (c) 30 kHz and (d) 80 kHz.

3.4 Optical transmission

Except for the modulation depth, the optical transmission is another optical property of great importance for liquid crystal modulators when they are used as intra-cavity modulators in the Q-switched or mode-locked laser cavity. In this work, the optical transmission of liquid crystal cells was measured by using Lambda 1050 UV/Vis/NIR Spectrophotometer. The spectrophotometer used in this work supports the measurement over a wide range of wavelengths from 175 nm to 3300 nm with good sensitivity. In the experiments, each liquid crystal cell was added as a thin film sample into this equipment individually for transmission measurements. The measured optical transmissions for four different liquid crystal cells are presented in fig. 3.15.

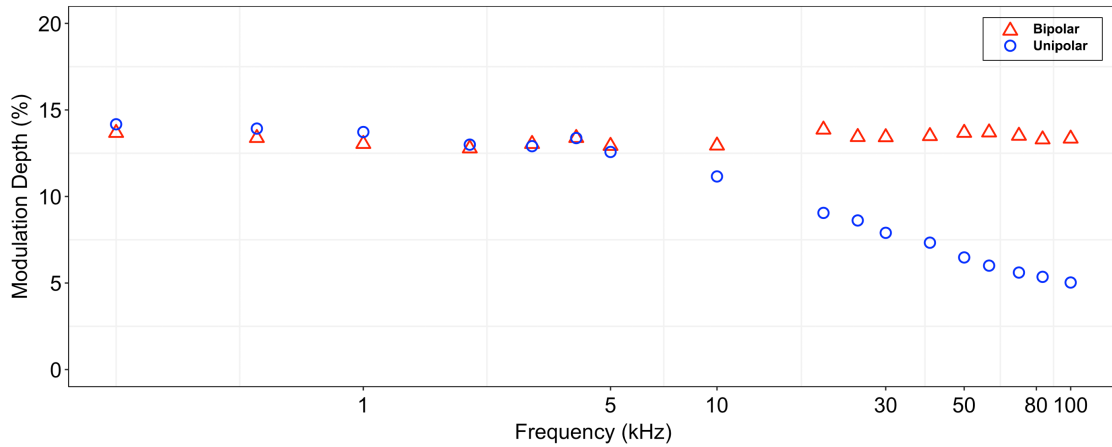


Fig. 3.14 The modulation depths driven by applying bipolar (red) and unipolar (blue) square-wave signals with different frequencies ranging from 0.2 kHz to 100 kHz.

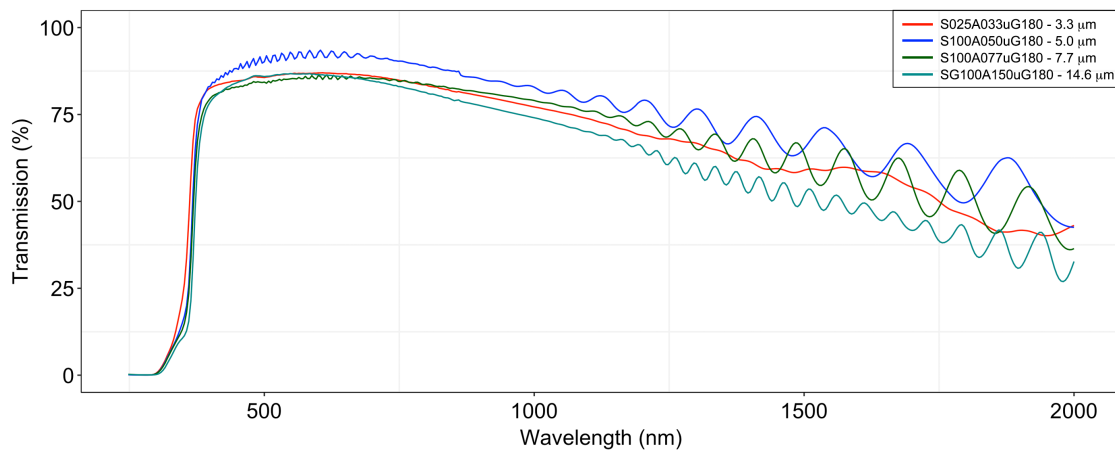


Fig. 3.15 Optical transmissions of different liquid crystal cells, 3.3 μm , 5.0 μm , 7.7 μm and 14.6 μm , over the wavelength ranging from 250 nm to 2000 nm.

The transmission measurement results illustrate that four liquid crystal cells have a high transmission rate from 87 % to 93 % over the visible wavelength ranging from 380 to about 750 nm. When the wavelength is increased to the infrared wavelength range, their transmission rates decrease down to 32 % at the longest wavelength of 2000 nm. The instability of transmission measurements was caused by the multiple reflection effects because the liquid crystal cells have multi-layer structures as shown in Fig. 2.7.

Chapter 4

Modelling of actively Q-switched waveguide lasers

4.1 Relevant publications

The numerical model and optimisation results have been published as a journal article entitled "Numerical modelling and optimisation of actively Q-switched waveguide lasers based on liquid crystal transducers" on OSA Optics Express in 2019.

1. **Xinyue Lei**, Christoph Wieschendorf, Josiah Firth, François Ladouceur, Alex Fuerbach, and Leonardo Silvestri, "Numerical modelling and optimisation of actively Q-switched waveguide lasers based on liquid crystal transducers," *Opt. Express*, vol. 27, pp. 8777–8791, 2019.

4.2 Liquid crystal cell design and characterisation

The deformed-helix ferroelectric (DHF) liquid crystal cell presented here is shown in Fig. 2.6 and Fig. 2.7 and has also been described in great detail in our previous papers [209]. The entire liquid crystal cell consists of one gold layer, two glass layers, two ITO layers, and two thin polyimide alignment layers. The middle layer is filled with the ferroelectric

liquid crystal mixture FLC-576A developed by P. N. Lebedev Physical Institute of Russian Academy of Sciences, in which the birefringence is controlled by the applied electric field [210]. To align the helical axis of the liquid crystal layer, the liquid crystals are sandwiched between two thin polyimide layers with anti-parallel rubbing, giving rise to a homogeneous alignment where the helical axis of the smectic-C* phase is parallel to the surface [211]. To generate an electric field in the liquid crystal layer, two ITO layers are deposited on top of the polyimide layers. Owing to its high optical transmittance in the visible and NIR combined with its low electrical resistivity, ITO is a suitable electrode material [212]. Additionally, a gold mirror is deposited on the back of the liquid crystal cell to provide broadband reflection. The directors of the molecules and the helical structure in the ferroelectric liquid crystal layer with Smectic-C* phase are shown in Fig. 2.4. This particular class of liquid crystals is made of rod-shaped chiral molecules and a dimensionless unit vector, called the director \vec{d} , can be introduced to represent the direction of the preferred orientation of these molecules in the neighborhood of any point. In the Smectic-C* phase, the molecules form smectic layers, in which all the directors are parallel and in which the molecules have a nematic-like order along with the director, \vec{d} . Successive layers show a precession of the director around a uniform twist axis perpendicular to the smectic layers (z-axis). This gives rise to a helical structure with a pitch p_0 and a tilt angle θ_t . We define φ as the azimuthal angle of rotation of the director in the smectic layer plane with respect to the x-axis, while \vec{P}_s is defined as the spontaneous polarization of molecules, which is perpendicular to the director \vec{d} in the xy plane. If an electric field is applied between the ITO layers, i.e., along the y-axis, it will cause a reorientation of the directors which can be described by the so-called "soft" and "Goldstone" modes. In the following sections, we will focus on the Goldstone mode which is the dominant relaxation mechanism for the liquid crystal cells described in my work. The dynamic behavior of the FLC director under an applied electric field along the y-axis can be described by the double sine-Gordon equation [209]:

$$\tau_c \frac{\partial \varphi(z,t)}{\partial t} = \left(\frac{p_0}{2\pi} \right)^2 \frac{\partial^2 \varphi(z,t)}{\partial z^2} - \frac{E(t)}{E_{\text{crit}}} \sin \varphi(z,t), \quad (4.1)$$

where the left-hand side represents the viscoelastic torque and the right-hand side refers to the elastic and ferroelectric torques respectively. In Eq. (4.1), p_0 is the helix pitch in the liquid crystal layer, τ_c is the elastic relaxation time, which depends on the material composition and the temperature but is independent of the applied electric field, and E_{crit} is the critical unwinding electric field at zero frequency.

According to the double sine-Gordon equation shown in Eq. (4.1), the external electric field could change the azimuthal rotation angle ϕ , which means that the helical structure of liquid crystals is deformed by an external electric field. At a macroscopic level, the deformation of the helical structure caused by an electric field is translated into a change of birefringence $\Delta n(E)$ and the optical axes rotation angle $\Omega(E)$ of the liquid crystal cell [213–215]. After propagation through a liquid crystal cell with an applied electric field E , two orthogonal polarizations of linearly polarized light experience a phase difference of $\phi(E) = \frac{2\pi}{\lambda} d\Delta n(E)$, which depends on the electric field intensity. Simultaneously, the optical axes of the liquid crystal cell are rotated by an electric field-dependent angle $\Omega(E)$. To translate these modulations into voltage-controlled optical transmissions, a crossed polarizer/analyser setup as shown in Fig. 2.8 is used, and a PBS cube separates the s- and p-polarization components. The reflectance of this configuration can be expressed as Eq. (2.9).

For practical considerations, it is difficult to adjust the angle β by rotating the liquid crystal cell without affecting the propagation path of the light beam within the liquid crystal cell. Instead, a half-wave plate is added into the setup to adjust the angle between the polarization of the incident light and the helical axis. In addition, to fine-tune the phase difference between the polarization of the incident and reflected waves, and thus to maximize the change in reflectance for a given step in applied voltage, a quarter-wave plate is inserted between the half-wave plate and liquid crystal cell. Using the analytical 4×4 transfer matrix algorithm introduced by Schubert in 1996 [196], the expression of the crossed reflectance then becomes

$$R'_{\perp} = \left(\sin \left(\frac{2\pi d \Delta n(E)}{\lambda} \right) \sin \left(2\theta_{\text{wpq}} \right) \cos \left[4\theta_{\text{wph}} - 2 \left(\theta_{\text{wpq}} + \beta - \Omega(E) \right) \right] \right. \\ \left. + \cos \left(\frac{2\pi d \Delta n(E)}{\lambda} \right) \sin \left[4\theta_{\text{wph}} - 2 \left(\theta_{\text{wpq}} + \beta - \Omega(E) \right) \right] \right)^2. \quad (4.2)$$

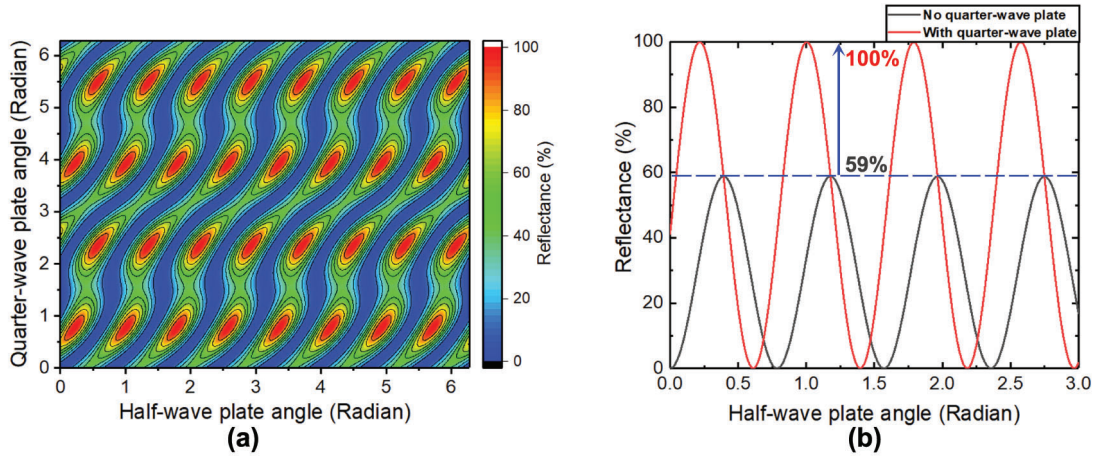


Fig. 4.1 (a) The crossed reflectance as a function of half-wave and quarter-wave plate angles and (b) crossed reflectance as a function of half-wave plate angle without (grey) / with a quarter-wave plate rotated by $\theta_{\text{wpq}} = 45^\circ$ (red) for the $9.0 \mu\text{m}$ thick liquid crystal cell.

Throughout this chapter, we define the angle between the helical axis of the liquid crystal cell and the fast axis of the quarter-wave plate (half-wave plate) as θ_{wpq} (θ_{wph}). From Eq. (4.2), the crossed reflectance as a function of half-wave plate and quarter-wave plate angles, θ_{wph} and θ_{wpq} , respectively, is shown in Fig. 4.1 (a). It can be seen that without the quarter-wave plate, the crossed reflectance R_{\perp} can oscillate only in the range from 0 to 59 %, whereas in the setup that contains a quarter-wave plate at an angle of $\theta_{\text{wpq}} = 45^\circ$, the crossed reflectance, R'_{\perp} , could have the full range from 0 to 100 %. In this chapter, the experimental and theoretical results presented in the following sections are all based on this optimal configuration. The crossed reflectance at optimal configuration can be expressed as

$$R_{\perp}^{\theta_{\text{wpq}}=45^\circ} = \frac{1}{2} + \frac{1}{2} \cos \left[\frac{4\pi d \Delta n(E)}{\lambda} + 8\theta_{\text{wph}} - 4 \left(\beta - \Omega(E) \right) \right]. \quad (4.3)$$

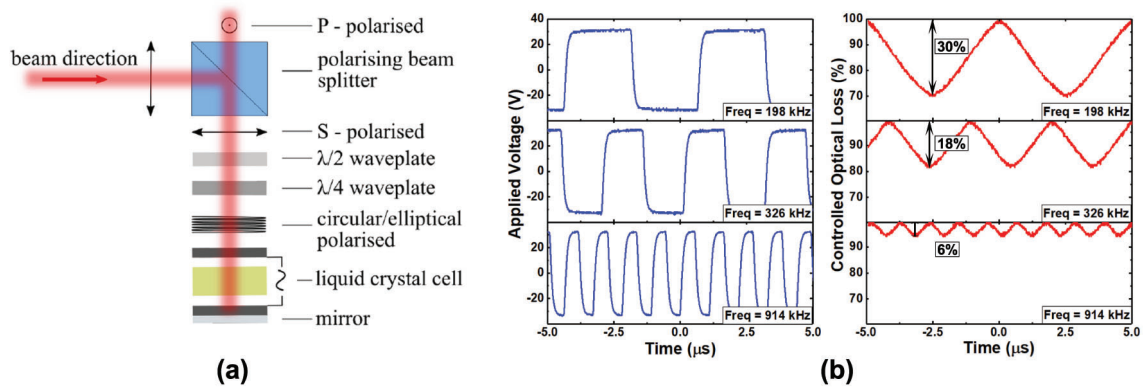


Fig. 4.2 (a) Schematic of the controlled optical loss measurement and (b) under the square wave signals with the constant amplitude of 60V, modulation depths are 30 % at 198 kHz, 18 % at 326 kHz and 6 % at 914 kHz.

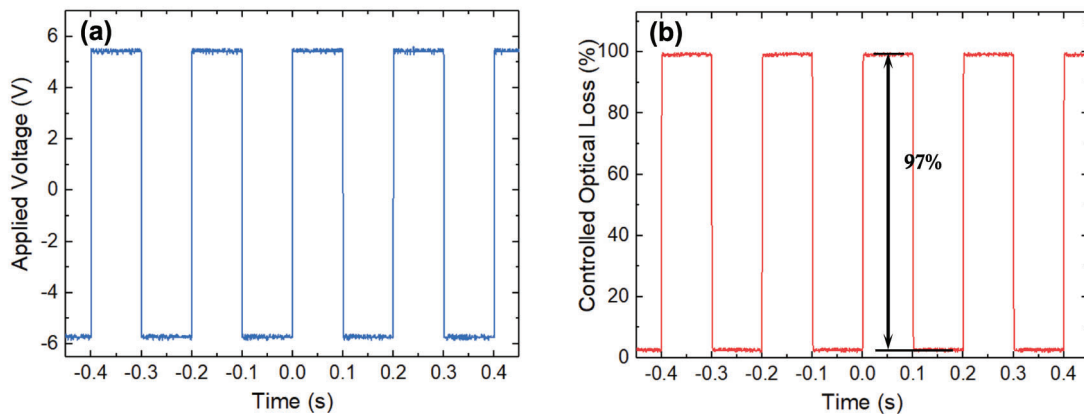


Fig. 4.3 (a) The square wave signals with the frequency of 5 Hz and the duty cycle of 50 % are applied on the liquid crystal cell and (b) corresponding optical loss controlled by the electrical signals, in which the modulation depth is around 97 % (close to 100 %).

As a first step, the properties of the liquid crystal transducer that are important for its intended use as an active intracavity Q-Switch modulator were characterised in a cross-polarized setup as shown in Fig. 4.2 (a). The modulation depth was investigated under a periodical electrical signal of constant amplitude and varying modulation frequencies and the results are shown in Fig. 4.2 (b). With a periodical electrical signal with a constant amplitude of 60V, the modulation depth was 30 % at 198 kHz and still 6 % at 914 kHz, showing that the liquid crystal cell has an ultrafast response and can be used under a very wide frequency range of up to 1 MHz. In addition to the fast response, the liquid crystal cell is capable

of providing a large modulation depth of 97 % at a low frequency (< 1 kHz), even if the amplitude of the externally applied voltage is as low as 12 V (see Fig. 4.3).

4.3 Numerical modelling for Q-switched waveguide lasers

In this section, we introduce an comprehensive numerical modelling to simulate the behaviour of waveguide lasers that are Q-switched utilising the liquid crystal transducers that have been described above. From the double sine-Gordon equation shown in Eq. (4.1), it is evident that the external electric field E can deform the helical structure of the liquid crystals by varying the azimuthal angle φ . The electric field-controlled deformation changes the birefringence $\Delta n(E)$ and the orientation of optical axes $\Omega(E)$ of the liquid crystal cell. To calculate the birefringence $\Delta n(E)$ and the orientation angle of optical axes $\Omega(E)$ under a time-varying electric field, our analytical model uses the effective dielectric tensor, which can be expressed as [196]

$$\boldsymbol{\epsilon}^{\text{eff}} = \begin{pmatrix} \epsilon_{xx}^{\text{eff}} & \epsilon_{xy}^{\text{eff}} & 0 \\ \epsilon_{xy}^{\text{eff}} & \epsilon_{yy}^{\text{eff}} & 0 \\ 0 & 0 & \epsilon_{zz}^{\text{eff}} \end{pmatrix}. \quad (4.4)$$

In the case of an electric field which is much smaller than the critical unwinding electric field ($E \ll E_{\text{crit}}$) and when the electric field change is on a much slower timescale than the relaxation time of liquid crystals, τ_c , the dynamic response of the azimuthal angle $\varphi(z, t)$ can be expressed as

$$\varphi(z, t) = q_0 z + \alpha_E \sin(q_0 z), \quad (4.5)$$

where $q_0 = 2\pi/p_0$ and α_E is defined as the ratio of the applied electric field to the critical unwinding electric field, $\alpha_E = E/E_{\text{crit}}$. Based on the assumption that $\alpha_E \ll 1$, the effective dielectric tensor elements are shown in Eq. (4.4) can be calculated by the approach introduced by our group in the previous paper [216]:

$$\begin{aligned}
\varepsilon_{xx}^{\text{eff}} &\approx \varepsilon_{\perp} + \delta\varepsilon \cos^2 \theta_t \\
\varepsilon_{xy}^{\text{eff}} &= -\alpha_E \frac{\delta\varepsilon}{2} \sin \theta_t \cos \theta_t \\
\varepsilon_{yy}^{\text{eff}} &\approx \frac{\varepsilon_{\perp}}{2} \left(1 + \frac{\varepsilon_{\parallel}}{\varepsilon_{xx}^{\text{eff}}} \right) + \alpha_E^2 \frac{\delta\varepsilon}{4} \sin^2 \theta_t \\
\varepsilon_{zz}^{\text{eff}} &\approx \frac{\varepsilon_{\perp}}{2} \left(1 + \frac{\varepsilon_{\parallel}}{\varepsilon_{xx}^{\text{eff}}} \right) + \alpha_E^2 \frac{\delta\varepsilon}{4} \frac{\varepsilon_{\perp}}{\varepsilon_{xx}^{\text{eff}}} \sin^2 \theta_t,
\end{aligned} \tag{4.6}$$

where $\delta\varepsilon = n_e^2 - n_o^2$, $\varepsilon_{\perp} = n_o^2$, $\varepsilon_{\parallel} = n_e^2$, and θ_t is the tilt angle of liquid crystals. In experiments, square-wave signals with a pulse duration of t_p and an amplitude of $V = E_0 d$ were applied to the liquid crystal cell. In this case, the time-dependent factor $\alpha_E(t)$ can be calculated as

$$\alpha_E(t) = E_{\text{eff}}(t)/E_{\text{crit}}, \tag{4.7}$$

where E_{eff} is defined as the effective electric field experienced by the liquid crystal cell, which can be expressed as

$$E_{\text{eff}}(t) = \begin{cases} \left[1 - \exp\left(-\frac{t}{\tau_c}\right) \right] E_0 & 0 \leq t \leq t_p \\ \left[\exp\left(-\frac{t-t_p}{\tau_c}\right) - \exp\left(-\frac{t}{\tau_c}\right) \right] E_0 & t > t_p. \end{cases} \tag{4.8}$$

In the above equation, the relaxation time constant τ_c of the liquid crystal cell indicates how fast the modulator can respond to varying electric signals. It is worth noting that even though, in our experiments, the applied electric field is larger than the critical unwinding electric field E_{crit} , the effective electric field E_{eff} is still below the critical unwinding electric field E_{crit} , due to its short pulse duration ($t_p = 2 \mu\text{s}$), which means the assumption of this model is valid. Based on the effective dielectric tensor shown in Eq. (4.4), the birefringence $\Delta n(t)$ and the rotation of optical axes $\Omega(t)$ can be approximated by

$$\Omega(t) = -\frac{\alpha_E(t) \delta \varepsilon \sin(2\theta_t)}{4 \frac{\varepsilon_{xx}^{\text{eff}} - \varepsilon_{yy,0}^{\text{eff}}}{\varepsilon_{xx}^{\text{eff}}}}, \quad (4.9)$$

$$\Delta n(t) = \sqrt{\varepsilon_{xx}^{\text{eff}}} - \sqrt{\varepsilon_{yy}^{\text{eff}}} + \alpha_E(t)^2 \frac{\sqrt{\varepsilon_{xx}^{\text{eff}}} \sqrt{\varepsilon_{yy,0}^{\text{eff}}} - \varepsilon_{\perp}}{\varepsilon_{xx}^{\text{eff}} \sqrt{\varepsilon_{yy,0}^{\text{eff}}} - \varepsilon_{yy}^{\text{eff}} \sqrt{\varepsilon_{xx}^{\text{eff}}}} \frac{\delta \varepsilon \sin^2(2\theta_t)}{8}. \quad (4.10)$$

where $\varepsilon_{xx}^{\text{eff}}$ and $\varepsilon_{yy}^{\text{eff}}$ are two elements of the effective dielectric tensor shown in Eq. (4.4). $\varepsilon_{yy,0}^{\text{eff}}$ is the value of $\varepsilon_{yy}^{\text{eff}}$ without an applied voltage and can be calculated by $\varepsilon_{yy,0}^{\text{eff}} = \frac{\varepsilon_{\perp}}{2} \left(1 + \frac{\varepsilon_{\parallel}}{\varepsilon_{xx}^{\text{eff}}}\right)$.

The full numerical model uses rate equations for the population inversion density n and the photon flux ϕ to simulate the generated Q-switched laser pulses within the cavity [217]. The overall laser system includes spontaneous emission, stimulated emission, and absorption. Radial and longitudinal variations within the gain medium are neglected. The rate equations of the population inversion density n and the photon flux ϕ within the cavity can be expressed as

$$\frac{\partial n}{\partial t} = -nc\phi\sigma_{\text{emi}} - \frac{n}{\tau_f} + W_p(n_{\text{tot}} - n), \quad (4.11)$$

$$\frac{\partial \phi}{\partial t} = c\phi\sigma_{\text{emi}}n - \frac{\phi}{\tau_d} + S, \quad (4.12)$$

$$\tau_d = \frac{2L}{c(R_{\perp} + \delta)}. \quad (4.13)$$

where σ_{emi} is the stimulated emission cross section, which depends on the gain medium used in experiments. c is the speed of light within the medium, τ_f is the fluorescence lifetime, W_p is the pump rate and n_{tot} is the total number of active laser ions within the system. S describes the spontaneous emission rate, τ_d is the decay time of photons and δ describes the combined cavity losses, which can be found in Table 4.1. R_{\perp} is the crossed reflectance at the

optimal configuration, which can be calculated by substituting Eq. (4.7) into Eq. (4.9) and Eq. (4.10), and then into Eq. (4.3).

4.4 Model Validation

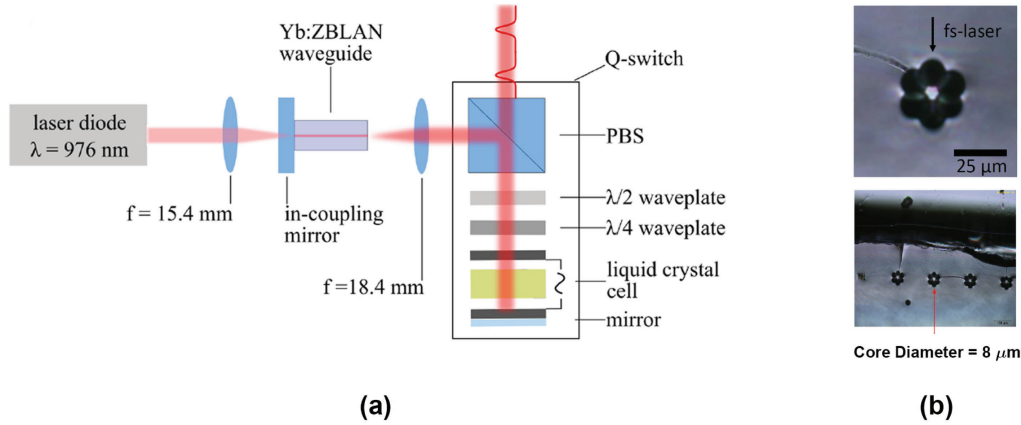


Fig. 4.4 (a) Schematic of the laser setup. In this setup, the pump light is coupled to a waveguide through a dichroic in-coupling mirror. Additionally, the PBS combined with waveplates and liquid crystal cell acts as a actively-controlled variable output-coupling mirror. (b) Cross-section of the depressed-cladding waveguides.

The setup for our experiments is shown in Fig. 4.4 (a). The active gain medium is a heavy-metal fluoride glass (ZBLAN - ZrF_4 , BaF_4 , LaF_4 , AlF_3 , NaF_3) doped with 2.5 mol% ytterbium (Yb). The length of the Yb:ZBLAN chip and the embedded waveguides is 10 mm. The fluorescence lifetime of Yb doped into ZBLAN is $\tau_f = 1.81$ ms and the emission cross-section is $\sigma_{emi} = 0.46 \times 10^{-20} \text{cm}^2$ [218]. The longer the fluorescence lifetime τ_f and the smaller the emission cross-section σ_{emi} , the longer the build-up time of laser pulses, which is more suitable for a slow Q-switch. The depressed cladding waveguide was inscribed using femtosecond lasers from Ti:sapphire extended-cavity oscillator [219]. The pulse energy on target was 80 nJ which resulted in a refractive index change of $\Delta n = -1.2 \times 10^{-3}$ to form a depressed cladding region. The inscribed waveguides have core diameters ranging from 6 μm to 14 μm . Further details can be found in [203]. For the following experiments, the 8 μm diameter waveguide as shown in Fig. 4.4 (b) was used, as it resulted in the highest output

power. The waveguide is pumped by a 976 nm fibre-coupled laser diode that can deliver a maximum pump power of 360 mW. The pump beam is focused into the waveguide through an input-coupling mirror via an aspheric focusing lens ($f = 15.4$ mm). The input-coupling mirror is a short pass dichroic mirror with a cutoff wavelength of 1000 nm and has a high transmission ($> 99.8\%$) at 976 nm and high reflectance ($> 99.99\%$) at a wavelength between 1010 nm and 1200 nm. Inside the laser cavity, the beam is collimated using another aspheric lens ($f = 18.4$ mm, anti-reflection coated 650 nm to 1050 nm). The diameter of the collimated beam is approximately 3 mm and exhibits negligible angular divergence. It is then directed onto a PBS followed by a zero-order half- and a zero-order quarter-wave plate, and finally the liquid crystal cell. As described earlier, the half- and the quarter-wave plate were introduced into the setup for two reasons:

(i) To maintain the light propagation path in the liquid crystal cell, the half-wave plate can be used to adjust the relative angle of the polarization with respect to the optical, instead of rotating the liquid crystal cell itself;

(ii) the quarter-wave plate can be used to optimise the modulation depth though changing the polarization state of the light incident on the liquid crystal cell as has been shown in Fig. 4.1.

To investigate the performance of liquid crystal cells with varying thicknesses, 3.3 μm and 9.0 μm thick liquid crystal cells are tested and compared. The total length of the laser cavity is 250 mm which is mainly limited by the size of off-the-shelf optical mounts used in the setup. Square wave electrical signals with a pulse duration of 2 μs and varying amplitudes are applied to both liquid crystal cells (3.3 μm and 9.0 μm thick) to control the crossed reflectance R_{\perp} . A small negative offset voltage is also added to keep the mean value of the electrical signals to be zero, as non-zero DC voltage could potentially damage the liquid crystal cell. The repetition rate of the electrical pulses f_{rep} is set to 5 kHz. The intensity of the generated Q-switched laser pulses is measured and recorded by a high-speed photo-detector. Additionally, the angle β between the polarization of the incident light and the LC helical axis without an applied electric field is $\beta = 45^{\circ}$. The cavity losses δ include waveguide propagation losses, Fresnel losses, and losses from the PBS and the liquid crystal cell. The

Table 4.1 Optical and Physical Parameters in Numerical Model

Component	Description	Symbol	Value
Yb-doped waveguide	Refractive index	n_d	1.5006
Yb-doped waveguide	Fluorescence lifetime	τ_f	1.810 ms
Yb-doped waveguide	Active laser ions (at 2.5 %)	n_{Yb}	$3.72 \times 10^{20} \text{cm}^{-3}$
Yb-doped waveguide	Emission cross section	σ_{emi}	$0.46 \times 10^{-20} \text{cm}^2$
Yb-doped waveguide	Diameter	D	8.0 μm
Yb-doped waveguide	Length	L_{active}	10 mm
Yb-doped waveguide	Propagation loss	L_p	13.1 %
Yb-doped waveguide	Fresnel loss	L_f	7.8 %
PBS	Reflectance loss	L_{PBS}	2.0 %
3.3 μm FLC	Transmission loss	L_{FLC}	62.0 %
3.3 μm FLC	Relaxation time	τ_c	38.9 μs
3.3 μm FLC	Critical electric field	E_{crit}	0.915 V/ μm
9.0 μm FLC	Transmission loss	L_{FLC}	65.0 %
9.0 μm FLC	Relaxation time	τ_c	13.6 μs
9.0 μm FLC	Critical electric field	E_{crit}	1.372 V/ μm
3.3 & 9.0 μm FLC	Helix pitch	p_o	0.2 μm
3.3 & 9.0 μm FLC	Tilt angle	θ_{tilt}	32°
3.3 & 9.0 μm FLC	Ordinary refractive index	n_o	1.50
3.3 & 9.0 μm FLC	Extraordinary refractive index	n_e	1.72
Cavity	Total length	L_{total}	250 mm
Cavity	Total background loss	L_{BG}	72.52 %

overall cavity losses in the setup are estimated to be 70.1 % for a 3.3 μm thick liquid crystal cell and 72.5 % for a 9.0 μm thick liquid crystal cell.

Optical and physical parameters of the experimental setup and microscopic parameters of LC mixture (FLC-576A) have been summarized in Table 4.1. For liquid crystal cells used in experiments, the ordinary (extraordinary) refractive index is $n_o = 1.5$ ($n_e = 1.72$), the tile angle is $\theta_t = 32^\circ$ and the helix pitch p_0 is 0.2 μm at the room temperature [220]. The thickness of two liquid crystal cells used in our experiments are 16 times and 45 times larger than the helix pitch, respectively, so the helical structure will not be affected by

the top and bottom substrates due to the boundary effects [210]. Based on the schematic shown in Fig. 4.2 (a), both 3.3 μm and 9.0 μm thick liquid crystal cells are tested under electrical signals with varying waveforms, frequencies, and amplitudes. It is worth noting that two important parameters of the model, namely the elastic relaxation time τ_c and critical unwinding electric fields E_{crit} , depend on the specific properties of the cell, particularly its thickness and the type of alignment layer. In our case, we measured unwinding electric fields E_{crit} and elastic relaxation times τ_c of two liquid crystal cells by applying sine wave voltage with varying amplitudes and rotating a half-wave plate. Experimental results show that the 9.0 μm thick liquid crystal cell has a smaller elastic relaxation time τ_c and a larger critical unwinding electric field E_{crit} than the 3.3 μm thick liquid crystal cell. It is because the thickness of the 3.3 μm liquid crystal cell approaches the critical thickness of the liquid crystal material. In this case, the effects of boundary surfaces on the helical structure of a ferroelectric smectic-C* liquid crystal (FLC) cannot be neglected. Indeed, solid surfaces bounding the FLC layer could induce the deformation and untwist of the helix, when the thickness of the cell approaches a critical thickness d_c [221]. The critical thickness d_c of the cell can be calculated as $d_c = (8W)/(\pi^2 k_\phi q_0^2)$, where W is the anchoring energy on LC-substrate surfaces, k_ϕ is the elastic constant and $q_0 = 2\pi/p_0$. For DHFLC cells in the Smectic-C* phase with the helix pitch of 0.2 - 1.0 μm , we can use typical values $W = 1 \times 10^{-2} \text{J/m}^2$ [222] and $k_\phi = 1 \times 10^{-11} \text{N}$ [223]. When the helix pitch of DHFLC cells p_0 is 0.2 μm at room temperature, the estimated value of critical thickness d_c is 0.8 μm . Because the thickness of the thinner liquid crystal cell (3.3 μm) is only 4 times larger than the critical thickness, its boundary surfaces can affect the helical structure and lead to a smaller unwinding electric field E_{crit} and a larger elastic relaxation time τ_c . Pozhidaev et al. [224] evaluated the electrically controlled birefringence via ellipticity measurements. In their experiments, the ferroelectric smectic-C* liquid crystal (FLC) material with the helix pitch p_0 of 0.33 μm was used, and two planar cells with different FLC layers thicknesses (16 and 44 μm) were assembled with the same configuration as we introduced. Their measurements proved that the thicker liquid crystal cell has a larger critical unwinding electric field E_{crit}

and a larger elastic constant k_ϕ , even though the thickness of the thinner FLC layer is 7 times larger than the critical thickness $d_c = 2.24 \mu\text{m}$.

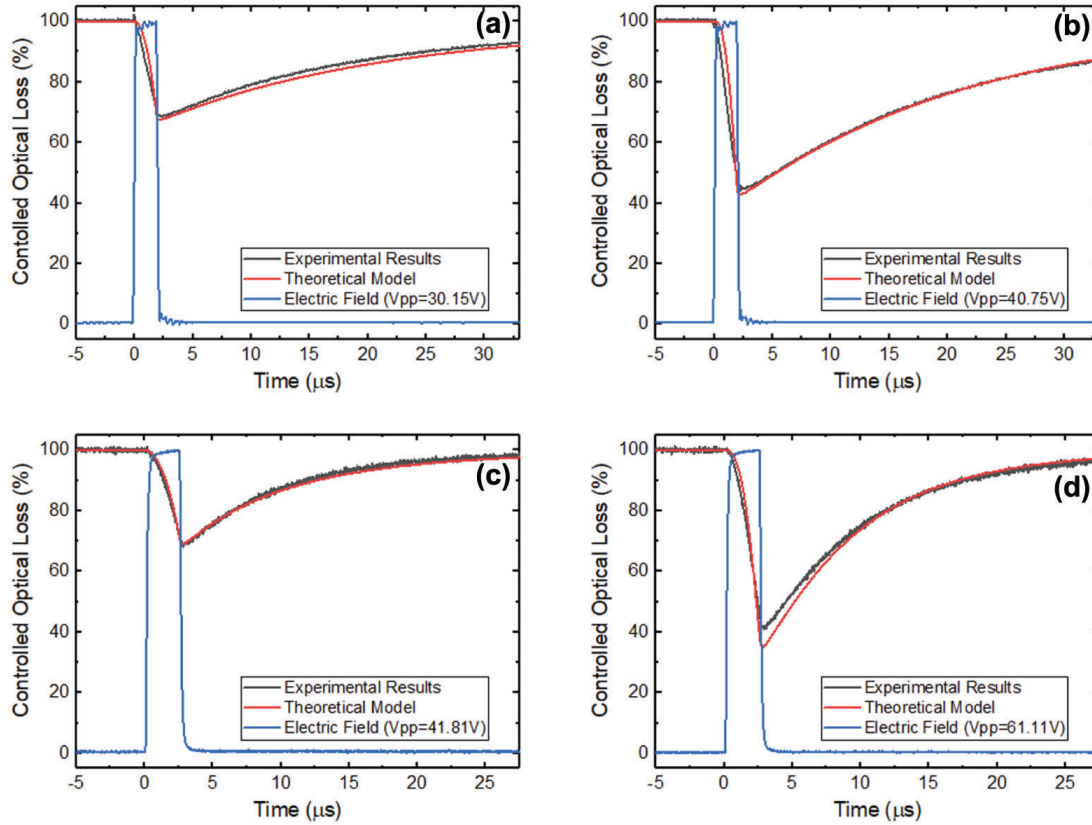


Fig. 4.5 The crossed reflectance of the (a) (b) $3.3 \mu\text{m}$ and the (c) (d) $9.0 \mu\text{m}$ thick liquid crystal cells as a function of time under varying electric signals. The grey line represents experimental measurement results, while the red line represents the corresponding numerical simulation results.

To investigate the validation of the proposed numerical model, we reported the experimental results and interpret them by using the model presented in the previous sections. Based on electro-optical parameters shown in Table 4.1, the experimental and numerical simulation results for the crossed reflectance for $3.3 \mu\text{m}$ and $9.0 \mu\text{m}$ thick liquid crystal cells subject to a single voltage pulse are shown in Fig. 4.5. It can be concluded that the numerical model can accurately reproduce the crossed reflectance R_\perp of liquid crystal cells under fast-changing applied voltages. It is evident that from both, experimental and simulation results for two liquid crystal cells, a stronger electric field can lead to a larger

modulation depth. Compared with the 3.3 μm thick liquid crystal cell, the 9.0 μm thick liquid crystal cell can give rise to a larger modulation depth under the same electric field intensity. To characterise the properties of generated Q-switched laser pulses, pulse width and peak power are the two most crucial performance parameters. Since it can be seen that the 9.0 μm thick liquid crystal cell can provide a larger modulation depth and can withstand applied voltages with larger amplitude, experimental and simulation results based on the 9.0 μm thick liquid crystal cell will mainly be analysed and discussed. In experiments, with the 9.0 μm thick liquid crystal cell, the square wave electric signal had a constant pulse duration of 2 μs with an amplitude range from 35 V to 90 V. The pulse width and peak power of the resulting laser pulses are shown in Fig. 4.6. When the applied voltage changes from 30 V to 90 V, the pulse width decreases from 70 ns down to 40 ns, and the peak power increases from 10 W to 50 W. However, when the amplitude of the applied voltage is larger than 70 V, both the pulse width and peak power start to saturate. The numerical simulation model also shows the same dependence of pulse width and peak power on the applied voltage, and all simulation results are in very good agreement with the experimental results.

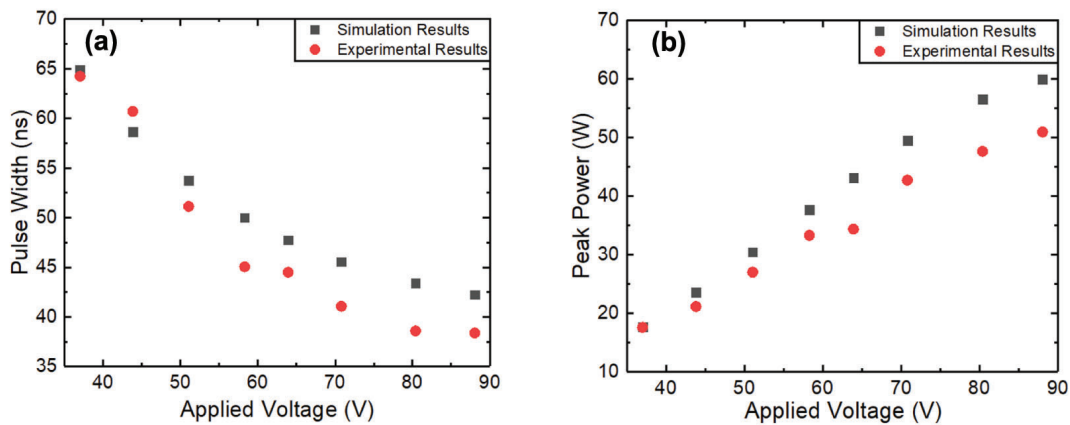


Fig. 4.6 (a) Experimental (red circles) and simulation results (grey squares) of pulse width and (b) peak power as a function of the applied voltage for the 9.0 μm thick cell.

In addition to the mentioned properties of Q-switched laser pulses, the conversion efficiency η is another important characteristic. It is defined as the fraction of pump power that can be converted into Q-switched laser pulses, and it can be calculated by $\eta = P_{\text{avg}}/P_{\text{pump}}$, in which P_{avg} is average output power and P_{pump} is absorbed pump power. The simulation

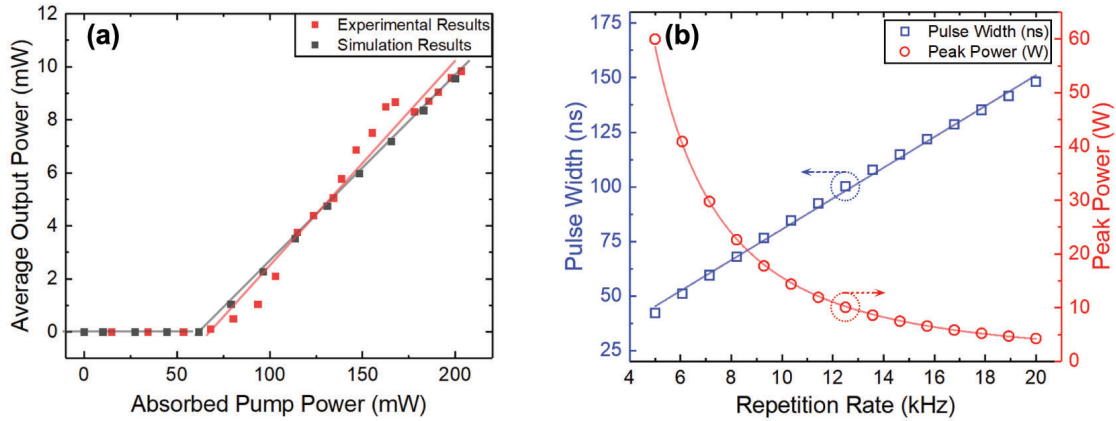


Fig. 4.7 (a) Experimental results (red squares) and simulation results (grey squares) of average output power as a function of absorbed pump power and (b) simulation results of pulse width and peak power as a function of repetition rate.

and experimental results of the average output power P_{avg} as a function of absorbed pump power P_{pump} are shown in Fig. 4.7 (a). It can be seen that the threshold absorbed pump power P_{th} is 70 mW. When the absorbed pump power is larger than P_{th} , the average output power P_{avg} starts to increase linearly with the absorbed pump power P_{pump} . The slope of this linear relationship dictates the conversion efficiency η and it is around 7.9 %. To investigate the impact of higher repetition rates on the output laser performance, the simulation results for peak power and pulse width as a function of repetition rate are shown in Fig. 4.7 (b). In this section, the theoretical model was characterised from different aspects, including the cross-polarized reflectance as well as pulse width, peak power, and average output power of the generated Q-switched lasers. The excellent agreement with the experimental results validates our theoretical model which means that this model can be used to optimise the performance and explore the limitations of our technology.

4.5 Optimisation of Q-switched waveguide lasers

To improve the performance of Q-switched waveguide lasers based on this approach, some specific physical parameters can be adjusted for optimisation purposes, including pump power, optical losses, and operation temperature. Although this specific type of liquid crystal

cell was developed as a transducer for sensing applications, it has not been optimised for its use in a laser setup. From measurements of optical losses summarized in Table 4.1, the total optical losses in the setup are around 72.52 %, which means that only 27.48 % of light remains after one round trip within the laser cavity. High optical losses and low available pump power are two critical limitations of the initial proof-of-principle setup. Increasing the absorbed pump power P_{pump} is straightforward by using commercial pump laser diodes with higher pump power levels. To reduce the optical losses, the bottom ITO layer could be removed from the liquid crystal cell as the bottom reflecting gold layer could also be used as an electrode. Additionally, the other ITO layer could be replaced by an Index-Matched Indium Tin Oxide (IMITO) layer [225], which has an average transmittance of 95 %. With this, it would be possible to reduce the optical losses from 72.52 % to at least 10.00 %. Based on the numerical model introduced in the last section, when the optical losses are reduced to 10.00 % and the pump power is increased from 200 mW to 400 mW, the predicted pulse width and peak power of the generated Q-switched laser pulses based on a 9 μm liquid crystal cell are shown in Table 4.2.

Table 4.2 Prediction of Q-switched Lasers with Low Optical Losses and/or High Pump Power

Voltage	Repetition rate	Pump power	Optical losses	Pulse width	Peak power
37 V	5 kHz	200 mW	72.52 %	58.30 ns	19.73 W
37 V	5 kHz	200 mW	10.00 %	52.25 ns	38.20 W
37 V	5 kHz	400 mW	72.52 %	23.06 ns	147.90 W
88 V	5 kHz	200 mW	72.52 %	37.94 ns	66.80 W
88 V	5 kHz	200 mW	10.00 %	39.37 ns	304.85 W
88 V	5 kHz	400 mW	72.52 %	20.00 ns	277.66 W
88 V	5 kHz	400 mW	10.00 %	20.25 ns	650.94 W
88 V	20 kHz	400 mW	10.00 %	70.40 ns	90.08 W

The impacts of lower optical losses and higher pump power on the pulse width and peak power of Q-switched lasers are further investigated separately. If the applied voltage is 37 V and the pump power is increased to 400 mW, the pulse width decreases dramatically from 58.30 ns to 23.06 ns, and the peak power increases from 19.73 W to 147.90 W, respectively.

In contrast, if the applied voltage is still 37 V, but the optical losses are reduced from 72.52 % to 10.00 %, the peak power increases from 19.73 W to 38.30 W, but the pulse width decreases to 52.25 ns slightly. Moreover, if the applied voltage is increased to 88 V and the pump power is maintained at 400 mW, the pulse width can be shortened to 20.00 ns, and the peak power can be improved to 277.66 W. Therefore, a higher pump power not only leads to higher peak power but also shortens the pulse width significantly. However, lowering the optical losses only improves the peak power but does not affect the pulse width. If optical losses and pump power are optimised at the same time, the pulse width can be 20.25 ns and the peak power can be up to 650.94 W. If the repetition rate is increased to 20 kHz, the pulse width of generated lasers is longer, and thus their peak power is lower. These optimised Q-switched laser pulses are shown in Fig. 4.8.

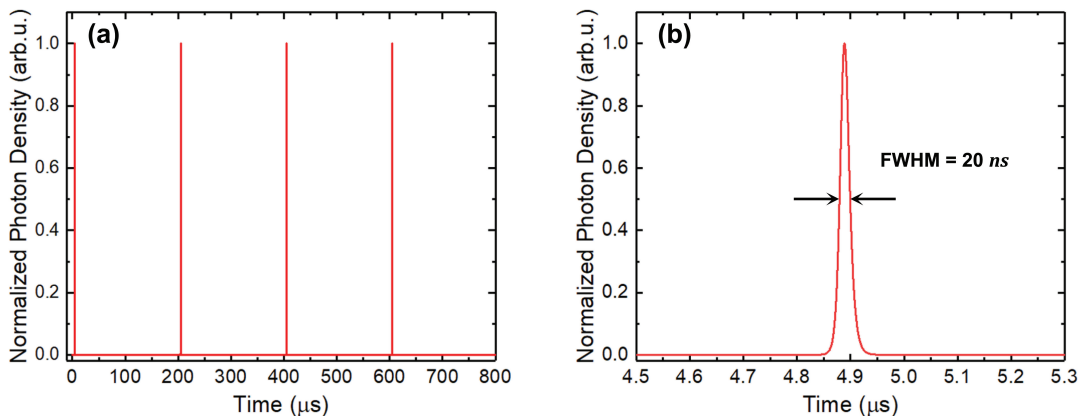


Fig. 4.8 (a) Q-switched laser pulses with a repetition rate of 5 kHz from the simulation model and (b) the shortest Q-switched laser pulses from the model with a pulse width of 20 ns and a peak power of 650.94 W. It could be achieved, when the amplitude of applied voltage is 88 V, the pump power is 400 mW and the optical losses is reduced to 10.00 %.

As has been shown by Pozhidaev et al., the azimuthal rotational viscosity of a ferroelectric liquid crystal is dependent on the operation temperature; and it is lower at higher temperatures resulting in faster responses and shorter relaxation times τ_c [214]. Thus, because the response time of the liquid crystal cell varies under different temperatures, even if the applied voltage is constant, the pulse width and peak power of the generated Q-switched laser pulses can be further optimised by adjusting the operation temperature. In experiments, we also measured the elastic relaxation time τ_c of the 9 μm liquid crystal cell under varying temperatures. The

experimental results show that the operation bandwidth of the liquid crystal cell varies with temperature and that the widest bandwidth can be achieved at a temperature of 55 °C, which means that the liquid crystal cell has its fastest response and the smallest elastic relaxation time τ_c at 55 °C. Therefore, when the temperature is adjusted to 55 °C, the elastic relaxation time τ_c of the 9 μm liquid crystal cell can be reduced from 15.2 μs to 7.6 μs , and the generated Q-switched laser pulses can be optimised further. The predicted pulse width and peak power of Q-switched laser pulses at a temperature of 55 °C are shown in Table 4.3.

Table 4.3 Prediction of Q-switched lasers at temperature of 55 °C

Temp	τ_c	Repetition rate	Voltage	Pump power	Losses	Pulse width	Peak power
25°C	16.3 μs	5 kHz	54 V	400 mW	10.00 %	20.00 ns	394.90 W
55°C	8.2 μs	5 kHz	54 V	400 mW	10.00 %	20.50 ns	711.83 W
55°C	8.2 μs	5 kHz	88 V	400 mW	10.00 %	23.75 ns	1055.90 W
55°C	8.2 μs	5 kHz	88 V	500 mW	10.00 %	17.00 ns	1154.10 W

At the optimal temperature of 55°C, a modulation depth of 100 % can be achieved at an applied voltage of 54 V. In this case, assuming a pump power of 400 mW and optical losses of 10.00 %, the pulse width of the generated Q-switched laser pulses is as short as 20.50 ns and the peak power is increased from 394.90 W to 711.83 W. Comparing the pulse width and peak power at 25°C and 55°C, it is worth noting that a temperature of 55°C does not lead to a shorter pulse width, but it results in a larger modulation depth and a higher peak power. If the pump power is further increased to 500 mW and temperature, applied voltage and optical losses are maintained at the values given above, the peak power of the generated laser pulses can reach 1.15 kW and the width of laser pulses can be shortened to 17.00 ns.

4.6 Summary

In this section, we have demonstrated a novel approach to generate actively Q-switched laser pulses based on an integrated waveguide chip and a liquid crystal cell in the DHF mode. In this approach, a liquid crystal cell can behave like an active Q-Switch modulator under

a wide range of repetition frequencies. Experimental results show that the pulse duration of generated Q-switched lasers is well below 40 ns, which is much shorter than the typical response time of liquid crystal. These surprising results have been reproduced and confirmed by numerical simulations that accurately reproduce pulse width, peak power and average output power for various operating conditions. Based on our numerical model, the impacts of lower optical losses and higher pump power on the optimisation of Q-switched lasers have been investigated and discussed. It was shown that lower optical losses can increase the peak power of laser pulses, but do not lead to shorter pulse widths. In contrast, higher pump power levels can increase the peak power and shorten the pulse width of the generated laser pulses simultaneously. From the prediction of optimisation based on our numerical simulation model, the shortest pulse width can be as low as 17.00 ns and the highest peak power can be as high as 1.15 kW, when the temperature is optimised and other parameters are optimised simultaneously. To achieve these performance values, the optical losses can be reduced by removing the bottom ITO layer from the liquid crystal cell, and the top ITO layer can be replaced with a conductive coating with better transparency, such as Index-Matched ITO with an average transmittance of 95 %. Besides, the liquid crystal cell can directly be integrated onto the waveguide chip to avoid Fresnel losses. Moreover, the maximum absorbed pump power in experiments was limited to 200 mW in our previous experiments, and increasing the pump power is straightforward. Based on experimental results and our theoretical model, it is possible to generate actively Q-switched laser pulses with a pulse width of 17.00 ns and a peak power in excess of 1 kW from a fully monolithic laser setup whose total length is in the order of only 1 cm.

Chapter 5

Compact actively Q-switched waveguide lasers operating at 1 μm

5.1 Relevant publications

The experimental results of actively Q-switched laser for sensing applications have been published on Elsevier Measurement as a journal article entitled "Compact actively Q-switched laser for sensing applications" in 2020 [226]. The optimised experimental results have been presented in two conference papers on the Australian and New Zealand Conferences on Optics and Photonics (ANZCOP 2019) [227] and Asia Communications and Photonics Conference (ACP 2020) [228].

1. **Xinyue Lei**, Victor Karaganov, François Ladouceur, Leonardo Silvestri, Alex Fuerbach, "Compact design of Q-switched laser systems based on liquid crystal transducers," Proc. SPIE 11200, AOS Australian Conference on Optical Fibre Technology (ACOFT) and Australian Conference on Optics, Lasers, and Spectroscopy (ACOLS), 2019.
2. **Xinyue Lei**, Lu Hao, Josiah Firth, François Ladouceur, Leonardo Silvestri, and Alex Fuerbach, "High Efficiency and Low Voltage Actively Q-Switched Yb-doped Waveguide Lasers Using a Liquid Crystal Modulator," In Asia Communications and Photonics Conference/International Conference on Information Photonics and Optical

Communications 2020 (ACP/IPOC), page M4D.8. Optical Society of America, Post-deadline, 2020.

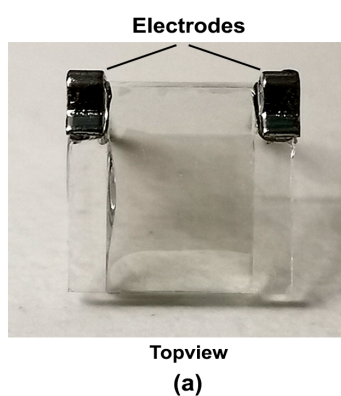
3. **Xinyue Lei**, Christoph Wieschendorf, Lu Hao, Josiah Firth, Leonardo Silvestri, Simon Gross, François Ladouceur, Michael Withford, David Spence, and Alex Fuerbach, "Compact actively Q-switched laser for sensing applications," *Measurement*, 173:108631, 2021.

5.2 Compact actively Q-switched laser for sensing applications

5.2.1 Theory and simulation

In the DHFLC cell as shown in Fig. 5.1, the liquid crystal mixture FLC-576A is sandwiched between two ITO electrodes, each with a deposited SD-1 alignment layer on it. The ITO layers are deposited on ordinary microscope glass slides (soda-lime-silica glass). For the reflection mode, a gold layer is deposited on one of the outer surfaces of glass plates to form a high reflective broadband mirror.

Type 1: Without Mirror



Type 2: With Mirror

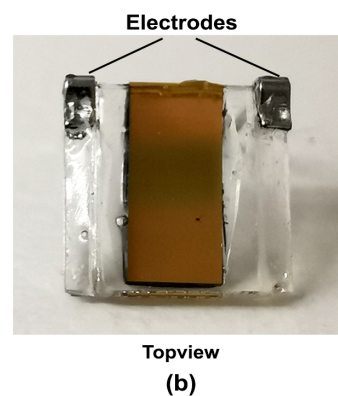


Fig. 5.1 Top views of the liquid crystal cell for (a) type 1 without a mirror and (b) type 2 with a mirror coated to the back.

Liquid crystals can be described as uniaxial materials and thus are characterised by an ordinary and an extraordinary refractive index, $n_o=1.5$ and $n_e=1.72$ for the liquid crystal mixture FLC-576A respectively [220]. Applying an electric field across liquid crystals results in a refractive index change Δn . An incident ray of light will see two different refractive indices depending on its initial polarization state with respect to the liquid crystal axis. The two orthogonal polarisation components will pass the material with different phase velocities. This results in phase retardation depending on the thickness of the liquid crystal layer and the applied electric field across the liquid crystal layer. In this section, the cross-polarized configuration was used by placing a PBS and a half-wave plate before a liquid crystal cell with a mirror coated to the back, as shown in Fig. 5.2 (a). In this setup, the transmitted light intensity after the PBS can be regarded as the optical loss controlled by the electric field, the liquid crystal thickness, and the optical axis of the half-wave plate, and it can be obtained from Eq. (3.6) and expressed as

$$R_{\perp} = \sin^2 \left(\frac{2\pi d \Delta n(E)}{\lambda} \right) \sin^2 \left[2\beta - 2 \left(\Omega(E) - 2\theta_{\text{wph}} \right) \right]. \quad (5.1)$$

The predicted transmitted intensity as a function of liquid crystal cell thickness from 0 to 10 μm at different wavelengths, 633 nm, 1030 nm, and 1880 nm separately, are shown in Fig. 5.2 (b).

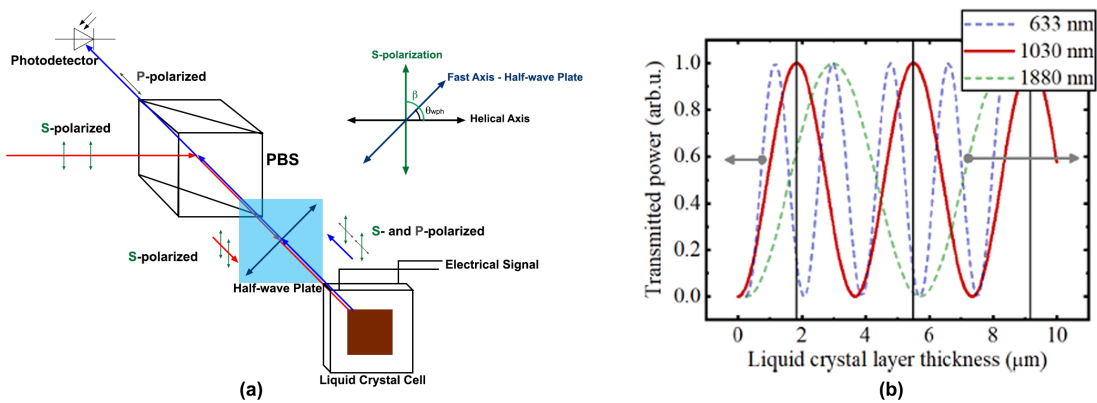


Fig. 5.2 (a) Schematic drawing of the cross-polarized setup used. (b) The simulated transmitted power through a cross-polarised setup as a function of liquid crystal cell thickness from 0 to 10 μm at 633 nm (blue line), 1030 nm (red line) and 1880 nm (green line) using Eq. (2.9), when $4\theta_{\text{wph}} - 2(\beta - \Omega(E=0)) = \frac{\pi}{2} + n\pi$.

To maximize the throughput transmitted power or the controlled optical loss when no electric field is applied, an additional quarter-wave plate at an angle of 45° was added between the half-wave plate and liquid crystal cell as shown in Fig. 5.3(a). The mathematical description can be retrieved by using the partial transfer matrix in the same manner as discussed earlier. The expression of the optimised crossed reflectance has been shown in Eq. (4.3).

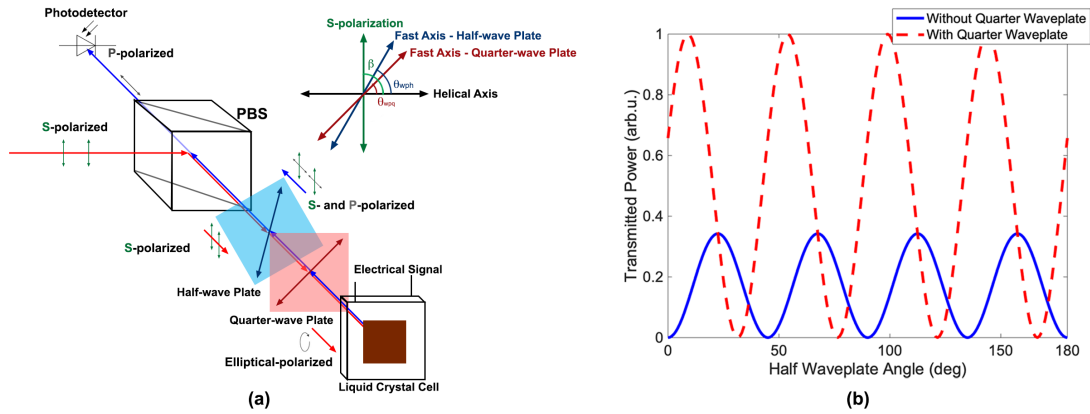


Fig. 5.3 (a) An additional half-wave and quarter-wave plate are added into the setup to prevent the beam from changing the position and maximize the through-put transmitted intensity with the absence of electric fields respectively. (b) At a wavelength of 1030 nm, a cell thickness of $3.3 \mu\text{m}$ results in a maximum transmission of 35 % (blue line). Adding a quarter waveplate at an angle of 45° to the setup increases the maximum transmission to 100 %.

To figure out the transmitted intensity R_{\perp} as a controlled optical loss after the PBS with an applied electric field for the simulation model based on Eq. (4.3), the values of the electric field-controlled birefringence $\Delta n(E)$ and the rotation of optical axes $\Omega(E)$ should be calculated. In this section, the effective dielectric tensor approach introduced by L. Silvestri et al in 2018 are utilised [216], and the effective birefringence $\Delta n(E)$ and the rotation of optical axes $\Omega(E)$ by using the effective dielectric tensor approach beyond space average approximation is given by

$$\Omega(E) = g_1 \alpha_E \quad (5.2)$$

$$\Delta n(E) = g_0 + g_2 \alpha_E^2 \quad (5.3)$$

$$\alpha_E = E_{\text{eff}}/E_{\text{crit}} \quad (5.4)$$

where g_1 is the linear coefficient of the rotation of optical axes, which contributes to the linear term in the optical response R_{\perp} , g_0 is the constant term representing the effective birefringence $\Delta n(E = 0)$ without the electric field, and g_2 refers to the quadratic coefficient of the birefringence $\Delta n(E)$ which contributes to the quadratic term in the optical response R_{\perp} . Additionally, E_{crit} is the critical electric field, at which the helix across the liquid crystal cell is fully unwind, and they are $0.915\text{V}/\mu\text{m}$ for a $3.3\ \mu\text{m}$ thick cell and $1.372\text{V}/\mu\text{m}$ for a $9.0\ \mu\text{m}$ thick cell [229]. E_{eff} is the effective electric field across the liquid crystal cell, while α_E is defined as the ratio between the effective electric field E_{eff} and the critical electric field E_{crit} . The expressions and values of crucial variables in the model are summarized in Table 5.1.

For the investigation on the dynamic behavior of Q-switched lasers, the well-known rate equations of a three-level gain medium with the population inversion density n and the photon flux ϕ were utilised in this section as shown in Eq. (4.11), Eq. (4.12) and Eq. (4.13) for the numerical simulation.

Based on the rate equations and the dynamic response of the liquid crystal cell shown in Eq. (4.3), the underlying dynamics of the pulse build-up when utilising a slow Q-switch are presented in Fig. 5.4. In general, the build-up process can be subdivided into three sections.

(i) The pulse will suppress the gain up to the point where the cavity losses are higher than the gain. As a result, the pulse sees no gain and will die out.

(ii) However, the cavity loss is still decreasing, at a certain time t_b , the gain overcomes the losses again and initiates a second laser pulse

(iii) This process will repeat until the final loss state is reached or the inversion is completely depleted. If the switching time is reduced to $2\ \mu\text{s}$ as shown in Fig. 5.4 (b), the second and following pulses can be avoided because the cavity loss will increase to a high

Table 5.1 Typical values of critical variables used in the simulation model

Symbol	Expression	Value	Ref
$\delta\varepsilon$	$\delta\varepsilon = n_c^2 - n_o^2 = 1.72^2 - 1.5^2$	0.71	[220]
ε_{\perp}	$\varepsilon_{\perp} = n_o^2$	2.25	[220]
ε_{\parallel}	$\varepsilon_{\parallel} = n_c^2$	2.96	[220]
θ_t		32°	[220]
$\varepsilon_{xx}^{\text{eff}}$	$\varepsilon_{xx}^{\text{eff}} \approx \varepsilon_{\perp} + \delta\varepsilon \cos^2 \theta_t$	2.76	[216]
$\varepsilon_{yy,0}^{\text{eff}}$	$\varepsilon_{yy,0}^{\text{eff}} = \frac{\varepsilon_{\perp}}{2} \left(1 + \frac{\varepsilon_{\parallel}}{\varepsilon_{xx}^{\text{eff}}} \right)$	2.33	[216]
g_0	$g_0 = \sqrt{\varepsilon_{xx}^{\text{eff}}} - \sqrt{\varepsilon_{yy,0}^{\text{eff}}} \approx \sqrt{\varepsilon_{xx}^{\text{eff}}} - \sqrt{\varepsilon_{yy,0}^{\text{eff}}}$	0.13	[216]
g_1	$-\frac{1}{4} \frac{\delta\varepsilon \sin(2\theta_t)}{\varepsilon_{xx}^{\text{eff}} - \varepsilon_{yy,0}^{\text{eff}}}$	-0.37	[216]
g_2	$g_2 = \frac{\sqrt{\varepsilon_{xx}^{\text{eff}}} \sqrt{\varepsilon_{yy,0}^{\text{eff}}} - \varepsilon_{\perp}}{\varepsilon_{xx}^{\text{eff}} \sqrt{\varepsilon_{yy,0}^{\text{eff}}} - \varepsilon_{yy,0}^{\text{eff}} \sqrt{\varepsilon_{xx}^{\text{eff}}}} \frac{\delta\varepsilon \sin^2(2\theta_t)}{8}$	0.06	[216]

level since the applied electric signal is removed. In this case, the modulation depth can be defined as the difference between the initial intracavity loss and final intracavity loss.

5.2.2 Material and methods

The experimental setup that we used to demonstrate the feasibility of the proposed device is shown in Fig. 5.5. A 300 mW, 976 nm laser diode was utilised to pump a waveguide within a Ytterbium-doped ZBLAN glass host. The waveguides were inscribed using a high-energy femtosecond oscillator (Femtosource XL 500, Spectra Physics) with a pulse duration of 45 fs at 800 nm and a repetition rate of 5 MHz [26]. The pump light was focused into the waveguide through the coupling mirror via an aspheric focusing lens ($f = 15.4$ mm). The input-coupling mirror was highly transmitting (> 99.8 %) at 976 nm and high reflective (> 99.99 %) in the wavelength range 1010 nm to 1200 nm. Inside the laser cavity, the beam was collimated using an aspheric collimating lens ($f = 18.4$ mm, anti-reflection coating 650 nm to

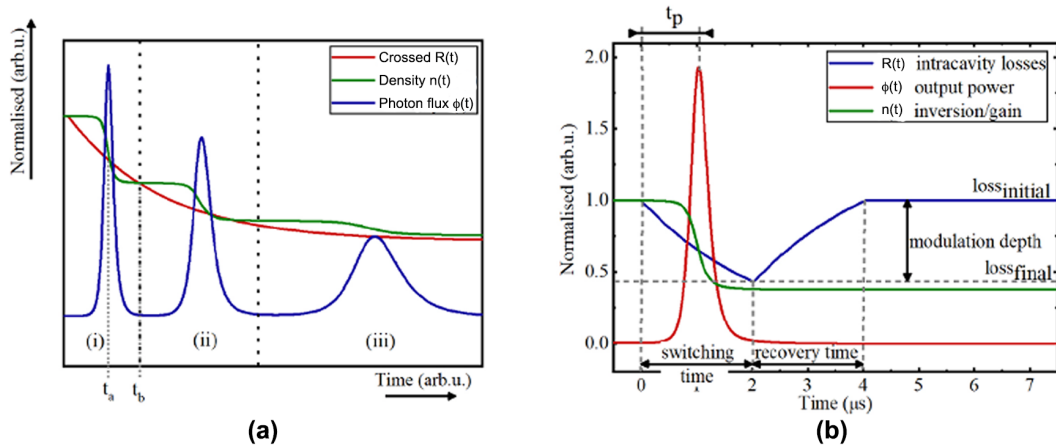


Fig. 5.4 (a) Laser dynamics of population inversion, photon density and cavity loss with a long switching time ($t > 5 \mu\text{s}$). Multiple laser pulses can be observed in this case. (b) The switching time is short ($t = 2 \mu\text{s}$), the cavity loss (red line) will increase, when the applied electric signal is removed. Therefore, the second and third pulse can be avoided.

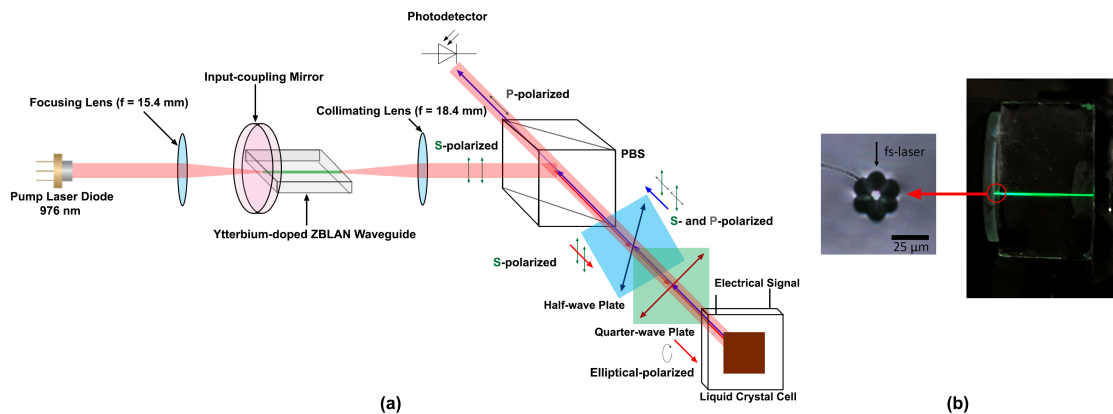


Fig. 5.5 (a) Q-switched laser setup. The resonator is formed by a dichroic in coupling mirror butt-coupled to the waveguide chip and a cavity including the liquid crystal cell. The PBS in combination with the liquid crystal cell acts as an actively controlled variable output-coupling mirror. (b) Cross-section of the depressed-cladding waveguides (left) and the top view of waveguide with the coupled pump light (right).

1050 nm). The collimated beam diameter measured approximately 3 mm. The out-coupling mirror consists of a PBS and a liquid crystal cell. Newport Optical Receiver (818-BB-30A 1000-1600 nm Biased InGaAs Detector, 1.5 GHz) is placed next to the PBS to record the laser pulses in real-time. The operation principles of the LC cell have been described in the previous section and other publications [209], when the incident light is polarized, the liquid crystal cell acts as a variable reflectance mirror, whose reflectance is controlled by an external voltage and can modulate the cavity losses of the resonator, see Eq. (4.3). The total length of the resonator in this setup is 250 mm. The cavity loss from each optic component of the overall setup is listed in Table 5.2.

Table 5.2 Cavity losses of Q-switched laser setup

Component	Description	Single-pass loss	Double-pass loss
Waveguide chip	Propagation losses	6.8 %	13.1 %
Waveguide chip	Fresnel losses	4.0 %	7.8 %
PBS	Reflection losses	1.0 %	2.0 %
LC cell (3.3 μm)	Transmission losses		62.0 %
LC cell (9.0 μm)	Transmission losses		65.0 %

In the experiments, the square wave electrical signal with a pulse duration of 2 μs is applied across 3.3 μm , 5.0 μm and 9.0 μm thick liquid crystal cells, while a small negative offset voltage is also added to keep the mean value of electrical signals to be zero, as non-zero DC voltage could potentially damage the liquid crystal cell. Note that the pulse repetition rate is determined by the frequency of the applied voltage waveform. The measured and simulated cavity losses as a function of time for 3.3 μm and 9.0 μm thick liquid crystal cells at a frequency of 5 kHz is shown in Fig. 5.6. It is worth noting that the measured and simulated cavity losses are in good agreement, especially when the amplitude of the applied voltage is relatively small. It is because the effective birefringence $\Delta n(E)$ and the rotation of optical axes $\Omega(E)$ are derived by using the effective dielectric tensor beyond the space average approximation, which are accurate when the effective electric field is small.

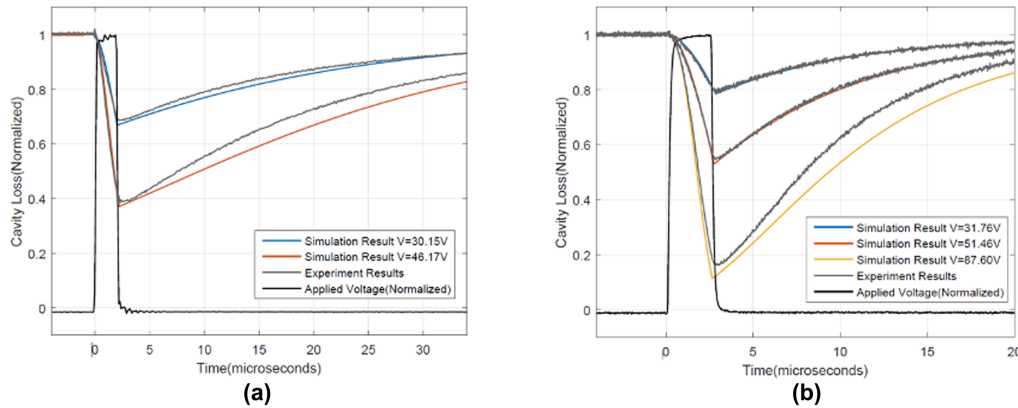


Fig. 5.6 The measured and simulated cavity losses as a function of time for (a) 3.3 μm and (b) 9.0 μm thick liquid crystal cell. The grey lines represent the measured cavity losses as a function of time for different applied voltages, while the black lines represent the applied electrical signal and other lines represent the simulated cavity losses.

When the same applied electric field with the same pulse duration of 2 μs is applied on three liquid crystal cells with different thicknesses based on the setup shown above, the modulation depth as a function of electric field strengths for 3.3 μm , 5.0 μm and 9.0 μm thick liquid crystal cells is measured and presented in Fig. 5.7 (a), which shows the thicker the liquid crystal layer the higher the modulation depth, which means a faster switching speed. Additionally, the modulation depth under a fixed voltage amplitude as a function of the applied voltage waveform frequency (repetition rate) for the 9.0 μm liquid crystal cell is shown in Fig. 5.7 (b). It is worth noting that when the repetition rate of the applied electrical signal exceeds the roll-off frequency, the modulation performance will degrade. For the 9.0 μm liquid crystal cell, the corresponding roll-off frequency is around 50 kHz.

5.2.3 Results and discussion

In another experiment, the step function is applied across a 3.3 μm liquid crystal layer with a frequency of 500 Hz and the maximum voltage amplitude of 4 V resulted in relaxation oscillation followed by a CW background, as depicted in the oscilloscope trace in Fig. 5.8. On the right of each graph, the applied voltage waveform is depicted. In Fig. 5.8 (a), the duty cycle was 50 % and the period was set to 2 ms. The maximum voltage amplitude was

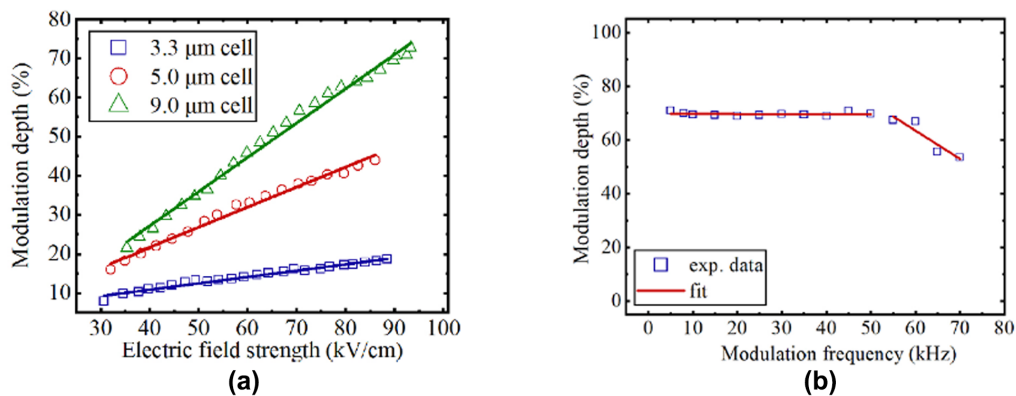


Fig. 5.7 (a) The modulation depths for three cells of different liquid crystal layer thicknesses are measured under 2 μs switching time. The thicker the liquid crystal layer the higher the modulation depth. (b) Modulation depth under a fixed voltage amplitude of 84 V as a function of the modulation (repetition) frequency for the 9.0 μm cell. The solid line (red) is a fit that emphasises the decline of modulation depth starting at frequencies above 50 kHz.

chosen to prevent the cell from being damaged. Reducing the duty cycle to 10 % diminishes the CW background, as shown by comparing Fig. 5.8 (a) and (b). The corresponding applied voltage waveform is shown in the bottom part of Fig. 5.8 (a) and (b) respectively. Further shortening the duty cycle to approximately 1 % resulted in a single pulse as shown in Fig. 5.8 (c). Besides enabling single pulse operation, such short duty cycles allowed for an increase in the maximum applied voltage amplitude without a damage on the liquid crystal cell. Additionally, increasing the applied voltage amplitude heightens the switching speed and thus maximises the peak power.

As discussed before in Fig. 5.7, the modulation depth of the liquid crystal cell increases when the thickness of the liquid crystal layer and/or the amplitude of the applied voltage is increased. Therefore, compared to thinner liquid crystal cells, e.g. 3.3 μm and 5.0 μm , 9.0 μm liquid crystal cell has better output laser performance than other liquid crystal cells, including higher average output power and shorter pulse width. To compare the output laser performance for 3.3 μm and 9.0 μm liquid crystal cells, the pulse duration and repetition rate of the applied electric pulses is fixed at 2 μs and 5 kHz respectively in the experiments. To make sure two cells operate under similar electric fields, the amplitude of the signal is adjusted to be 30 V and 84 V for 3.3 μm and 9.0 μm liquid crystal cells respectively. The

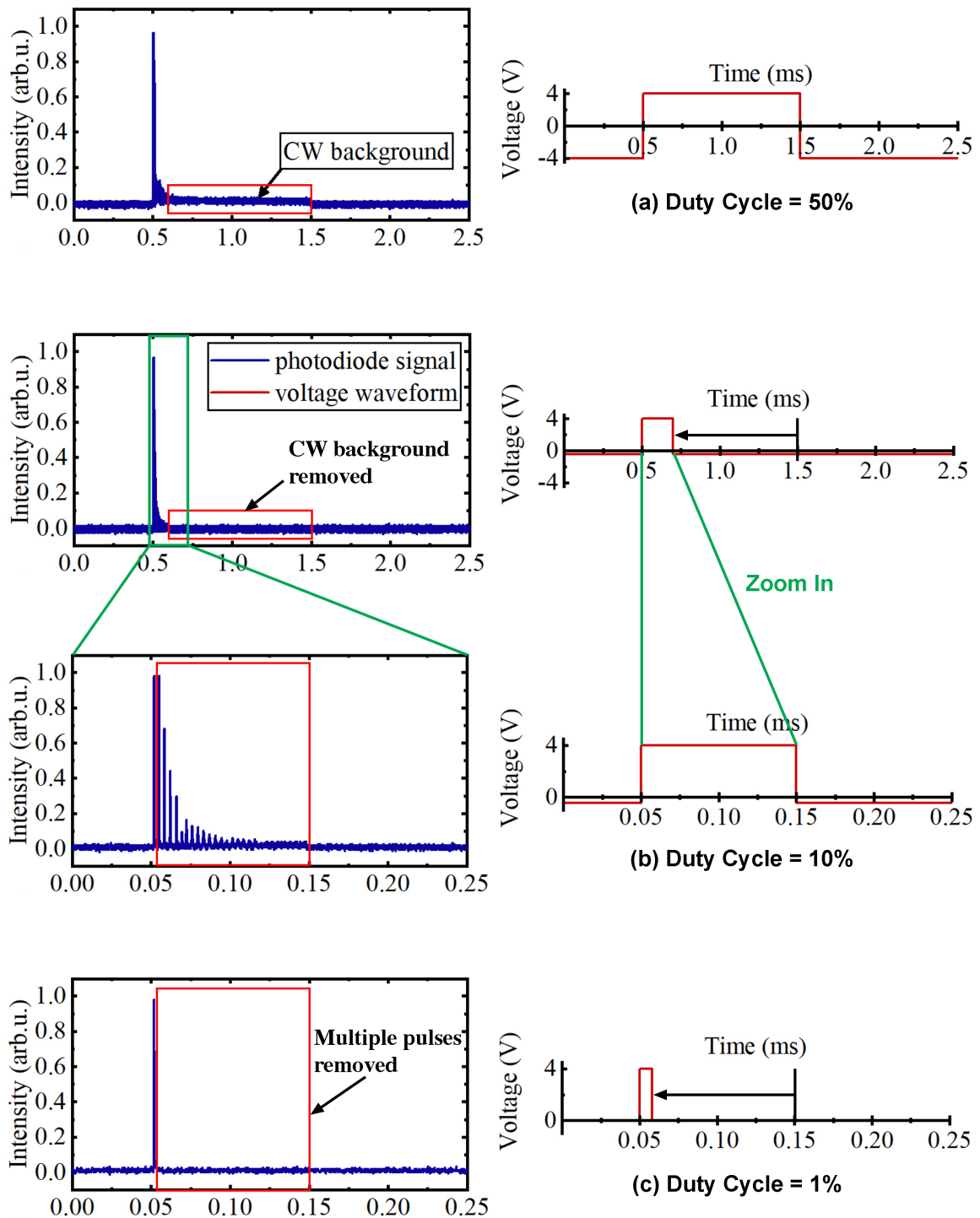


Fig. 5.8 Oscilloscope trace of the emitted laser beam behind the cavity and the applied voltage waveform. Note that the voltage amplitude was 4 V for each measurement; however, to keep the time average zero a small negative voltage was applied when the waveform was not in a high state. Decreasing the duty cycle of the applied voltage waveform from 50 % in (a) to 10 % in (b) results in a reduction of almost all the continuous wave backgrounds. Further decreasing the duty cycle to below 1 % in (c) results in a single Q-switched pulse.

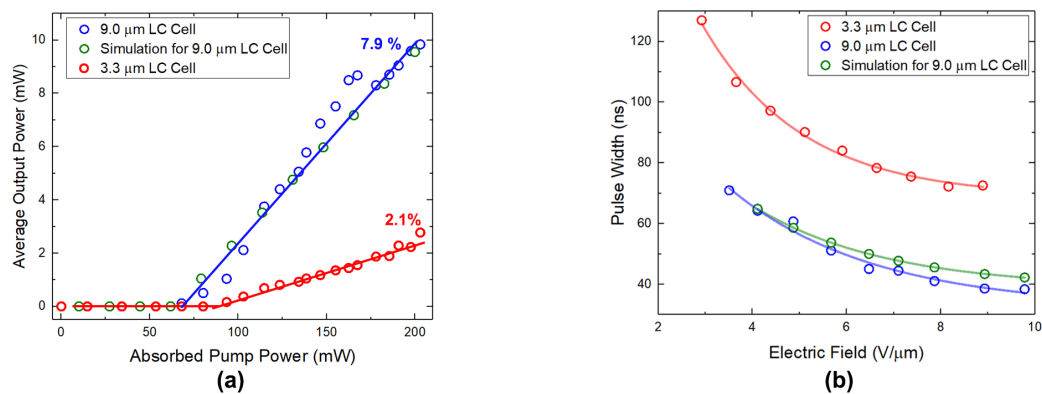


Fig. 5.9 (a) The simulated (cyan) and measured average output power for 3.3 μm (red) and 9.0 μm (blue) liquid crystal cells as a function of the absorbed pump power up to 200 mW. (b) The simulated (cyan) and measured pulse width for 3.3 μm (red) and 9.0 μm (blue) liquid crystal cells as a function of the applied electric field.

average output power and the pulse width for 3.3 μm (blue) and 9.0 μm (red) liquid crystal cells are presented in Fig. 5.9. It is clear that with the same pump power and electric field, the 9.0 μm liquid crystal cell has a larger slope efficiency around 7.9 % and a shorter pulse width below 40 ns because the 9.0 μm liquid crystal cell has a larger modulation depth and faster switching speed as discussed above. From Fig. 5.9 (b), we can see that the pulse width decreases with the increasing electric field when the electric field is relatively low. When the electric field is increased further, the pulse width will not decrease as significantly as before and the pulse width starts to approach its limit. It is also worth noting that the slope efficiency increases with the repetition rate until 20 kHz, at which the average output power increases to 27 mW and the slope efficiency reaches the maximum round 22 %. When the repetition rate is higher than 20 kHz, no pulsed lasers can be observed, and the laser operation is changed from the Q-switching mode to the continuous wave mode. The oscilloscope trace of the output signal associated with the shortest pulse duration is shown in Fig. 5.10 (a). The spectral width was approximately 50 pm FWHM centred at 1016.02 nm as shown in Fig. 5.10 (b). In addition to this, when the shortest pulse duration is achieved, the peak power is around 51 W.

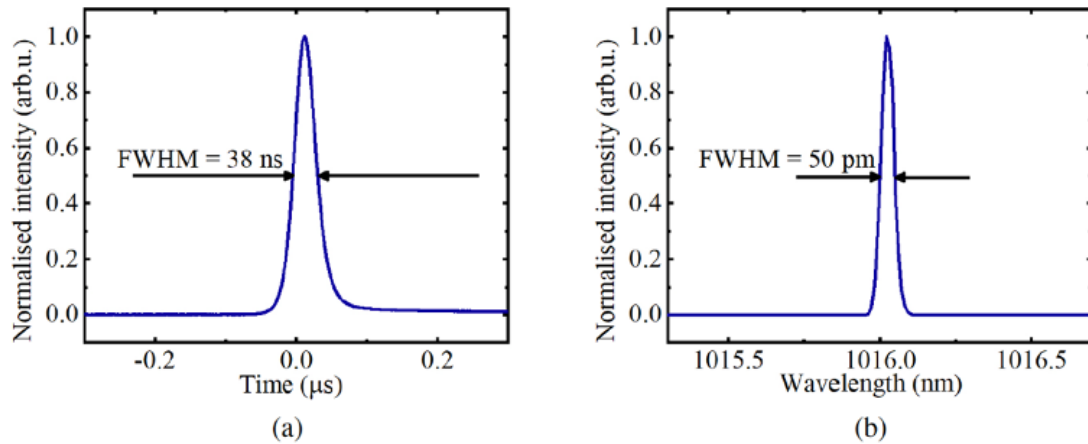


Fig. 5.10 Laser characteristics at a repetition rate of 5 kHz utilising the cell with a $9.0 \mu\text{m}$ thick liquid crystal layer: (a) oscilloscope trace of pulse form and (b) emission spectrum of the laser output.

5.2.4 Conclusion

We have demonstrated a novel approach to actively Q-switch an integrated waveguide chip laser, which makes use of a liquid crystal cell in the DHF mode of operation. Our experimental results show that laser pulse durations below 38 ns can be achieved, which is much shorter than the typical response time of liquid crystals. This somehow surprising result is confirmed and explained by the numerical simulations. This device can be directly integrated onto the waveguide chip and controlled by a low power ($< 0.84 \text{ W}$), low voltage ($< 84 \text{ V}$) driver. We believe that this novel, integrated and low-cost laser source is a promising tool for a broad range of applications such as trace gas sensing and LIDAR.

5.3 Compact design of actively Q-switched waveguide lasers

In this section, we will propose an optimised compact actively Q-switched laser using a liquid crystal modulator with high efficiency and low voltage. This project is in collaboration with collaboration between University of New South Wales, Macquarie University, and Lastek. Pty. Ltd in Adelaide. The total length of the laser cavity is only 22 mm, which makes the

whole setup compact and portable. Additionally, the required driving voltage is lower than 100 V, while the shortest pulse width of Q-switched laser pulses is 15.6 ns with a peak power of 110 W.

5.3.1 Experimental setup

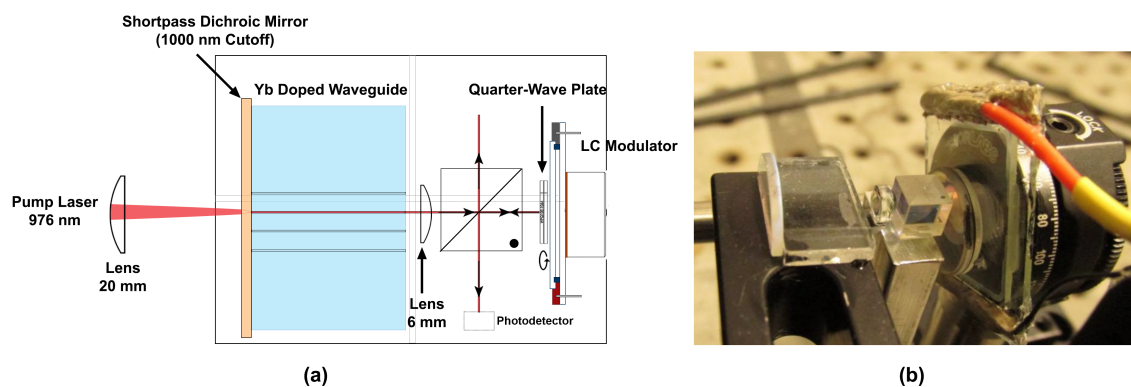


Fig. 5.11 (a) The schematic of the experimental setup and (b) the laser cavity which is 22 mm long.

From the experimental setup presented in Fig. 5.11, the input-coupling mirror is integrated with the Yb-doped waveguide chip via UV adhesive to reduce the cavity length and improve the laser performance. A 300 mW, 976 nm fibre-coupled laser diode is utilised to pump a femtosecond-laser direct-written waveguide within a Ytterbium-doped ZBLAN glass host [80]. The unabsorbed pump light transmitted from the waveguide is collimated by a B-coated lens with a focal length of 6 mm. A quarter-wave plate is placed between the PBS and modulator to maximize the cavity loss with the absence of electric fields. Once the optimal orientation of the quarter-wave plate is found, it can be integrated with the liquid crystal modulator. In this setup, the PBS in combination with the waveplate and liquid crystal modulator acts as an actively controlled variable output-coupling mirror. It is worth noting that the shorter laser cavity can result in a shorter pulse width and higher pulse peak power. Because the theoretical minimum value of pulse width is the cavity lifetime, the shorter cavity lifetime induced by the shorter cavity can shorten the pulse width of lasers and then improve the peak power of laser pulses.

5.3.2 Experimental results

Based on the setup shown in Fig. 5.11, the CW laser can be observed both without the liquid crystal modulator and with the liquid crystal modulator when no pulsed electrical signal is applied on the liquid crystal modulator. The maximum average output power at 1030 nm is 44 mW and 18 mW respectively at the maximum absorbed pump power of 196 mW. The output powers in two cases as a function of the absorbed pump power are shown in Fig. 5.12.

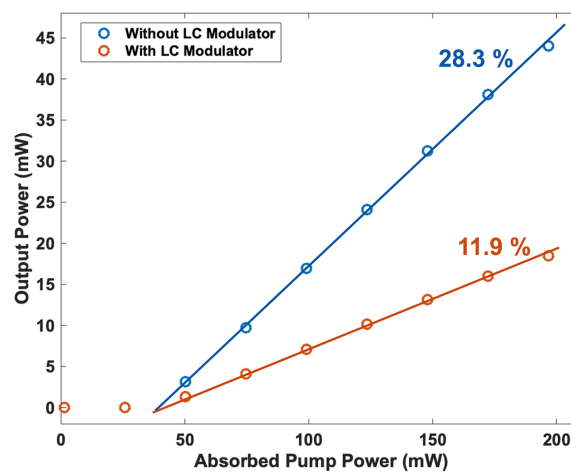


Fig. 5.12 (a) Without the LC modulator, a CW output laser at 1030 nm can be observed with a slope efficiency of 28.3 %, and (b) with the LC modulator but no electrical signal, a CW output laser at 1030 nm can be observed with a slope efficiency of 11.9 %.

To achieve the Q-Switched pulsed lasers at 1030 nm, a pulsed electrical signal with a peak-to-peak voltage of 98 V and a duration of 1 μ s is applied on the liquid crystal modulator in the experiments. The preliminary experimental results show that the Q-Switched lasers are achieved with the shortest pulse width of 15.6 ns, the highest peak power of 110 W, and the largest pulse energy of 1.7 μ J with a pump power of 260 mW. In the experiments, the stable train of Q-switched laser pulses can be observed in a wide range of repetition rates from 2 kHz to 16 kHz. The effects of repetition rate on the laser performance parameters have been investigated and presented in Fig. 5.13 (a) and (b), including pulse width, peak power, average output power, and pulse energy.

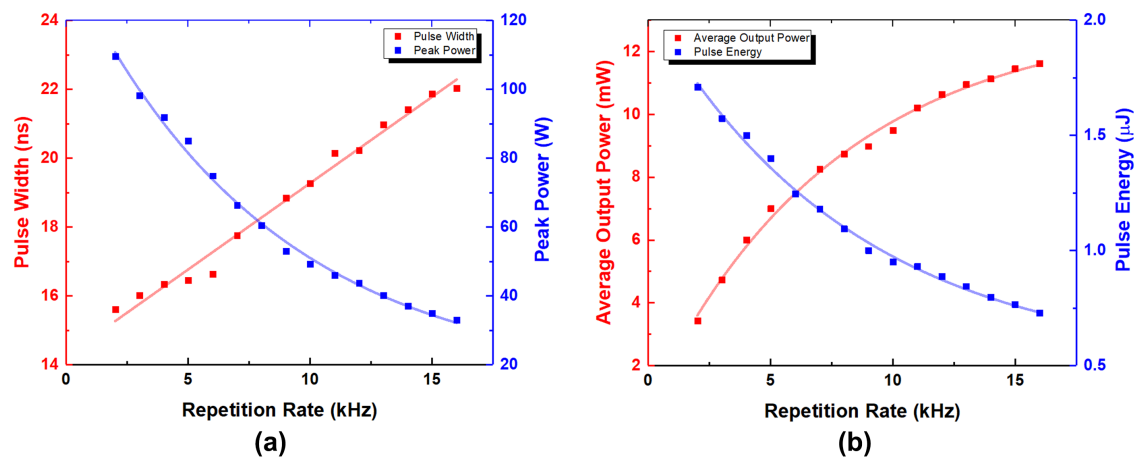


Fig. 5.13 (a) the pulse width, peak power, (b) average output power and pulse energy as a function of the repetition rate from 2 to 16 kHz.

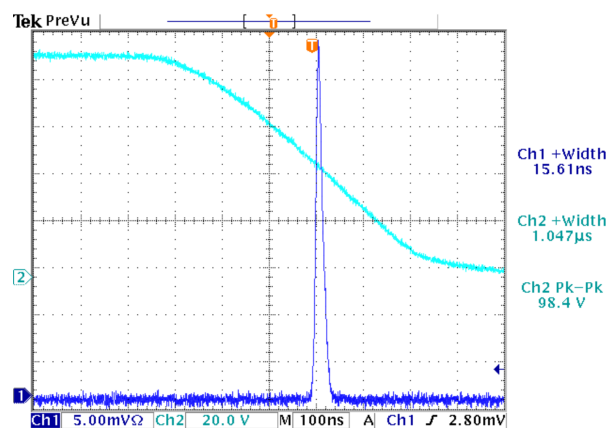


Fig. 5.14 The measured oscilloscope trace of the shortest Q-Switched laser pulses around 15.6 ns.

It is clear that the pulse width increases from 15 ns up to 23 ns and the peak power decreased from 110 W down to 33 W for the repetition rate varying from 2 to 16 kHz. Additionally, the average output power increases linearly with the repetition rate, until it starts to saturate above 10 kHz due to the properties of the Yb:ZBLAN gain medium. The maximum pulse energy achieved in the experiments is around 1.7 μJ . The optimal laser pulses show the shortest pulse width of 15.6 ns, the highest peak power of 110 W and the

largest pulse energy of 1.7 μJ at the repetition rate of 2 kHz. The measured oscilloscope trace of generated Q-Switched laser pulses with the shortest pulse width is shown in Fig. 5.14.

5.4 Summary

In this section, I have demonstrated a novel approach to actively Q-switch of integrated waveguide chip lasers, which makes use of a liquid crystal cell in the DHF mode of operation. Our preliminary experimental results show that a stable train of Q-switched lasers with a laser pulse duration below 38 ns can be achieved, which is much shorter than the typical response time of liquid crystals. This somehow surprising result is confirmed and explained by the numerical simulation model introduced in the previous section. Recently, this device has been directly integrated onto the waveguide chip and controlled by a low power (< 0.84 W), low voltage (peak-to-peak voltage of 98 V) driver with an electrical signal duration of 1 μs only. With the designed prototype of a compact setup, the pulse width of optimised Q-switched lasers has been shortened to only 15.6 ns. Moreover, the highest peak power of 110 W and largest pulse energy of 1.7 μJ have been measured from a stable train of generated Q-switched laser pulses respectively. We believe that this novel, integrated and low-cost laser source is a promising tool for a broad range of applications such as LIDAR, laser ablation, and nonlinear applications.

Chapter 6

Q-switched Tm^{3+} :ZBLAN waveguide lasers operating at $1.86 \mu\text{m}$

6.1 Introduction

Short infrared laser sources around $2 \mu\text{m}$ have been crucial to many applications over the past decades, including trace gas spectroscopy, eye safe range-finding and coherent LIDAR. To achieve diode pumped Tm lasers operating on the ${}^3\text{F}_4 \rightarrow {}^3\text{H}_6$ transition, choosing a suitable Tm-doped laser material is of significant importance. Among the many glass systems available, Tm^{3+} -doped ZBLAN exhibits broad absorption and emission features because the amorphous glass host possesses a lower phonon energy ($\approx \text{cm}^{-1}$) than Tm^{3+} -doped silica glass ($\approx 1000 \text{cm}^{-1}$) and the wavenumber for ZBLAN is around cm^{-1} . Because a lower phonon energy can lead to a higher efficiency of the “two-for-one” Tm–Tm self-quenching process between Tm ions and a longer Tm_3F_4 lifetime due to the multiphonon decay, the experiments demonstrated by B.M. Walsh in 2003, showed that Tm:ZBLAN is a factor of 2 higher in slope efficiency and a factor of 3 lower in threshold than Tm:silica [230].

The radiative and non-radiative properties of ZBLAN glass doped with individual rare earth elements (Pr^{3+} , Nd^{3+} , Dy^{3+} , Ho^{3+} , Er^{3+} and Tm^{3+}) at different concentration levels between 0.1 and 4 mol% have been investigated in detail by L. Wetenkamp in 1992 [231]. After that, ZBLAN (ZrF_4 - BaF_4 - LaF_4 - AlF_3 - NaF_3) as a laser host material has been widely

utilised to develop fibre lasers at diverse wavelengths from the visible through to 3.9 μm [232, 233], due to its wide transparency from the UV through to 5 μm [234], a low phonon energy of 500 cm^{-1} [230] and a high rare-earth solubility.

In this work, the DHFLC modulator is incorporated with a femtosecond laser written Tm³⁺-doped ZBLAN waveguide chip to generate actively Q-switched laser pulses of up to 1.3 kW peak-power with 31 ns pulse width. The stable train of Q-switched laser pulses can be observed over a large range of repetition rate from 200 Hz to 30 kHz. Compared to commercially available AOMs and EOMs, the comparable performance of active Q-switching can be achieved with a lower control voltage (peak-to-peak voltage from 10 V to 65 V) and a more compact setup. The work presented in this section also shows the potential of utilising this compact Q-switched Thulium waveguide laser source to observe nonlinear effects in specific fibres (microwire or chalcogenide fibre), such as FWM and spectral broadening, because of its short pulse duration and high peak power.

6.2 Femtosecond direct-written Tm³⁺:ZBLAN waveguide

In 2010, F. Fusari et. al reported the first lasing action and performance at around 1.9 μm by using an ultrafast laser inscribed channel waveguide in a Tm³⁺-doped fluorogermanate glass [235]. After the first demonstration of Tm³⁺ waveguide lasers in the MIR region, the solid-state lasers operating around 2 μm using Tm³⁺-doped glass are heavily developed at the end of the last century for various applications, such as laser surgery due to strong water absorption around 2 μm and environmental sensing (LIDAR). In addition to the advantages of using ZBLAN glass as a host material, the optical emission transition ${}^3\text{F}_4 \rightarrow {}^3\text{H}_6$ found in Tm³⁺ ions has gained a lot of attention for three reasons. First of all, Tm³⁺ ions can be directly pumped via ${}^3\text{H}_6 \rightarrow {}^3\text{H}_4$ absorption transition around 790 nm from a wide variety of commercially available laser diodes [236]. Secondly, because the cross-relaxation mechanism occurring in the Tm³⁺-doped ZBLAN glass, especially with high dopant concentrations, can excite two ions in the ${}^3\text{F}_4$ level by absorbing only one pump photon at 790 nm, the ${}^3\text{F}_4 \rightarrow {}^3\text{H}_6$ emission transition can give rise to a high laser efficiency up to 50 % [80]. Thirdly, Tm³⁺ and

Ho^{3+} ions can be co-doped in the ZBLAN glass to enable the $^5\text{I}_7 \rightarrow ^5\text{I}_8$ emission transition of Ho^{3+} ions to develop fixed or tunable lasers around 2 μm for eye-safe applications [237–239].

In my experiments, the waveguide is inscribed in the $\text{Tm}^{3+}(\text{TmF}_3)$ -doped ZBLAN ($\text{ZrF}_4\text{-BaF}_2\text{-LaF}_3\text{-AlF}_3\text{-NaF}$) glass chip with the dopant concentration level of 2.0 mol%. The waveguide chip is diced and polished in the dimension of $9 \times 8 \times 2$ mm. To obtain a high refractive index contrast and low confinement loss in direct-written Tm-doped waveguide and thus a high slope efficiency in the lasing performance, the waveguide written in the ZBLAN glass is composed of 108 partially overlapping cylinders in the form of three rings, in which 36 partially overlapping cylinders form one ring as shown in Fig. 6.1. To investigate the effects of core diameter, cladding width, and structure complexity on the lasing performance, a group of waveguides with various core diameters ranging from 15 to 45 μm and different structure complexities (refer to the number of overlapping cylinders and the number of rings) were fabricated and characterised individually in the previous work which was carried out by other researchers at Macquarie University. Based on previous measurements, the Tm^{3+} -doped ZBLAN waveguide with 35 μm core diameter and 30 μm cladding width could offer the highest slope efficiency and the best lasing performance.

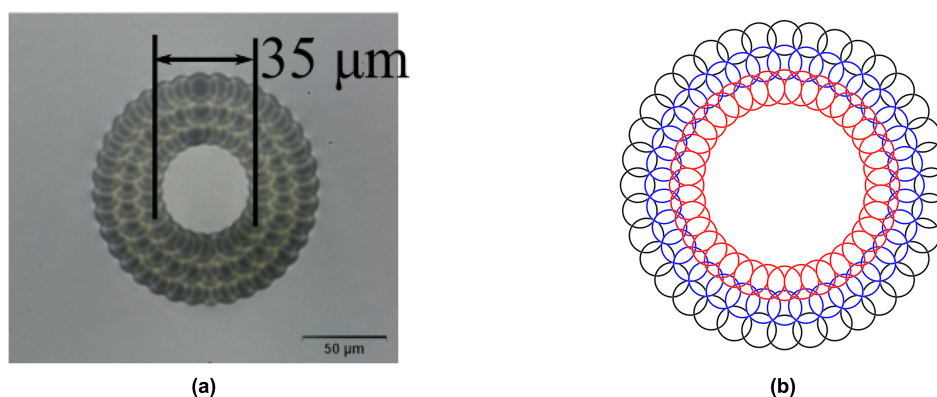


Fig. 6.1 (a) Waveguide structure with a core diameter of 35 μm and a cladding width of 30 μm . The femtosecond laser inscribed waveguide is composed of three rings in which 36 partially overlapping cylinders form one ring. (b) The schematic drawing of Tm^{3+} -doped ZBLAN waveguide chip used in the experiments.

6.3 Experimental setup

The schematic drawing of the experimental setup for the Q-switched $\text{Tm}^{3+}:\text{ZBLAN}$ waveguide lasers is shown in Fig. 6.2. In the experimental setup, two TO-can laser diodes from Thorlabs (LD785-SE400) operating at 785 nm are used to pump the Tm^{3+} -doped waveguide via ${}^3\text{H}_6 \rightarrow {}^3\text{H}_4$ absorption transition of Tm^{3+} ions around 790 nm. Each laser diode can offer the maximum output power of 400 mW with the absolute maximum current of 600 mA. Because the beams emitted from laser diodes are elliptical, an anamorphic prism is required for each laser diode to reshape the profile of the laser beam from elliptical to nearly circular via the asymmetric surfaces of the anamorphic prism. In most cases, the anamorphic prism pair has one interface with normal incidence and Brewster's angle at the other interface to modify the beam shape. In practical work, the anamorphic prism pairs are needed for many applications, such as light coupling between laser diode and waveguide or optical fibre. In the experiments shown in this section, to optimise the coupling efficiency between laser diodes and waveguide chip and the lasing performance of the whole setup, the beam needs to be circular to match well with the mode field of the inscribed waveguide, which is circular as well due to the circular waveguide structure shown in Fig. 6.1. Therefore, two anamorphic prism pairs are placed between laser diodes and PBS, and the measured beam spot size after the B-coated collimating lens and anamorphic prism pair is around 5 mm.

In this setup, a PBS is used to combine two incident beams emitted by two laser diodes to increase the maximum pump power up to 800 mW. Please note that the beam profiles and beam propagation directions need to be identical via adjusting the anamorphic prism pairs and silver mirror finely before the combination of two beams, thus the coupling efficiency can be optimised. To maximize the output power of the PBS as a beam combiner, a halfwave plate is inserted between the silver mirror and PBS to modify the polarization state of the incident beam from the second laser diode (Laser Diode 2 in Fig. 6.2). Due to the shortage of the halfwave plate, the polarization state of the first laser diode (Laser Diode 1 in Fig. 6.2) is controlled manually by rotating the mount of the first laser diode. To prevent the unexpected damage of laser diodes due to the high current, the maximum current applied to laser diode

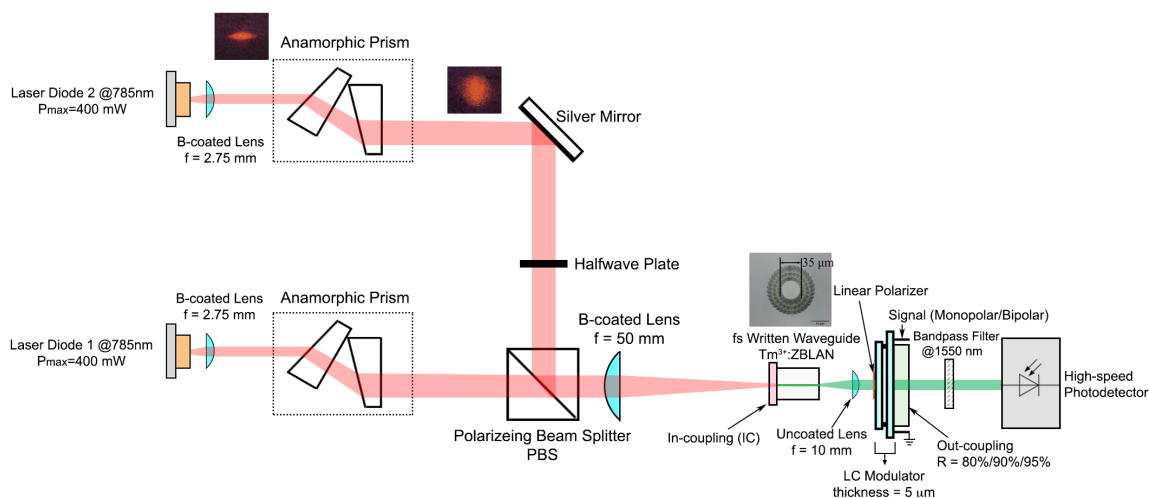


Fig. 6.2 Schematic drawing of the experimental setup for Tm^{3+} -doped ZBLAN Waveguide Lasers. Two laser diodes operating at 785 nm are used to pump the Tm^{3+} -doped waveguide. By using the PBS as a beam combiner, the maximum pump power of 637.2 mW is obtained, when the driving current of 500 mA is applied to each laser diode. The pump is coupled into the waveguide chip with a $35 \mu\text{m}$ core diameter via a B-coated lens ($f = 50 \text{ mm}$) and the output beam is collimated by an uncoated lens ($f = 10 \text{ mm}$) before passing through the polarizer and $5 \mu\text{m}$ thick liquid crystal cell. Three output coupling mirrors ($R = 80 \%$, 90% , 95%) are tested individually. A high-speed photodetector is placed next to the output coupling mirror to monitor the output laser pulses. It is worth noting that the cavity length within this setup is only 35 mm.

in the experiments is 500 mA, which is smaller than the absolute maximum current of laser diodes around 600 mA. The measured maximum output power of LD-1 and LD-2 after the PBS (beam combiner) is 318.8 mW and 318.4 mW respectively with the driving current of 500 mA. As a result, the maximum pump power in the experiments is up to 637.2 mW. To couple the incident pump beam into the waveguide with the optimal coupling efficiency, because the incident beam spot size and the core diameter of the inscribed waveguide are 5 mm and $35 \mu\text{m}$ respectively and the refractive index contrast Δn is around 1.5×10^{-3} , a B-coated (anti-reflective from 650 to 1050 nm) plano-convex lens with a focal length of 50 mm is selected and placed in front of the waveguide chip. From the measurements, the maximum absorbed pump power is 433.26 mW, which means the maximum absorption efficiency is 68 % in these experiments. The optical losses of waveguide chip and PBS in this

setup are similar to the losses listed in Table 5.2. The input-coupling mirror (Pump Mirror 104237 from LAYERTEC GmbH) is integrated with the waveguide chip using the Norland Optical Adhesive (NOA 60) to minimize the cavity length. The input-coupling mirror has the anti-reflectance coating for the wavelength ranging from 780 to 980 nm on its rear side with a very low reflectance smaller than 0.25 % and the high reflectance coating for the wavelength ranging from 1850 nm to 1950 nm on its front side with a very high reflectance greater than 99.9 %. As a result, the pump laser operating at 785 nm can pass through the input coupling mirror with a small optical loss, while the emitted laser at 1880 nm will be maintained in the laser cavity due to the high reflectance of the input-coupling mirror. To collimate the output beam from the waveguide chip, an uncoated plano-convex lens with a focal length of 10 mm is used in front of the liquid crystal cell. The measured spot size of the collimated beam is around 1 mm. The thin-film linear polarizer (colorPol® IR 1550) is placed in front of the liquid crystal cell to confine the polarization to be linear at a specific direction. Next to the polarizer, the liquid crystal cell with a thickness of $5 \mu\text{m} \pm 0.3 \mu\text{m}$ is used with an optical loss of 73 % per round trip in the experiments shown in this section. The presence of the linear polarizer can transform the phase change introduced by the liquid crystal cell to the change in the optical intensity or optical cavity loss, thus the combination of a liquid crystal cell and a linear polarizer can lead to an actively controllable intensity (or cavity loss) modulator as a Q-Switch module in the cavity. It is worth noting that the polarizer is integrated with the liquid crystal cell via Norland Optical Adhesive, as shown in Fig. 6.3, to accomplish the aim of developing a compact Q-switched laser source. To find out the optimal reflectance of output-coupling mirror (output coupler) based on the lasing slope efficiency, three output-coupling mirrors with different reflectances (80 %, 90 %, 95 %) are tested individually. In the experiments, the average power of output laser around 1880 nm is measured by a compact power and energy meter (PM100D from Thorlabs), while the pulse width of Q-Switched laser pulses is measured by the 10 GHz 2 μm Extended InGaAs Photodetector (ET-5000 EXT from Electro-Optics Technology, Inc). Both power meter and high-speed photodetector are placed after the optical bandpass filter at 1550 nm, which means

only the output beam operating at 1880 nm (longer than 1550 nm) is measured by power meter and high-speed photodetector.

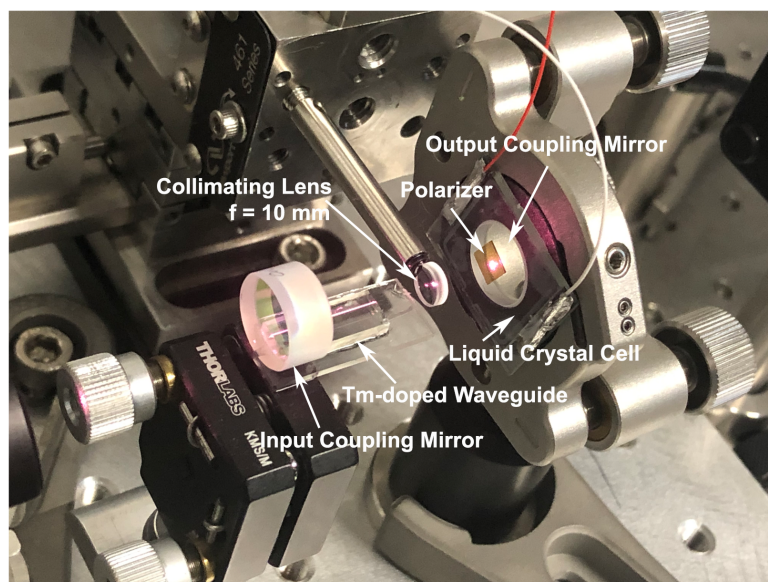


Fig. 6.3 The compact laser cavity is composed of an input-coupling mirror, Tm^{3+} -doped ZBLAN waveguide chip, an uncoated collimating lens ($f = 10$ mm), a linear polarizer, a $5 \mu\text{m}$ thick liquid crystal cell, and an output-coupling mirror. The total length of the laser cavity is around 35 mm. The optical bandpass filter at 1550 nm is used to filter out the pump beam at 785 nm and only maintain the output beam around 1880 nm.

6.4 Laser Performance

At the NIR region, three output coupling mirrors are available with different reflectances, 80 %, 90 %, and 95 % respectively. To find out the optimal reflectance of the output-coupling mirror (output coupler) and achieve the highest internal slope efficiency in the continuous wave (CW) mode, three output coupling mirrors are tested individually within the setup shown in Fig. 6.2. It is worth noting that the measurement of slope efficiencies is carried out with the absence of linear polarizer and liquid crystal cell in the setup. The average output power measured by the optical power meter as a function of absorbed pump power for three output couplers is shown in Fig. 6.4. The measured internal slope efficiencies in the continuous wave (CW) mode for different output couplers are shown in Table 6.1. The

largest internal slope efficiency is obtained using an output coupling mirror (OC#2) with 90 % reflectance. In the experiments, the largest internal slope efficiency is around 17.8 % with the pump threshold of 276.0 mW.

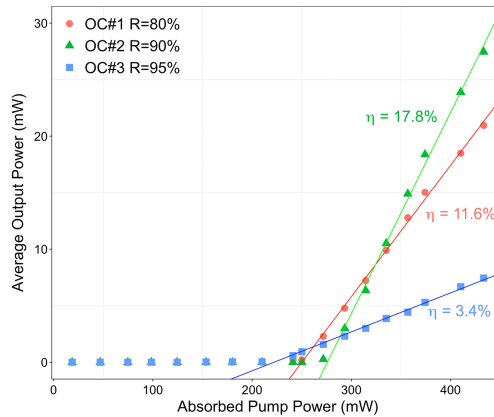


Fig. 6.4 The average output power measured by the optical power meter as a function of the absorbed pump power for three output coupling mirrors with different reflectances, namely 80 %, 90 % and 95 %.

Table 6.1 Internal slope efficiencies for different output coupling mirrors

	Reflectance@1880nm	Pump Threshold	Max Output Power	Internal Slope Efficiency
OC#1	80 %	250.2 mW	21.0 mW	11.6 %
OC#2	90 %	276.0 mW	27.5 mW	17.8 %
OC#3	95 %	222.6 mW	7.5 mW	3.4 %

Based on the comparison of internal slope efficiencies measured using different output coupling mirrors, the output coupling mirror with 90 % reflectance is selected and used in the following experiments. To enable Q-switch lasers, the liquid crystal cell combined with the linear polarizer is integrated with the selected output coupling mirror (R = 90 %). As explained in the previous section, the liquid crystal is a kind of anisotropic material that has normal phase delay caused by its birefringence and geometric phase delay caused by the rotation of its optical axes. Because the modulator cell is filled with DHFLCs, the molecular structure of DHF liquid crystals will be deformed due to the existence of electric fields. Thus,

both birefringence and rotation of optical axes of liquid crystals can be controlled by the electrical signal and corresponding electric field. To transform the electric field-controlled phase delay to the optical intensity change, a linear polarizer is placed in front of the liquid crystal cell. As a result, the combination of the linear polarizer and liquid crystal cell can be considered as an active Q-Switch modulator. The measured average output powers as a function of the absorbed pump power with or without the active Q-Switch modulator using liquid crystal are shown in Fig. 6.5,

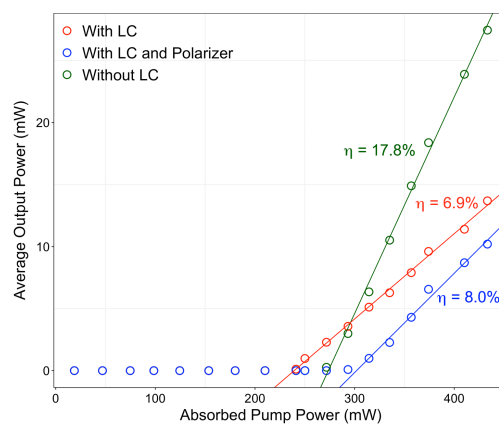


Fig. 6.5 The average output power measured by the optical power meter as a function of the absorbed pump power for laser cavities with or without the 5 μm thick liquid crystal modulator and/or polarizer. When the 5 μm thick liquid crystal modulator is placed within the laser cavity, the slope efficiency η is reduced from 17.8 % to 6.9 %. When both the liquid crystal cell and linear polarizer are placed into the laser cavity, the internal slope efficiency of 8.0 % is achieved with a pump threshold of 302.8 mW.

Based on transmission measurements of liquid crystal cells and the linear polarizer, the double-pass transmission loss of the 5 μm thick liquid crystal cell is around 70 % at the wavelength of 1880 nm. As a result, the measured internal slope efficiency of the laser cavity with a 5 μm thick liquid crystal modulator decreased from 17.8 % to 6.9 % as shown in Fig. 6.5. The measured internal slope efficiencies and pump thresholds of laser cavities with or without the liquid crystal modulator are shown in Table 6.2.

As discussed earlier, the multiple pulse problem always occurs when the Q-Switch turns on and off too slowly. Moreover, the generation of more than one single Q-switched laser

Table 6.2 Internal slope efficiencies and pump thresholds with or without liquid crystal modulator

	OC Reflectance	Pump Threshold	Max Output Power	Slope Efficiency
Without LC	90 %	276.0 mW	27.5 mW	17.8 %
With LC	90 %	239.7 mW	13.7 mW	6.9 %
With LC and Polarizer	90 %	302.8 mW	10.2 mW	8.0 %

pulse could result in the degradation of Q-Switched laser performance and some potential errors in some applications, such as LIDAR. To minimize the switch-off time of the liquid crystal modulator and avoid the generation of multiple pulses, electrical signals with a bipolar waveform are applied on the liquid crystal modulator with different repetition rates, amplitudes, and pulse duration. The effects of changing the repetition rate, amplitude, and pulse duration of applied signals on the performance of Q-switched lasers are investigated in experiments separately. In experiments, the absorbed pump power and repetition rate is maintained at 433.26 mW and 200 Hz respectively, while the peak to peak voltage of the applied electrical signal varies from 10 V to 65 V. The measured pulse width, peak power, average output power, and pulse energy have been shown in Fig. 6.6.

In Fig. 6.6, the pulse width of Q-Switched laser pulses decreases significantly from 109.50 ns to 31.16 ns, with the increasing peak to peak voltage of applied electrical signals. When the electrical signal with a larger peak to peak voltage is applied on the liquid crystal modulator, the electric field on the liquid crystal layer is more intense, which can result in a faster switching (modulation) speed and then a larger modulation depth as shown in Fig. 5.7. As a result, the generated Q-Switched laser pulses become shorter, when the peak to peak voltage of applied electrical signals increases. Because of the larger modulation depth induced by the increasing peak to peak voltage, the average output power, and pulse energy slightly increase from 7.90 mW to 8.35 mW and from 39.50 μ J to 41.75 μ J respectively, which means the higher modulation speed and larger modulation depth can improve the energy extraction efficiency of the energy conversion from initial inversion energy to Q-Switched output energy to some extent [240]. Because the pulse duration reduces and average output

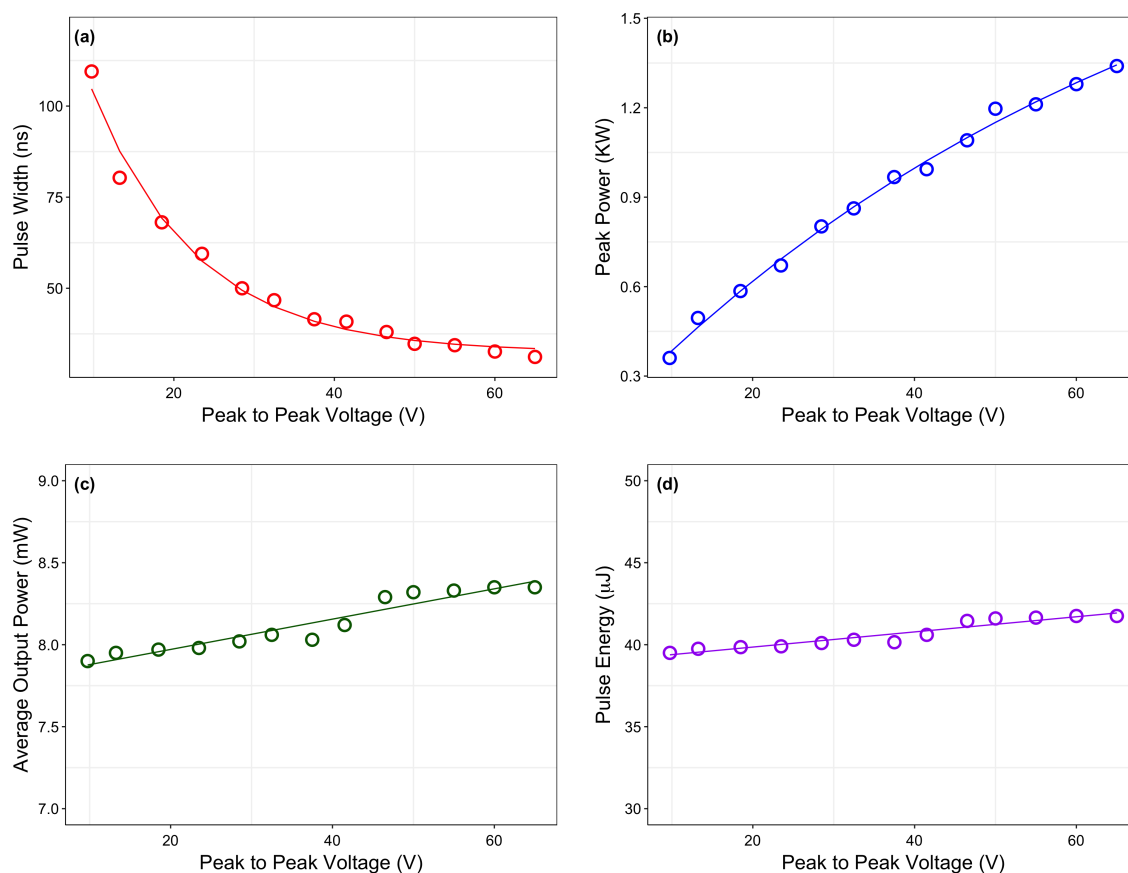


Fig. 6.6 The (a) pulse width, (b) peak power, (c) average output power, and (d) pulse energy measured as a function of the peak to peak voltage of applied electrical signals. The pulse width of Q-Switched lasers decreases from 109.50 ns to 31.16 ns when the peak-to-peak voltage increases to the maximum around 65 V. The average output power increases slightly and proportionally to the peak to peak voltage from 7.90 mW to 8.35 mW. Similar to the average output power, the pulse energy increases slightly from 39.50 μJ to 41.75 μJ when the peak to peak voltage increases to 65 V. Due to the decreasing pulse width and increasing average output power, the peak power of Q-Switched laser increases almost linearly with the peak to peak voltage from 0.36 kW to 1.34 kW.

power increases with the increasing peak to peak voltage of applied signals, the peak power of Q-Switched laser pulses increases with the increasing peak to peak voltage from 0.36 kW to 1.34 kW. When the peak to peak voltage is smaller than 50 V, the peak power shows a linear relation with the peak to peak voltage. However, when the peak to peak voltage exceeds 50 V, both the pulse width and peak power start to saturate, because the generated

electric field intensity is close to the critical electric field of the liquid crystal modulator, and the modulation depth will become stable and will not increase further.

With the maximum peak to peak voltage of 65 V and the absorbed pump power of 433.26 mW, the performance parameters of Q-Switched laser pulses are measured and studied under the varying repetition rate ranging from 0.1 kHz to 40.0 kHz. From the experiments, the stable train of Q-Switched laser pulses can be observed when the repetition rate is greater than 0.2 kHz and smaller than 30 kHz. When the repetition rate is smaller than 0.2 kHz, e.g. 0.1 kHz, multiple Q-switched laser pulses are observed in one period, because the Q-Switch is too slow and then the initial inversion needs to be dumped by multiple laser pulses due to the small initial inversion ratio of slow Q-Switch. By contrast, Q-Switched laser pulses are not observable when the repetition rate is greater than 30 kHz. It is because the initial stored energy in the cavity decreases when the period of laser pulse emission is shortened by the increasing repetition rate. The measured Q-Switched laser performance parameters as a function of the repetition rate tuning from 0.2 kHz to 30 kHz have been shown below in Fig. 6.7.

In Fig. 6.7, it is clear that the repetition rate of the Q-Switch modulator has significant effects on the laser performance, including pulse duration, average output power, peak power, and pulse energy. For the pulse width of Q-Switched laser pulses, the pulse width increases almost linearly, from 31.44 ns to 115.00 ns, with the increasing repetition rate, because the initial stored energy before the laser pulse occurs decreases with the increasing repetition rate. If the initial stored energy in the cavity is less, the effective inversion ratio is smaller and then the pulse width becomes larger. In addition to this, the average output power of Q-Switched laser pulses increases significantly and almost linearly when the repetition rate is smaller than 5 kHz. When the repetition rate is greater than 5 kHz, the average output power increases slower and becomes maximum and steady at 10.18 mW with the repetition rate of 30 kHz. The linear relation observed at a repetition rate below 5 kHz is caused by the larger amount of pulses occurring within a unit of time with the increasing repetition rate. However, when the repetition rate is greater than 5 kHz, the average output power increases more and more slowly and then becomes saturate at 10.18 mW. It is because the Q-Switched

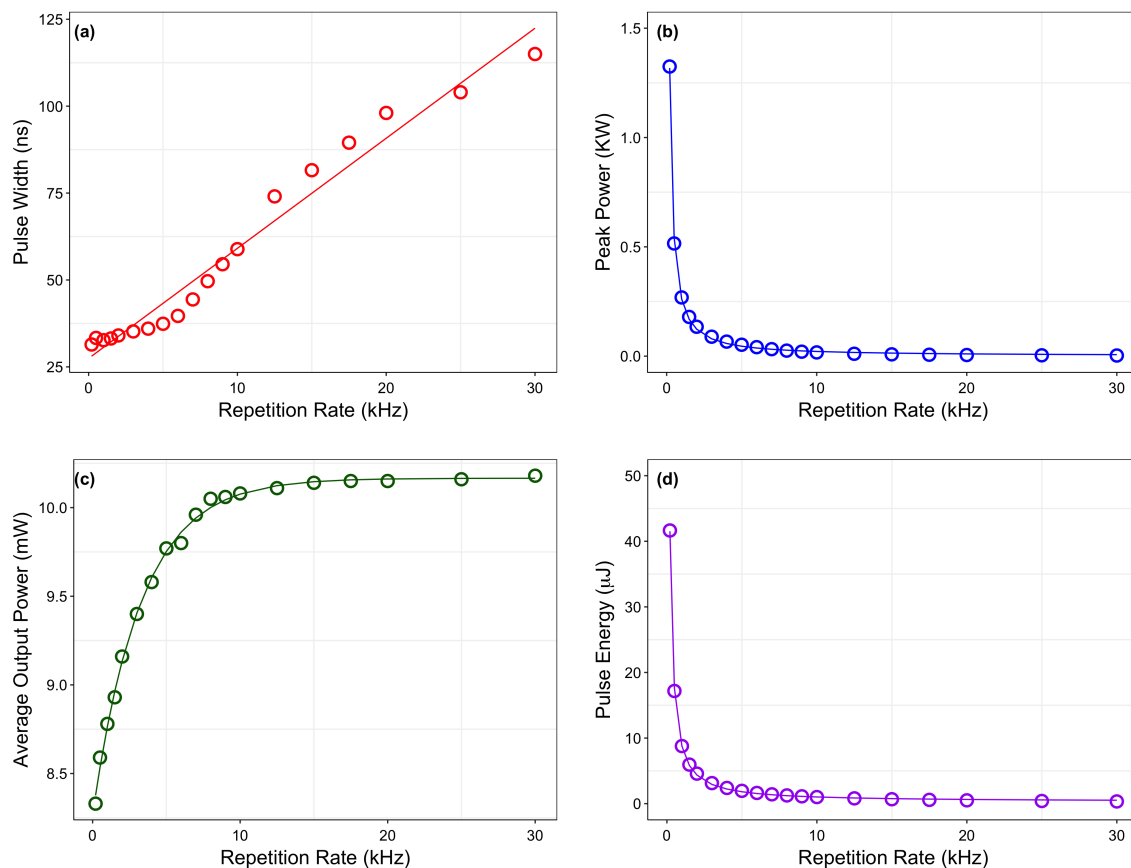


Fig. 6.7 The (a) pulse width, (b) peak power, (c) average output power and (d) pulse energy measured as a function of the repetition rate of applied electrical signals. The pulse width of Q-Switched lasers increases from 31.44 ns to 115.00 ns when the repetition rate increases to 30 kHz. The average output power increases significantly and almost linearly when the repetition rate is smaller than 5 kHz. When the repetition rate is greater than 5 kHz, the average output power increases slower and becomes maximum and steady at 10.18 mW with the repetition rate of 30 kHz. Unlike the average output power, the peak power decays exponentially from 1.34 kW down to 3W when the repetition rate tunes from 0.2 kHz to 30 kHz. Similar to the peak power, the pulse energy decreases exponentially as well, from 41.75 μJ to 0.34 μJ with the increasing repetition rate.

laser pulses with a high repetition rate are similar to the CW lasers and will not increase further with increasing repetition rate. At the repetition rate of 30 kHz, the Q-Switched laser pulses show the maximum internal slope efficiency, which is around 8.0 %. By contrast, the peak power of Q-Switched laser pulses decays significantly from 1.34 kW down to 3 W only when the repetition rate increases from 0.2 kHz to 30 kHz. Because the time interval or period of the Q-Switched laser pulse emission decreases with the increasing repetition rate,

the initial stored energy in the cavity decreases, and then less stored energy is converted into Q-Switched pulse energy, which results in lower peak power. Similar to the peak power, the pulse energy decreases from 41.75 μJ down to 0.34 μJ due to the lower initial stored energy before the laser pulse emission, which is resulted from the increasing repetition rate.

In addition to the peak to peak voltage and repetition rate of the applied signal, the effects of absorbed pump power on the Q-Switched laser performance are studied as well, in different aspects, including pulse width, peak power, average output power, and pulse energy. With the repetition rate of 0.2 kHz and the peak to peak voltage of 65 V, the performance parameters as a function of the absorbed pump power are measured and shown in Fig. 6.8.

As shown in Fig. 6.8, when the absorbed pump power is smaller than the threshold pump power around 312.69 mW, no Q-Switched laser pulses can be observed in experiments. Thus, the average output power remains 0 mW until the absorbed pump power is greater than 312.69 mW. Once the absorbed pump power increases and becomes larger than the threshold pump power, the average output power starts to increase linearly, and then a stable train of Q-Switched laser pulses can be detected and observed by using the high-speed photodetector. Thus, the peak power and pulse energy of Q-Switched laser pulses can be calculated. During the process of increasing absorbed pump power larger than the threshold power, the measured pulse width decreases from 46.11 ns down to 32.50 ns and the average output power increases from 0.17 mW to 8.76 mW, because the larger pumping energy can make a larger number of atoms jump to a higher energy level and thus increase the initial stored energy before switching, which means the Q-Switched laser pulses will demonstrate a larger output power, higher pulse energy, and shorter pulse duration. As a result, the peak power of Q-Switched laser pulses increases from 0.02 kW to 1.34 kW with the increasing absorbed pump power as well.

From our experiments, the stable train of Q-Switched laser pulses with the shortest pulse width around 31.44 ns and highest peak power around 1.34 kW can be obtained, when the absorbed pump power increased to a maximum of 433.26 mW and the periodical bipolar square waveform electrical signal is applied on the liquid crystal modulator with a rectangular

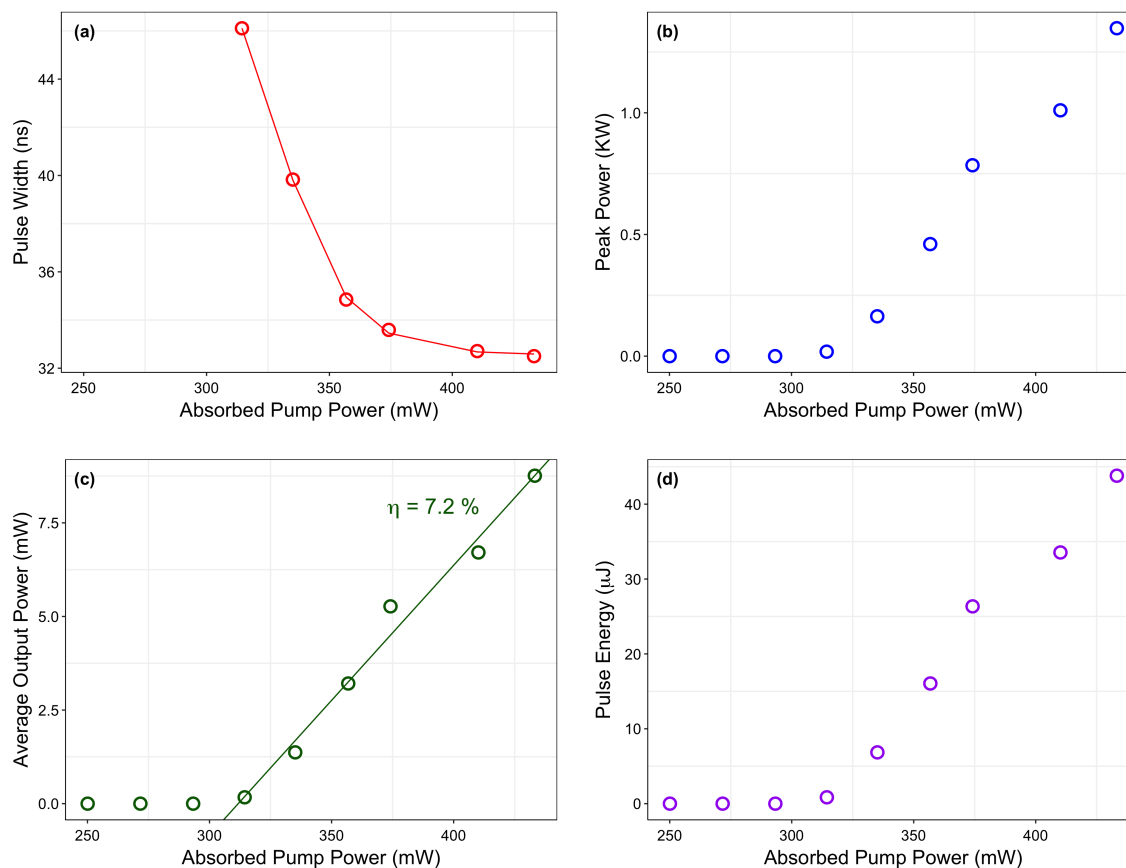


Fig. 6.8 The (a) pulse width, (b) peak power, (c) average output power, and (d) pulse energy measured as a function of the absorbed pump power. The pulse width of Q-Switched lasers drops from 46.11 ns down to 32.50 ns when the pump power increases from 314.41 mW to 433.26 mW which is the maximum absorbed pump power by applying two laser diodes. The average output power increases linearly with the absorbed pump power when the absorbed power is greater than the threshold pump power around 312.69 mW. The internal slope efficiency of Q-Switched lasers is around 7.2%. Similar to the average output power, both the peak power and pulse energy of Q-Switched lasers increase linearly with the increasing absorbed pump power greater than threshold power, from 0 W to 1.34 kW and from 0 μJ to 43.80 μJ respectively.

pulse duration of 2.5 μs , a peak to peak voltage of 65 V and a repetition rate of 0.2 kHz. The measured Q-Switched laser pulse and the corresponding control signal are shown in Fig. 6.9.

As shown in Fig. 6.9, the bipolar control signal is formed by two rectangular pulses with opposite polarities. In experiments, the amplitude and duration of two rectangular pulses are the same, 32.5 V and 2.5 μs respectively. To ensure the average voltage of the control signal is 0 V, the positive pulse is designed to be followed by a negative rectangular pulse

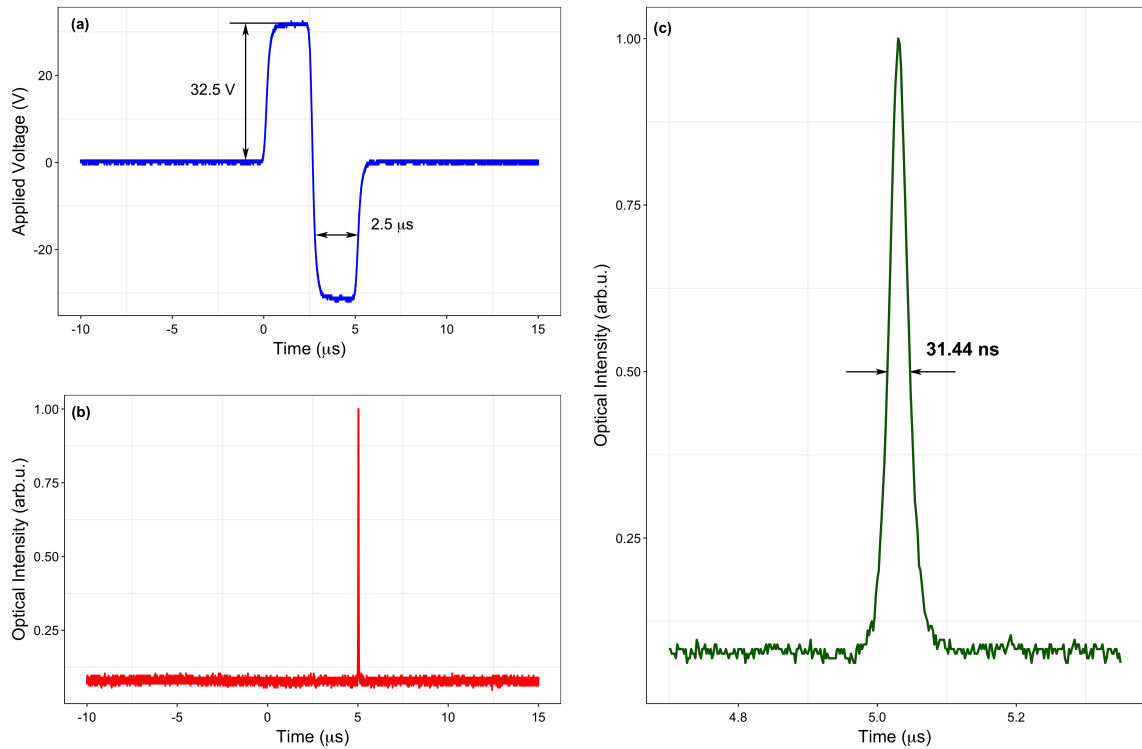


Fig. 6.9 (a) The applied electrical signal with a bipolar square waveform, (b) the oscilloscope trace of the Q-Switched laser pulse, and (c) the pulse shape of a single Q-switched laser pulse with a FWHM pulse width of 31.44 ns. The bipolar square waveform electrical signal consists of two parts, including a positive rectangular pulse with an amplitude of 32.5 V, followed by a negative rectangular pulse with an amplitude of - 32.5 V. The duration of two rectangular pulses is the same, which is around 2.5 μ s.

with the same amplitude and duration because non-zero average voltage potentially results in long-term damage on the liquid crystal modulator due to the ion migration. Therefore, the bipolar square-wave control signal not only can simplify the control voltage settings due to no required bias voltage but also can minimize the switch-off time of the liquid crystal modulator for avoiding multiple pulse problems as discussed in Chapter 3. Moreover, the duration of the rectangular pulse is set to be 2.5 μ s for the optimisation of output laser performance. In experiments, the effects of the pulse duration varying from 1 μ s to 4 μ s on the output laser performance are studied. When the pulse duration of the control signal increases from 1 μ s to 2.5 μ s, the pulse width of generated Q-Switched laser pulses decreases from 108 ns to 31.44 ns, because the control signal with a longer pulse duration can make the modulation depth

larger and the modulation or switching speed higher. However, when the pulse duration of the control signal increases further to $4 \mu\text{s}$, multiple output pulses are observed from the oscilloscope, because the switch-off time of the liquid crystal modulator is not short enough to prevent the laser output from multiple pulse problems. To ensure the single output laser pulse and optimal pulse characteristics, the pulse duration of the control signal is set to be $2.5 \mu\text{s}$. In Fig. 6.9 (b), the Q-Switched pulse appears after the liquid crystal modulator turned on. The time delay between when the modulator is switched on and when the Q-Switched laser pulse is detected is around $2 \mu\text{s}$. To measure the pulse width of output laser pulse precisely, a smaller time scale is used on the oscilloscope, and the shortest Q-Switched laser pulse is recorded with an FWHM pulse width of only 31.44 ns , as shown in Fig. 6.9 (c).

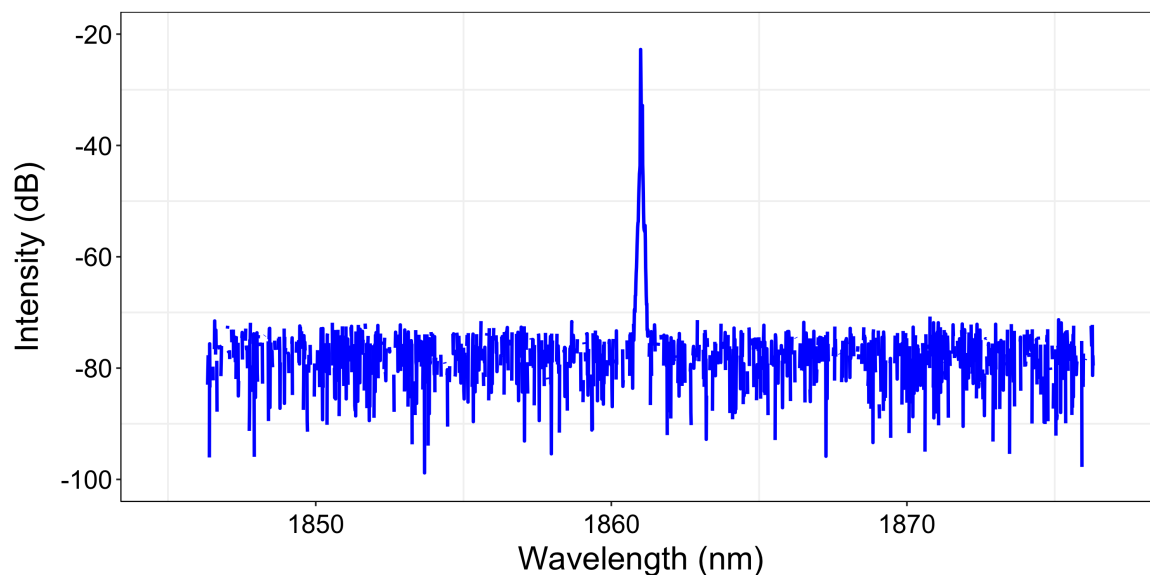


Fig. 6.10 The emission spectrum of output Q-Switched laser pulses with the center wavelength of 1861 nm and the FWHM spectral width smaller than 100 pm .

Besides the laser performance parameters discussed early, optical spectrum analysis plays a crucial role in the laser characteristics as well. In experiments, the output Q-Switched laser pulses are coupled into single-mode fibre (SMF) with a flat and clean surface cleaved by the FITEL S326A high precision optical fibre cleaver at one end and an FC UPC round connector at the other end. The connector of the SMF patch cord is connected to YOKOGAWA AQ6375B Long Wavelength Optical Spectrum Analyser (OSA) which supports a long-

wavelength measurement range from 1200 to 2400 nm, high sensitivity down to -70 dBm and high resolution to 0.050 nm. In experiments, the wavelength span of OSA is set to be 10 nm from 1852.59 nm to 1862.59 nm, and the measurement sensitivity of OSA is set to be HIGH 1/CHOP with the wavelength measurement resolution of 0.05 nm. From Fig. 6.10, the emission spectrum of output Q-Switched laser pulses is centered at 1861 nm with the FWHM spectral width less than 100 pm.

6.5 Four wave mixing phenomenon

As demonstrated in the previous section, the maximum peak power achieved in the experiments exceeded 1 kW at a relatively low repetition rate of 200 Hz. The generated high peak power Q-switched laser pulses illustrated the possibility of initiating nonlinear phenomena in nonlinear fibres. Unlike the SRS and stimulated Brillouin scattering (SBS), FWM is originated by the refractive index modulation and phase-matching condition [241]. The FWM is a kind of nonlinear effect, which is also called the third-order parametric process, because it is mainly dependant on the third-order susceptibility $\chi^{(3)}$ [242, 243]. In the four-wave mixing (FWM) process, the energy of two photons at different frequencies (or at the same frequency in the case of degenerate FWM) is transferred to new photons. This energy transfer can give rise to the generation of photons at new frequencies that are given by the laws of conservation of energy and momentum. Because the efficiency of the FWM process is highly dependant on the phase-matching condition, this process can occur only if the phase mismatching can be reduced to near zero. Therefore, the pump wavelength and optical properties of nonlinear fibre play a crucial role in obtaining the FWM effect.

Generally speaking, four frequency components can be observed in the output optical spectrum, when the FWM occurs due to a good phase-matching condition. If two pump beams at different frequencies of ω_1 and ω_2 are launched to a nonlinear fibre, two photons at two new frequencies of ω_3 and ω_4 can be created by the generated energy in the process. The law of conservation of energy illustrates the relation between the input and output wavelengths, ω_1 , ω_2 , ω_3 and ω_4 as

$$\omega_1 + \omega_2 = \omega_3 + \omega_4. \quad (6.1)$$

However, if there is only one pump wave launched to a nonlinear fibre, $\omega_1 = \omega_2$, the degenerate FWM will occur. As a result, three frequency components will be observed in the output optical spectrum. Therefore, the relation between the input and output wavelength can be simplified to be

$$2\omega_{pump} = \omega_{signal} + \omega_{idler}. \quad (6.2)$$

where ω_{pump} is the wavelength of the pump wave, ω_{signal} and ω_{idler} are wavelengths for signal and idler waves.

So far, the supercontinuum generation and FWM have been studied mainly based on the generation of ultrashort laser pulses with a pulse width of a few picoseconds or femtoseconds from the mode-locked fibre lasers [244, 245]. Generally, the widely used nonlinear media for the supercontinuum generation include PCFs [246–248], fluoride fibres [78, 249, 250], tapered chalcogenide fibres [40, 251–253] and a variety of waveguides [254–256]. Instead of using ultrashort laser pulses, the supercontinuum generation and FWM phenomena are observed and studied by using Q-switched pulses with the sub-nanosecond pulse width in 2002 [52] and 2004 [53]. In their works, the PCFs are used as the nonlinear medium to provide the required nonlinearity for experiments.

In our work, the required nonlinearity is provided by a tapered chalcogenide fibre developed in the Department of Electrical and Computer Engineering, McGill University, Montréal, Canada. Compared with the normal step-index fibre, the tapered chalcogenide fibres can be designed to shift the zero-dispersion wavelength (ZDW) λ_0 to the operating wavelengths of output lasers, so it can provide great flexibility on the pump wavelength. Moreover, because the tapered fibres with As_2Se_3 chalcogenide wires can have a larger nonlinear index coefficient, $n_2 = 1.1 \times 10^{-17} \text{ m}^2/\text{W}$ and higher nonlinear parameter, $\gamma = 176 \text{ W}^{-1}\text{m}^{-1}$, than As_2S_3 fibres and highly nonlinear silica fibre [257]. The As_2Se_3 chalcogenide fibres illustrate the possibility of achieving the supercontinuum generation at a

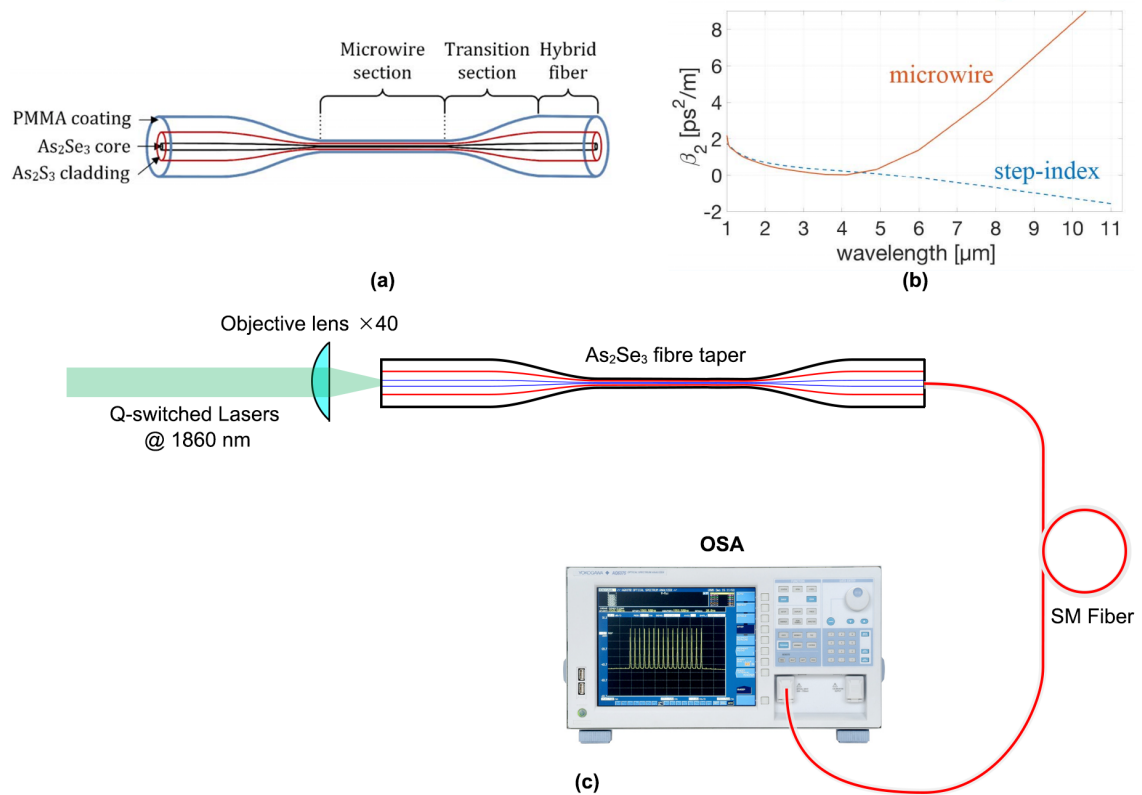


Fig. 6.11 (a) A As_2Se_3 fibre taper is consisted of a 5 cm long microwire section, a 1.6 cm long transition section and a 1 cm long hybrid or untapered section. From the untapered section to microwire section, the As_2Se_3 core diameter gradually decreases from 14 μm to 3 μm . (b) The measured dispersion parameter β_2 for both microwave and step-index (untapered) sections. (c) Schematic of experimental setup for the nonlinearity study of Q-switched lasers at 1860 nm. (a) and (b) are reproduced from Darren D. Hudson [40].

lower peak power than other fibres. The structure of the As_2Se_3 fibre taper, the measured dispersion parameter β_2 as a function of wavelength for both microwave and step-index (untapered) sections and experimental setup are shown in Fig. 6.11. As shown in the figure, the fibre taper can be divided into three sections, namely microwire, transition, and hybrid or untapered sections. The core diameter is around 14 μm in the untapered section and then it is narrowed down to 3 μm in the middle. Because of the large core diameter at the two ends of the fibre taper, the pump light can be coupled into the fibre taper with reduced difficulty and high coupling efficiency. According to the dispersion measurements over the wavelength ranging from 1 μm to 11 μm , the ZDW λ_0 of the fibre taper is around 2.8 μm , and it can be

controlled by changing the core diameter in the microwire section. Because the emission wavelength of output Q-switched lasers is smaller than the ZDW λ_0 of the fibre taper ($1.86 \mu\text{m} < 2.8 \mu\text{m}$), it will make the pump wavelength to be at the normal dispersion regime and give rise to the FWM. In the experiment, the Q-switched laser pulses from a liquid crystal modulator as Fig. 6.9 are coupled into a fibre taper using a microscope lens with a microscope objective with a magnification of 40 times. The output end of the fibre taper is butt coupled into a SMF which is connected to the input connector of OSA. Because of the unavoidable transmission loss of microscope objective, Fresnel reflections at the end of the fibre taper and SMF and extra loss caused by the defective fibre cleaves, the coupling efficiency of the Q-switched pump lasers to the fibre taper is around 40 %. When the peak power of Q-switched lasers is increased to around 1 kW with a pulse width of 34 ns, the coupled peak power is around 400 W and the resulted optical spectrum is measured and shown in Fig. 6.12. It is clear that photons at new frequencies can be created within the high nonlinearity As_2Se_3 chalcogenide fibre taper by the Q-switched laser pulses with a high peak power of 400 W and a long pulse width of 34 ns. The observation indicates the degenerate FWM process in a As_2Se_3 chalcogenide tapered fibre. This preliminary experiment illustrates the possibility of utilising the actively Q-switched lasers generated from a Tm^{3+} :ZBLAN waveguide chip and liquid crystal modulators in a variety of nonlinear optics and relevant applications.

6.6 Summary

In this section, we demonstrated an eye-safe Q-Switched laser source operating in the near-IR region around 1.86 μm using a liquid crystal modulator, which can be potentially used in a variety of applications, such as trace gas spectroscopy, eye-safe range-finding, and coherent LIDAR. In our experiments, the stable Q-Switched laser emission is observed over a wide range of peak-to-peak voltage of applied electrical signals from 10 V to 65 V, repetition rate from 200 Hz up to 30 kHz, and absorbed pump power from 250 mW to 433 mW. The laser performance parameters, such as pulse width, peak power, output power, and pulse

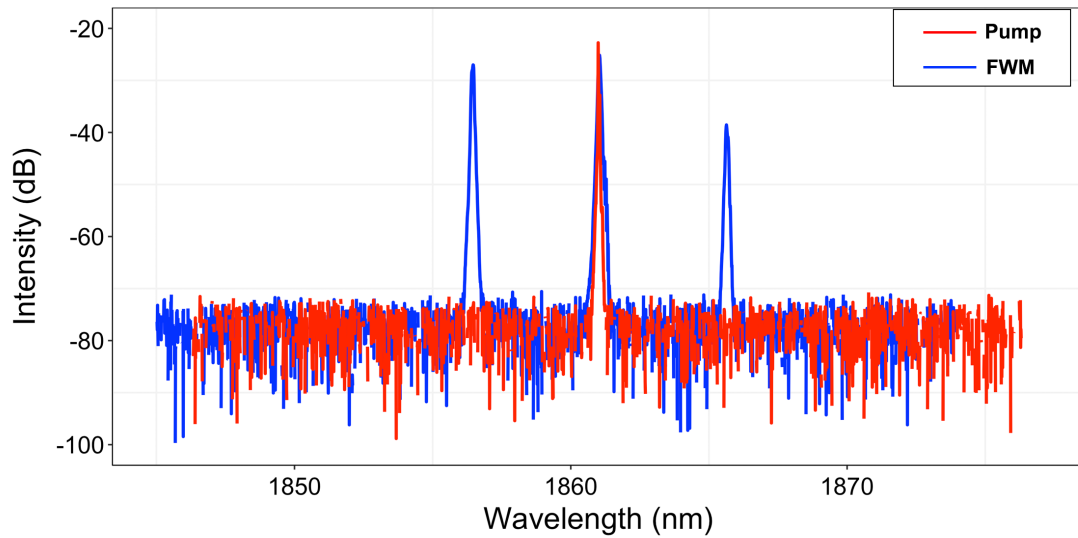


Fig. 6.12 Measured output optical spectrum (blue) for a As_2Se_3 chalcogenide tapered fibre and input spectrum of the pump Q-switched lasers (red). The coupled peak power of Q-switched lasers are 400 W and the pulse width is around 34 ns. The optical spectrum is measured at the maximum measurement sensitivity with a wavelength resolution of 0.05 nm.

energy are measured and compared under different peak-to-peak voltages, repetition rates, and absorbed pump powers to find out their effects on the Q-Switched laser performance. The preliminary experimental results illustrate that Q-switched laser pulses with the shortest pulse width around 31 ns and highest peak power around 1.3 kW are obtained via applying a periodical bipolar rectangular waveform electrical signal on the liquid crystal modulator with a rectangular pulse duration of 2.5 μs , a peak to peak voltage of 65 V and a repetition rate of 0.2 kHz when the absorbed pump power is 433 mW, which is the maximal absorbed pump power from two pump laser diodes. The presented experimental results indicate that the liquid crystal modulator can be used as an alternative optical modulator in Q-Switched lasers other than AOMs and EOMs. Additionally, the generated Q-Switched laser pulses with a peak power greater than 1 kW and a pulse duration less than 50 ns can potentially be used to observe nonlinear effects in nonlinear fibres (microwire or chalcogenide fibre), such as FWM and spectral broadening, in the near future. The study on nonlinear effects caused by the generated Q-Switched laser pulses is still in progress.

Chapter 7

All-in-one fibre lasers operating at 1.55 μm

7.1 Relevant publications

The experimental results of an all-in-one mode-locked laser based on a liquid crystal transducer have been presented in a conference paper entitled "All-in-one fiber laser based on a liquid crystal transducer" and a journal article on IEEE Photonics Technology letter in 2019 [229].

1. **Xinyue Lei**, Christoph Wieschendorf, Josiah Firth and François Ladouceur and Leonardo Silvestri and Alex Fuerbach, "All-in-one fiber laser based on a liquid crystal transducer," IEEE Photonics Technology Letters, vol. 31, no. 17, pp. 1409-1412, 2019.
2. **Xinyue Lei**, Christoph Wieschendorf, Alex Fuerbach, François Ladouceur, and Leonardo Silvestri, "All-in-one fiber laser based on liquid crystal transducer," in Advanced Photonics 2018 (BGPP, IPR, NP, NOMA, Sensors, Networks, SPCom, SOF), OSA Technical Digest (online) (Optical Society of America, 2018), paper ITh4H.3.

7.2 Introduction

In this chapter, we now present a comprehensive study and show that the liquid crystal cell can not only be used as an active Q-switch in a waveguide laser resonator but that the modulator can also be utilised for the generation of CW radiation as well as AM and FM mode-locked laser pulses from the same linear fibre laser resonator. Using a liquid crystal transducer cell terminated by a high-reflecting mirror, the desired mode of operation can be selected by simply changing the electric signal that is applied to this modulator device, thus transforming the fibre laser into a highly versatile and universal light source.

7.3 Experimental setup

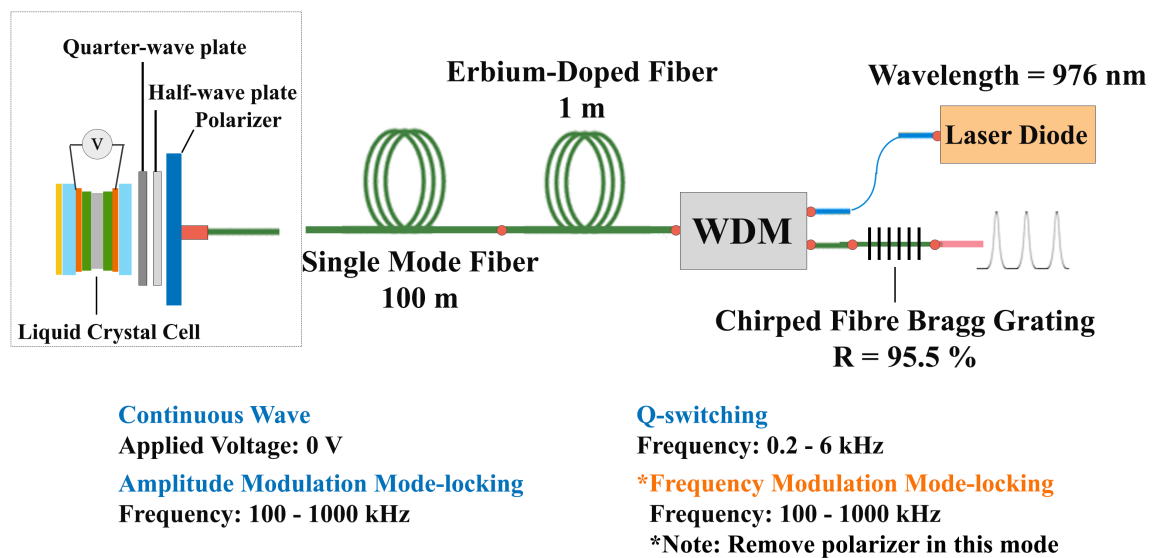


Fig. 7.1 Schematic of all-in-one fibre lasers based on a liquid crystal transducer.

The experimental setup of the liquid crystal transducer-based all-in-one fibre laser is shown in Fig. 7.1. In the Fabry-Perot-type cavity, a 1-m-long erbium-doped fibre (LIEKKI Er80-8/125) with a peak core absorption of 80.0 ± 8.0 dB/m at 1530 nm is used as the gain medium. It is pumped by a fibre-coupled laser diode with a center wavelength of 976 nm. The maximum pump power coupled into the active fibre is 82.5 mW. The erbium-doped fibre

is spliced on one side to a 100 m/200m/300m/400m/500m long non-zero dispersion-shifted fibre (Thorlabs DCF4) with a dispersion of $-4.0 \text{ ps/nm}\cdot\text{km}$ at 1550 nm while the other side is spliced to a pump coupler, WDM in this case. The passive fibre is used to increase the cavity length and thus to decrease the frequency spacing of the longitudinal resonator modes without adding excessive amounts of dispersion. The other side of the dispersion-shifted fibre is spliced to a gradient index (GRIN) lens to collimate the light beam and thus to realize a short free space section within the cavity. The liquid crystal cell, a half-wave and a quarter-wave plate as well as a linear polarizer are placed in this free space section which is finally terminated by a high-reflecting silver mirror. As explained in more detail in previous sections, rotating the half-wave plate is equivalent to rotating the liquid crystal cell. The quarter-wave plate is included in this setup to optimise the modulation depth, however, this could also be achieved by fine-tuning the thickness of the liquid crystal layer. In the future, the free-space section could thus be avoided by coating a specifically designed cell assembly (without waveplates) directly onto the fibre end facet which would greatly reduce the optical losses. It is worth noting that this chapter aims to demonstrate this new method, and not to optimise the performance of the laser system. Finally, the reflected port of the WDM is spliced to a fibre Bragg grating (FBG), which is used as an output coupler with a measured reflectivity of 95.5 % at 1551.2 nm and a bandwidth of about 2 nm as shown in Fig. 7.2. The FBG is directly written via the line-by-line inscription method [258]. The laser output is monitored by a 1.2 GHz InGaAs FC/PC-Coupled Photodetector (Thorlabs DET01CFC) and a 200 MHz digital oscilloscope with a maximum sampling rate of 4 GSa/s (Agilent InfiniiVision DSO-X 3034A).

The deformed-helix ferroelectric (DHF) liquid crystal (LC) cell used throughout these experiments has been described in great detail in previous sections and is commercially available for use in distributed sensing networks from Zedelef, Australia (TRP-0001). The measured optical losses that are introduced by a 5 μm thick liquid crystal cell as a function of the applied voltage are shown in Fig. 7.3 (a). Note that this does not include any constant background losses (e.g. absorption or scattering) but only shows the losses that are controlled by the applied voltage, i.e., that is caused by a change in the polarization state of the optical

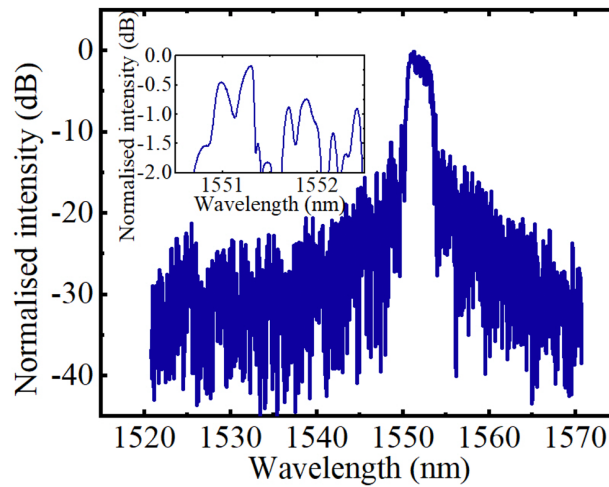


Fig. 7.2 Measured reflection of the laser-inscribed chirped-fibre Bragg grating used in this research. Inscription method used is line-by-line [258].

signal upon propagation from the polarizer to the silver mirror and back to the polarizer. The experimental results are fitted by the expression that can be derived for optimised parallel reflectance, $R_{\parallel} = 1 - R_{\perp}$ in [229]. In this experiment, a sinusoidal electrical signal with a frequency of 1 kHz and a peak-to-peak voltage of 18 V is applied to the liquid crystal cell. The frequency is chosen to be low enough so that any dynamic delay of the response of the liquid crystal cell to the applied signal could be neglected. As can be seen, under low-frequency electric signals with a peak-to-peak voltage of 18 V, the controlled optical loss can oscillate between 3 % and 98 %, i.e., the modulation depth is 95 %. Additionally, we measured the modulation depth at a higher peak-to-peak voltage of 60 V and higher frequencies over 100 kHz and compared the results with the predictions of the numerical model that is introduced in [229]. Fig. 7.3 (b) shows that the measured modulation depths of the liquid crystal cell are 29.7 %, 22.7 %, 17.9 %, 11.4 % and 5.9 % at repetition rates of 198.08 kHz, 247.08 kHz, 325.87 kHz, 480.45 kHz and 913.90 kHz, respectively, and that the simulation results are in excellent agreement with the experimental results. The figure also shows that applying electric signals with increasingly higher amplitudes can partially compensate for the reduction in modulation depth at high frequencies. It is worth noting that the voltage amplitude of 30 V ($V_{pp} = 60$ V) is not close to the breakdown voltage of the cell,

but is the maximum voltage of the driver electronics used. Although the modulation depth is greatly reduced at higher frequencies, the cell is still capable of introducing a significant loss modulation at frequencies approaching 1 MHz, showing the potential of using a liquid crystal cell as an active modulator in a mode-locked laser cavity. In the following sections, the different operation modes of the all-in-one laser will be discussed in detail.

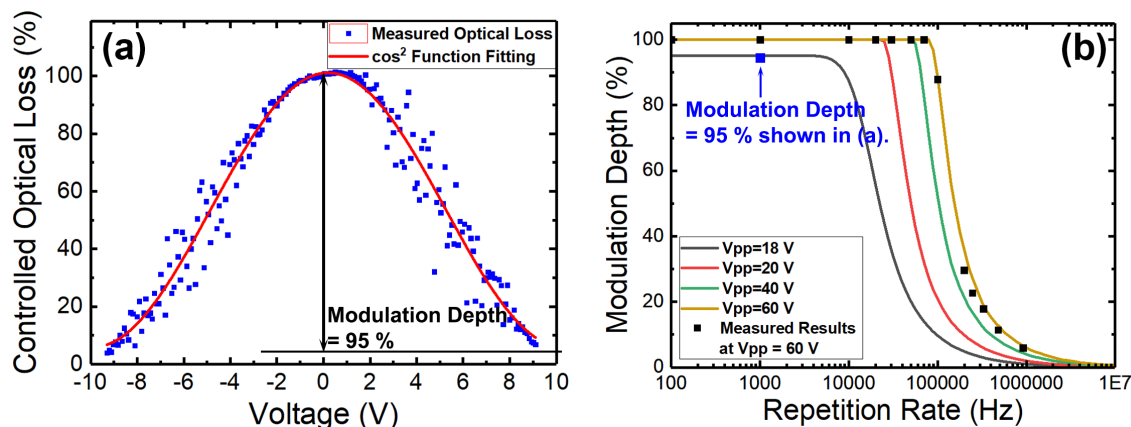


Fig. 7.3 (a) Measured optical loss as a function of applied voltages to a 5 μm thick liquid crystal cell at low modulation frequency (1 kHz, quasi-DC). Measurement points (blue squares) are fitted by a \cos^2 function (red line). (b) Measured (black squares) and numerically simulated (lines) modulation depth as a function of the repetition rate for electric signals with varying amplitudes.

7.4 Continuous-wave mode

If no electric signal is applied to the liquid crystal cell, the laser operates in CW mode. Fig. 7.4 shows the measured average output power as a function of pump power. As can be seen, the pump threshold is 28 mW and the slope efficiency is 3.0%. As mentioned before, the liquid crystal modulator used throughout this chapter is an off-the-shelf transducer cell for sensing applications that is optimised for maximum linearity and sensitivity, but not for maximum modulation and low losses. By customizing the thickness of the liquid crystal layer and by using Index Matched ITO (IMITO) as the electrode material, the background losses could be reduced substantially, and the slope efficiency could be increased accordingly.

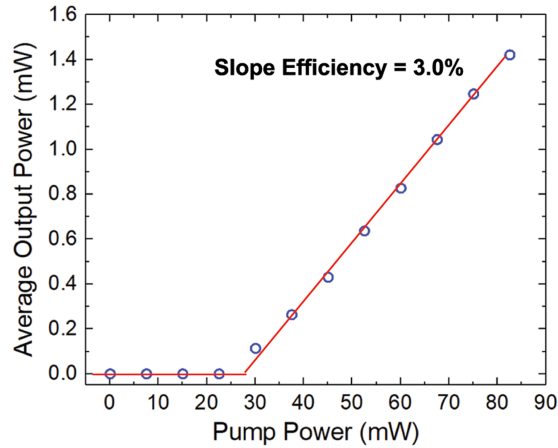


Fig. 7.4 The measured average output power as a function of the pump power.

7.5 Q-switching mode

When using the liquid crystal as an amplitude modulator of Q-Switch or active amplitude mode-lock, a polariser must be added to the beam path, as shown in Fig. 7.1. The polariser defined the polarization state of the whole system. The advantage of using the liquid crystal as an amplitude modulator rather than a phase modulator is that it enables switching between mode-locked, Q-switch, and CW operation by simply changing the frequency and waveforms of applied electrical signals. For Q-switching, the repetition rate of the applied voltage waveform is spanning from 0.2 kHz to 6 kHz. To find out the optimal configuration of the designed fibre laser cavity, the impacts of multiple factors on the Q-Switched laser performance have been investigated individually in the following subsections, including duty cycles, repetition rate, the voltage amplitude of driven signals, and the cavity length as well.

7.5.1 Q-switched Laser Performance v.s. Cavity Length

To investigate the impacts of cavity length on the Q-Switched lasers, a 100 m/200 m/300 m/400 m/500 m long non-zero dispersion-shifted fibre (Thorlabs DCF4) is selected and spliced between liquid crystal modulator and Erbium-Doped fibre. In experiments, the liquid crystal modulator is modulated by the square-wave signals with the same repetition rate of 5

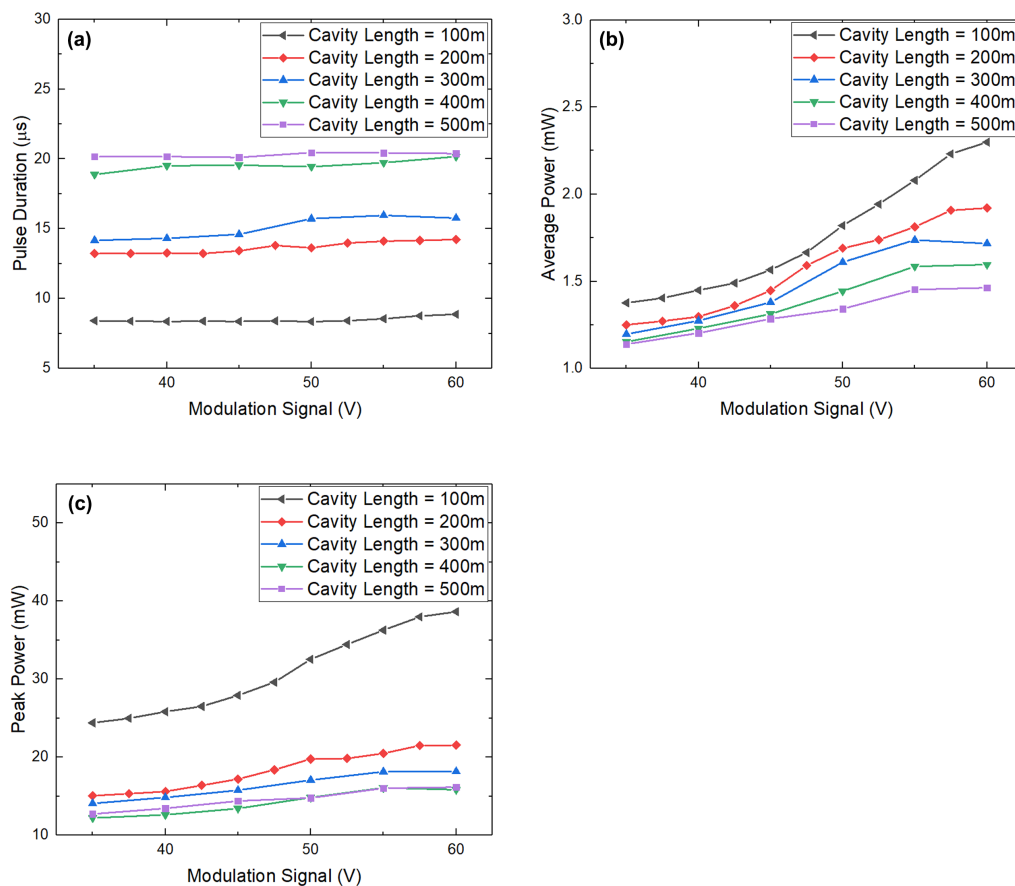


Fig. 7.5 Measured (a) pulsed duration, (b) average output power and (c) peak power as a function of peak to peak voltage of applied signal with 5 kHz repetition rate and 20 % duty cycle for the Q-Switched fibre laser with different cavity lengths (length of passive fibre in the cavity).

kHz and the same duty cycle of 20 %. To compare laser performances achieved by various cavity lengths ranging from 100 m to 500 m, pulse width, average output power, and peak power are measured, calculated, and shown as a function of peak to peak voltage of applied signal in Fig. 7.5.

Based on the pulse duration shown in Fig. 7.5 (a), it is worth noting that with the same repetition rate and voltage amplitude, a shorter fibre cavity resulted in a shorter Q-Switched laser pulse. When the length of non-zero dispersion-shifted fibre (Thorlabs DCF4) spliced in the cavity decreases from 500 m to 100 m, the measured pulse duration is reduced from

20 μs to 8 μs . In Fig. 7.5 (b) and (c), we can see that, no matter how long the fibre cavity is, both average output power and peak power increase with the increasing amplitude of the applied voltage linearly at the beginning and starts to approach the saturation point, because the increasing applied voltage amplitude gives rise to a larger modulation depth, heightens the switching speed and thus maximizes the average output power and peak power. Also, note that the saturation point mentioned here is related to the critical electric field of the liquid crystal modulator discussed in Chapters 3 and 4. If the signal with the same amplitude of 60 V and duty cycle of 20 % is applied to the liquid crystal modulator, the average output power increases from 1.4 mW to 2.3 mW, when the length of passive fibre decreases from 500 m to 100 m. Moreover, the peak power of Q-Switched lasers generated from the shortest cavity is around 40 mW, which is also higher than that of other cavities (< 20 mW). Based on the comparison of Q-Switched lasers between different cavity lengths, we conclude that the shortest passive fibre (100 m) should be spiced into the fibre cavity because it can lead to shorter pulse duration, higher average output power, and higher peak power than other options. This is worth noting that although a passive fibre shorter than 100 m theoretically can optimise the performance of Q-Switch operation further, the shorter cavity length will make it very difficult for the same setup to switch the operation mode from Q-Switching to AM mode-locking. It is because the maximum repetition rate of the liquid crystal modulator is around 1 MHz. To achieve the AM mode-locking, the cavity length should not be shorter than 100 m, which will be discussed in detail in the following subsections.

7.5.2 Q-switched Laser Performance v.s. Duty Cycle

For actively Q-switched lasers, repetition rate and pump power are two important parameters which in most cases can affect the performance of lasers, including pulse width, output power, peak power and single pulse energy. In addition to the repetition rate and pump power, the duty cycle of applied square-wave signals is another crucial factor which has a significant impact on the output laser performance. In this section, I will discuss two cases. In experiments, two different square-wave signals are applied to the same liquid crystal modulator, namely signal A and signal B. Both signal A and signal B are modulated at the

frequency of 800 Hz. However, the duty cycle of signal A is 20 %, while the duty cycle of signal B is 50 %. In this experiment, the non-zero dispersion-shifted fibre (Thorlabs DCF4) spliced in the fibre laser cavity is 100 m long. The measured Q-switched laser pulses driven by signal A and signal B are presented in Fig. 7.6 (a) and (b) respectively.

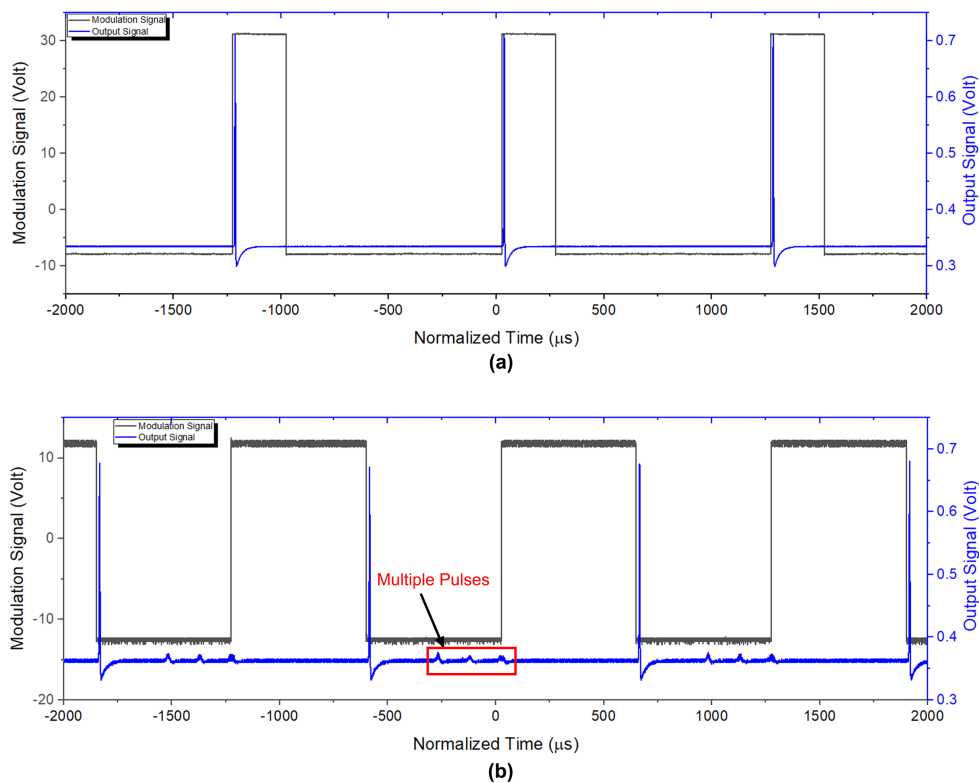


Fig. 7.6 Q-switched laser pulses driven by (a) square-wave signal with the 20 % duty cycle (signal A) and (b) square-wave signal with the 50 % duty cycle (signal B).

From Fig 7.6, it is clear that, at the low frequency or repetition rate (e.g. 800 Hz), the square-wave signal with the 50 % duty cycle resulted in multiple pulses. With the presence of second and third laser pulse in the output, the peak power of the first (biggest) laser pulse is reduced, because the partial output laser energy is allocated to the second, third, and even fourth laser pulse. As discussed in Chapter 5 and shown in Fig. 5.8 (c), shortening the duty cycle not only can enable the single pulse operation but also can allow a high voltage beyond the damage threshold to be applied to the liquid crystal modulator without any damage. It is because the switch-on time of applied signal ($>$ damage threshold) with a small duty cycle is

short, the effective electric field on the liquid crystal modulator will not exceed the damage threshold. Additionally, increasing the applied voltage amplitude improves the modulation depth, heightens the switching speed, and thus maximizes the peak power. With a short duty cycle presented in Fig. 7.6 (a), although the applied voltage amplitude is larger than Fig. 7.6 (a), the single pulse operation is still maintained, and the peak power is also higher. To conclude, the duty cycle of 20 % is better than the 50 % duty cycle in terms of the pulse duration, peak power, and pulse energy as well. Therefore, the duty cycle of 20 % is selected for the optimal configuration of the Q-switching operation mode.

7.5.3 Optimised Configuration of Q-Switch Mode

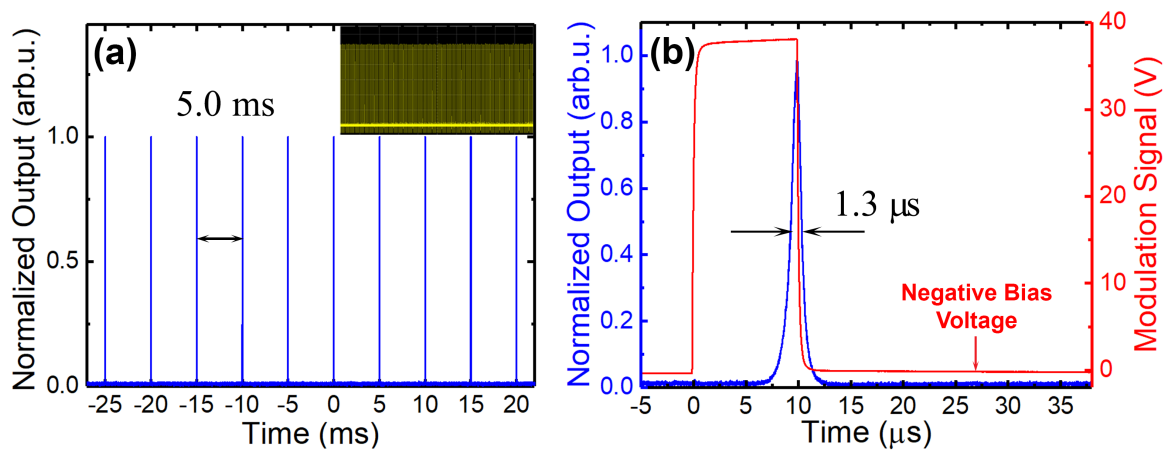


Fig. 7.7 (a) Measured oscilloscope trace of the Q-Switched laser pulses at a repetition rate of 0.2 kHz and (b) a single generated Q-Switched laser pulse with a pulse duration of 1.3 μs .

When the liquid crystal cell is modulated by square-waveform electric signals with the optimal voltage amplitude and duty cycle, actively Q-Switched laser pulses can be optimised as demonstrated in Fig. 7.7. In these experiments, we varied the repetition rate of the applied electric signal from 0.2 kHz to 6 kHz, while the peak-to-peak voltage is kept constant at 40 V and the temporal duration of the applied electrical pulses is fixed at 10 μs to avoid the generation of multiple pulses. A small negative bias voltage is used to keep the average voltage to zero for avoiding potential long-term damage due to ion migration. Fig. 7.7 (a) shows the generated pulse train at a frequency of 0.2 kHz which exhibits excellent pulse-

to-pulse stability with a pulse-to-pulse fluctuation less than 1 %. In Fig. 7.7 (b), a single Q-switched laser pulse with a duration of 1.3 μs is shown.

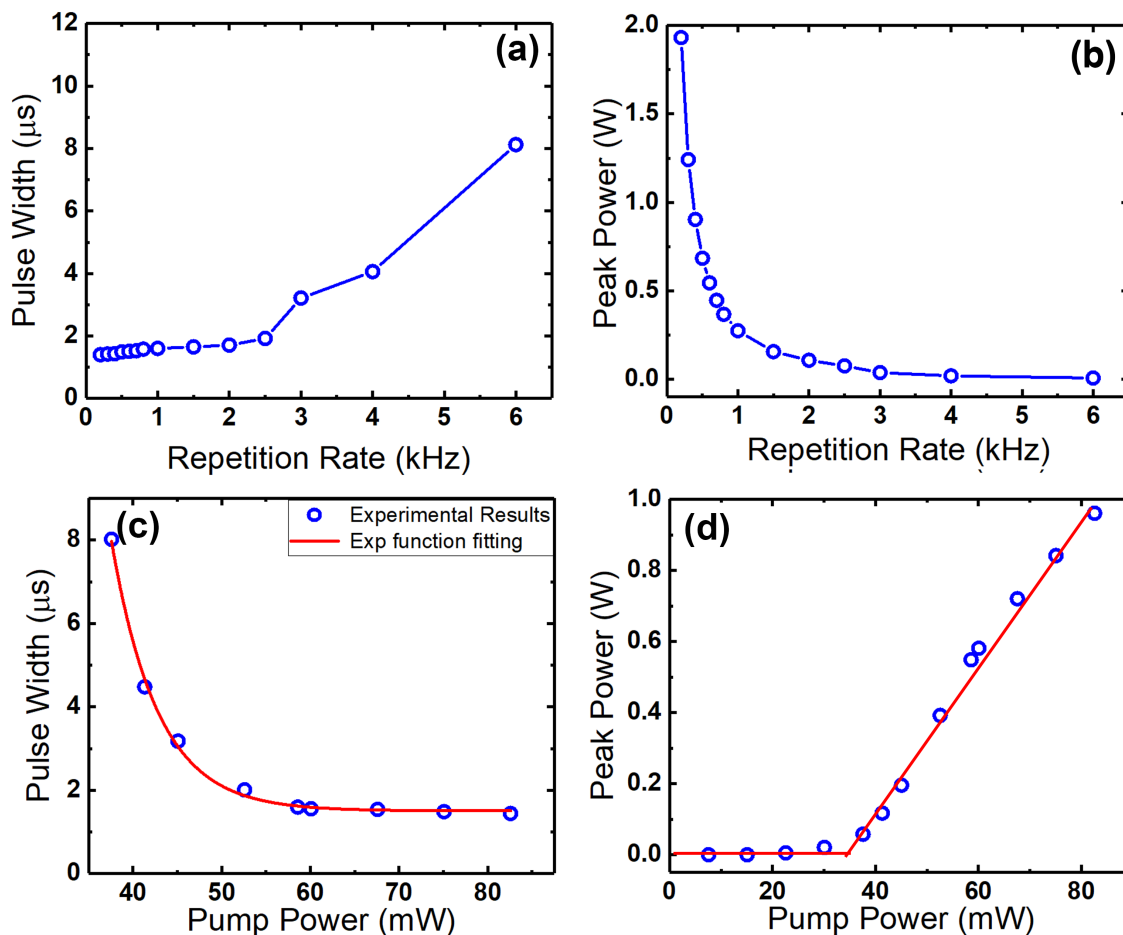


Fig. 7.8 (a) Measured pulse width; (b) measured peak power of the generated Q-Switched laser pulses as a function of repetition rate; (c) measured pulse width and (d) measured peak power of the generated Q-Switched laser pulses as a function of absorbed pump power.

We also change the repetition rate of the modulator and the pump power separately to investigate their impacts on the pulse duration and peak power of the generated Q-Switched laser pulses. In the experiment of the repetition rate, the pump power, the peak-to-peak voltage, and the electric signal duration are fixed at 82.5 mW, 40 V, and 10 μs , respectively. The pulse width and the peak power of Q-Switched laser pulses as a function of repetition rate are shown in Fig.7.8 (a) and (b). The pulse width decreases slightly from 1.92 μs to 1.33 μs , while the corresponding peak power increases significantly with decreased repetition rates.

At the repetition rate of 200 Hz, Q-Switched laser pulses with the maximum pulse energy of 2.7 μJ and peak power of 1.93 W are obtained. In the experiment of the pump power, the pulse width and peak power of Q-Switched laser pulses are measured at a repetition rate of 400 Hz, a constant electrical pulse duration of 10 μs and a constant peak-to-peak voltage of 40 V. Fig. 7.8 (c) shows that the measured pulse width of Q-Switched laser pulses decreases with the increasing pump power, while Fig. 7.8 (d) shows that the output peak power increases linearly with the increasing pump power once the pump power is above the threshold pump power of 35 mW. The maximum output peak power is almost 1 W achieved at the maximum pump power of 82.5 mW.

7.6 Amplitude Modulation Mode-Locking Mode

There are two distinct approaches to mode-locked operation, namely passive and active. In the present work, an actively controlled liquid crystal modulator is used to generate both AM and FM mode-locked fibre lasers, and thus only the theory behind this particular area is discussed here. For active mode-locking, either an amplitude modulator or a frequency modulator can be placed inside the cavity. Driving them precisely with the same frequency as the mode spacing of the axial modes, these modulators can generate a train of mode-locked pulses with a repetition rate that equals the axial mode spacing. In the following section, the different mechanism of AM and FM are described.

7.6.1 Fundamentals of Amplitude Modulation Mode-Locking

To explain the AM mode-locking behaviour, the pulse propagation through an amplitude modulator should be analysed. The time-varying transmission function for a simple amplitude modulator can be written in the form as

$$L(t)_{AM} = \exp[-\Delta_m(1 - \cos \omega_m t)] \quad (7.1)$$

where ω_m is the modulation frequency of the amplitude modulator, and the quantity $2\Delta\Omega$ is the peak-to-peak modulation index.

In our research, the designed setup shown in Fig. 7.1 is an optical Fabry–Pérot resonator formed of two mirrors, in which the axial modes in frequency domain are separated by $\Delta\Omega = \frac{2\pi}{t_r}$. t_r is the round trip time in the resonator, which can be expressed as $t_r = \frac{2n_{\text{eff}}L}{c}$, where n_{eff} is the effective refractive index of a specific medium, L is the cavity length from one mirror to the other mirror and c is the speed of light in vacuum. As a result, the spacing between axial modes can be expressed by $\Delta\Omega = \frac{c\pi}{n_{\text{eff}}L}$. Here, we assume that an amplitude (AM) modulator is placed inside an optical Fabry–Pérot laser cavity. When the modulator is driven at the modulation frequency ω_M , the modulator introduces side-bands of every mode in the frequency domain as shown in Fig. 7.9 (a). From the figure, we can see that each mode competes for gain with adjacent modes. If the repetition rate of the optical modulator ω_M equals or is very close to the spacing of adjacent axial-modes $\omega_M = \Delta\Omega = \frac{c\pi}{n_{\text{eff}}L}$, or one of its integer multiples $\omega_M = m \times \Delta\Omega = m \times \frac{c\pi}{n_{\text{eff}}L}$, then, the modulation sidebands introduced by the modulator from each axial mode, $\omega_0 \pm m \times \omega_M$ for $m = 1, 2, 3$, will overlap with or be very close to, another axial mode in the cavity, $\omega_0 \pm m \times \Delta\Omega$ for $m = 1, 2, 3$, because $\omega_M = \Delta\Omega$. As a result, each side-band will then tend to "injection lock" the axial mode. Therefore, the modulator in the cavity will tend to couple together, or lock each axial mode to one or other adjacent modes. In other words, many frequencies ("modes") oscillate simultaneously in a laser, and when their phases are locked, an ultrashort pulse occurs. According to the time domain of mode-locking behavior shown in Fig. 7.9, laser begins to oscillate in the form of a short pulse and the passage of short pulse through the modulator will be centered at those peaks of the modulator transmission function, $t = \frac{2m\pi}{\omega_M} = \frac{2n_{\text{eff}}mL}{c}$.

Theoretically, the required modulation frequency to initiate active amplitude (AM) mode-locking can be calculated from the cavity length [240] by

$$f_{\text{mod}}^{\text{AM}} = f_{\text{spacing}} = \frac{c}{2n_{\text{eff}}L_{\text{cavity}}} \quad (7.2)$$

Based on the dynamic optical response of the liquid crystal cell to applied electrical signals shown in Fig. 7.3, the device should be capable of generating mode-locked laser

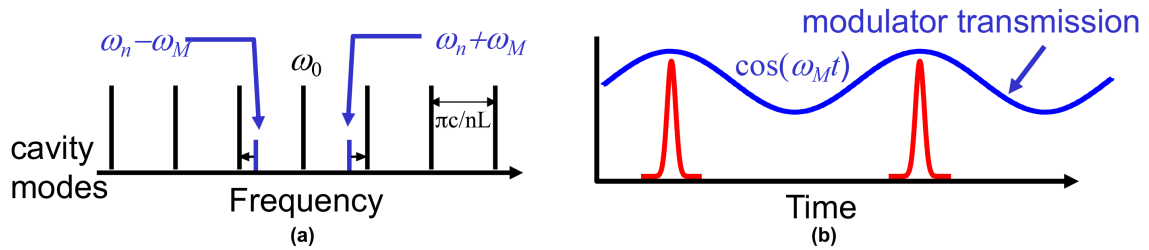


Fig. 7.9 (a) Frequency domain and (b) time domain of active mode-locking.

pulses in laser cavities longer than 100 m ($f_{\text{mod}} < 1$ MHz), because an active loss modulation can still be achieved at these frequencies. Therefore, the total length of the fibre laser cavity is increased by adding a dispersion-shifted fibre around 100 m.

7.6.2 Indication of AM Mode-Locking

Practically, mode-locking can be confirmed in both time domain and frequency domain. In the time domain, only if the modulation frequency ω_M is equal or very close to the axial-mode spacing $\Delta\Omega$ or one of its integer multiples, a stable train of periodic mode-locked laser pulses can be observed using a high-speed photodetector or autocorrelation. In order to precisely tune the modulation frequency to be as same as the axial mode spacing, pulse duration, average output power, peak power and output pulse energy are measured at varying modulation frequencies from 248.28 to 249.88 kHz. Note that, in Fig. 7.10, the cavity length is approximately 412.8 m with a 400 m long passive fibre. It is clear that, the background-free mode-locked laser pulses have the shortest pulse duration and highest peak power only at the modulation frequency of 249.08 kHz. When the modulation frequency is detuned by a small value, e.g. 0.2 kHz, the peak power of output laser pulses reduced significantly from 20 mW to 12 mW. The obvious degradation occurring in both pulse duration and peak power implies the presence of mode-locking at the modulation frequency of 249.08 kHz for the 412.8 m long fibre cavity.

In addition to the time domain measurements, frequency spectrum measurement is another approach to confirm the occurrence of mode-locking. Based on the experimental setup shown in Fig. 7.1, the total laser cavity length is approximately 106 m and the corresponding axial

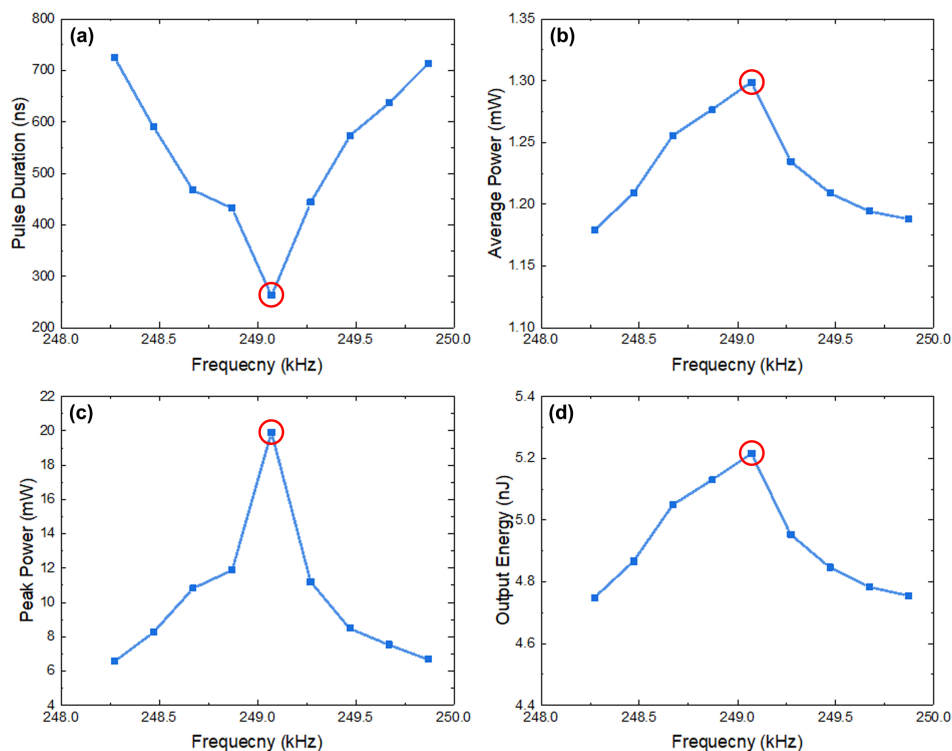


Fig. 7.10 (a) Pulse duration, (b) average output power, (c) peak power and (d) pulse energy as a function of modulation frequency.

mode spacing is 944.5 kHz. In experiments, a square-waveform modulation function with a duty cycle of 50 % is used with a modulation frequency of 944.5 kHz. Because the duration of a half-cycle is only 0.53 μs , the peak-to-peak voltage is increased further to 60 V to improve the modulation depth. At this frequency, the modulation depth is around 5.9 % as shown in Fig. 7.3 (b). In experiments, the radio frequency (RF) spectrum is measured and analysed in the range from 0 MHz to 7 MHz. Note that, in Fig. 7.10, the cavity length is approximately 106 m with a 100 m long passive fibre spliced into the cavity. The highest peak of the radio frequency (RF) spectrum is located at the axial mode spacing of 944.5 kHz, which is corresponding to a cavity length of 106 m. The magnitude difference between the fundamental peak and the first harmonic is 2 dB in Fig. 7.11 (a), which means most axial modes are coupled and phase-locked efficiently. For the fundamental peak at 944.5 kHz, the magnitude is 80 dB above the noise floor, which indicates a good SNR and stable

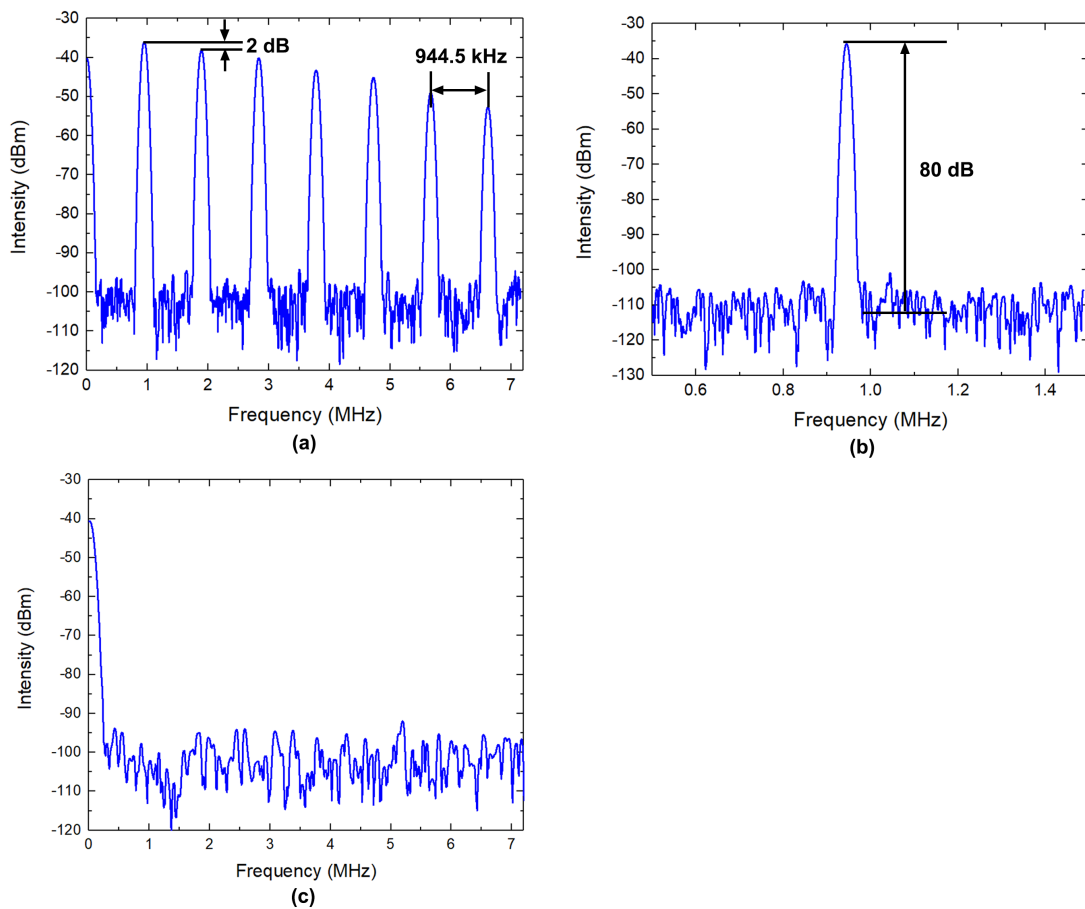


Fig. 7.11 (RF spectrum of the mode-locked lasers for a Fabry–Pérot fibre resonator with a cavity length of 106 m. (a) The measured spacing of axial modes is around 944.5 kHz and the magnitude difference between the fundamental peak and the first harmonic is 2 dB, which indicates a stable mode-locking. (b) The close-up view of the fundamental peak shows a SNR of as high as 80 dB, indicating stable mode-locking. (c) When the operation mode is switched to continuous wave by turning off the modulation signals applied to the liquid crystal modulator, the peaks in the RF spectrum drop by more than 60 dB. Mode-locked operation features strong and distinct harmonics of the laser repetition rate compared to the continuous wave laser.

mode-locking, as shown in Fig. 7.11 (b). When the operation mode is switched to continuous wave by turning off the modulation signals applied to the liquid crystal modulator, the peaks in the RF spectrum drop by more than 60 dB, as illustrated in Fig. 7.11(c).

7.6.3 AM Mode-Locking Performance v.s. Modulation Signal

As discussed in previous sections, increasing the voltage amplitude of the applied signal can result in a larger modulation depth, higher switching speed, and then improves the output energy and peak power of either mode-locked or Q-switched lasers. In this section, both cavity length and voltage amplitude will be taken into consideration with regard to the performance of AM mode-locked lasers, including the pulse duration, average output power, peak power, and pulse energy. With the various cavity lengths, e.g. 106 m/206 m/306 m/412 m/506 m, the corresponding modulation frequencies for AM mode-locking calculated by Eq. (7.2) are shown in Table. 7.1.

Table 7.1 Modulation Frequency for AM Mode-Locking

106 m Cavity	206 m Cavity	306 m Cavity	412 m Cavity	506 m Cavity
944.5 kHz	485.9 kHz	327.0 kHz	249.1 kHz	197.7 kHz

In experiments, the voltage amplitude of applied signal to the liquid crystal modulator is increased by a step of 5 V from 35 V to 60 V. The pulse duration, average output power, peak power and pulse energy as a function of voltage amplitude for different cavity lengths are shown in Fig. 7.12. As discussed in the previous section, when the voltage amplitude increases, the modulation depth of liquid crystal modulation is larger, which means the modulator has a higher switching speed. Moreover, the increasing amplitude of applied signal can also enable the laser resonator to yield a higher output power and a larger pulse energy as shown in Fig. 7.12 (b)-(d). Due to the larger modulation depth and higher switching speed caused by the increasing voltage amplitude, the pulse duration decreases significantly, when the voltage amplitude increases, especially when the cavity is short shown in Fig. 7.12 (a). It is because the modulation signal required by the short cavity needs to have both large modulation frequency and high amplitude to achieve axial mode-locking and enough modulation depth respectively. At the modulation frequency of 944.5 kHz for a 106 m long cavity, the modulation depth is around 5.9 %, when the peak-to-peak voltage of applied signal is increased to 60 V. Besides of the modulation signal, the cavity length also has some

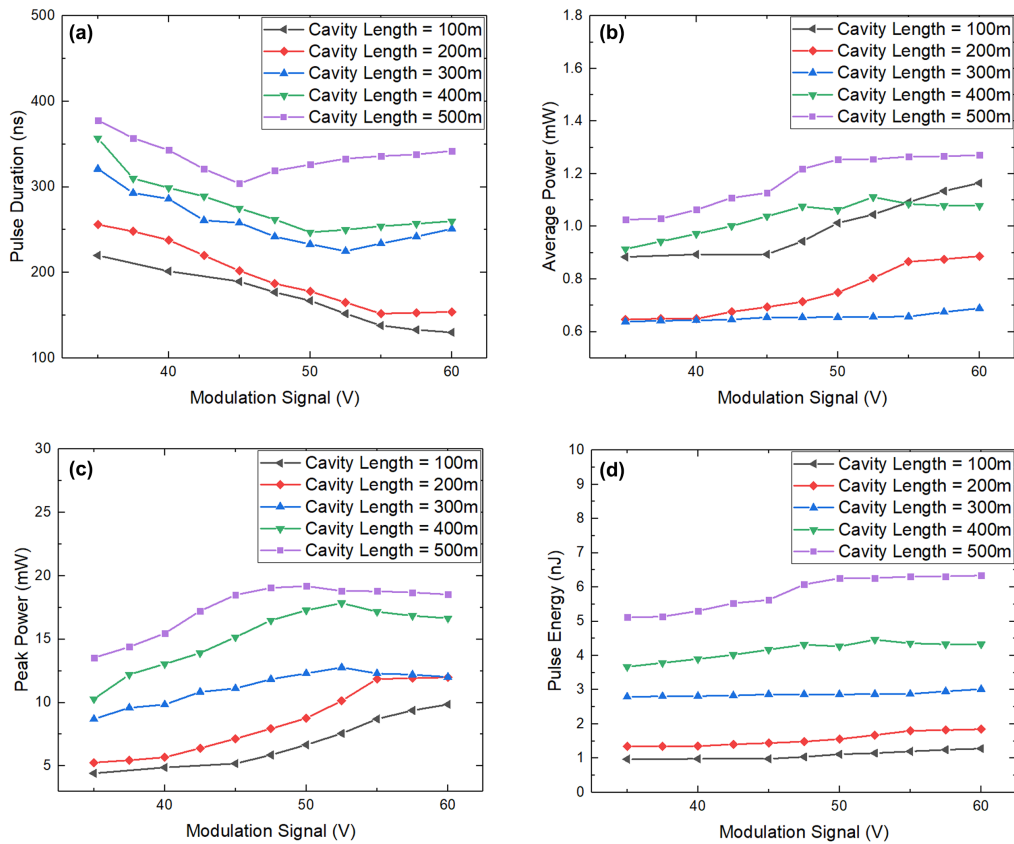


Fig. 7.12 The (a) pulse duration, (b) average output power, (c) peak power, and (d) pulse energy as a function of voltage amplitude for 106 m/206 m/306 m/412 m/506m long cavities. In (a), pulse width decreases with the decreasing cavity length. A shorter cavity requires a larger axial mode spacing, so theoretically the pulse width is in inverse proportion to the axial mode spacing. In (c) and (d), the output power is reduced, when the cavity length is shortened, because the required modulation frequency and axial mode spacing are larger for a shorter cavity, and the larger modulation frequency results in a decrease in modulation depth and switching time. Therefore, the output efficiency and output pulse energy decrease, when the cavity length reduces.

obvious impacts on the AM mode-locking performance. As shown in Fig. 7.12 (a), the pulse width decreases from 300 ns to 100 ns, when the cavity length decreases from 506 m to 106 m. It is because theoretically the pulse width is in inverse proportion to the axial mode spacing for mode-locking operation. As presented in Fig. 7.12 (c) and (d), the output power is reduced, when the cavity length is shorten. The reason is, the required modulation

frequency and axial mode spacing is larger for a shorter cavity, and the larger modulation frequency results in a decrease in the modulation depth and the switching speed. Therefore, the output efficiency and output pulse energy decrease, when the cavity length is shortened.

7.6.4 AM Mode-Locking Performance v.s. Pump Power

For CW and Q-switched lasers, the pump power is one of the important factors which affects the laser performance and the quality of laser pulses. In this section, both different cavity lengths and pump powers will be taken into consideration, regard to the performance of AM mode-locked lasers, including pulse duration, average output power, peak power, and pulse energy. With various cavity lengths, the pump power used in the setup increases from 52.5 mW to 82.5 mW. Multiple performance parameters are measured and presented in Fig. 7.13.

As shown in Fig. 7.13 (b)-(d), average power, peak power and pulse energy of AM mode-locked lasers with different cavity lengths increase in linear proportion to the absorbed pump power, because the pumped gain ($<$ gain saturation) in the resonator is directly proportional to the absorbed pump power. When the gain is larger than the loss in the resonator, or the pump power is larger than the threshold value, the power and energy of output lasers increases with the increasing absorbed pump power. In contrast, no obvious change in the pulse width is observed in Fig. 7.13, when the pump power increases. It indicates that the pump power mainly affects the output power and the output efficiency, not the pulse width in the case of AM mode-locking operation. In addition to the investigation on impacts of the pump power on the laser performance, the pulse duration, average output power, peak power and pulse energy are also measured and recorded for different cavity lengths, which are represented in different colors in Fig. 7.13. With the same pump power, e.g. 82.5 mW, the pulse duration reduces from 300 ns to 120 ns, when the cavity is shorten. Its reason has been discussed in the previous subsection. For other performance parameters, such as output power and pulse energy, they all increase, when the fibre laser cavity is longer. It is because in a longer cavity, the modulation signal with the same amplitude but a lower modulation frequency has a larger modulation depth, then it can lead to a higher output power and output energy.

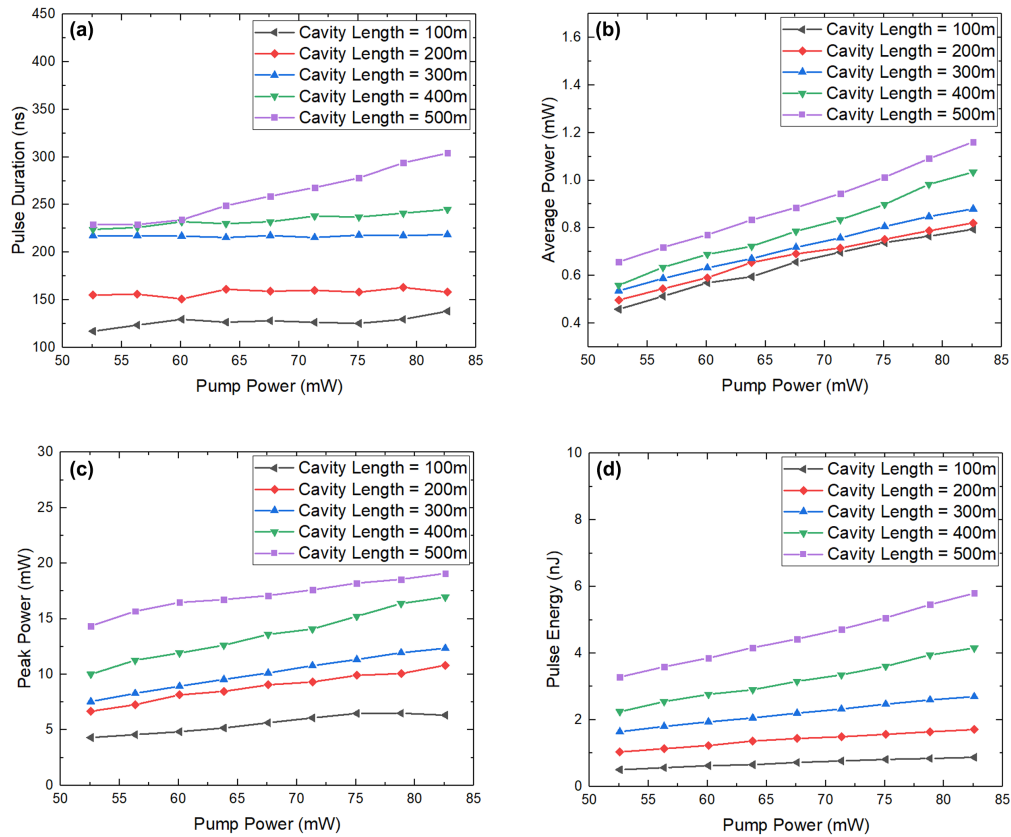


Fig. 7.13 (a) Pulse width, (b) average power, (c) pulse energy and (d) peak power as a function of the absorbed pump power from 52.5 to 82.5 mW for the AM mode-locked fibre laser with different cavity lengths from 106 m to 506 m. The modulation frequency is calculated using Eq. (7.2) and listed in Table. 7.1.

7.6.5 AM Mode-Locking Output

After achieving some preliminary experimental results analysed earlier, the linear polarizer, quarter-wave plate and half-wave plate are placed very close to the liquid crystal cell, so the free space part became more compact and insensitive to environmental influences, such as the small vibration. When the polarized and two wave plates are fine-tuned for the best mode-locking performance, a stable train of mode-locked laser pulses can be observed from the oscilloscope. In our experiments, a square-waveform modulation function with a duty cycle of 50 % is used with a modulation frequency of 944.5 kHz for a 106 m long fibre

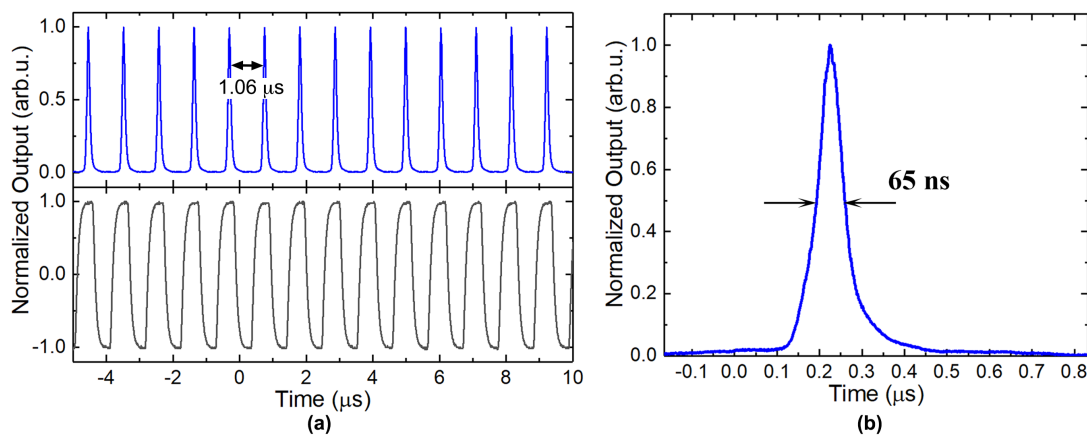


Fig. 7.14 (a) Measured oscilloscope trace of AM mode-locked laser pulses (blue line) at a repetition rate of 944.5 kHz and corresponding driving electric signal (grey line). (b) The measured AM mode-locked laser pulse with a pulse width of 65 ns.

cavity. Because the duration of a half cycle is only 0.53 μs , the peak-to-peak voltage is increased further to 60 V to maintain a large enough modulation depth. At this frequency, the modulation depth is around 5.9 % as shown in Fig. 4.2.

The measured oscilloscope trace of the mode-locked laser pulse train with a temporal pulse spacing of 1.06 μs is shown in Fig. 7.14 (a), showing excellent pulse-to-pulse stability. A close-up view of a single mode-locked pulse with a pulse width of 65 ns is shown in Fig. 7.14 (b). It is worth noting that only when the modulation frequency exactly matches the axial mode spacing frequency of the resonator (± 5 kHz), a stable pulse train can be obtained, otherwise the pulse train will be destroyed. The oscilloscope trace of output lasers illustrates a periodic, yet noise-like output signal, confirming that the laser is indeed fully mode-locked. In our experiments, the optical spectrum is also measured and recorded for analyzing the wavelength and optical bandwidth of generated AM mode-locked laser pulses. The optical spectra measured at the CW mode and AM mode-locking mode are presented in Fig. 7.15 (a) and (b) separately.

As shown in Fig. 7.15, when the modulation is turned on, the 3-dB bandwidth increases from about 72 pm for the CW operation to 368 pm when the laser is mode-locked.

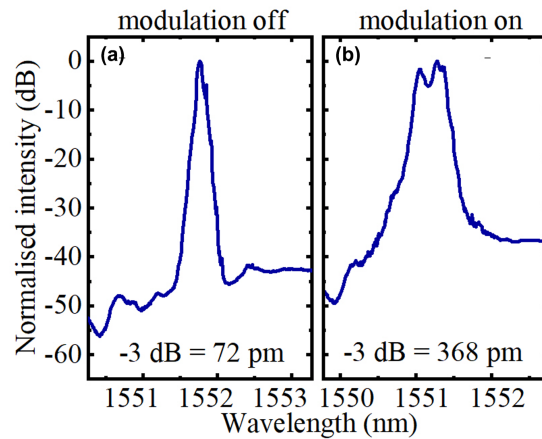


Fig. 7.15 The optical spectrum measured at the (a) CW mode and (b) AM mode-locking mode. At the CW mode, the 3-dB bandwidth is around 72 pm, while the 3-dB bandwidth is broadened to 368 pm at the AM mode-locking mode.

7.7 Frequency Modulation Mode-Locking Mode

Generally, the mode-locking operation can be initiated not only by using an amplitude modulator, but also a frequency or phase modulator within the cavity. In addition to the AM mode-locking as discussed in the previous section, the short pulses can also be generated in FM mode-locking situation. In the process of active mode-locking, the pulse formation process is controlled and synchronized by the modulation frequency of applied signals. Theoretically, the shorter the circulating pulse becomes in such an actively mode-locked laser, the less loss it experiences in pass through the modulator. When the pulse width is narrowing down, the pulse spectrum becomes wider and also more axial modes are contained. If the spectral width is smaller than the amplitude bandwidth of the laser medium (or gain medium) in the cavity, the laser medium can still keep providing gain, and the following pulse becomes narrower and its spectrum becomes wider. The gain provided by the laser medium can continue to shorten the pulse, until the spectral width of laser pulses begins to approach the amplification bandwidth of the laser medium. At the same time, the pulse width of output pulses reaches the limit point.

7.7.1 Fundamentals of Frequency Modulation Mode-Locking

For mode-locked lasers, the circulating pulse can be described by a Gaussian pulse envelope. To explain the FM mode-locking behavior, the pulse propagation through a phase or frequency modulator should be analysed. Similar to the modulator transmission function for a simple amplitude modulator shown in Eq. (7.1), the phase modulation effects of FM modulator can be expressed in the form of complex function as

$$L(t)_{FM} = \exp[j\Delta_m \cos \omega_m t]. \quad (7.3)$$

where $2\Delta_m$ refers to the peak-to-peak phase deviation and modulation index of a simple frequency modulator. It turns out that circulating pulses in the frequency mode-locked laser always passes through the modulator at the two peaks (positive and negative peak) of phase modulation cycles as shown in Fig. 7.16.

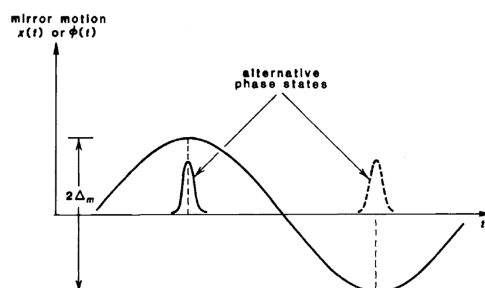


Fig. 7.16 Pulse transmission through an FM (phase) modulator. Images are from Anthony E Siegman [240].

In the complex function of phase modulation produced by a frequency modulator, the time-varying phase term at positive and negative peaks can be simplified by using quadratic approximation. Therefore, the phase modulation at two peaks $L(t)_{FM}$ can be expressed in form as

$$L(t)_{FM} = \exp \left[\pm j\Delta_m \left(1 - \frac{\omega_m^2 t^2}{2} \right) \right]. \quad (7.4)$$

where the constant part in the phase shift can represent a very small change in the total effective length of the laser cavity, while the quadratic part represents a small chirp on the pulse after each round trip. If the Gaussian pulse passes through a phase modulator, it can give rise to a purely imaginary phase change, while that is purely real through an amplitude (AM) modulator as shown in Eq. (7.1).

For the phase modulation in the laser cavity, the periodic phase shift produced by a phase modulator can be considered as the periodic change in the effective cavity length by moving the end mirror position back and forth. When the pulse circulates in the cavity and strikes the moving end mirror, the Doppler shifts will be introduced into the pulse propagation and accumulated rapidly on successive round trips. Therefore, the accumulated Doppler shift pushes the pulse spectrum entirely out of the atomic gain curve, and then no stable mode-locked pulses can be generated and observed. However, the circulating pulses will strike the end mirror without a Doppler shift, if the end mirror is at either of the turning points at which the moving direction of the end mirror is reverse and the slope of mirror motion is zero. The steady-state FM mode-locking thereby can be obtained when the small quadratic phase modulation or frequency chirp is just canceled at two turning points. It is worth noting that a small quadratic phase modulation or a frequency chirp can broaden the pulse spectrum slightly. Based on the pulse propagation behavior of FM mode-locking operation, the short pulses can occur equally well at either of the two-phase turning points, which are completely out of phase as shown in Fig. 7.16. Therefore, the required modulation frequency to initiate active frequency (FM) mode-locking should be half of the spacing of axial modes.

$$f_{\text{mod}}^{\text{FM}} = \frac{f_{\text{spacing}}}{2} = \frac{c}{4n_{\text{eff}}l_{\text{cavity}}} \quad (7.5)$$

7.7.2 Modified Liquid Crystal Modulator for Phase Modulation

As discussed in previous sections, liquid crystal consists of long rod-shaped molecules and shows a sufficient anisotropic structure, in which both the fast and slow axes exist. Due to its anisotropic structure, when the light passing through liquid crystals, the incident light can be decomposed into ordinary and extraordinary waves and then engender phase retardation. If

the incident light is linearly polarized, the phase retardation introduced by liquid crystal can result in changes in the polarization state of light. Since the molecule orientation and optical birefringence are easily controllable by an external electric field, the phase retardation of the incident light can be precisely controlled, and thus the phase modulation can be obtained. If a polarizer and an analyser are placed in front of and behind the liquid crystal cell respectively, the phase modulation can be converted into the intensity modulation of light as discussed in the amplitude (AM) mode-lock section. In the case of FM mode-locking, the linear polarizer is removed from the liquid-crystal cell assembly, so the device introduces a pure phase modulation, instead of AM, i.e., FM mode-locking can be realized. The modified setup is shown in Fig. 7.17. The mechanism of FM mode-lock leads to similar output laser pulses as AM mode-locked laser pulses. However, the difference is the phase modulator introduces two-phase extrema (at which the slope of the sine function is zero) and these pulses can occur on either of them. Therefore, FM mode-locking can be achieved, if the modulation frequency is equal to only half the axial mode spacing. In our experiments, a sine-waveform modulation signal is applied on the modified liquid crystal cell (i.e., with the polarizer removed) with a constant peak-to-peak voltage of 60 V and varying modulation frequency depending on the cavity length. In this section, different cavity lengths will be compared, with the regard to the performance of FM mode-locked lasers, including pulse duration, average output power, peak power, and pulse energy. With the various cavity lengths, e.g. 106 m/206 m/306 m/412 m/506 m, the corresponding modulation frequencies for FM mode-locking calculated by Eq. (7.5) are shown in Table. 7.2.

Table 7.2 Modulation Frequency for FM Mode-Locking

106 m Cavity	206 m Cavity	306 m Cavity	412 m Cavity	506 m Cavity
472.2 kHz	242.9 kHz	163.5 kHz	124.5 kHz	98.8 kHz

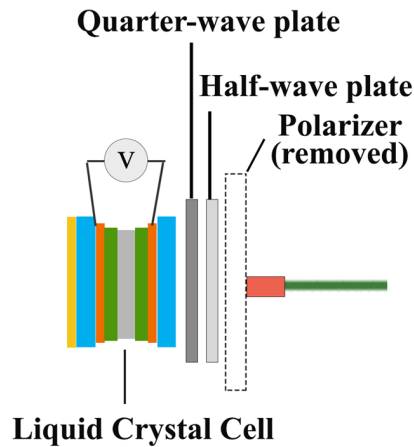


Fig. 7.17 Liquid crystal cell without polarizer for FM mode-locking

7.7.3 FM Mode-Lock Output

In our experiments, when the quarter- and half-wave plates are fine-tuned for the best FM mode-locking performance, a stable train of mode-locked laser pulses can be observed from the oscilloscope. For the FM mode-lock, a sinusoidal signal with a zero offset is used with a modulation frequency of 472.2 kHz for a 106 m long fibre cavity. Because a modulation frequency around 500 kHz is relatively high for liquid crystal devices, the peak-to-peak voltage of the applied signal is increased to 60 V to enhance the phase modulation depth of the liquid crystal modulator under external electrical signals. The measured oscilloscope trace of the FM mode-locked laser pulse train is shown in Fig. 7.18 (a), showing excellent pulse-to-pulse stability. From the measured output pulses, it is clear that the phase modulator introduces two phase extrema (positive and negative) at which the slope of the sine function is zero and that pulses can occur on either of them. A close-up view of a single FM mode-locked pulse with a pulse width of 72 ns is shown in Fig. 7.18 (b).

In our experiments, a sinusoidal waveform signal is applied to the liquid crystal modulator with a constant peak-to-peak voltage of 60 V and varying modulation frequency. To investigate the impacts of modulation frequency mismatch on the output laser performance, the output pulses at a modulation frequency of 472.0 kHz, 472.2 kHz, 472.4 kHz, and 473.2 kHz are recorded and shown in Fig. 7.19 respectively. It is clear that when

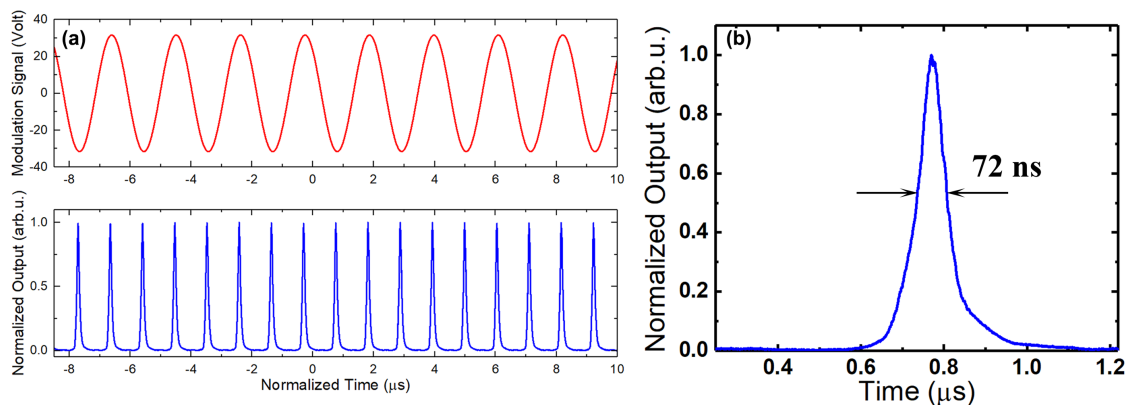


Fig. 7.18 (a) Measured oscilloscope trace of the FM mode-locked laser pulses (blue line) and the external electrical signal with a sine waveform at a frequency of 472.2 kHz (red line) is applied to the liquid crystal modulator and (b) measured FM mode-locked laser pulse with a pulse width of 72 ns.

the modulation frequency accurately matches the half of axial mode spacing ($f=472.2$ kHz) in the second plot, a stable pulse train with sharp peaks can be observed. A slight mismatch (e.g. 472.2 ± 0.2 kHz) between the half of axial mode spacing and the actual modulation frequency of liquid crystal modulator can result in significant performance degradation of output laser pulses with longer pulse width and lower peak power as shown at 472.0 kHz and 472.4 kHz. When the mismatch of modulation frequency is larger than 1 kHz (e.g. 472.2 ± 1 kHz), there is no mode-locked pulses observed, only a periodic noise-like output signal. We can see that the mode-locked laser performance is very sensitive to the modulation frequency, which confirms the laser can be mode-locked efficiently at 472.2 kHz for a 106 m long cavity with a sinusoidal modulation waveform.

7.7.4 FM Mode-Locking Performance v.s. Cavity Length

As discussed in the AM mode-locking operation, the pulse duration reduces and peak power increases with the increasing voltage amplitude shown in Fig. 7.12, because the larger voltage amplitude can result in a larger modulation depth and a higher switching speed. The same relation can be observed and confirmed in the FM mode-locking operation as well.

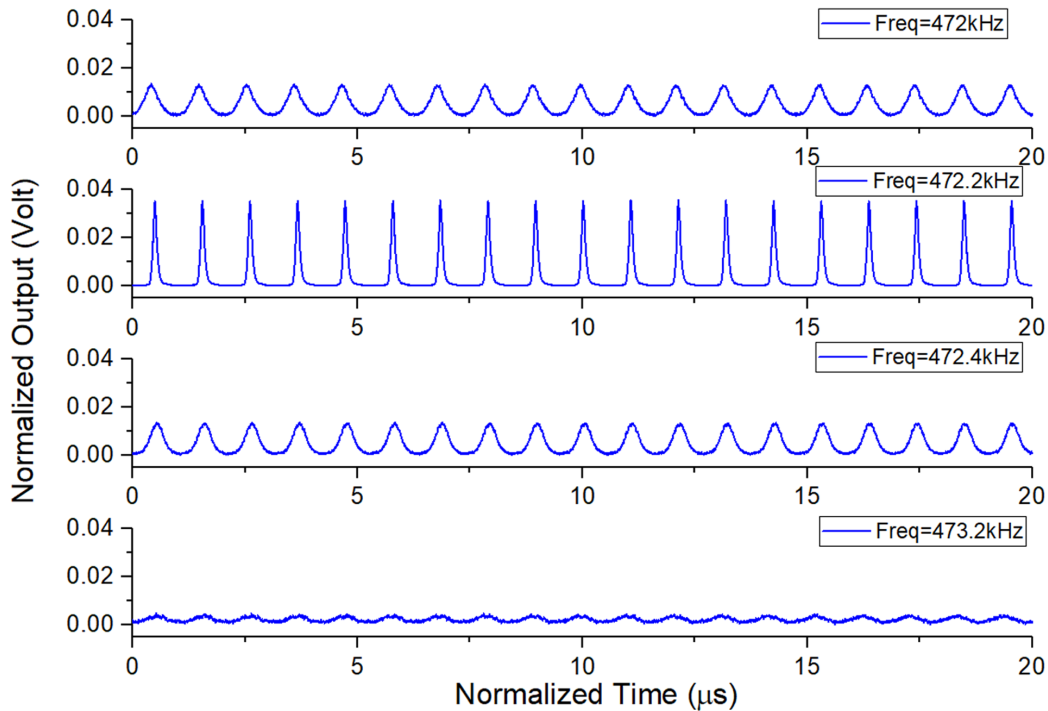


Fig. 7.19 The measured output pulses with increasing modulation frequency from 472.0 to 473.2 kHz. When the modulation frequency accurately matches the half of axial mode spacing ($f = 472.2$ kHz), a stable pulse train with sharp peaks can be observed. A slight mismatch (e.g. 472.2 ± 0.2 kHz) between the half of axial mode spacing and actual modulation frequency of liquid crystal modulator can result in significant performance degradation of output laser pulses, such as longer pulse width and lower peak power. If the mismatch of modulation frequency is larger than 1 kHz (e.g. 472.2 ± 1 kHz), there is no mode-locked pulses observed, only a periodic noise-like output signal. It shows that the mode-locked laser performance is very sensitive to the modulation frequency, which means the laser can be mode-locked efficiently at 472.2 kHz. The measurements are taken for a 106 m long cavity with a sinusoidal modulation waveform.

In the laser resonator, when the pump power is larger than the threshold value and smaller than pump gain saturation, the pumped gain in the resonator is directly proportional to the absorbed pump power. Therefore, the average power, peak power, and pulse energy of either AM or FM mode-locked lasers increase in linear proportion to the absorbed pump power. In the experimental study of FM mode-locking operation, the impacts of the modulation voltage amplitude and absorbed pump power on laser performance parameters are similar to those of AM mode-locking operation. Therefore, the discussion of modulation voltage amplitude

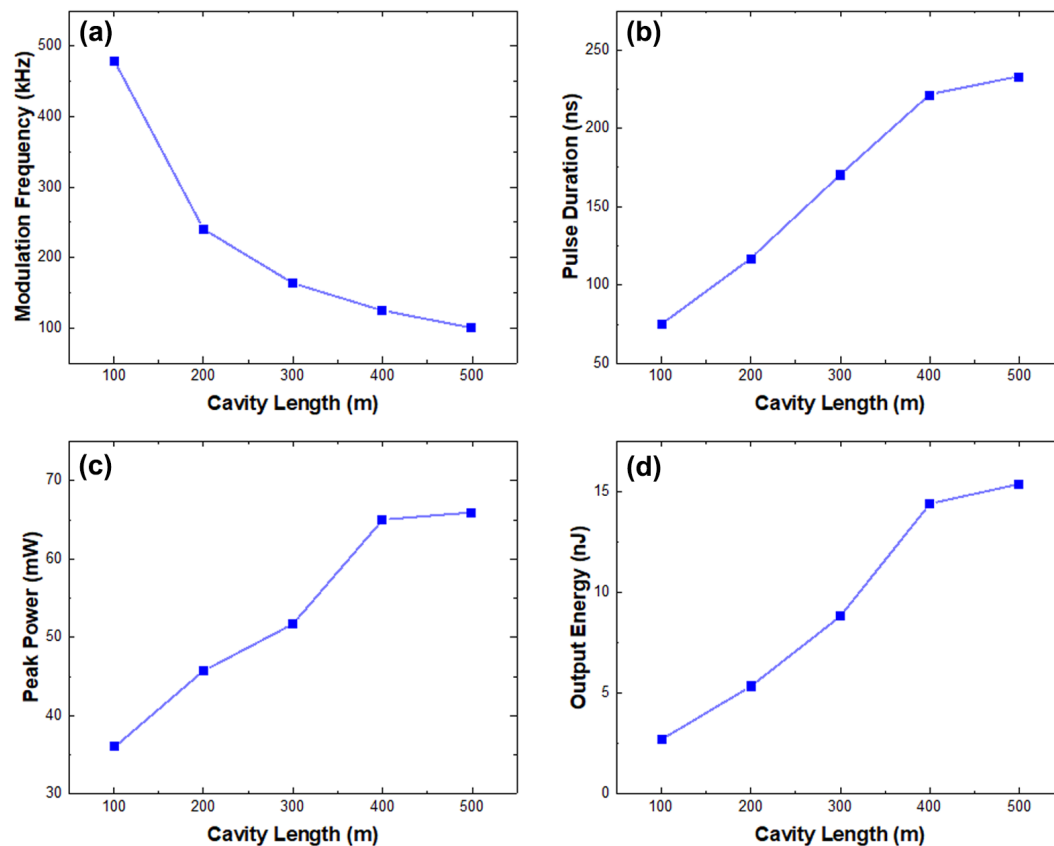


Fig. 7.20 The (a) modulation frequency, (b) pulse duration, (c) peak power, and (d) output energy as a function of cavity lengths, including 106 m, 206 m, 306 m, 412 m, and 506 m. In (a), the required modulation frequency for FM mode-locking decreases from 472.2 kHz to 98.8 kHz with the increasing cavity length from 106 m to 506 m. In (b), the pulse width of generated mode-locked lasers increases with the increasing cavity length due to the reduced axial mode spacing. In (c) and (d), both peak power and output energy are enhanced, due to a larger modulation depth caused by a longer cavity length and lower modulation frequency of liquid crystal modulators.

and pump power will not be repeated in this section. The modulation frequency (half of the axial mode spacing) and laser performance parameters are plotted as a function of cavity length from 106 m to 506 m in Fig. 7.20. It is clear that the required modulation frequency to initiate the active frequency (FM) mode-locking is exactly half of the spacing of axial modes, and then it is inversely proportional to the cavity length as shown in Eq. (7.5). The highest peak power of 66.2 mW and the largest output energy of 15.8 nJ are observed at the same time with the longest cavity, which is around 506 m long. Because the longer cavity

results in a smaller spacing between adjacent axial modes making the required modulation frequency lower to initiate mode-locking, the modulation depth of liquid crystal modulator at the same amplitude is larger and then it results in mode-locked laser pulses with higher output power and pulse energy.

7.8 Summary

In this chapter, we have introduced a novel fibre laser architecture that incorporates a liquid crystal transducer as a loss or alternative pure phase modulator. We demonstrate that the liquid crystal cell enables switching between Q-switched, AM mode-locked, FM mode-locked, and CW operations, simply by changing the applied electric signal. To the best of our knowledge, this is the first time a liquid crystal has been used as an active modulator for generating mode-locked laser pulses. In Q-switching mode, laser pulses with a duration of 1.3 μs , pulse energy of 2.7 μJ , and peak power of 1.93 W are demonstrated at a repetition rate of 200 Hz. In mode-locking mode, two kinds of modulation are utilised, namely AM and FM mode-locking. We demonstrated both AM and FM mode-locked laser pulses with a duration of 65 ns and 72 ns at a modulation frequency of 944.5 kHz and 472.3 kHz, respectively. The proof-of-principle experiments presented here using an off-the-shelf sensing component pave the way for the development of liquid crystal cells that are tailored towards their applications as an intracavity modulator in a fibre laser resonator. In the future, liquid crystal cells can be optimised for laser applications by increasing their operating temperature and by modifying their composition to increase their bandwidth and to reduce their background loss. In addition, a reduction of the pulse duration is feasible via the use of dispersion compensating fibres. Finally, the reflectivity of the FBG and the length of the used fibres could also be optimised.

Chapter 8

Conclusion and future work

The major goal of my Ph.D. study and this thesis is to demonstrate the possibility and novelty of applying liquid crystal-based modulators in laser applications, including waveguide and fibre lasers in a wide range of wavelengths from 1 μm to 2 μm . The motivation of this research topic is the current advances of liquid crystal technologies in recent years. Because the switching speed and switch time of liquid crystal transducers have been improved significantly due to the latest research outcomes, including nano-scale pitch ferroelectric liquid crystal materials [259, 260], optimisation of alignment quality [223] and photo-alignment layers with polymer and azo-dye composite [261, 262]. AS a result, the fast electro-optical response can be obtained from the DHFLC cells, which presents the feasibility of liquid crystal technology in laser applications and paves the way for the development of high efficiency, high peak power, low driving voltage, and monolithic pulsed lasers based on liquid crystal modulators in the near-IR wavelength ranging from 1 μm to 2 μm .

8.1 Conclusion

To achieve the major goal of my Ph.D. study, my major contributions to this research topic include the optical characterisation of liquid crystal cells with different liquid crystal thickness (3.3 μm , 5.0 μm , and 9.0 μm), numerical modeling study and optimisation of actively Q-switched waveguide lasers using liquid crystal modulator, development of high efficiency and

low voltage actively Q-switched Yb-doped waveguide lasers for future commercialization, the first demonstration of all-in-one liquid crystal modulator based fibre lasers supporting Q-switched, AM mode-locked, FM mode-locked and continuous wave operations operating at 1.55 μm and actively Q-switched Tm^{3+} :ZBLAN waveguide laser operating at 1.88 μm .

In the numerical modeling study, the electro-optical response of liquid crystal cells in the DHF mode was characterised and tested from multiple aspects, including the modulation depth and modulation or switching speed. The simulation results from the numerical model were in very good agreement with the experimental results, which validates the reliability of the numerical model. Thus, the numerical model became an effective and useful tool to guide the future optimisation of the actively Q-switched laser performance in an integrated waveguide chip using liquid crystal cells. Without the optimisation, the preliminary experiments demonstrated a stable train of Q-Switched laser pulses with a pulse width or duration well below 40 ns, which is much shorter than the typical response time of liquid crystal in microseconds. To optimise the laser performance by adjusting physical parameters, the impacts of reducing optical losses and increasing pump power on the optimisation of Q-Switched lasers were studied in detail using the developed numerical model. With a smaller optical loss and higher absorbed pump power, the predicted results from the numerical model illustrated that the pulse width can be reduced to 17.00 ns only and the peak power can be enhanced up to 1.15 kW, if the temperature is optimised at 50 °C, the absorbed pump power is increased to 500 mW and the external optical loss is minimized to be 10 %. To reduce the external optical loss, one promising solution is to replace the bottom ITO layer from the liquid crystal cell with a thin gold layer with a specific reflection rate and select a conductive coating with better transparency as the top ITO layer, such as index-matched ITO with an average transmittance of 95 %. The other promising solution is to directly integrate the liquid crystal cell with the waveguide chip via optical adhesive to avoid Fresnel losses. In addition to reducing the optical, increasing absorbed pump power is another easy way to improve the overall laser performance, which can be achieved by using the laser diode with higher output power. The results from the preliminary experiments and numerical model

simulation pave the way for the development of high peak power actively Q-switched with a fully monolithic laser setup whose total length could be around 1 cm only in the future.

After demonstrating the predicted results of an optimised laser setup for actively Q-switched laser operating around 1 μm based on liquid crystal cell, the idea of developing a compact actively Q-switched laser for sensing applications have attracted a lot of attention from the industry. The project "High Efficiency and Low Voltage Actively Q-Switched Yb-doped Waveguide Lasers Using a Liquid Crystal Modulator" was started in 2017 under the collaboration between the University of New South Wales, Macquarie University, and Lastek Pty. Ltd in Adelaide. This project aims to develop a commercial prototype of compact and portable actively Q-switched lasers with high efficiency and a relatively low driving voltage based on liquid crystal technology. The potential applications of this project include remote sensing, LIDAR, laser ablation, nonlinear applications, and other industrial fields. So far, the length of the entire setup has been minimized to only 22 mm by directly integrating the liquid crystal cell onto the waveguide chip, which is one of the promising solutions proposed earlier based on the numerical model. With the minimized setup, the liquid crystal cell was triggered by electrical signals with a duration of 1 μs from the self-developed driver with low power consumption less than 0.84 W and low driving voltage of less than 98 V. The proposed compact prototype of laser setup presented a better laser performance, in which the pulse width of generated Q-switched lasers was shortened to 15.6 ns only and the highest peak power was increased to 110 W with the largest pulse energy of 1.7 μJ from Q-switched laser pulses. From the current experimental results, there is no doubt that the laser performance can be improved further by minimizing the external optical loss and optimising the pump power. The compact and portable Q-Switched laser source could become a promising tool in a variety of industrial applications.

As we knew, light has been used in the optical communication system/network in the past decades for several reasons. First, the optical communication system provides a large transmission bandwidth, which indicates a high information transmission capacity compared with its electrical counterparts, such as cable and microwave. Second, the attenuation of light operating at 1330 nm and 1550 nm in the single-mode optical fibre is 0.5dB/km and

0.4 dB/km respectively. The extremely low attenuation over the optical fibre enables long-distance information transmission over 1000 km. Third, the optical fibre is made of silica, which is rich in natural resources and it is much lighter than transitional cables. Fourth, the optical signals transmitted in the optical fibre can get rid of the external interference from the electromagnetic field or environment. All these advantages motivate people to develop a wide variety of optical devices operating at optical communication wavelength 1550 nm. After showing the feasibility of using liquid crystal cells as an active optical loss modulator in waveguide lasers operating at 1 μm , we started to study the Q-Switched and mode-locked laser behaviors induced by liquid crystal cells as optical loss modulator in the all-fibre setup. The aim of this project is to design an all-in-one fibre lasers operating at 1.55 μm which can support four different operation modes, including continuous wave, Q-switched, AM mode-locked and FM mode-locked operation modes. The novelty of this approach is that the operation mode can be easily switched between continuous wave, Q-switched, AM mode-locked, and FM mode-locked by applying different electrical signals with varying waveforms and frequencies. The preliminary experimental results demonstrated that the Q-switching mode can provide stable Q-Switched laser pulses with a pulse duration of 1.3 μs , pulse energy of 2.7 μJ , and peak power of 1.93 W at the low repetition rate of 200 Hz. When the repetition rate of the applied electrical signal increased to 944.5 kHz, the AM mode-locked laser pulses were achieved from the same setup with a pulse duration of 65 ns. In the experiments, removing the linear polarizer from the liquid crystal cell can change the role of the liquid crystal cell in the setup from an amplitude modulator to a frequency modulator. As a result, the FM mode-locked lasers were generated from the setup with a minor change, and its pulse duration was around 72 ns. The proof-of-principle experiments we have demonstrated are the first time a liquid crystal has been used as an active modulator for generating mode-locked laser pulses. Using an off-the-shelf sensing component like liquid crystal cell in the fibre lasers paves the way for the development of fast switching liquid crystal-based intracavity modulator in a fibre laser resonator. From our study, the biggest limitation of the liquid crystal modulator in the fibre lasers is its long switching time of about a few microseconds, which is much longer than the typical switching time

of the acousto-optical modulators (AOMs) around a few nanoseconds. To overcome this limitation in the future, the operation temperature and the structure of the liquid crystal cell can be optimised to increase its response bandwidth and reduce its background optical loss. Additionally, the pulse duration of mode-locked laser pulses can be reduced via the use of dispersion compensating fibres. Moreover, the mode-locked laser performance can be improved by optimising the reflectivity of the FBG and adjusting the length of Er-doped fibre in the setup.

As demonstrated earlier, the feasibility of liquid crystal cells in the waveguide and fibre lasers has been studied theoretically and experimentally at two different operating wavelengths, namely 1 μm and 1.55 μm . To extend the operation wavelength range of liquid crystal modulator, the project "Q-switched Tm^{3+} :ZBLAN waveguide laser operating at 1.88 μm " was started in 2020 and it is still in progress now. The eye-safe laser source operating in the near-IR region around 2 μm has attracted more and more attention in recent decades, because it is playing a critical role in the development of a variety of applications, such as trace gas spectroscopy, eye-safe range-finding, and coherent LIDAR. Because the transmission rate of the liquid crystal cells at 1.88 μm is around 55 %, which varies slightly with the thickness of the liquid crystal layer, it is worth studying the Q-Switched laser behaviors induced by the liquid crystal modulator in the waveguide setup operating at 1.88 μm . In the experiments, the DHFLC modulator with the liquid crystal thickness of 5 μm was incorporated with a femtosecond laser written Tm^{3+} -doped ZBLAN waveguide chip in the laser cavity. Although the liquid crystal cell presented a larger optical loss at 1.88 μm , the stable train of Q-switched laser pulses was obtained over a large range of repetition rate and peak-to-peak voltage of applied signals from 200 Hz to 30 kHz and from 10 V to 65 V respectively. The measured shortest pulse duration of generated Q-Switched laser pulses was around 31 ns, which provided the highest peak power of 1.3 kW at the repetition rate of 200 Hz. The effects of using different output coupling mirrors with varying reflection rates, peak-to-peak voltage, repetition rate, and absorbed pump power on the laser performance were studied in detail in our study. Compared with commercially available AOMs and EOMs, the most critical advantages of liquid crystal modulators are the lower driving peak-to-peak

voltage which is from 10 V to 65 V, and smaller size for compact design. As the highest peak power in the experiments has been greater than 1 kW, our study demonstrates the possibility of utilising this compact Q-switched Thulium waveguide laser source to observe nonlinear effects in nonlinear fibres (microwire or chalcogenide fibre), such as FWM and spectral broadening, in the near future. The non-linearity phenomenon has been being studied since 2021 and this project is still in progress.

8.2 Future work: fully monolithic actively Q-switched waveguide lasers

As discussed in Chapter 5, the relatively compact laser setup has been designed and tested for actively Q-switched waveguide lasers operating at 1 μm . To achieve fully monolithic and even portable Q-switched lasers using a liquid crystal modulator, the laser cavity has to be more compact by integrating all optical elements without using free-space components. In the previous work, a commercially available in-coupling mirror was integrated into the femtosecond direct written waveguide, so a collimating lens and a focusing lens were required for coupling the pump laser into the inscribed waveguide, and the numerical aperture and focal length needed to be selected carefully to maximize the coupling efficiency. Similarly, a collimating lens was placed after the waveguide chip for light collimation and expansion. Therefore, the compactness of the current laser setup was limited by the presence of free space components and the size of the required component mounts.

To avoid using the free space components and eliminate the wasted space caused by the component mounts, the schematic of a fully monolithic Q-switched laser setup is shown in Fig. 8.1. In the proposed design, the dichroic mirror coating can be carried out on the front-end surface of the inscribed waveguide chip. Therefore, the coated thin layer can act as a dichroic mirror, which has high transmission at the pump wavelength and high reflectivity at the laser emission wavelength on the coated surface. Because the dichroic mirror can be coated as a thin layer next to the waveguide chip and the core diameter of the inscribed waveguides are generally (13-34 μm) larger than the mode-field diameter of the

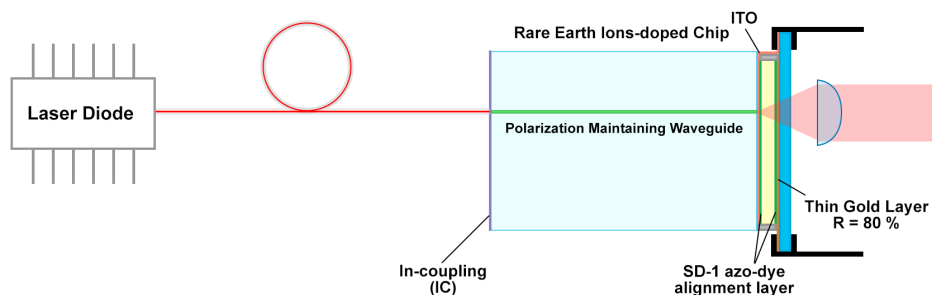


Fig. 8.1 Schematic of fully monolithic Q-switched laser setup.

polarization-maintaining (PM) fibre (6-10 μm), it provides the possibility of coupling the pump light beam delivered by the PM fibre into the waveguide chip directly by aligning the PM fibre with the inscribed waveguide precisely. It is worth noting that, the waveguide chip needs to be polished before the dichroic mirror layer is coated. In the existing setups for all lasers, a PBS or linear polarizer was required to convert the electric-field controlled phase retardation into a controllable light intensity or optical loss. However, if the cross-section of the direct written waveguide is more elliptical, instead of circular, the polarization state of the pump light beam can be maintained along with the propagation in the waveguide. Therefore, the inscribed waveguides have the properties of PM fibres, which only allow the light component along the slow axis to be transmitted, while all other components are filtered out. The conversion from phase retardation to intensity can be achieved without the PSB or polarizer, which gives rise to the reduction of required optical elements. Since the thickness of the liquid crystal layer is only a few micrometers, the collimating lens behind the waveguide chip can also be removed to reduce the cavity length further. In the fully monolithic setup, the top ITO layer and top polyimide alignment layer can be coated on the other end of the waveguide chip, so the waveguide chip will act as the top substrate of the liquid crystal cell. To reduce the optical transmission of liquid crystal cells, the bottom substrate of the liquid crystal cell has no ITO layer. Instead, a thin gold layer coated with the glass substrate can act as both an electrically conductive layer and an output-coupling mirror, because the coated metal layer can provide the conducting medium and the coating thickness

can be calculated to obtain the desired reflectivity for the out-coupling layer. To form the liquid crystal cell, two glass spacers have to be used to separate the waveguide chip and the bottom substrate, so the liquid crystal material can be sealed in a created thin gap. The output lasers can be collimated or coupled into an optical fibre for light delivery. According to the presented schematic, the compactness of the laser cavity can be significantly improved and the Fresnel reflection loss and other optical losses can be minimized by the component integration and the reduction of optical components or layers. Developing a fully monolithic Q-switched laser is a goal for me and Lastek Pty. Ltd in Adelaide to achieve in the near future.

References

- [1] T. H. Maiman. Stimulated optical radiation in ruby. *Nature*, 187:493 – 494, 1960.
- [2] T. H. Maiman, R. H. Hoskins, I. J. D’Haenens, C. K. Asawa, and V. Evtuhov. Stimulated optical emission in fluorescent solids. ii. spectroscopy and stimulated emission in ruby. *Phys. Rev.*, 123:1151–1157, Aug 1961.
- [3] Vasyi Molebny, Paul F. McManamon, Ove Steinvall, Takao Kobayashi, and Weibiao Chen. Laser radar: historical prospective—from the East to the West. *Optical Engineering*, 56(3):1 – 24, 2016.
- [4] J. C. Lin. Noninvasive microwave measurement of respiration. *Proceedings of the IEEE*, 63(10):1530–1530, 1975.
- [5] James C. Lin. Microwave sensing of physiological movement and volume change: A review. *Bioelectromagnetics*, 13(6):557–565, 1992.
- [6] Larry C. HardinLarry V. Nash. Electro-optical range finding and speed detection system, U.S. Patent 5642299A, June. 1997.
- [7] Ari Kilpelä, Riku Pennala, and Juha Kostamovaara. Precise pulsed time-of-flight laser range finder for industrial distance measurements. *Review of Scientific Instruments*, 72(4):2197–2202, 2001.
- [8] Tatsuaki Hashimoto, Takashi Kubota, and Takahide Mizuno. Light weight sensors for the autonomous asteroid landing of MUSES-C mission. *Acta Astronautica*, 52(2):381

- 388, 2003. Selected Proceedings of the 4th IAA International conference on Low Cost Planetary Missions.
- [9] Marius A. Albota, Richard M. Heinrichs, David G. Kocher, Daniel G. Fouche, Brian E. Player, Michael E. O'Brien, Brian F. Aull, John J. Zayhowski, James Mooney, Berton C. Willard, and Robert R. Carlson. Three-dimensional imaging laser radar with a photon-counting avalanche photodiode array and microchip laser. *Appl. Opt.*, 41(36):7671–7678, Dec 2002.
- [10] John J Zayhowski. Passively Q-switched Nd:YAG microchip lasers and applications. *Journal of Alloys and Compounds*, 303-304:393 – 400, 2000.
- [11] Do-Hyun Park, Hyoung-Ha Jeon, and Seung-Il Oh. Eyesafe microchip laser for laser range finder application. *Chin. Opt. Lett.*, 5(S1):S243–S245, May 2007.
- [12] A Biernat and G Kompa. Powerful picosecond laser pulses enabling high-resolution pulsed laser radar. *Journal of Optics*, 29(3):225–228, jun 1998.
- [13] H. K. Tsang, C. S. Wong, T. K. Liang, I. E. Day, S. W. Roberts, A. Harpin, J. Drake, and M. Asghari. Optical dispersion, two-photon absorption and self-phase modulation in silicon waveguides at 1.5 μm wavelength. *Applied Physics Letters*, 80(3):416–418, 2002.
- [14] Ozdal Boyraz, Tejaswi Indukuri, and Bahram Jalali. Self-phase-modulation induced spectral broadening in silicon waveguides. *Opt. Express*, 12(5):829–834, Mar 2004.
- [15] Georg W. Rieger, Kuljit S. Virk, and Jeff F. Young. Nonlinear propagation of ultrafast 1.5 μm pulses in high-index-contrast silicon-on-insulator waveguides. *Applied Physics Letters*, 84(6):900–902, 2004.
- [16] Eric Dulkeith, Yurii A. Vlasov, Xiaogang Chen, Nicolae C. Panoiu, and Richard M. Osgood. Self-phase-modulation in submicron silicon-on-insulator photonic wires. *Opt. Express*, 14(12):5524–5534, Jun 2006.

- [17] Alain Haché and Martin Bourgeois. Ultrafast all-optical switching in a silicon-based photonic crystal. *Applied Physics Letters*, 77(25):4089–4091, 2000.
- [18] R. Dekker, A. Driessen, T. Wahlbrink, C. Moormann, J. Niehusmann, and M. Först. Ultrafast kerr-induced all-optical wavelength conversion in silicon waveguides using 1.55 μm femtosecond pulses. *Opt. Express*, 14(18):8336–8346, Sep 2006.
- [19] I-Wei Hsieh, Xiaogang Chen, Jerry I. Dadap, Nicolae C. Panoiu, Richard M. Osgood, Sharee J. McNab, and Yurii A. Vlasov. Cross-phase modulation-induced spectral and temporal effects on co-propagating femtosecond pulses in silicon photonic wires. *Opt. Express*, 15(3):1135–1146, Feb 2007.
- [20] Ricardo Claps, Dimitri Dimitropoulos, Yan Han, and Bahram Jalali. Observation of Raman emission in silicon waveguides at 1.54 μm . *Opt. Express*, 10(22):1305–1313, Nov 2002.
- [21] D. Dimitropoulos, B. Houshmand, R. Claps, and B. Jalali. Coupled-mode theory of the Raman effect in silicon-on-insulator waveguides. *Opt. Lett.*, 28(20):1954–1956, Oct 2003.
- [22] Richard L. Espinola, Jerry I. Dadap, Richard M. Osgood, Sharee J. McNab, and Yurii A. Vlasov. Raman amplification in ultrasmall silicon-on-insulator wire waveguides. *Opt. Express*, 12(16):3713–3718, Aug 2004.
- [23] Qianfan Xu, Vilson R. Almeida, and Michal Lipson. Time-resolved study of Raman gain in highly confined silicon-on-insulator waveguides. *Opt. Express*, 12(19):4437–4442, Sep 2004.
- [24] Ansheng Liu, Haisheng Rong, Mario Paniccia, Oded Cohen, and Dani Hak. Net optical gain in a low loss silicon-on-insulator waveguide by stimulated Raman scattering. *Opt. Express*, 12(18):4261–4268, Sep 2004.

- [25] V. Raghunathan, R. Claps, D. Dimitropoulos, and B. Jalali. Wavelength conversion in silicon using Raman induced four-wave mixing. *Applied Physics Letters*, 85(1):34–36, 2004.
- [26] Richard L. Espinola, Jerry I. Dadap, Richard M. Osgood, Sharee J. McNab, and Yurii A. Vlasov. C-band wavelength conversion in silicon photonic wire waveguides. *Opt. Express*, 13(11):4341–4349, May 2005.
- [27] Hiroshi Fukuda, Koji Yamada, Tetsufumi Shoji, Mitsutoshi Takahashi, Tai Tsuchizawa, Toshifumi Watanabe, Jun ichi Takahashi, and Sei ichi Itabashi. Four-wave mixing in silicon wire waveguides. *Opt. Express*, 13(12):4629–4637, Jun 2005.
- [28] Haisheng Rong, Ying-Hao Kuo, Ansheng Liu, Mario Paniccia, and Oded Cohen. High efficiency wavelength conversion of 10 Gb/s data in silicon waveguides. *Opt. Express*, 14(3):1182–1188, Feb 2006.
- [29] K. Yamada, H. Fukuda, T. Tsuchizawa, T. Watanabe, T. Shoji, and S. Itabashi. All-optical efficient wavelength conversion using silicon photonic wire waveguide. *IEEE Photonics Technology Letters*, 18(9):1046–1048, 2006.
- [30] M. Dinu, F. Quochi, and H. Garcia. Third-order nonlinearities in silicon at telecom wavelengths. *Applied Physics Letters*, 82(18):2954–2956, 2003.
- [31] John M. Dudley, Goëry Genty, and Stéphane Coen. Supercontinuum generation in photonic crystal fiber. *Rev. Mod. Phys.*, 78:1135–1184, Oct 2006.
- [32] R. R. Alfano and S. L. Shapiro. Emission in the Region 4000 to 7000 Å Via Four-Photon Coupling in Glass. *Phys. Rev. Lett.*, 24:584–587, Mar 1970.
- [33] R. R. Alfano and S. L. Shapiro. Observation of self-phase modulation and small-scale filaments in crystals and glasses. *Phys. Rev. Lett.*, 24:592–594, Mar 1970.
- [34] F. Silva, D.R. Austin, A. Thai, M. Baudisch, M. Hemmer, D. Faccio, A. Couairon, and J. Biegert. Multi-octave supercontinuum generation from mid-infrared filamentation in a bulk crystal. *Nature Communications*, 3:807, May 2012.

- [35] P. B. Corkum, Claude Rolland, and T. Srinivasan-Rao. Supercontinuum generation in gases. *Phys. Rev. Lett.*, 57:2268–2271, Nov 1986.
- [36] Lianghong Yin, Qiang Lin, and Govind P. Agrawal. Soliton fission and supercontinuum generation in silicon waveguides. *Opt. Lett.*, 32(4):391–393, Feb 2007.
- [37] A. V. Husakou and J. Herrmann. Supercontinuum generation of higher-order solitons by fission in photonic crystal fibers. *Phys. Rev. Lett.*, 87:203901, Oct 2001.
- [38] Jonathan C. Knight. Photonic crystal fibres. *Nature*, 424:847–851, Aug 2003.
- [39] Philip Russell. Photonic crystal fibers. *Science*, 299(5605):358–362, 2003.
- [40] Darren D. Hudson, Sergei Antipov, Lizhu Li, Imtiaz Alamgir, Tomonori Hu, Mohammed El Amraoui, Younes Messaddeq, Martin Rochette, Stuart D. Jackson, and Alexander Fuerbach. Toward all-fiber supercontinuum spanning the mid-infrared. *Optica*, 4(10):1163–1166, Oct 2017.
- [41] Neetesh Singh, Darren D. Hudson, Yi Yu, Christian Grillet, Stuart D. Jackson, Alvaro Casas-Bedoya, Andrew Read, Petar Atanackovic, Steven G. Duvall, Stefano Palomba, Barry Luther-Davies, Stephen Madden, David J. Moss, and Benjamin J. Eggleton. Midinfrared supercontinuum generation from 2 to 6 μm in a silicon nanowire. *Optica*, 2(9):797–802, Sep 2015.
- [42] D. Grassani, E. Tagkoudi, H. Guo, C. Herkommer, F. Yang, T. J. Kippenberg, and C. Brès. Mid infrared gas spectroscopy using efficient fiber laser driven photonic chip-based supercontinuum. *Nature Communications*, 10:1553, 2019.
- [43] B. Schenkel, J. Biegert, U. Keller, C. Vozzi, M. Nisoli, G. Sansone, S. Stagira, S. De Silvestri, and O. Svelto. Generation of 3.8-fs pulses from adaptive compression of a cascaded hollow fiber supercontinuum. *Opt. Lett.*, 28(20):1987–1989, Oct 2003.

- [44] Birgit Schenkel, Rüdiger Paschotta, and Ursula Keller. Pulse compression with supercontinuum generation in microstructure fibers. *J. Opt. Soc. Am. B*, 22(3):687–693, Mar 2005.
- [45] William J. Wadsworth, Arturo Ortigosa-Blanch, Jonathan C. Knight, Tim A. Birks, T.-P. Martin Man, and Phillip St. J. Russell. Supercontinuum generation in photonic crystal fibers and optical fiber tapers: a novel light source. *J. Opt. Soc. Am. B*, 19(9):2148–2155, Sep 2002.
- [46] Goëry Genty, Stéphane Coen, and John M. Dudley. Fiber supercontinuum sources (invited). *J. Opt. Soc. Am. B*, 24(8):1771–1785, Aug 2007.
- [47] Teppei Nakasyotani, Hiroyuki Toda, Toshiaki Kuri, and Ken ichi Kitayama. Wavelength-division-multiplexed millimeter-waveband radio-on-fiber system using a supercontinuum light source. *J. Lightwave Technol.*, 24(1):404, Jan 2006.
- [48] Takuya Ohara, Hidehiko Takara, Takashi Yamamoto, Hiroji Masuda, Toshio Morioka, Makoto Abe, and Hiroshi Takahashi. Over-1000-channel ultradense wdm transmission with supercontinuum multicarrier source. *J. Lightwave Technol.*, 24(6):2311, Jun 2006.
- [49] Jinendra K. Ranka, Robert S. Windeler, and Andrew J. Stentz. Visible continuum generation in air–silica microstructure optical fibers with anomalous dispersion at 800 nm. *Opt. Lett.*, 25(1):25–27, Jan 2000.
- [50] W. H. Reeves, D. V. Skryabin, F. Biancalana, J. C. Knight, P. St. J. Russell, F. G. Omenetto, A. Efimov, and A. J. Taylor. Transformation and control of ultra-short pulses in dispersion-engineered photonic crystal fibres. 424:511–515, Jul 2003.
- [51] A. Ortigosa-Blanch, J. C. Knight, and P. St. J. Russell. Pulse breaking and supercontinuum generation with 200-fs pump pulses in photonic crystal fibers. *J. Opt. Soc. Am. B*, 19(11):2567–2572, Nov 2002.

- [52] John M. Dudley and Stéphane Coen. Coherence properties of supercontinuum spectra generated in photonic crystal and tapered optical fibers. *Opt. Lett.*, 27(13):1180–1182, Jul 2002.
- [53] W. J. Wadsworth, N. Joly, J. C. Knight, T. A. Birks, F. Biancalana, and P. St. J. Russell. Supercontinuum and four-wave mixing with Q-switched pulses in endlessly single-mode photonic crystal fibres. *Opt. Express*, 12(2):299–309, Jan 2004.
- [54] Zijie Yan and Douglas B. Chrisey. Pulsed laser ablation in liquid for micro-/nanosstructure generation. *Journal of Photochemistry and Photobiology C: Photochemistry Reviews*, 13(3):204 – 223, 2012.
- [55] N M Bulgakova and A V Bulgakov. Pulsed laser ablation of solids: transition from normal vaporization to phase explosion. *Applied Physics A*, 73(2):199–208, 2001.
- [56] Alfred Vogel and Vasan Venugopalan. Mechanisms of pulsed laser ablation of biological tissues. *Chemical Reviews*, 103(2):577–644, 2003. PMID: 12580643.
- [57] Franziska Bauer, Andreas Michalowski, Thomas Kiedrowski, and Stefan Nolte. Heat accumulation in ultra-short pulsed scanning laser ablation of metals. *Opt. Express*, 23(2):1035–1043, Jan 2015.
- [58] Johannes Finger and Martin Reininghaus. Effect of pulse to pulse interactions on ultra-short pulse laser drilling of steel with repetition rates up to 10 MHz. *Opt. Express*, 22(15):18790–18799, Jul 2014.
- [59] Rudolf Weber, Thomas Graf, Christian Freitag, Anne Feuer, Taras Kononenko, and Vitaly I. Konov. Processing constraints resulting from heat accumulation during pulsed and repetitive laser materials processing. *Opt. Express*, 25(4):3966–3979, Feb 2017.
- [60] Adela Ben-Yakar and Robert L. Byer. Femtosecond laser ablation properties of borosilicate glass. *Journal of Applied Physics*, 96(9):5316–5323, 2004.

- [61] Daniel Nieto, Justo Arines, Gerard M. O'Connor, and María Teresa Flores-Arias. Single-pulse laser ablation threshold of borosilicate, fused silica, sapphire, and soda-lime glass for pulse widths of 500 fs, 10 ps, 20 ns. *Appl. Opt.*, 54(29):8596–8601, Oct 2015.
- [62] Andreas Ostendorf, Frank Korte, Guenther Kamlage, Ulrich Klug, Juergen Koch, Jesper Serbin, Niko Baersch, Thorsten Bauer, and Boris N. Chichkov. *Applications of Femtosecond Lasers in 3D Machining*, chapter 12, pages 341–377. John Wiley & Sons, Ltd, 2006.
- [63] Milton M. Zaret, Goodwin M. Breinin, Herbert Schmidt, Harris Ripps, Irwin M. Siegel, and Leonard R. Solon. Ocular lesions produced by an optical maser (laser). *Science*, 134(3489):1525–1526, 1961.
- [64] J. Sabine Becker, Andreas Matusch, and Bei Wu. Bioimaging mass spectrometry of trace elements – recent advance and applications of LA-ICP-MS: A review. *Analytica Chimica Acta*, 835:1 – 18, 2014.
- [65] Alessandra Sussulini, Julia Susanne Becker, and Johanna Sabine Becker. Laser ablation ICP-MS: Application in biomedical research. *Mass Spectrometry Reviews*, 36(1):47–57, 2017.
- [66] J. Susanne Becker, Miroslav Zoriy, Carola Pickhardt, Michael Przybylski, and J. Sabine Becker. Investigation of Cu-, Zn- and Fe-containing human brain proteins using isotopic-enriched tracers by LA-ICP-MS and MALDI-FT-ICR-MS. *International Journal of Mass Spectrometry*, 242(2):135 – 144, 2005. Isotope Ratio Measurements SI.
- [67] Pornwilard M-M, Ralf Weiskirchen, Nikolaus Gassler, Anja K. Bosserhoff, and J. Sabine Becker. Novel Bioimaging Techniques of Metals by Laser Ablation Inductively Coupled Plasma Mass Spectrometry for Diagnosis Of Fibrotic and Cirrhotic Liver Disorders. *PLOS ONE*, 8(3):1–12, 03 2013.

- [68] Orazio Svelto and David C Hanna. *Principles of lasers*, volume 4. Springer, 1998.
- [69] F. J. McClung and R. W. Hellwarth. Giant Optical Pulsations from Ruby. *Appl. Opt.*, 1(S1):103–105, Jan 1962.
- [70] T. Kitagawa, K. Hattori, M. Shimizu, Y. Ohmori, and M. Kobayashi. Guided-wave laser based on erbium-doped silica planar lightwave circuit. *Electronics Letters*, 27(4):334–335, 1991.
- [71] H. Suche, T. Oesselke, J. Pandavenes, R. Ricken, K. Rochhausen, W. Sohler, S. Balsamo, I. Montrosset, and K.K. Wong. Efficient Q-switched Ti:Er:LiNbO₃ waveguide laser. *Electronics Letters*, 34:1228–1230(2), June 1998.
- [72] K. M. Davis, K. Miura, N. Sugimoto, and K. Hirao. Writing waveguides in glass with a femtosecond laser. *Opt. Lett.*, 21(21):1729–1731, Nov 1996.
- [73] G. Della Valle, S. Taccheo, R. Osellame, A. Festa, G. Cerullo, and P. Laporta. 1.5 μm single longitudinal mode waveguide laser fabricated by femtosecond laser writing. *Opt. Express*, 15(6):3190–3194, Mar 2007.
- [74] Graham D. Marshall, Peter Dekker, Martin Ams, James A. Piper, and Michael J. Withford. Directly written monolithic waveguide laser incorporating a distributed feedback waveguide-bragg grating. *Opt. Lett.*, 33(9):956–958, May 2008.
- [75] I. Melngailis. The use of lasers in pollution monitoring. *IEEE Transactions on Geoscience Electronics*, 10(1):7–17, Jan 1972.
- [76] B I Vasil'ev and Oussama Mannoun. IR differential-absorption lidars for ecological monitoring of the environment. *Quantum Electronics*, 36(9):801–820, sep 2006.
- [77] S. V. Chernikov, Y. Zhu, J. R. Taylor, and V. P. Gapontsev. Supercontinuum self-Q-switched ytterbium fiber laser. *Opt. Lett.*, 22(5):298–300, Mar 1997.
- [78] Michael Eckerle, Christelle Kieleck, Jacek Świdorski, Stuart D. Jackson, Gwenael Mazé, and Marc Eichhorn. Actively Q-switched and mode-locked Tm³⁺-doped silicate

- 2 μm fiber laser for supercontinuum generation in fluoride fiber. *Opt. Lett.*, 37(4):512–514, Feb 2012.
- [79] D. G. Lancaster, S. Gross, H. Ebendorff-Heidepriem, A. Fuerbach, M. J. Withford, and T. M. Monro. 2.1 μm waveguide laser fabricated by femtosecond laser direct-writing in Ho^{3+} , Tm^{3+} :ZBLAN glass. *Opt. Lett.*, 37(6):996–998, Mar 2012.
- [80] D. G. Lancaster, S. Gross, H. Ebendorff-Heidepriem, K. Kuan, T. M. Monro, M. Ams, A. Fuerbach, and M. J. Withford. Fifty percent internal slope efficiency femtosecond direct-written Tm^{3+} :ZBLAN waveguide laser. *Opt. Lett.*, 36(9):1587–1589, May 2011.
- [81] Ashraf F. El-Sherif and Terence A. King. High-energy, high-brightness Q-switched Tm^{3+} -doped fiber laser using an electro-optic modulator. *Optics Communications*, 218(4):337 – 344, 2003.
- [82] Rick Trebino. The generation of ultrashort laser pulses. [online] <https://onedrive.live.com/view.aspx?cid=651160a0fab1c3ef&page=view&resid=651160A0FAB1C3EF!22519&parId=651160A0FAB1C3EF!20326&authkey=!AGfsRuXqVEbgaYo&app=PowerPoint>.
- [83] Supriyo Datta and Biswajit Das. Electronic analog of the electro-optic modulator. *Applied Physics Letters*, 56(7):665–667, 1990.
- [84] Tomonori Hu, Darren D. Hudson, and Stuart D. Jackson. Actively Q-switched 2.9 μm $\text{Ho}^{3+}\text{Pr}^{3+}$ -doped fluoride fiber laser. *Opt. Lett.*, 37(11):2145–2147, Jun 2012.
- [85] E. A. Donley, T. P. Heavner, F. Levi, M. O. Tataw, and S. R. Jefferts. Double-pass acousto-optic modulator system. *Review of Scientific Instruments*, 76(6):063112, 2005.
- [86] Jeffrey A. Morris and Clifford R. Pollock. Passive Q switching of a diode-pumped Nd:YAG laser with a saturable absorber. *Opt. Lett.*, 15(8):440–442, Apr 1990.

- [87] J. I. Mackenzie and D. P. Shepherd. End-pumped, passively Q-switched yb:yag double-clad waveguide laser. *Opt. Lett.*, 27(24):2161–2163, Dec 2002.
- [88] Sean A. McDaniel, Patrick A. Berry, Gary Cook, David Zelmon, Stephanie Meissner, Helmuth Meissner, and Xiaodong Mu. CW and passively Q-Switched operation of a Ho:YAG waveguide laser. *Optics & Laser Technology*, 91:1 – 6, 2017.
- [89] S.G. Li, Z. Zhuo, T. Li, and J. Li. Short-pulse-width and high-peak-power Q-switched YVO₄/Nd:YVO₄ laser with an acousto-optical modulator. *Laser Physics Letters*, 6(4):275–278, apr 2009.
- [90] Xingpeng Yan, Qiang Liu, Xing Fu, Hailong Chen, Mali Gong, and Dongsheng Wang. High repetition rate dual-rod acousto-optics Q-switched composite Nd:YVO₄ laser. *Opt. Express*, 17(24):21956–21968, Nov 2009.
- [91] Ryusuke Horiuchi, Koji Adachi, Goro Watanabe, Kazuyoku Tei, and Shigeru Yamaguchi. 1.4-MHz repetition rate electro-optic Q-switched Nd:YVO₄ laser. *Opt. Express*, 16(21):16729–16734, Oct 2008.
- [92] Zhaojun Liu, Qingpu Wang, Xingyu Zhang, Zejin Liu, Aijian Wei, Jun Chang, Fufang Su, and Guofan Jin. Pulse-off electro-optic Q-switch made of La₃Ga₅SiO₁₄. *Opt. Express*, 13(18):7086–7090, Sep 2005.
- [93] Keming Du, Daijun Li, Hengli Zhang, Peng Shi, Xiaoyu Wei, and Robert Diart. Electro-optically Q-switched Nd:YVO₄ slab laser with a high repetition rate and a short pulse width. *Opt. Lett.*, 28(2):87–89, Jan 2003.
- [94] Shihui Ma, Haohai Yu, Huaijin Zhang, Xuekun Han, Qingming Lu, Changqin Ma, Robert I Boughton, and Jiyang Wang. Efficient high repetition rate electro-optic Q-switched laser with an optically active langasite crystal. *Scientific Reports*, 6(1):30517, 2016.
- [95] Esrom Kifle, Xavier Mateos, Javier Rodríguez Vázquez de Aldana, Airan Ródenas, Pavel Loiko, Sun Yung Choi, Fabian Rotermund, Uwe Griebner, Valentin Petrov,

- Magdalena Aguiló, and Francesc Díaz. Femtosecond-laser-written Tm:KLu(WO₄)₂ waveguide lasers. *Opt. Lett.*, 42(6):1169–1172, Mar 2017.
- [96] Esrom Kifle, Xavier Mateos, Pavel Loiko, Sun Yung Choi, Ji Eun Bae, Fabian Rotermund, Magdalena Aguiló, Francesc Díaz, Uwe Griebner, and Valentin Petrov. Tm:KY_{1-x-y}Gd_xLu_y(WO₄)₂ planar waveguide laser passively Q-switched by single-walled carbon nanotubes. *Opt. Express*, 26(4):4961–4966, Feb 2018.
- [97] Chen Cheng, Hongliang Liu, Zhen Shang, Weijie Nie, Yang Tan, Blanca del Rosal Rabes, Javier R. Vázquez de Aldana, Daniel Jaque, and Feng Chen. Femtosecond laser written waveguides with MoS₂ as saturable absorber for passively Q-switched lasing. *Opt. Mater. Express*, 6(2):367–373, Feb 2016.
- [98] Sun Young Choi, Thomas Calmano, Mi Hye Kim, Dong-Il Yeom, Christian Kränkel, Günter Huber, and Fabian Rotermund. Q-switched operation of a femtosecond-laser-inscribed Yb:YAG channel waveguide laser using carbon nanotubes. *Opt. Express*, 23(6):7999–8005, Mar 2015.
- [99] Ziqi Li, Chen Cheng, Ningning Dong, Carolina Romero, Qingming Lu, Jun Wang, Javier Rodríguez Vázquez de Aldana, Yang Tan, and Feng Chen. Q-switching of waveguide lasers based on graphene/WS₂ van der Waals heterostructure. *Photon. Res.*, 5(5):406–410, Oct 2017.
- [100] Yang Tan, Chen Cheng, Shavkat Akhmadaliev, Shengqiang Zhou, and Feng Chen. Nd:YAG waveguide laser Q-switched by evanescent-field interaction with graphene. *Opt. Express*, 22(8):9101–9106, Apr 2014.
- [101] Yang Tan, Han Zhang, Chujun Zhao, Shavkat Akhmadaliev, Shengqiang Zhou, and Feng Chen. Bi₂Se₃ Q-switched Nd:YAG ceramic waveguide laser. *Opt. Lett.*, 40(4):637–640, Feb 2015.
- [102] Yang Tan, Zhinan Guo, Linan Ma, Han Zhang, Shavkat Akhmadaliev, Shengqiang Zhou, and Feng Chen. Q-switched waveguide laser based on two-dimensional

- semiconducting materials: tungsten disulfide and black phosphorous. *Opt. Express*, 24(3):2858–2866, Feb 2016.
- [103] Zhaozheng Chu, Jie Liu, Zhinan Guo, and Han Zhang. 2 μm passively Q-switched laser based on black phosphorus. *Opt. Mater. Express*, 6(7):2374–2379, Jul 2016.
- [104] Sargis Hakobyan, Valentin J. Wittwer, Kore Hasse, Christian Kränkel, Thomas Südmeyer, and Thomas Calmano. Highly efficient Q-switched Yb:YAG channel waveguide laser with 5.6 W of average output power. *Opt. Lett.*, 41(20):4715–4718, Oct 2016.
- [105] David J. Ottaway, Lachlan Harris, and Peter J. Veitch. Short-pulse actively Q-switched Er:YAG lasers. *Opt. Express*, 24(14):15341–15350, Jul 2016.
- [106] B. Charlet, L. Bastard, and J. E. Broquin. 1 kW peak power passively Q-switched Nd³⁺-doped glass integrated waveguide laser. *Opt. Lett.*, 36(11):1987–1989, Jun 2011.
- [107] Martha Segura, Martin Kadankov, Xavier Mateos, Maria Cinta Pujol, Joan Josep Carvajal, Magdalena Aguiló, Francesc Díaz, Uwe Griebner, and Valentin Petrov. Passive Q-switching of the diode pumped Tm³⁺:KLu(WO₄)₂ laser near 2 μm with Cr²⁺:ZnS saturable absorbers. *Opt. Express*, 20(4):3394–3400, Feb 2012.
- [108] Jun Wan Kim, Sun Young Choi, Shanmugam Aravazhi, Markus Pollnau, Uwe Griebner, Valentin Petrov, Sukang Bae, Kwang Jun Ahn, Dong-II Yeom, and Fabian Rotermund. Graphene Q-switched Yb:KYW planar waveguide laser. *AIP Advances*, 5(1):017110, 2015.
- [109] Y. F. Chen, Y. P. Lan, and S. W. Tsai. High-power diode-pumped actively Q-switched Nd:YAG laser at 1123 nm. *Optics Communications*, 234(1):309–313, 2004.
- [110] Yongguang Zhao, Zhengping Wang, Haohai Yu, Lei Guo, Lijuan Chen, Shidong Zhuang, Xun Sun, Dawei Hu, and Xinguang Xu. 6.5-ns actively Q-switched Nd:YVO₄ laser operating at 1.34 μm . *Chin. Opt. Lett.*, 9(8):081401–081401, Aug 2011.

- [111] Han Rao, Zhaojun Liu, Zhenhua Cong, Qingjie Huang, Yang Liu, Sasa Zhang, Xingyu Zhang, Chao Feng, Qingpu Wang, Lin Ge, and Jiang Li. High power YAG/Nd:YAG/YAG ceramic planar waveguide laser. *Laser Physics Letters*, 14(4):045801, Feb 2017.
- [112] Daniel Sebbag, Arik Korenfeld, Udi Ben-Ami, David Elooz, Eran Shalom, and Salman Noach. Diode end-pumped passively Q-switched Tm:YAP laser with 1.85-mJ pulse energy. *Opt. Lett.*, 40(7):1250–1253, Apr 2015.
- [113] Brian Cole and Lew Goldberg. Highly efficient passively Q-switched Tm:YAP laser using a Cr:ZnS saturable absorber. *Opt. Lett.*, 42(12):2259–2262, Jun 2017.
- [114] Haohai Yu, Valentin Petrov, Uwe Griebner, Daniela Parisi, Stefano Veronesi, and Mauro Tonelli. Compact passively Q-switched diode-pumped Tm:LiLuF₄ laser with 1.26 mJ output energy. *Opt. Lett.*, 37(13):2544–2546, Jul 2012.
- [115] YongLing Hui, Qi Liu, Xing Hu, Zhanda Zhu, Hong Lei, and Qiang Li. High efficiency active Q-switched laser operation with a large size rectangular core crystalline waveguide. *Opt. Express*, 29(2):2099–2105, Jan 2021.
- [116] Rafael R Gattass and Eric Mazur. Femtosecond laser micromachining in transparent materials. *Nature Photonics*, 2(4):219–225, 2008.
- [117] X. Liu, D. Du, and G. Mourou. Laser ablation and micromachining with ultrashort laser pulses. *IEEE Journal of Quantum Electronics*, 33(10):1706–1716, Oct 1997.
- [118] P Rairoux, H Schillinger, S Niedermeier, M Rodriguez, F Ronneberger, R Sauerbrey, B Stein, D Waite, C Wedekind, H Wille, L Wöste, and C Ziener. Remote sensing of the atmosphere using ultrashort laser pulses. *Applied Physics B*, 71(4):573–580, 2000.
- [119] D. Kuizenga and A. Siegman. FM and AM mode locking of the homogeneous laser - Part I: Theory. *IEEE Journal of Quantum Electronics*, 6(11):694–708, November 1970.

- [120] H. A. Haus. Mode-locking of lasers. *IEEE Journal of Selected Topics in Quantum Electronics*, 6(6):1173–1185, Nov 2000.
- [121] M. DiDomenico. Small-Signal Analysis of Internal (Coupling-Type) Modulation of Lasers. *Journal of Applied Physics*, 35(10):2870–2876, 1964.
- [122] L. E. Hargrove, R. L. Fork, and M. A. Pollack. LOCKING OF He–Ne LASER MODES INDUCED BY SYNCHRONOUS INTRACAVITY MODULATION. *Applied Physics Letters*, 5(1):4–5, 1964.
- [123] F Wang, A G Rozhin, V Scardaci, Z Sun, F Hennrich, I H White, W I Milne, and A C Ferrari. Wideband-tuneable, nanotube mode-locked, fibre laser. *Nature Nanotechnology*, 3(12):738–742, 2008.
- [124] Jihwan Kim, Joonhoi Koo, and Ju Han Lee. All-fiber acousto-optic modulator based on a cladding-etched optical fiber for active mode-locking. *Photon. Res.*, 5(5):391–395, Oct 2017.
- [125] Hermann A. Haus. Theory of mode locking with a fast saturable absorber. *Journal of Applied Physics*, 46(7):3049–3058, 1975.
- [126] Won Bae Cho, Andreas Schmidt, Jong Hyuk Yim, Sun Young Choi, Soonil Lee, Fabian Rotermund, Uwe Griebner, Günter Steinmeyer, Valentin Petrov, Xavier Mateos, Maria C. Pujol, Joan J. Carvajal, Magdalena Aguiló, and Francesc Díaz. Passive mode-locking of a Tm-doped bulk laser near 2 μm using a carbon nanotube saturable absorber. *Opt. Express*, 17(13):11007–11012, Jun 2009.
- [127] You Min Chang, Junsu Lee, and Ju Han Lee. A Q-switched, mode-locked fiber laser employing subharmonic cavity modulation. *Opt. Express*, 19(27):26627–26633, Dec 2011.
- [128] Jan K. Jabczyński, Waldemar Zendzian, and Jacek Kwiatkowski. Q-switched mode-locking with acousto-optic modulator in a diode pumped nd:yvo₄ laser. *Opt. Express*, 14(6):2184–2190, Mar 2006.

- [129] K. Y. Lau. Gain switching of semiconductor injection lasers. *Applied Physics Letters*, 52(4):257–259, 1988.
- [130] Sigang Yang, Yue Zhou, Jia Li, and Kenneth K.-Y. Wong. Actively mode-locked fiber optical parametric oscillator. *IEEE Journal of Selected Topics in Quantum Electronics*, 15(2):393–398, 2009.
- [131] Jian Yao, Jianping Yao, Yong Wang, Swee Chuan Tjin, Yan Zhou, Yee Loy Lam, Jian Liu, and Chao Lu. Active mode locking of tunable multi-wavelength fiber ring laser. *Optics Communications*, 191(3):341–345, 2001.
- [132] N. Myren and W. Margulis. All-fiber electrooptical mode-locking and tuning. *IEEE Photonics Technology Letters*, 17(10):2047–2049, 2005.
- [133] K. Yvind, D. Larsson, L.J. Christiansen, C. Angelo, L.K. Oxenlwe, J. Mrk, D. Birkedal, J.M. Hvam, and J. Hanberg. Low-jitter and high-power 40-GHz all-active mode-locked lasers. *IEEE Photonics Technology Letters*, 16(4):975–977, 2004.
- [134] You Min Chang, Junsu Lee, and Ju Han Lee. Active Mode-Locking of an Erbium-Doped Fiber Laser Using an Ultrafast Silicon-Based Variable Optical Attenuator. *Japanese Journal of Applied Physics*, 51:072701, jun 2012.
- [135] Zhi-Bo Liu, Xiaoying He, and D. N. Wang. Passively mode-locked fiber laser based on a hollow-core photonic crystal fiber filled with few-layered graphene oxide solution. *Opt. Lett.*, 36(16):3024–3026, Aug 2011.
- [136] Xiaohui Li, Xueming Liu, Xiaohong Hu, Leirang Wang, Hua Lu, Yishan Wang, and Wei Zhao. Long-cavity passively mode-locked fiber ring laser with high-energy rectangular-shape pulses in anomalous dispersion regime. *Opt. Lett.*, 35(19):3249–3251, Oct 2010.
- [137] Zhi-Chao Luo, Meng Liu, Hao Liu, Xu-Wu Zheng, Ai-Ping Luo, Chu-Jun Zhao, Han Zhang, Shuang-Chun Wen, and Wen-Cheng Xu. 2 GHz passively harmonic

- mode-locked fiber laser by a microfiber-based topological insulator saturable absorber. *Opt. Lett.*, 38(24):5212–5215, Dec 2013.
- [138] G. Galzerano, M. Marano, S. Longhi, E. Sani, A. Toncelli, M. Tonelli, and P. Laporta. Sub-100-ps amplitude-modulation mode-locked Tm-Ho:BaY₂F₈ laser at 2.06 μm. *Opt. Lett.*, 28(21):2085–2087, Nov 2003.
- [139] Xiong Wang, Pu Zhou, Xiaolin Wang, Rumao Tao, and Lei Si. 2 μm Tm-Doped All-Fiber Pulse Laser With Active Mode-Locking and Relaxation Oscillation Modulating. *IEEE Photonics Journal*, 5(6):1502206–1502206, 2013.
- [140] I. L. Villegas, C. Cuadrado-Laborde, J. Abreu-Afonso, A. Díez, J.L. Cruz, M.A. Martínez-Gámez, and M.V. Andrés. Mode-locked Yb-doped all-fiber laser based on in-fiber acoustooptic modulation. *Laser Physics Letters*, 8(3):227–231, Jan 2011.
- [141] Kan Wu, Xiaoyan Zhang, Jun Wang, and Jianping Chen. 463-MHz fundamental mode-locked fiber laser based on few-layer MoS₂ saturable absorber. *Opt. Lett.*, 40(7):1374–1377, Apr 2015.
- [142] Dong Mao, Xiaoqi Cui, Xuetao Gan, Mingkun Li, Wending Zhang, Hua Lu, and Jianlin Zhao. Passively Q-Switched and Mode-Locked Fiber Laser Based on an ReS₂ Saturable Absorber. *IEEE Journal of Selected Topics in Quantum Electronics*, 24(3):1–6, 2018.
- [143] R. C. Sharp, D. E. Spock, N. Pan, and J. Elliot. 190-fs passively mode-locked thulium fiber laser with a low threshold. *Opt. Lett.*, 21(12):881–883, Jun 1996.
- [144] Hao Liu, Xu-Wu Zheng, Meng Liu, Nian Zhao, Ai-Ping Luo, Zhi-Chao Luo, Wen-Cheng Xu, Han Zhang, Chu-Jun Zhao, and Shuang-Chun Wen. Femtosecond pulse generation from a topological insulator mode-locked fiber laser. *Opt. Express*, 22(6):6868–6873, Mar 2014.

- [145] D. Popa, Z. Sun, F. Torrisi, T. Hasan, F. Wang, and A. C. Ferrari. Sub 200 fs pulse generation from a graphene mode-locked fiber laser. *Applied Physics Letters*, 97(20):203106, 2010.
- [146] Jakub Bogusławski, Yadong Wang, Hui Xue, Xiaoxia Yang, Dong Mao, Xuetao Gan, Zhaoyu Ren, Jianlin Zhao, Qing Dai, Grzegorz Soboń, Jarosław Sotor, and Zhipei Sun. Graphene actively mode-locked lasers. *Advanced Functional Materials*, 28(28):1801539, 2018.
- [147] Yu Wang, Sze Y. Set, and Shinji Yamashita. Active mode-locking via pump modulation in a Tm-doped fiber laser. *APL Photonics*, 1(7):071303, 2016.
- [148] D. Popa, Z. Sun, T. Hasan, W. B. Cho, F. Wang, F. Torrisi, and A. C. Ferrari. 74-fs nanotube-mode-locked fiber laser. *Applied Physics Letters*, 101(15):153107, 2012.
- [149] Sergey Kobtsev, Sergey Kukarin, and Yurii Fedotov. Ultra-low repetition rate mode-locked fiber laser with high-energy pulses. *Opt. Express*, 16(26):21936–21941, Dec 2008.
- [150] Bo Guo, Shi-Hao Wang, Zhi-Xin Wu, Ze-Xin Wang, Da-He Wang, Hao Huang, Feng Zhang, Yan-Qi Ge, and Han Zhang. Sub-200 fs soliton mode-locked fiber laser based on bismuthene saturable absorber. *Opt. Express*, 26(18):22750–22760, Sep 2018.
- [151] L. A. Gomes, L. Orsila, T. Jouhti, and O. G. Okhotnikov. Picosecond SESAM-based ytterbium mode-locked fiber lasers. *IEEE Journal of Selected Topics in Quantum Electronics*, 10(1):129–136, 2004.
- [152] Gongwen Zhu, Xiushan Zhu, Fengqiu Wang, Shuo Xu, Yao Li, Xinli Guo, Kaushik Balakrishnan, R. A. Norwood, and N. Peyghambarian. Graphene mode-locked fiber laser at 2.8 μm . *IEEE Photonics Technology Letters*, 28(1):7–10, 2016.
- [153] S.M. Kelly and M. O’Neill. Chapter 1 - liquid crystals for electro-optic applications. In Hari Singh Nalwa, editor, *Handbook of Advanced Electronic and Photonic Materials and Devices*, pages 1 – 66. Academic Press, Burlington, 2001.

- [154] K. M. Johnson, D. J. McKnight, and I. Underwood. Smart spatial light modulators using liquid crystals on silicon. *IEEE Journal of Quantum Electronics*, 29(2):699–714, Feb 1993.
- [155] Jeffrey A. Davis, Philbert S. Tsai, Don M. Cottrell, Tomio Sonehara, and Jun Amako. Transmission variations in liquid crystal spatial light modulators caused by interference and diffraction effects. *Optical Engineering*, 38(6):1051 – 1057, 1999.
- [156] Ignacio Moreno, Jeffrey A. Davis, Travis M Hernandez, Don M. Cottrell, and David Sand. Complete polarization control of light from a liquid crystal spatial light modulator. *Opt. Express*, 20(1):364–376, Jan 2012.
- [157] Shi-Qiang Li, Xuewu Xu, Rasna Maruthiyodan Veetil, Vytautas Valuckas, Ramón Paniagua-Domínguez, and Arseniy I. Kuznetsov. Phase-only transmissive spatial light modulator based on tunable dielectric metasurface. *Science*, 364(6445):1087–1090, 2019.
- [158] Yan qing Lu, Fang Du, Yi-Hsin Lin, and Shin-Tson Wu. Variable optical attenuator based on polymer stabilized twisted nematic liquid crystal. *Opt. Express*, 12(7):1221–1227, Apr 2004.
- [159] Xiao Liang, Yan-Qing Lu, Yung-Hsun Wu, Fang Du, Hai-Ying Wang, and Shin-Tson Wu. Dual-frequency addressed variable optical attenuator with submillisecond response time. *Japanese Journal of Applied Physics*, 44(3):1292–1295, mar 2005.
- [160] Mikhail A. Osipov. *Theory of the Liquid Crystalline State: Molecular Theories of Liquid Crystals*, chapter III.2, pages 39–71. John Wiley & Sons, Ltd, 1998.
- [161] Shin-Tson Wu and Deng-Ke Yang. *Fundamentals of Liquid Crystal Devices*. John Wiley & Sons, Ltd, Hoboken, NJ, USA, 2006.
- [162] L. Vicari(Ed.). *Optical Applications of Liquid Crystals*. CRC Press, Boca Raton, 2003.

- [163] Svetlana P. Kotova, Evgeny P. Pozhidaev, Sergey A. Samagin, Vladimir V. Kesaev, Vadim A. Barbashov, and Sofia I. Torgova. Ferroelectric liquid crystal with sub-wavelength helix pitch as an electro-optical medium for high-speed phase spatial light modulators. *Optics & Laser Technology*, 135:106711, 2021.
- [164] Noel A. Clark and Sven T. Lagerwall. Submicrosecond bistable electro-optic switching in liquid crystals. *Applied Physics Letters*, 36(11):899–901, 1980.
- [165] H. J. Eichler, D. Grebe, I. Iryanto, and R. Macdonald. Active Q-Switching of a Solid State Laser Using Nematic Liquid Crystal Modulators. *Molecular Crystals and Liquid Crystals Science and Technology. Section A. Molecular Crystals and Liquid Crystals*, 320(1):89–99, 1998.
- [166] D. Grebe, R. Macdonald, and H. J. Eichler. Cholesteric Liquid Crystal Mirrors for Pulsed Solid-State Lasers. *Molecular Crystals and Liquid Crystals Science and Technology. Section A. Molecular Crystals and Liquid Crystals*, 282(1):309–314, 1996.
- [167] Manuel Decker, Christian Kremers, Alexander Minovich, Isabelle Staude, Andrey E. Miroshnichenko, Dmitry Chigrin, Dragomir N. Neshev, Chennupati Jagadish, and Yuri S. Kivshar. Electro-optical switching by liquid-crystal controlled metasurfaces. *Opt. Express*, 21(7):8879–8885, Apr 2013.
- [168] O. Buchnev, J. Y. Ou, M. Kaczmarek, N. I. Zheludev, and V. A. Fedotov. Electro-optical control in a plasmonic metamaterial hybridised with a liquid-crystal cell. *Opt. Express*, 21(2):1633–1638, Jan 2013.
- [169] Josiah Firth, Francois Ladouceur, Zourab Brodzeli, Matthew Wyres, and Leonardo Silvestri. A novel optical telemetry system applied to flowmeter networks. *Flow Measurement and Instrumentation*, 48:15–19, 2016.
- [170] N. Collings, W. A. Crossland, P. J. Ayliffe, D. G. Vass, and I. Underwood. Evolutionary development of advanced liquid crystal spatial light modulators. *Appl. Opt.*, 28(22):4740–4747, Nov 1989.

- [171] K. Hirabayashi, H. Tsuda, and T. Kurokawa. Tunable liquid-crystal Fabry-Perot interferometer filter for wavelength-division multiplexing communication systems. *Journal of Lightwave Technology*, 11(12):2033–2043, 1993.
- [172] S. Ahderom, M. Raisi, K. Lo, K.E. Alameh, and R. Mavaddat. Applications of liquid crystal spatial light modulators in optical communications. In *5th IEEE International Conference on High Speed Networks and Multimedia Communication (Cat. No.02EX612)*, pages 239–242, 2002.
- [173] Friedrich Reinitzer. Beiträge zur Kenntniss des Cholesterins. *Monatshefte für Chemie und verwandte Teile anderer Wissenschaften*, 9(1):421–441, 1888.
- [174] O. Lehmann. Über fließende krystalle. *Zeitschrift für Physikalische Chemie*, 4U(1):462–472, 1889.
- [175] P.G. de Gennes and J. Prost. *The Physics of Liquid Crystals*. International Series of Monographs on Physics. Clarendon Press, 1993.
- [176] S. Chandrasekhar. *Liquid Crystals*. Cambridge University Press, 2 edition, 1992.
- [177] Deng-Ke Yang and Shin-Tson Wu. *Liquid Crystal Physics*, chapter 1, pages 1–50. John Wiley & Sons, Ltd, 2014.
- [178] Anne-Marie Giroud-Godquin and Peter M. Maitlis. Metallomesogens: Metal complexes in organized fluid phases. *Angewandte Chemie International Edition in English*, 30(4):375–402, 1991.
- [179] Sarah A. Hudson and Peter M. Maitlis. Calamitic metallomesogens: metal-containing liquid crystals with rodlike shapes. *Chemical Reviews*, 93(3):861–885, 1993.
- [180] Richard J Bushby and Owen R Lozman. Discotic liquid crystals 25 years on. *Current Opinion in Colloid I& Interface Science*, 7(5):343–354, 2002.
- [181] Hideo Takezoe and Yoichi Takanishi. Bent-core liquid crystals: Their mysterious and attractive world. *Japanese Journal of Applied Physics*, 45(2A):597–625, feb 2006.

- [182] R. Amaranatha Reddy and Carsten Tschierske. Bent-core liquid crystals: polar order, superstructural chirality and spontaneous desymmetrisation in soft matter systems. *J. Mater. Chem.*, 16:907–961, 2006.
- [183] *Liquid Crystal Physics*, chapter 1, pages 1–50. John Wiley & Sons, Ltd, 2014.
- [184] Jürgen Nehring and Alfred Saupe. On the elastic theory of uniaxial liquid crystals. *The Journal of Chemical Physics*, 54(1):337–343, 1971.
- [185] T.J Dingemans, L.A Madsen, N.A Zafiroopoulos, Wenbin Lin, and E.T Samulski. Uniaxial and biaxial nematic liquid crystals. *Philosophical Transactions of the Royal Society A: Mathematical, Physical and Engineering Sciences*, 364(1847):2681–2696, 2006.
- [186] Meyer, R.B., Liebert, L., Strzelecki, L., and Keller, P. Ferroelectric liquid crystals. *J. Physique Lett.*, 36(3):69–71, 1975.
- [187] J. S. Patel and Robert B. Meyer. Flexoelectric electro-optics of a cholesteric liquid crystal. *Phys. Rev. Lett.*, 58:1538–1540, Apr 1987.
- [188] Denis Andrienko. Introduction to liquid crystals. *Journal of Molecular Liquids*, 267:520–541, 2018. Special Issue Dedicated to the Memory of Professor Y. Reznikov.
- [189] Meyer, R. B., Liebert, L., Strzelecki, L., and Keller, P. Ferroelectric liquid crystals. *J. Physique Lett.*, 36(3):69–71, 1975.
- [190] J. W. GOODBY. Ferroelectric liquid crystals. principles, properties and applications. *Ferroelectricity and Related Phenomena*, 7, 1991.
- [191] Dwight W. Berreman. Alignment of liquid crystals by grooved surfaces. *Molecular Crystals and Liquid Crystals*, 23(3-4):215–231, 1973.
- [192] Masaki Hasegawa and Nobuyuki Itoh. *Alignment Technologies And Applications Of Liquid*. Taylor and Francis, Abingdon, 2005.

- [193] Oleg Yaroshchuk and Yuriy Reznikov. Photoalignment of liquid crystals: basics and current trends. *J. Mater. Chem.*, 22:286–300, 2012.
- [194] Tadatsugu Minami. Present status of transparent conducting oxide thin-film development for Indium-Tin-Oxide (ITO) substitutes. *Thin Solid Films*, 516(17):5822–5828, 2008. 5th International Symposium on Transparent Oxide Thin Films for Electronics and Optics.
- [195] R. Clark Jones. A new calculus for the treatment of optical systems. description and discussion of the calculus. *J. Opt. Soc. Am.*, 31(7):488–493, Jul 1941.
- [196] Mathias Schubert. Polarization-dependent optical parameters of arbitrarily anisotropic homogeneous layered systems. *Phys. Rev. B*, 53:4265–4274, Feb 1996.
- [197] Dwight W. Berreman. Optics in stratified and anisotropic media: 4×4-matrix formulation. *J. Opt. Soc. Am.*, 62(4):502–510, Apr 1972.
- [198] Xiushan Zhu and N Peyghambarian. High-Power ZBLAN Glass Fiber Lasers: Review and Prospect. *Advances in OptoElectronics*, 2010:501956, 2010.
- [199] Michel Poulain, Marcel Poulain, and Jacques Lucas. Verres fluores au tetrafluorure de zirconium proprietes optiques d'un verre dope au Nd_{3+} . *Materials Research Bulletin*, 10(4):243 – 246, 1975.
- [200] A. Fernandez, T. Fuji, A. Poppe, A. Fürbach, F. Krausz, and A. Apolonski. Chirped-pulse oscillators: a route to high-power femtosecond pulses without external amplification. *Opt. Lett.*, 29(12):1366–1368, Jun 2004.
- [201] V L Kalashnikov, E Podivilov, A Chernykh, and A Apolonski. Chirped-pulse oscillators: theory and experiment. *Applied Physics B*, 83(4):503, 2006.
- [202] Simon Gross, David G. Lancaster, Heike Ebendorff-Heidepriem, Tanya M. Monro, Alexander Fuerbach, and Michael J. Withford. Femtosecond laser induced structural changes in fluorozirconate glass. *Opt. Mater. Express*, 3(5):574–583, May 2013.

- [203] Guido Palmer, Simon Gross, Alexander Fuerbach, David G. Lancaster, and Michael J. Withford. High slope efficiency and high refractive index change in direct-written Yb-doped waveguide lasers with depressed claddings. *Opt. Express*, 21(14):17413–17420, Jul 2013.
- [204] David G. Lancaster, Yahua Li, Yuwen Duan, Simon Gross, Michael W. Withford, and Tanya M. Monroe. Er³⁺ Active Yb³⁺Ce³⁺ Co-Doped Fluorozirconate Guided-Wave Chip Lasers. *IEEE Photonics Technology Letters*, 28(21):2315–2318, 2016.
- [205] David G. Lancaster, Simon Gross, Heike Ebendorff-Heidepriem, Michael J. Withford, Tanya M. Monroe, and Stuart D. Jackson. Efficient 2.9 μm fluorozirconate glass waveguide chip laser. *Opt. Lett.*, 38(14):2588–2591, Jul 2013.
- [206] Simon Gross, Nemanja Jovanovic, Adam Sharp, Michael Ireland, Jon Lawrence, and Michael J. Withford. Low loss mid-infrared zblan waveguides for future astronomical applications. *Opt. Express*, 23(6):7946–7956, Mar 2015.
- [207] Shin-Tson Wu, Uzi Efron, and LaVerne D. Hess. Birefringence measurements of liquid crystals. *Appl. Opt.*, 23(21):3911–3915, Nov 1984.
- [208] Alfredo Strigazzi, Sofia Torgova, Evgeny Pozhidaev, and Antonio S. Gliozzi. The quadratic electro-optical effect in ferroelectric liquid crystal helical nanostructures: role of the driving voltage shape. *Liquid Crystals*, 43(2):153–161, 2016.
- [209] Zourab Brodzeli, Leonardo Silvestri, Andrew Michie, Qi Guo, Evgeny P. Pozhidaev, Vladimir Chigrinov, and François Ladouceur. Sensors at Your Fibre Tips: A Novel Liquid Crystal-Based Photonic Transducer for Sensing Systems. *J. Lightwave Technol.*, 31(17):2940–2946, Sep 2013.
- [210] Alexei D. Kiselev and Vladimir G. Chigrinov. Optics of short-pitch deformed-helix ferroelectric liquid crystals: Symmetries, exceptional points, and polarization-resolved angular patterns. *Phys. Rev. E*, 90:042504, Oct 2014.

- [211] S. R. Restaino and S. W. Teare. *Introduction to liquid crystals for optical design and engineering*. SPIE, 2015.
- [212] Byung Hak Lee, Iee Gon Kim, Sung Woo Cho, and Si-Hyun Lee. Effect of process parameters on the characteristics of indium tin oxide thin film for flat panel display application. *Thin Solid Films*, 302(1):25 – 30, 1997.
- [213] Heinz-Siegfried Kitzerow and Christian Bahr. *Chirality in Liquid Crystals*. Springer, Jan 2001.
- [214] Eugene Pozhidaev, Vladimir Chigrinov, Anatoli Murauski, Vadim Molkin, Du Tao, and Hoi-Sing Kwok. V-shaped electro-optical mode based on deformed-helix ferroelectric liquid crystal with subwavelength pitch. *Journal of the Society for Information Display*, 20(5):273–278, 2012.
- [215] L. A. Beresnev, V. G. Chigrinov, D. I. Dergachev, E. P. Poshidaev, J. Fünfschilling, and M. Schadt. Deformed helix ferroelectric liquid crystal display: A new electrooptic mode in ferroelectric chiral smectic C liquid crystals. *Liquid Crystals*, 5(4):1171–1177, 1989.
- [216] Leonardo Silvestri, Hrishikesh Srinivas, and François Ladouceur. Effective dielectric tensor of deformed-helix ferroelectric liquid crystals with subwavelength pitch and large tilt angle. *Phys. Rev. E*, 98:052707, Nov 2018.
- [217] D. Marcuse. Classical derivation of the laser rate equation. *IEEE Journal of Quantum Electronics*, 19(8):1228–1231, August 1983.
- [218] Xuelu Zou and Hisayoshi Toratani. Evaluation of spectroscopic properties of Yb³⁺-doped glasses. *Phys. Rev. B*, 52:15889–15897, Dec 1995.
- [219] ALEXANDER FUERBACH, A. FERNANDEZ, A. APOLONSKI, T. FUJI, and F. KRAUSZ. Chirped-pulse oscillators for the generation of high-energy femtosecond laser pulses. *Laser and Particle Beams*, 23(2):113–116, 2005.

- [220] Alexei D. Kiselev, Eugene P. Pozhidaev, Vladimir G. Chigrinov, and Hoi-Sing Kwok. Polarization-gratings approach to deformed-helix ferroelectric liquid crystals with subwavelength pitch. *Phys. Rev. E*, 83:031703, Mar 2011.
- [221] A V Kaznacheev and E P Pozhidaev. Effect of boundary surfaces on the effective dielectric susceptibility of the helical structure of a ferroelectric liquid crystal. *Journal of Experimental and Theoretical Physics*, 121(2):355–361, 2015.
- [222] A V Kaznacheev and E P Pozhidaev. Anchoring energy and orientational elasticity of a ferroelectric liquid crystal. *Journal of Experimental and Theoretical Physics*, 114(6):1043–1051, 2012.
- [223] Qi Guo, Abhishek K. Srivastava, Evgeny P. Pozhidaev, Vladimir G. Chigrinov, and Hoi-Sing Kwok. Optimization of alignment quality of ferroelectric liquid crystals by controlling anchoring energy. *Applied Physics Express*, 7(2):021701, jan 2014.
- [224] Evgeny Pozhidaev, Sofia Torgova, Maxim Minchenko, Cesar Augusto Refosco Yednak, Alfredo Strigazzi, and Elio Miraldi. Phase modulation and ellipticity of the light transmitted through a smectic C* layer with short helix pitch. *Liquid Crystals*, 37(8):1067–1081, 2010.
- [225] Xing Yan, Frank W. Mont, David J. Poxson, Martin F. Schubert, Jong Kyu Kim, Jaehee Cho, and E. Fred Schubert. Refractive-Index-Matched Indium–Tin-Oxide Electrodes for Liquid Crystal Displays. *Japanese Journal of Applied Physics*, 48(12):120203, dec 2009.
- [226] Xinyue Lei, Christoph Wieschendorf, Lu Hao, Josiah Firth, Leonardo Silvestri, Simon Gross, Francois Ladouceur, Michael Withford, David Spence, and Alex Fuerbach. Compact actively Q-switched laser for sensing applications. *Measurement*, 173:108631, 2021.
- [227] Xinyue Lei, Victor Karaganov, Francois Ladouceur, Leonardo Silvestri, and Alex Fuerbach. Compact design of Q-switched laser systems based on liquid crystal

- transducers. In Arnan Mitchell and Halina Rubinsztein-Dunlop, editors, *AOS Australian Conference on Optical Fibre Technology (ACOFT) and Australian Conference on Optics, Lasers, and Spectroscopy (ACOLS) 2019*, volume 11200, pages 120 – 121. International Society for Optics and Photonics, SPIE, 2019.
- [228] Xinyue Lei, Lu Hao, Josiah Firth, Francois Ladouceur, Leonardo Silvestri, and Alex Fuerbach. High Efficiency and Low Voltage Actively Q-Switched Yb-doped Waveguide Lasers Using a Liquid Crystal Modulator. In *Asia Communications and Photonics Conference/International Conference on Information Photonics and Optical Communications 2020 (ACP/IPOC)*, page M4D.8. Optical Society of America, 2020.
- [229] Xinyue Lei, Christoph Wieschendorf, Josiah Firth, Francois Ladouceur, Alex Fuerbach, and Leonardo Silvestri. Numerical modelling and optimization of actively q-switched waveguide lasers based on liquid crystal transducers. *Opt. Express*, 27(6):8777–8791, Mar 2019.
- [230] B M Walsh and N P Barnes. Comparison of Tm:ZBLAN and Tm:silica fiber lasers; Spectroscopy and tunable pulsed laser operation around 1.9 μm . *Applied Physics B*, 78(3):325–333, 2004.
- [231] L. Wetenkamp, G.F. West, and H. Többen. Optical properties of rare earth-doped ZBLAN glasses. *Journal of Non-Crystalline Solids*, 140:35 – 40, 1992. Proceedings of the Seventh International Symposium on HALIDE GLASSES.
- [232] R. Paschotta, N. Moore, W. A. Clarkson, A. C. Tropper, D. C. Hanna, and G. Maze. 230 mW of blue light from a thulium-doped upconversion fiber laser. *IEEE Journal of Selected Topics in Quantum Electronics*, 3(4):1100–1102, Aug 1997.
- [233] Jutta Schneide, Carsten Carbonnier, and Udo B. Unrau. Characterization of a Ho³⁺-doped fluoride fiber laser with a 3.9 μm emission wavelength. *Appl. Opt.*, 36(33):8595–8600, Nov 1997.
- [234] D. Tran, G. Sigel, and B. Bendow. Heavy metal fluoride glasses and fibers: A review. *Journal of Lightwave Technology*, 2(5):566–586, October 1984.

- [235] F. Fusari, R. R. Thomson, G. Jose, F. M. Bain, A. A. Lagatsky, N. D. Psaila, A. K. Kar, A. Jha, W. Sibbett, and C. T. A. Brown. Ultrafast Laser Inscribed Tm^{3+} :Germanate Glass Waveguide Laser at 1.9 μm . In *Conference on Lasers and Electro-Optics 2010*, page CTuU5. Optical Society of America, 2010.
- [236] P. Camy, J.L. Doualan, S. Renard, A. Braud, V. Ménard, and R. Moncorgé. Tm^{3+} : CaF_2 for 1.9 μm laser operation. *Optics Communications*, 236(4):395–402, 2004.
- [237] K Scholle, E Heumann, and G Huber. Single mode Tm and Tm,Ho:LuAG lasers for LIDAR applications. *Laser Physics Letters*, 1(6):285–290, jun 2004.
- [238] Sammy W. Henderson, Charley P. Hale, James R. Magee, Michael J. Kavaya, and A. Vincent Huffaker. Eye-safe coherent laser radar system at 2.1 μm using Tm,Ho:YAG lasers. *Opt. Lett.*, 16(10):773–775, May 1991.
- [239] Guanghui Xue, Bin Zhang, Ke Yin, Weiqiang Yang, and Jing Hou. Ultra-wideband all-fiber tunable Tm/Ho-co-doped laser at 2 μm . *Opt. Express*, 22(21):25976–25983, Oct 2014.
- [240] Anthony E. Siegman. *Lasers*. University Science Books, 1986.
- [241] Govind Agrawal. Chapter 10 - four-wave mixing. In Govind Agrawal, editor, *Nonlinear Fiber Optics (Fifth Edition)*, Optics and Photonics, pages 397–456. Academic Press, Boston, fifth edition edition, 2013.
- [242] M. Schubert and B. Wilhelmi. *Nonlinear optics and quantum electronics*. 1986.
- [243] Paul N. Butcher and David Cotter. *The Elements of Nonlinear Optics*. Cambridge Studies in Modern Optics. Cambridge University Press, 1990.
- [244] Karen Marie Hilligsøe, Thomas Vestergaard Andersen, Henrik Nørgaard Paulsen, Carsten Krogh Nielsen, Klaus Mølmer, Søren Keiding, Rene Kristiansen, Kim Per Hansen, and Jakob Juul Larsen. Supercontinuum generation in a photonic crystal fiber with two zero dispersion wavelengths. *Opt. Express*, 12(6):1045–1054, Mar 2004.

- [245] J. R. Taylor J. M. Dudley. *Supercontinuum Generation in Optical Fibers*. Cambridge University Press, 2010.
- [246] Stéphane Coen, Alvin Hing Lun Chau, Rainer Leonhardt, John D. Harvey, Jonathan C. Knight, William J. Wadsworth, and Philip St. J. Russell. Supercontinuum generation by stimulated Raman scattering and parametric four-wave mixing in photonic crystal fibers. *J. Opt. Soc. Am. B*, 19(4):753–764, Apr 2002.
- [247] John M. Dudley, Goëry Genty, and Stéphane Coen. Supercontinuum generation in photonic crystal fiber. *Rev. Mod. Phys.*, 78:1135–1184, Oct 2006.
- [248] J. C. Travers, A. B. Rulkov, B. A. Cumberland, S. V. Popov, and J. R. Taylor. Visible supercontinuum generation in photonic crystal fibers with a 400W continuous wave fiber laser. *Opt. Express*, 16(19):14435–14447, Sep 2008.
- [249] Chenan Xia, Malay Kumar, Ojas P. Kulkarni, Mohammed N. Islam, Jr. Fred L. Terry, Mike J. Freeman, Marcel Poulain, and Gwenael Mazé. Mid-infrared supercontinuum generation to 4.5 μm in ZBLAN fluoride fibers by nanosecond diode pumping. *Opt. Lett.*, 31(17):2553–2555, Sep 2006.
- [250] Guanshi Qin, Xin Yan, Chihiro Kito, Meisong Liao, Chitrarekha Chaudhari, Takenobu Suzuki, and Yasutake Ohishi. Ultrabroadband supercontinuum generation from ultraviolet to 6.28 μm in a fluoride fiber. *Applied Physics Letters*, 95(16):161103, 2009.
- [251] T. A. Birks, W. J. Wadsworth, and P. St. J. Russell. Supercontinuum generation in tapered fibers. *Opt. Lett.*, 25(19):1415–1417, Oct 2000.
- [252] Alireza Marandi, Charles W. Rudy, Victor G. Plotnichenko, Evgeny M. Dianov, Konstantin L. Vodopyanov, and Robert L. Byer. Mid-infrared supercontinuum generation in tapered chalcogenide fiber for producing octave-spanning frequency comb around 3 μm . *Opt. Express*, 20(22):24218–24225, Oct 2012.

- [253] Alaa Al-kadry, Chams Baker, Mohammed El Amraoui, Younès Messaddeq, and Martin Rochette. Broadband supercontinuum generation in As_2Se_3 chalcogenide wires by avoiding the two-photon absorption effects. *Opt. Lett.*, 38(7):1185–1187, Apr 2013.
- [254] S. G. Leon-Saval, T. A. Birks, W. J. Wadsworth, P. St.J. Russell, and M. W. Mason. Supercontinuum generation in submicron fibre waveguides. *Opt. Express*, 12(13):2864–2869, Jun 2004.
- [255] C. R. Phillips, Carsten Langrock, J. S. Pelc, M. M. Fejer, J. Jiang, Martin E. Fermann, and I. Hartl. Supercontinuum generation in quasi-phase-matched LiNbO_3 waveguide pumped by a Tm-doped fiber laser system. *Opt. Lett.*, 36(19):3912–3914, Oct 2011.
- [256] Michael R.E. Lamont, Barry Luther-Davies, Duk-Yong Choi, Steve Madden, and Benjamin J. Eggleton. Supercontinuum generation in dispersion engineered highly nonlinear ($\gamma = 10 \text{ /W/m}$) As_2S_3 chalcogenide planar waveguide. *Opt. Express*, 16(19):14938–14944, Sep 2008.
- [257] Benjamin J Eggleton, Barry Luther-Davies, and Kathleen Richardson. Chalcogenide photonics. *Nature Photonics*, 5(3):141–148, 2011.
- [258] Sergei Antipov, Martin Ams, Robert J. Williams, Eric Magi, Michael J. Withford, and Alexander Fuerbach. Direct infrared femtosecond laser inscription of chirped fiber bragg gratings. *Opt. Express*, 24(1):30–40, Jan 2016.
- [259] Sidra Khan, Shikha Chauhan, Achu Chandran, Michał Czerwiński, Jakub Herman, Ashok M. Biradar, and Jai Prakash. Enhancement of dielectric and electro-optical parameters of a newly prepared ferroelectric liquid crystal mixture by dispersing nano-sized copper oxide. *Liquid Crystals*, 47(2):263–272, 2020.
- [260] Vadim Mikhailenko, Alexander Krivoshey, Evgeny Pozhidaev, Ekaterina Popova, Alexander Fedoryako, Saniyat Gamzaeva, Vadim Barbashov, Abhishek K. Srivastava, Hoi Sing Kwok, and Valerii Vashchenko. The nano-scale pitch ferroelectric liquid

- crystal materials for modern display and photonic application employing highly effective chiral components: Trifluoromethylalkyl diesters of p-terphenyldicarboxylic acid. *Journal of Molecular Liquids*, 281:186–195, 2019.
- [261] Qi Guo, Zourab Brodzeli, Eugene P. Pozhidaev, Fan Fan, Vladimir G. Chigrinov, Hoi Sing Kwok, Leonardo Silvestri, and Francois Ladouceur. Fast electro-optical mode in photo-aligned reflective deformed helix ferroelectric liquid crystal cells. *Opt. Lett.*, 37(12):2343–2345, Jun 2012.
- [262] Qi Guo, A.K. Srivastava, V.G. Chigrinov, and H.S. Kwok. Polymer and azo-dye composite: a photo-alignment layer for liquid crystals. *Liquid Crystals*, 41(10):1465–1472, 2014.
- [263] François Ladouceur, Xinyue Lei, Yuan Wei, Josiah Firth, Alexander Fuerbach, Nigel Lovell, and Leonardo Silvestri. Towards the next generation of brain/machine interface. In Arnan Mitchell and Halina Rubinsztein-Dunlop, editors, *AOS Australian Conference on Optical Fibre Technology (ACOFT) and Australian Conference on Optics, Lasers, and Spectroscopy (ACOLS) 2019*, volume 11200, pages 35 – 36. International Society for Optics and Photonics, SPIE, 2019.
- [264] Yuan Wei, Amr Al Abed, Nathalie Gouailhardou, Han Wang, Xinyue Lei, François Ladouceur, Torsten Lehmann, Nigel H. Lovell, and Leonardo Silvestri. Optically measuring nerve activity based on an electro-optical detection system. In Ewa M. Goldys and Brant C. Gibson, editors, *Biophotonics Australasia 2019*, volume 11202, pages 72 – 73. International Society for Optics and Photonics, SPIE, 2019.
- [265] Han Wang, Udo Römer, Xinyue Lei, Yuan Wei, Amr Al Abed, Francois Ladouceur, Leonardo Silvestri, and Nigel Lovell. Towards bi-directional electro-optic neuronal interfaces. In Ewa M. Goldys and Brant C. Gibson, editors, *Biophotonics Australasia 2019*, volume 11202, pages 70 – 71. International Society for Optics and Photonics, SPIE, 2019.

- [266] Amr Al Abed, Hrishikesh Srinivas, Josiah Firth, François Ladouceur, Nigel H Lovell, and Leonardo Silvestri. A biopotential optrode array: operation principles and simulations. *Scientific Reports*, 8(1):2690, 2018.
- [267] Thomas Lewis, M. A. Rothschild, and Ernest Henry Starling. Iv. the excitatory process in the dog's heart. part ii.- the ventricles. *Philosophical Transactions of the Royal Society of London. Series B, Containing Papers of a Biological Character*, 206(325-334):181–226, 1915.
- [268] Lior Gepstein, Gal Hayam, and Shlomo A. Ben-Haim. A novel method for nonfluoroscopic catheter-based electroanatomical mapping of the heart. *Circulation*, 95(6):1611–1622, 1997.
- [269] LIOR GEPSTEIN and STEVEN J. EVANS. Electroanatomical mapping of the heart: Basic concepts and implications for the treatment of cardiac arrhythmias. *Pacing and Clinical Electrophysiology*, 21(6):1268–1278, 1998.
- [270] Hiroshi Nakagawa, Atsushi Ikeda, Tushar Sharma, Ralph Lazzara, and Warren M. Jackman. Rapid high resolution electroanatomical mapping. *Circulation: Arrhythmia and Electrophysiology*, 5(2):417–424, 2012.

Appendix A

Other Liquid Crystal Related Research

A.1 Liquid crystal optrode for electro-physiology recording

In addition to laser applications, we also investigated the possibility of using a novel optical technology to develop a new generation of neural interfaces that can record activation potentials at different positions in parallel based on the optical multiplexing technique. Due to the high optical response speed and the good linearity of liquid crystal transducer to the electric field, the liquid crystal-based optical sensor, which is liquid crystal optrode, becomes a promising approach to realize the new generation of neural interfaces. The liquid crystal optrodes offer a high spatial and temporal resolution in either vitro or vivo environments. Moreover, this optical approach does not suffer from impedance matching issues plaguing their electronic counterparts when the density of electrodes (or optrodes in our case) is scaled up to form interfaces with a high channel count. It is worth noting that this scaling issue is probably one of the most important parameters determining the scope of potential applications, e.g. control of a robotic arm or restoring speech abilities because it limits the number of channels that can be recorded and transmitted in parallel [263].

In experiments, liquid crystal transducers are connected with probes to convert electrical signals to corresponding optical signals. The intensity of reflected light from the liquid crystal transducer is detected and measured by InGaAs photo-detectors. In this process, the light intensity can be converted into a current and then a voltage at the output terminal of the

photo-detector. The output voltage of the photo-detector consists of DC and AC components, in which the DC component represents the constant background light reflected from the liquid crystal transducer and the AC component represents detected signals corresponding to activation potentials detected from biological tissues. Thus, the detection of bio-potential becomes the detection of light intensity.

As the experimental setup shown in Fig. A.1, an optical circular is placed between the broadband light source and the optical multiplexer to separate the incoming light from the light source and the reflected light from the LC transducer. The optical wavelength multiplexer was added for splitting the incident broadband light into two light beams in two separate channels with different wavelengths. Two electrodes are allocated at different positions to extract different nerve action potentials. One metal pin of the LC transducer was connected to one electrode, while the other pin of the LC transducer was connected to the ground reference electrode from the electro-optical detection system. As a result, the LC transducer enables the passive conversion of the nerve action potential into an optical signal indicated by the light intensity and then reflects the optical signal via the same optical path to the multiplexer. By using the optical multiplexer, the action potential signals detected by two LC transducers (optrodes) are transmitted in one single fibre at different wavelengths before the optical demultiplexer. At the receiver, the demultiplexer separates two optical channels by wavelengths, and then the optical signals from two channels are converted back to electrical signals again by using two photo-detectors. For the signal processing and analysis, the electrical signals are amplified and collected by the data acquisition (DAQ) device (National Instruments NI USB-6251) installed on the personal computer (PC). The simultaneous electrical or/and optical detection at two positions via two separate optical channels offers the feasibility of signal comparison and nerve velocity calculation [264].

To obtain the in-vitro nerve action potential in experiments, we stimulate the nerve by a train of periodical square wave pulses with a duration of 50 μ s and an amplitude of 1 V. As shown in Fig. A.2, both stimulus artifacts and nerve responses are detected by two electrodes and two optrodes (LC transducers) in two channels separately. From measured signals, it is clear that the first peak is the artifact and the following peak and tail are nerve responses

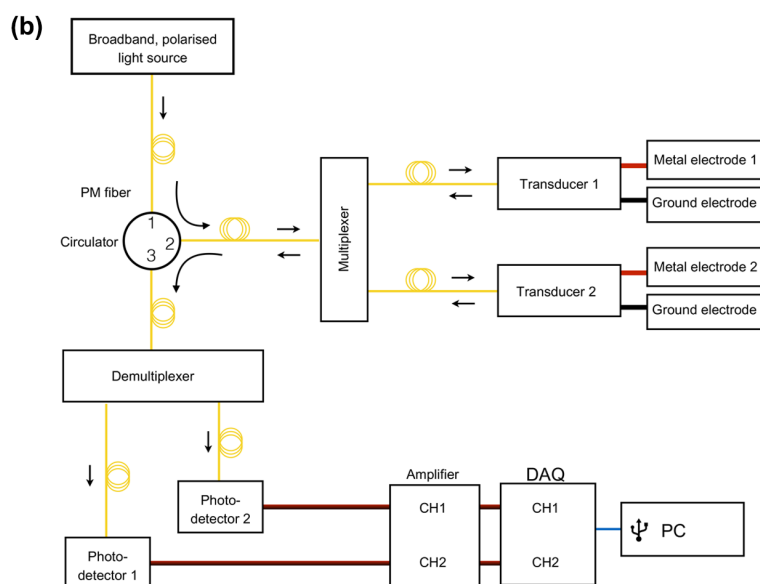
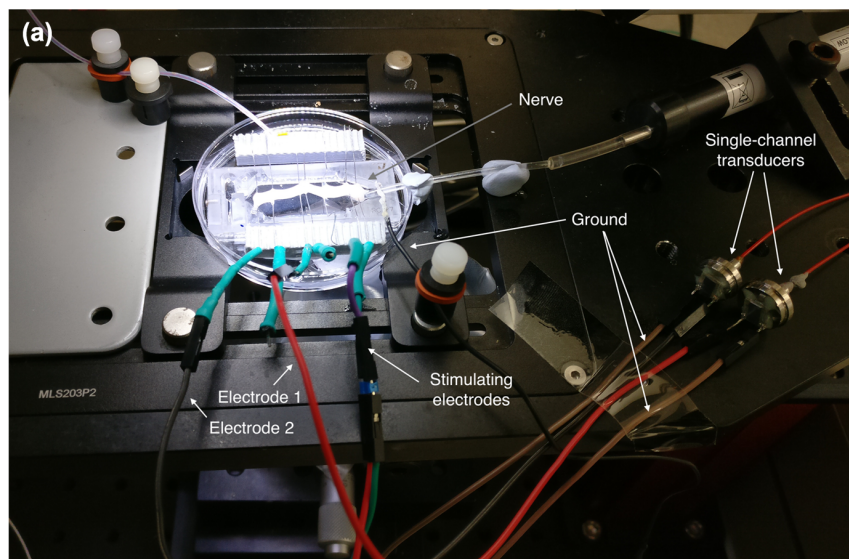


Fig. A.1 (a) The experimental setup in vitro with the spatial multiplexing of two separate optical channels. To evoke the action potential of the rabbit sciatic nerve in the dish, the electrical stimulus is applied. The action potentials are recorded by two electrodes and two transducers known as optrodes at two different locations separately. (b) The schematic of the experimental setup for this electro-optical detection system. Images are from our previous publication [264].

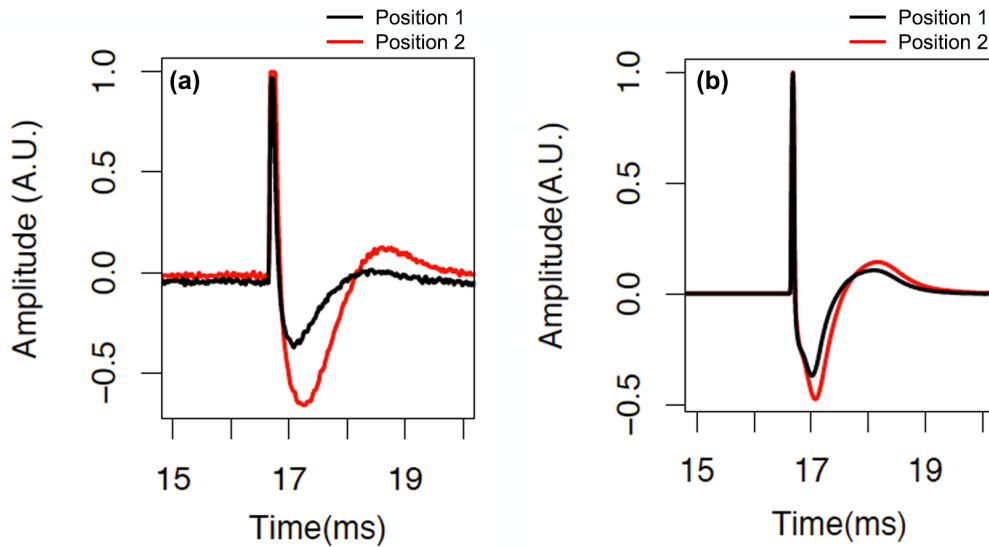


Fig. A.2 The averaged (a) optical and (b) electrical recording from the rabbit sciatic nerve preparation in vitro at position 1 (black) and position 2 (red). The estimated nerve conduction velocity is 52 m/s. Images are from our previous publication [264].

because the first peak appears at the same time in two channels. With the comparison of two-channel recordings, a short time delay between the successive peaks can be observed and calculated after signal processing. The estimated nerve conduction velocity around is 52 m/s in this experiment, which is in a well-accepted normal range of a healthy rabbit sciatic nerve. More details of research results can be found in our published papers [263–265].

To compare noise levels of optical and electrical recordings, baseline noise levels of two recording methods are measured and analysed in experiments individually. As shown in Fig. A.3 (a), the root mean square (RMS) value of optical recording noise was around 60 μV . In the electrical recording, the RMS value of noise was around 60 μV as well, but the most of noises in the electrical recording are at higher frequencies than the optical recording. The differences between distributions of noise power in the frequency spectrum of optical and electrical recordings demonstrate the low pass filtering properties of liquid crystal transducer because of its impedance, capacitance and equivalent electronic circuit model [266]. The recording shows that the presence of a liquid crystal transducer affects the amplitude of the stimulus artifact, but has a negligible impact on the signal. From Fig. A.3, it is clear that,

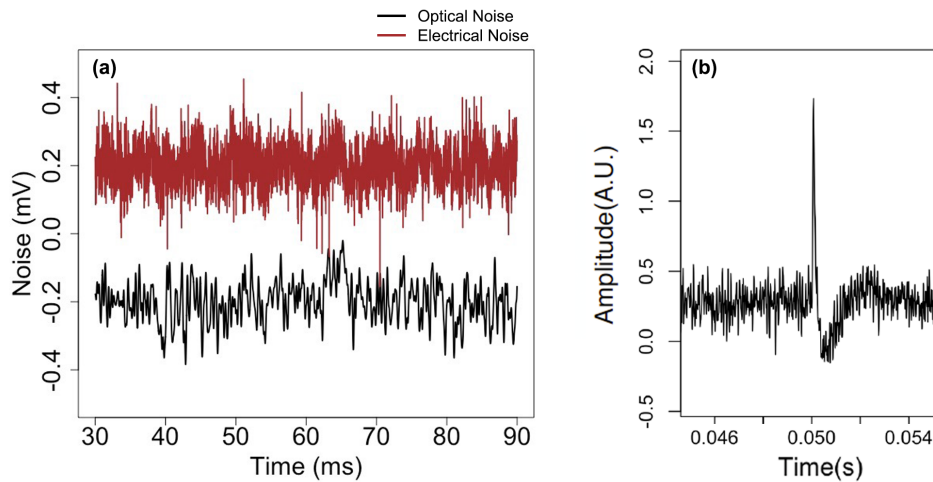


Fig. A.3 (a) The measured baseline noise from optical (black) and electrical (red) recordings of the rabbit sciatic nerve preparation in vitro and (b) the optical recording under one electrical stimulation without averaging in the rabbit sciatic nerve preparation in vitro. Images are from our previous publications [263–265].

although the noise in the optical recording is one of the biggest challenges for us to deal with, the nerve action potentials still can be detected using the proposed optical approach with or without averaging if the RMS value of noise is smaller than $100\ \mu\text{V}$.

Besides the studying of action potentials of the rabbit sciatic nerve, cardiac tissue activities are detected using the liquid crystal-based optical sensing technology, which presents the possibility of utilising this new optical approach in the field of cardiac physiology. Unlike the sciatic nerve, the cardiac tissue can generate electrical signals by itself. The study of electrical activities of the cardiac tissue, such as activation patterns, can help people understand its function and obtain important information from observation. Additionally, the continuous detection of electrical activities in the cardiac tissue at multiple positions allows us to understand the activation conduction in the organ. To demonstrate the feasibility of the liquid crystal-based optical approach in the cardiac tissue activity recording, electrical signals are recorded from rabbit sino-atrial cardiac preparations using two LC transducers (optrodes) from different positions at different temperatures. It is worth noting that the sino-atrial node (SAN) does not need to be activated by the external stimulus because it can drive the beating

by itself. The schematic of the experimental setup for the ex-vivo cardiac electro-physiology recording system is shown in Fig. A.4.

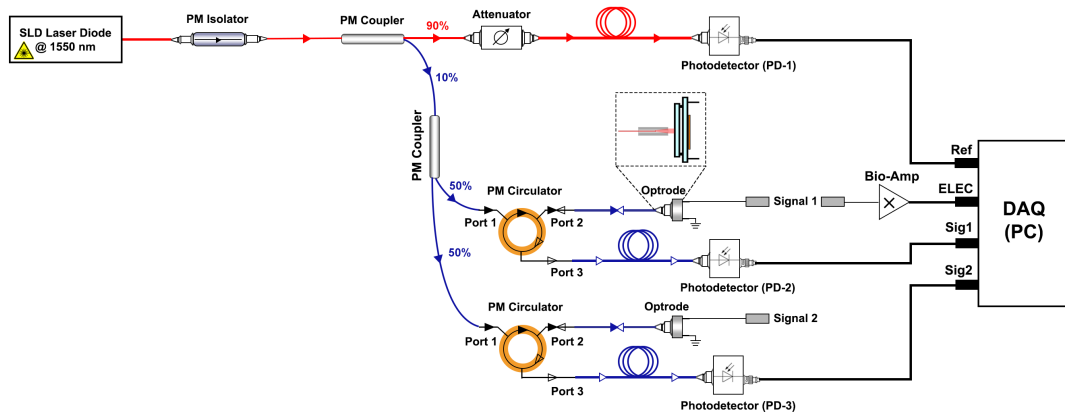


Fig. A.4 The schematic of ex-vivo cardiac electro-physiology recording system.

In the experimental setup, the light from the low noise super-luminescent diode is split into three light beams using one 90:10 optical coupler and one 50:50 optical coupler, instead of using the multiplexer as shown in Fig. A.1. One optical channel with 90 % optical power is detected by a photo-detector (PD-1) as a reference channel. The rest 10 % optical power is shared by two optical channels for recording cardiac tissue activities at two positions. The optical responses from two LC transducers (optrodes) are detected and recorded using two photo-detectors (PD-2 and PD-3) after optical circulators. Signals from three photo-detectors and one bio-amplifier are collected and recorded via DAQ and PC for further signal processing and analysis. Cardiac electrograms recorded by one LC transducer (optrode) is shown in Fig. A.5.

A.1.1 Improvement of the sensitivity of optrode

Although nerve compound action potentials and cardiac tissue activities are recorded using the sensing optrode recording system in proof-of-principle experiments, the performance of the optrode recording system is significantly limited by the sensitivity and the bandwidth of the LC transducer. To ensure the reliable detection of nerve action potentials or cardiac tissue activities with a peak amplitude lower than $50 \mu\text{V}$, one major goal of the future work is to

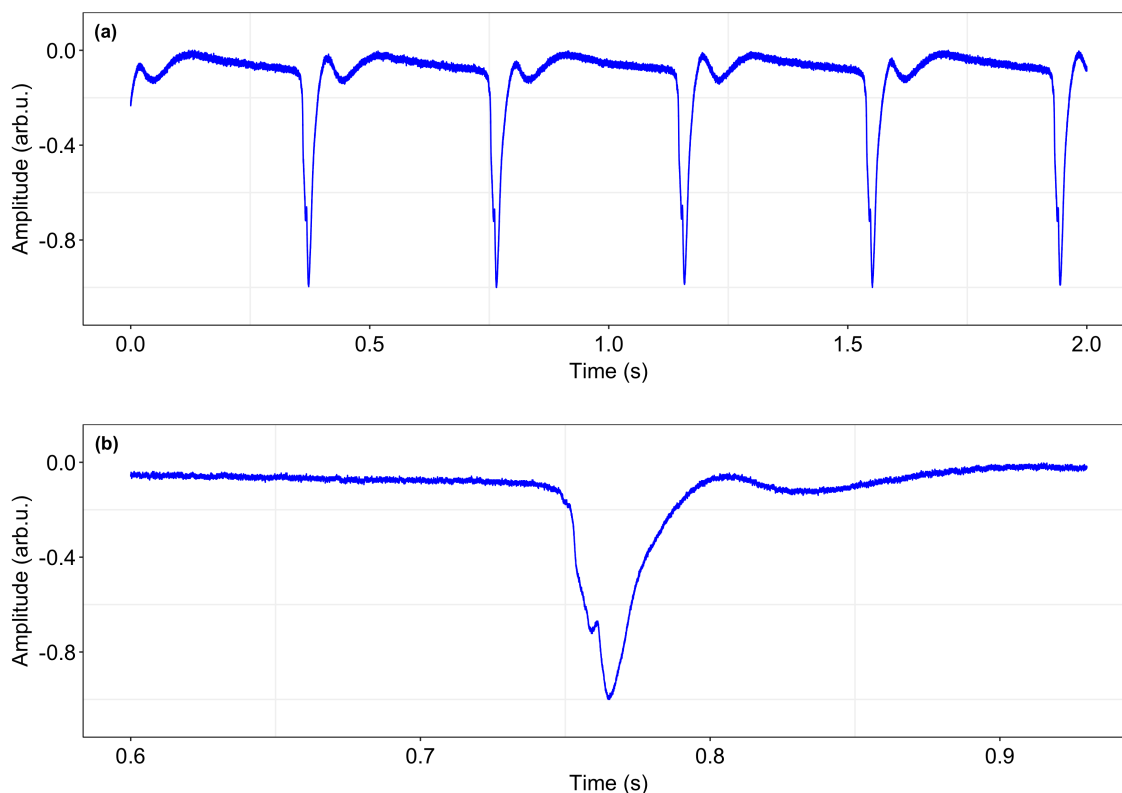


Fig. A.5 (a) The train of signals obtained from rabbit sino-atrial cardiac preparations ex-vivo, measured by LC transducer filled with D311 LC mixture. (b) One waveform extracted from the recording over 10 seconds.

enhance the sensitivity and the bandwidth of the LC transducer used in the optrode recording system. From our previous study on the LC transducer, its sensitivity and bandwidth of response are mainly determined by the liquid crystal mixture (e.g. 311, 313, 382, 383, 384, 397, 431, and 576) and the material of alignment layers (e.g. from Instec or Depo). In addition to the effects of physical parameters of the LC transducer on the detection performance, the quarter-wave plate can be added to the transducer to improve its sensitivity. To investigate the effects of LC material, alignment material, and presence of quarter-wave plate on the sensitivity and bandwidth and find out the optimal combination, a couple of LC transducers with different LC mixtures and alignment materials are characterised individually using the experimental setup shown in Fig. A.6.

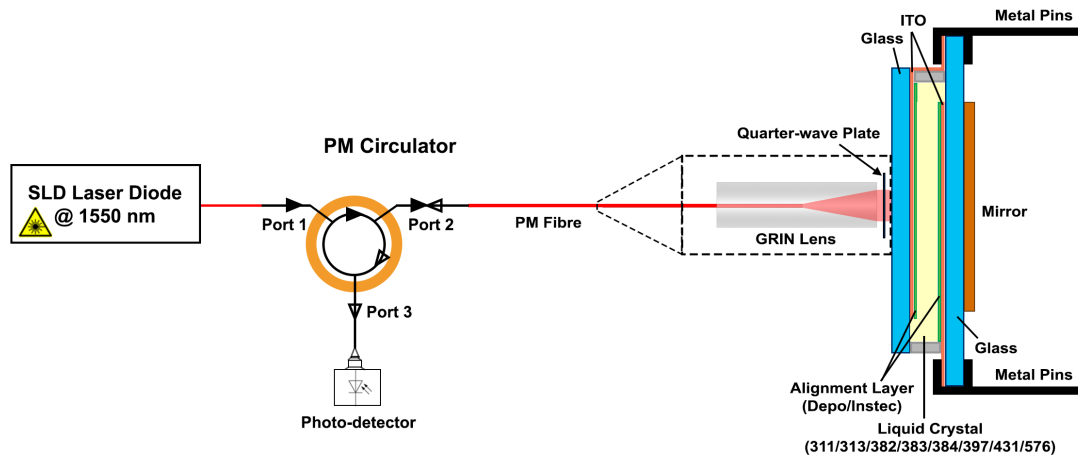


Fig. A.6 The experimental setup for the characterisation of LC transducers with different liquid crystal mixtures and alignment materials

In characterisation experiments, a sinusoidal signal with a frequency of 1 kHz and an amplitude of 0.5 V is applied across LC transducers, while optical responses from LC transducers are detected by the photo-detector. The S value is defined as a parameter representing the sensitivity of LC transducers, which can be calculated by the ratio of the peak-to-peak voltage to the mean voltage of the optical response. In other words, the S value can be understood as the ability of the LC transducer to respond to weak electrical signals. The -3 dB bandwidth of the LC transducer is obtained from the frequency response curve by applying a sinusoidal signal with varying frequencies ranging from 10 Hz to 50 kHz. The summary of sensitivity and bandwidth measurement results for the existing LC transducers with different LC mixtures or alignment materials is shown in Fig. A.7.

From measurement results of existing LC transducers, the maximal sensitivity is obtained by LC transducer D397 with a quarter-wave plate, which is around 96.90 %. However, its bandwidth is only 642.9 Hz, which means transducer D311 is not suitable for an optrode recording system. In contrast, the maximum bandwidth is around 10.7 kHz, which is achieved by transducer I397 with a quarter-wave plate, but its sensitivity is not as good as that of D397, which is around 19.04 %. Therefore, maximizing the sensitivity of the LC transducer without bandwidth trade-off becomes the major goal of this project. Based on the previous study on the liquid crystal cell, its sensitivity potentially can be improved in several ways.

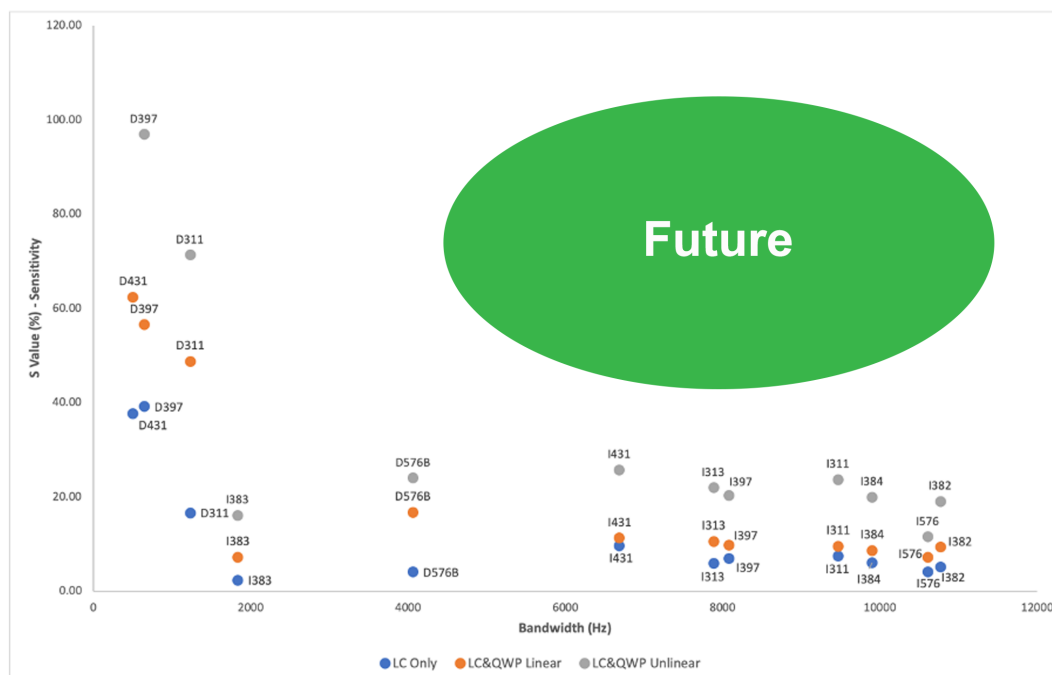


Fig. A.7 The measured S values and bandwidth results of existing LC transducers with different LC mixtures (e.g. 311, 313, 382, 383, 384, 397, 431 and 576) or alignment materials (e.g. from Instec or Depo).

1. Use other liquid crystal mixtures with a shorter helix pitch less than $0.2 \mu\text{m}$.
2. Try a new fabrication method of the LC alignment layer, e.g. photo-alignment technique, instead of rubbed planar-aligning polyimide substrates.
3. Develop the new generation of optical recording system based on the detection of the crossed reflection from the LC transducer, instead of the current parallel reflection.

A.1.2 Fabrication of the multi-optrode device

As discussed earlier, the objective of this project is to demonstrate the feasibility of our liquid crystal-based optical technology in the development of the new generation of neural interfaces that can record activation potentials from multiple positions in parallel. Therefore, the design and fabrication of the multi-optrode device become the next milestone to be achieved in the coming years. Cardiac mapping technology has been playing a crucial role in the study of arrhythmia and directing surgical procedures. The first cardiac mapping was

demonstrated on the dog's heart in 1915 by Thomas Lewis and M. A. Rothschild [267]. The idea of cardiac mapping is to simultaneously record the extracellular electrograms at multiple sensing points and thus to determine the electrical activity of the heart. The accurate location and orientation information exacted from extracellular electrograms recording are highly desirable for researchers to understand the pathophysiological mechanisms of arrhythmia and enhance the safety of directing curative procedures, such as catheter-ablation [268, 269]. The conventional electro-anatomical mapping (EAM) systems simultaneously acquire electrograms from multiple locations by using a multi-electrode array (MEA) with a fixed spatial resolution (around 1 mm) to achieve the spatio-temporal mapping of extracellular electrophysiology signals from the excitable tissue [270].

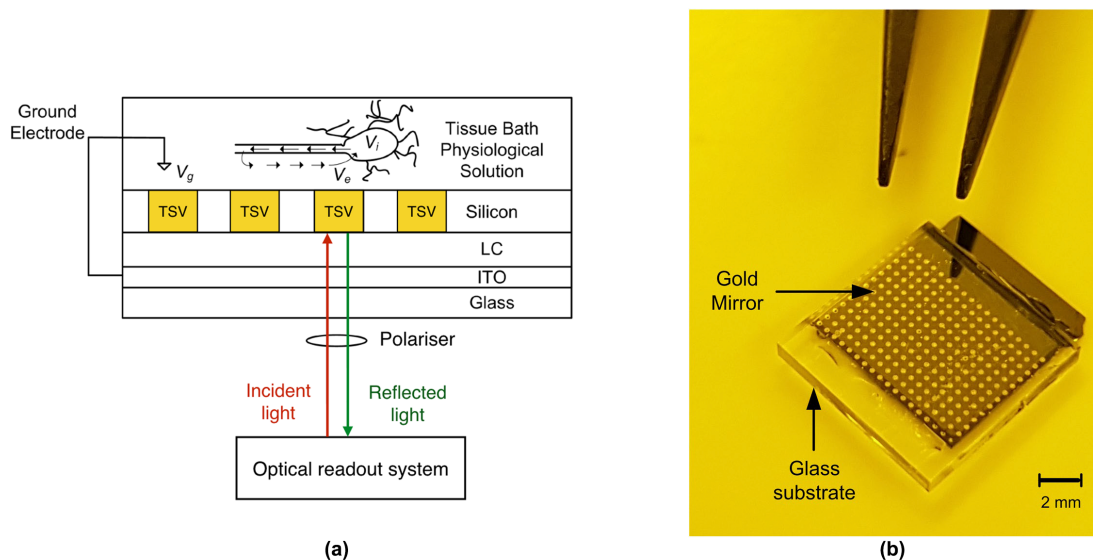


Fig. A.8 (a) The schematic of an optical readout system and (b) the fabricated optrode sensor array prototype with 13 rows of 18 vias (234 optrodes) in which the centre-centre spacing between the adjacent optrode is 500 μm . Images are reproduced from [266].

Unlike existing MEAs, the multi-optrode arrays (MOAs) can be easily scaled up to support a large number of sensing points (hundreds or thousands of channels) with a small dimension and a high spatial resolution, because it can get rid of the impedance matching issues plaguing their electronic counterparts. Therefore, the development of MOAs paves the way for the fabrication of the robust brain/machine interface which can scale up to millions of channels with a high spatial density, which makes it to be an attractive alternative to the

existing MEAs for EAM. To detect extracellular electrophysiology signals from excitable tissues at more than one position, an optical readout system was proposed in the previous publication as shown in Fig. A.8. The proposed prototype of the MOA device consists of a matrix of “pixels”, where the excitable tissue is in contact with the top of the gold TSVs and the ITO layer is a ground common to all pixels and the tissue bath [266].

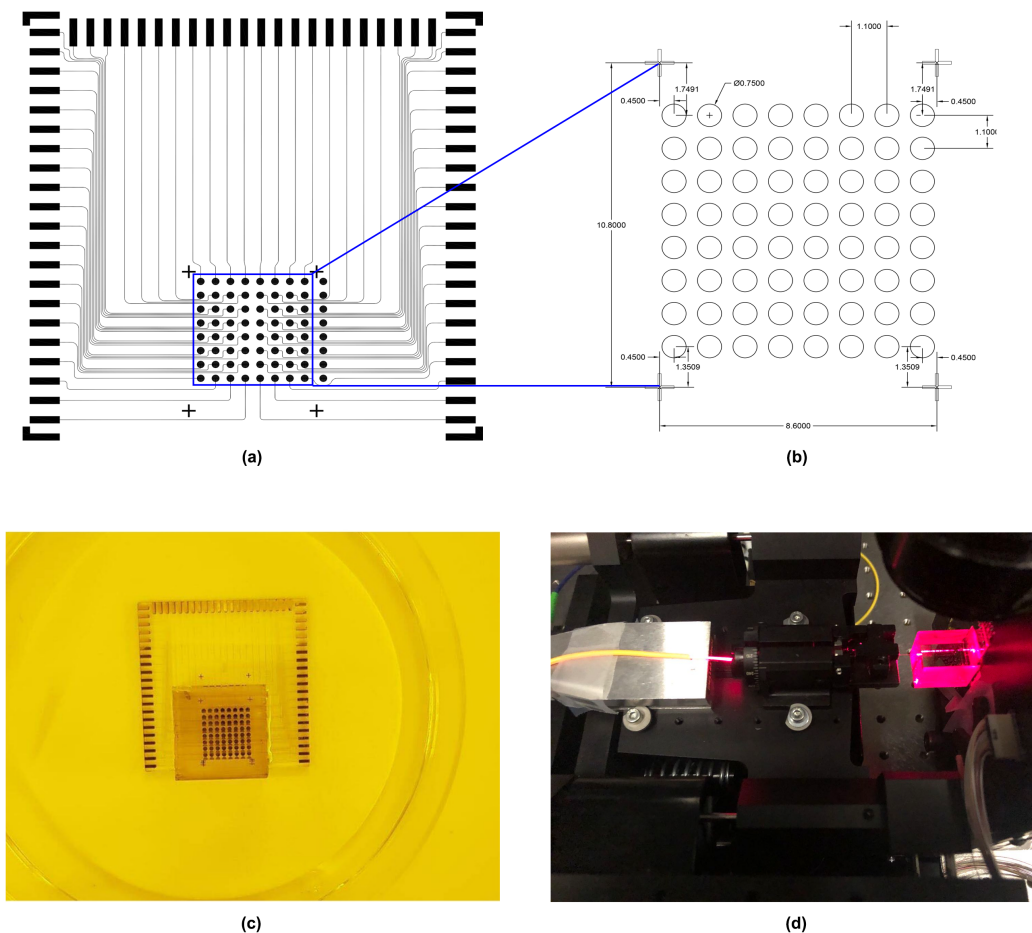


Fig. A.9 (a) The design schematic of a 64-channel multi-optrode device with electronic connections to the bottom side of the glass substrate. (b) The dimension of mirror arrays in the device demonstrates the center-center spacing between the adjacent mirrors is 1.1 mm. (c) The fabricated 64-channel multi-optrode device is integrated with 12 slices of glass. It is worth noting that 8 depressed cladding waveguides were directly inscribed in 8 glass substrates by ultrafast laser pulse inscription. (d) The visible (red) light from a single fibre is successfully coupled into an inscribed waveguide in the glass substrate.

To realize the simultaneous electrogram acquisition of MOAs with a high spatial resolution, two different designs are proposed now and will be investigated in the future. In the first design, multiple waveguides are inscribed within each glass substrate using the femtosecond laser line-by-line inscription method to build a two-dimension electro-anatomical map. The light from each fibre can be coupled into one inscribed waveguide and then guided to an individual optrode (LC transducer unit). The schematic of the 64-channel multi-optrode device with the inscribed waveguides is shown in Fig. A.9. The measured optical responses to applied signals demonstrate that its performance is comparable to the single-channel optical transducer. However, the challenge with this design is the coupling of light from a polarization-maintaining fibre into an inscribed waveguide in the glass substrate. In the fabrication process, the assembly procedure takes a long time and it is very sensitive to small misalignment. For this reason, the performance of the individual optrode is not consistent and often worse than expected. To improve its performance in the future, the glass substrate can be shortened to reduce the optical loss caused by the light propagation in the waveguide. In addition to this, we can improve the precision of the assembly procedure by using manual or automatic high precision positioning tools and enhance the stability of the assembly procedure by applying other optical adhesives instead of UV light-curing optical adhesive.

The second design is to make use of a pre-assembled two-dimensional fibre array as one substrate of the multiple optrode array device shown in Fig. A.8. As a result, the fibre array can replace the waveguide array in the first design to deliver light to each optrode, without an intermediate medium. In the future, we plan to fabricate 2-channel, 4-channel, and 16-channel multiple optrode array devices using these pre-assembled two-dimensional fibre arrays. The 9×9 81-channel pre-assembled two-dimensional fibre array is shown in Fig. A.10.

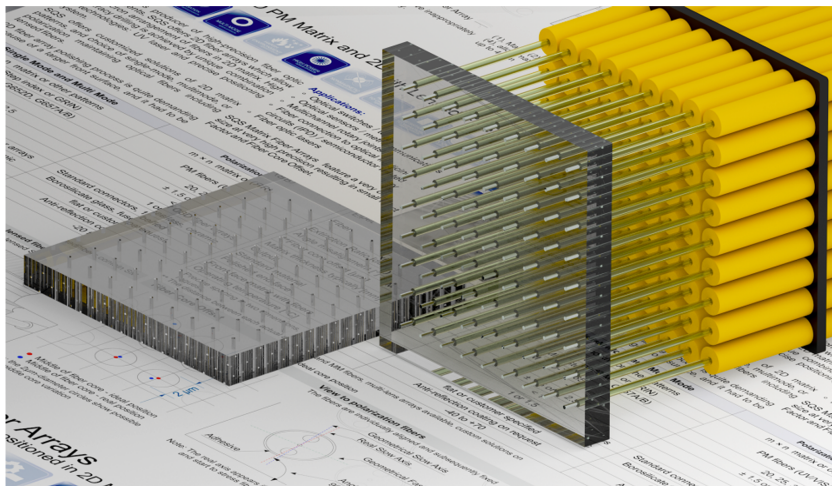


Fig. A.10 The photo of a pre-assembled two-dimensional fibre array, which is similar to the multi-channel light delivery section of the multiple optrode array that we plan to fabricate and test in the future. Image is from the manufacturer.